Extracellular Matrix Mechanics and Implications for Cellular Mechanosensing

Karin Albertina Jansen

The work described in this thesis was performed at the FOM Institute (AMOLF), Science Park 104, 1098 XG Amsterdam, The Netherlands. This work is part of the research programme of the *Stichting voor Fundamenteel Onderzoek der Materie* (FOM), which is financially supported by the *Nederlandse Organisatie voor Wetenschappelijk Onderzoek* (NWO).

ISBN 978-94-92323-00-2

A digital version of this thesis can be obtained from http://www.ub.vu.nl. Printed copies can be obtained by addressing the library at the FOM Institute AMOLF: library@amolf.nl.

VRIJE UNIVERSITEIT

Extracellular Matrix Mechanics and Implications for Cellular Mechanosensing

ACADEMISCH PROEFSCHRIFT

ter verkrijging van de graad Doctor aan
de Vrije Universiteit Amsterdam,
op gezag van de rector magnificus
prof.dr. V. Subramaniam,
in het openbaar te verdedigen
ten overstaan van de promotiecommissie
van de Faculteit der Exacte Wetenschappen
op donderdag 11 februari 2016 om 13.45 uur
in de aula van de universiteit,
De Boelelaan 1105

door

Karin Albertina Jansen

geboren te Doetichem

promotor: prof.dr. G.H. Koenderink

PUBLICATIONS COVERED IN THIS THESIS

K.A. Jansen, D.M. Donato, H.E. Balcioglu, T. Schmidt, E.H.J. Danen, G.H. Koenderink, A Guide to Mechanobiology: Where Biology and Physics Meet, BBA 1853, 2015, 3043-3052 *(Chapter 1)*

I.K. Piechocka, K.A. Jansen, C.P. Broedersz, N.A. Kurniawan, F.C. MacKintosh, G. H. Koenderink, Multiscale strain-stiffening of semiflexible bundle networks, Soft Matter, in review *(Chapter 2)*

K.A. Jansen, R.G. Bacabac, I. K. Piechocka, G.H. Koenderink, Cells actively stiffen fibrin networks by generating contractile stress, Biophysical Journal 105(10), 2013, 2240-51 *(Chapter 3)*

K.A. Jansen, A. Zhmurov, G. Portale, D.H. Merino, R.I. Litvinov, B.E. Vos, V. Tutwiler, I.K. Piechocka, N.A. Kurniawan, W. Bras, J.W. Weisel, V. Barsegov, G.H. Koenderink, Unfolding of fibrin gels under strain, manuscript in preparation *(Chapter 4)*

K.A. Jansen, A. Zhmurov, G. Portale, D.H. Merino, R.I. Litvinov, V. Tutwiler, B.E. Vos, N.A. Kurniawan, W. Bras, J.W. Weisel, V. Barsegov, G.H. Koenderink, Fibrin Scattering Depends on Bundle Size, manuscript in preparation *(Chapter 4)*

K.A. Jansen, Andre Scholich, G.H. Koenderink, Microscopic view of fibrin blood clots, manuscript in preparation *(Chapter 5)*

A. Sharma, A.J. Licup, K.A. Jansen, R. Rens, M. Sheinman, G.H. Koenderink, F.C. MacKintosh, Strain-controlled criticality governs the nonlinear mechanics of fibre networks, Nature Physics, accepted *(Chapter 6)*

K.A. Jansen, A. J. Licup, A. Sharma, R. Rens, F.C. MacKintosh, G.H. Koenderink, Architecture and Normal Stress Govern Collagen Mechanics, manuscript in preparation *(Chapter 6)*

OTHER PUBLICATIONS

J.L. Elliott, M. Der Perng, A. R. Prescott, K.A. Jansen, G.H. Koenderink, Roy A. Quinlan, The specificity of the interaction between CRYAB and desmin filaments and its impact on filament aggregation and cell viability, Philosophical Transactions B 368(1617), 2013, 20120375

N.A. Kurniawan, T.H.S. van Kempen, S. Sonneveld, T.T. Rosalina, B.E. Vos, K.A. Jansen, G.W.M. Peters, F.N. van de Vosse, G.H. Koenderink, Buffers Affect Fibrin Clot Structure by Slowing Down Lateral Aggregation of Protofibrils, manuscript in preparation

For my brother

Contents

1. Introduction: A Guide to Mechanobiology, where Physics and Biology Meet

Cells actively sense and process mechanical information that is provided by the extracellular environment to make decisions about growth, motility and differentiation. It is important to understand the underlying mechanisms given that dysregulation of the mechanical properties of the extracellular matrix (ECM) is implicated in various diseases, such as cancer and fibrosis. Moreover, matrix mechanics can be exploited to program stem cell differentiation for organ-on-chip and regenerative medicine applications. Mechanobiology is an emerging multidisciplinary field that encompasses cell and developmental biology, bioengineering and biophysics. Here we provide an introductory overview of the key players important to cellular mechanobiology, taking a biophysical perspective. In view of the focus of this thesis on the interaction of cells with the extracellular matrix, we focus on a comparison between artificial flat substrates, which have been the most widely studied model system until now, with more physiologically relevant, three dimensional substrates.

Karin A. Jansen, Dominique M. Donato, Hayri E. Balcioglu, Thomas Schmidt, Erik H.J. Danen, Gijsje H. Koenderink

1.1 Cellular Environments

Cells in our body actively sense and respond to a variety of mechanical signals. The mechanical stiffness of the surrounding extracellular matrix (ECM) critically determines normal cell function, stem cell differentiation and tissue homeostasis [1, 2]. Conversely, abnormal changes in ECM stiffness contribute to the onset and progression of various diseases, such as cancer and fibrosis [3]. Cancer tissues can be up to 10-fold stiffer than healthy tissues, which is correlated with tumor cell survival and enhanced proliferation [3–5]. Additionally, cells often experience forces in the form of shear stress during breathing and blood flow, compression and tension due to muscle contraction. Forces also play a crucial role in regulating tissue morphogenesis in developing embryos [6, 7]. The sensitivity of cells to forces and substrate stiffness has been recognized as a powerful tool in tissue engineering, where it can be harnessed to design biomaterials that optimally guide stem cells or resident cells in the patient towards generating a functional replacement tissue. Given its central importance in cell function and human health, mechanobiology has emerged as a new and growing field that attracts researchers from disciplines ranging from cell and developmental biology, to bioengineering, materials science and biophysics.

A central element in mechanobiology is cellular 'mechanosensing' (see Box 1). Cells actively probe the rigidity of their extracellular environment by exerting traction forces via transmembrane proteins termed integrins [8]. It is still poorly understood how probing by traction forces allows cells to sense matrix stiffness and how cells transduce this mechanical information into a cellular response. Answering these questions is complicated by the large number of mechanosensors and -transducers that have been identified so far [9]. Prominent examples are paxillin [10], vinculin [11, 12], talin [13], p130CAS [14, 15], integrins [16, 17], the actin cytoskeleton (CSK) [18–20] and mechanosensitive ion channels [21]. It is still unclear how these components work together to regulate mechanosensing. Also, most experimental studies until now were performed with cells cultured on top of two dimensional (2D), and often rigid, substrates, which inadequately mimic most physiological contexts.

Mechanosensing and -transduction are cellular processes that involve both intra- and extracellular components, as illustrated in Fig. 1.1. The main structural components that contribute are (1) integrins, (2) the extracellular matrix and (3) the intracellular CSK. Mechanical forces and biochemical signaling are integrated by various intracellular signaling pathways. In this introductory chapter, we will provide an overview of the roles of these contributors to cellular mechanobiology and the techniques to measure cellular traction forces. Note that we will not touch upon mechanosensitive ion channels, which are reviewed elsewhere [21], nor will we discuss cell-cell interactions, which also play an important role in mechanosensing [22, 23]. Given the focus of this thesis on

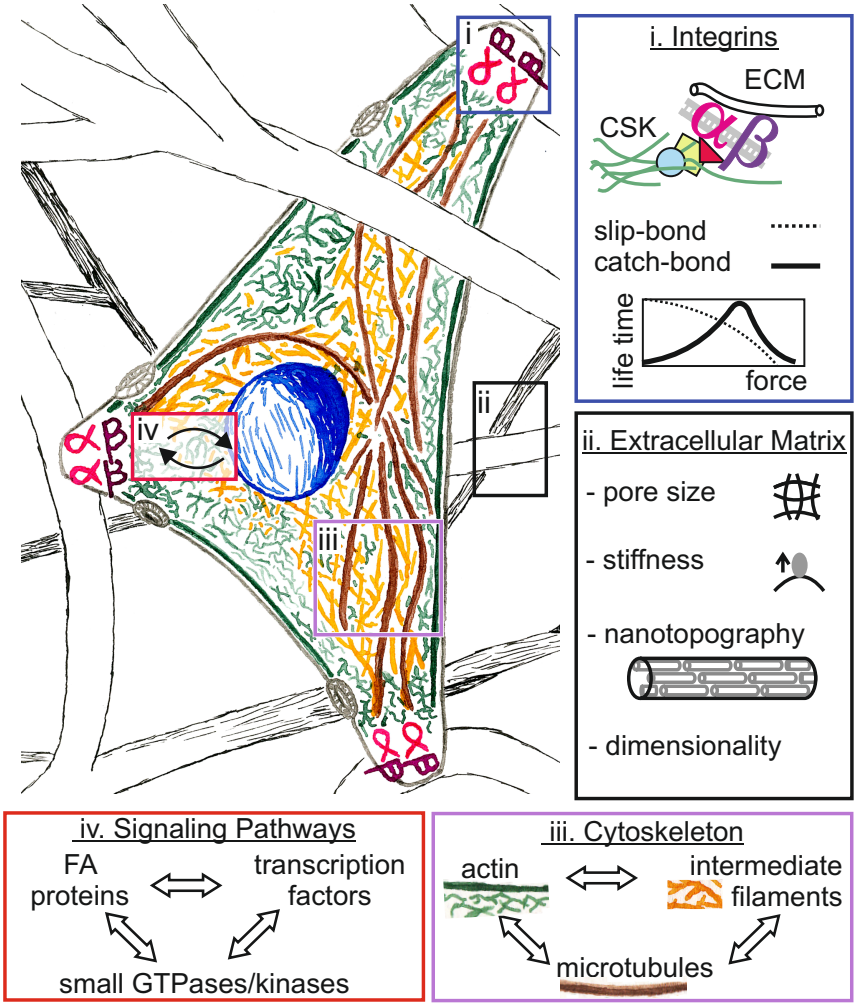

Figure 1.1: Schematic showing a cell inside a three dimensional fibrous extracellular network. The boxes indicate the focus areas of this introductory review. (i) Integrins are composed of an α (pink) and β subunit (purple) and are clustered in focal adhesions (FAs) together with other FA proteins (triangle, square and circle). The adhesions connect the extracellular matrix (ECM) and the (actin) cytoskeleton. Integrins can be classified as slip- or catch-bond adhesion molecules, which differ in their bond life time under an applied force. (ii) The ECM provides multiple cues to the cell, specifically pore size, stiffness, nanotopography and dimensionality. (iii) The cytoskeleton is composed of actin (green), intermediate filaments (yellow) and microtubules (brown). (iv) Summary of important signaling pathways. Note that we will not discuss mechanosensitive ion channels (gray pores). The cell nucleus is depicted in blue.

cell behavior in reconstituted 3D ECM networks, we will focus this review in particular on a comparison between cellular mechanobiology on 2D substrates and inside 3D environments designed to mimic connective tissue. The measurement of traction forces has a long history, which we will briefly review. We also introduce two model systems that are widely used for creating 3D cellular environments, and will also be used in this thesis: fibrin and collagen networks. Both of these proteins form a fibrous mesh work, but they exhibit very different mechanical properties. The physical basis for this difference is one of the central topics of this thesis. Furthermore, we will comment on the applications of mechanobiology in tissue engineering. We will conclude with a brief outline of the aims and topics of this thesis.

1.2 Contributors to Cellular Mechanosensing

Integrins play a central role in cellular mechanosensing because they physically connect the CSK to the ECM, typically in clusters termed 'focal adhesions' (FAs). Integrins are transmembrane proteins that are heterodimers of an α and β subunit and are restricted to the metazoa [8]. So far, 24 different heterodimers formed by combinations of 18 different α subunits and 8 β subunits have been identified [8]. Most integrins recognize multiple ligands, which share common binding motifs such as the RGD or LDV motif [24]. The integrin $\alpha v\beta 3$ can for instance bind vitronectin, fibronectin and fibrinogen through the RGD-binding motif.

The *extracellular matrix* (ECM) is a complex protein mesh work that forms the scaffold to which cells adhere. It provides mechanical support to cells and tissues, and acts as a reservoir for growth factors, cytokines and proteolytic enzymes. There are two broad classes of ECM: basement membrane and connective tissue. Basement membranes are thin structures that provide a two-dimensional (2D) substrate onto which polarized cells such as epithelial and endothelial cells adhere. Its main components are laminin, collagen IV, nidogen and heparan sulfate proteoglycans [25]. In contrast, connective tissues provide a fibrous 3D scaffold whose structural components are mainly fibrillar collagens (mostly type I and II, mixed with III and/or V), proteoglycans and glycosaminoglycans [26]. The diameter and organization of the collagen fibers are tailored to the biomechanical function of each tissue. The fibrils are, for example, thick and aligned in stiff tissues like tendon to ensure tensile strength, whereas they are thin and organized in meshworks in the cornea to ensure optical transparency. Proteoglycans and glycosaminoglycans are hydrophilic macromolecules forming a background matrix for the collagen fibers, which facilitate water retention and influence cell migration and ECM deposition [27]. The ECM also contains non-structural components that modulate cell-ECM interactions, such as thrombospondin 1 and tenascins [28]. Under influence of force, ECM proteins could also act as a mechanotransducer by exposing cryp−

Box 1: Terms that are often used in the field of mechanobiology

Mechanobiology: A field at the interface of biology, physics, and bioengineering, which focuses on how cell/tissue mechanics and physical forces influence cell behavior, cell and tissue morphogenesis, and diseases related to these processes.
Mechanosensing (/sensation): The process of a cell sensing mechanical signals provided by its environment.
Mechanotransduction: The process of translating mechanical signals into a cellular response.
Durotaxis: Directed cell motility in response to gradients in substrate rigidity.
Contact guidance: Directed cell migration or orientation based on anisotropy (alignment) of the microenvironment, such as collagen fibers in 3D or micropatterned adhesive lines on a 2D substrate.
Outside-in signaling: Mechanical cues in the environment causing intracellular signaling cascades, which affect cellular processes such as migration, growth, and differentiation.
Inside-out signaling: Intracellular processes affecting the mechanical properties of the environment by exertion of traction forces and secretion/breakdown of ECM material.
Integrin: Heterodimeric transmembrane protein that physically connects the ECM to the CSK and acts as a bidirectional signaling receptor.
Slip-bond: Receptor-ligand interaction whose lifetime is reduced when mechanically loaded.
Catch-bond: Receptor-ligand interaction whose lifetime is enhanced with increasing load to a maximum value, followed by a gradual decrease when the load is further increased.
Cell-matrix adhesion: Cell-ECM connections mediated by clusters of integrin in the plasma membrane. This term includes FAs, focal complexes, focal contacts, fibrillar adhesions, and nascent adhesions.
Adhesome: The collection of more than 150 proteins associated with cell-matrix adhesions that links the ECM and the CSK.
Nascent adhesion: A cell-matrix adhesion during its initial phase of formation. Usually, such an adhesion is significantly smaller and more punctuate than mature FAs. Nascent adhesions are thought to be enriched with FA proteins such as talin and paxillin.
Focal complex: A cell-matrix adhesion that is usually found at the leading edge of migrating cells. Focal complexes can either be nascent adhesions on their way to maturation or simply short-lived ECM-cell contacts.

(continues on next page)

(Box 1 continued)

Like nascent adhesions, they are smaller and more punctuate than focal adhesions. They contain a larger subset of adhesome proteins than nascent adhesions, but still a smaller subset than FAs.

Focal adhesion (FA, a.k.a. focal contact): Cell-matrix adhesions that are usually associated with actin stress fibers. They have an elongated form and are found at the front, rear, and periphery of the cell. They are one of the most mature ECM-cell contact types, besides fibrillar adhesions, and are therefore associated with a larger variety of proteins from the adhesome. They are also usually at least twice as large as nascent adhesions or focal complexes.

Fibrillar adhesion: Elongated cell-matrix adhesions that are usually not found in the lamellipodium, but under the nucleus and the lamella behind the lamellipodium. The length of these adhesions is several times larger than that of FAs.

Acto-myosin contractility: Contractile activity of the actin cytoskeleton mediated by non-muscle myosin II-A and II-B.

tic sites and growth factors [29]. During wound healing, cells encounter a provisional ECM that forms as a result of blood clotting. This matrix consists of a scaffold of fibers made of the plasma proteins fibrin and fibronectin. Due to their biocompatibility and physiological scaffold role, both collagen and fibrin are popular biomaterials for *in vitro* studies and tissue engineering. However, it is important to emphasize that such simplified matrices do not mimic the full tissue-specific context (in terms of architecture and chemical composition) that is offered by the *in vivo* ECM. The architecture, composition and stiffness of the *in vivo* ECM is further subject to changes during disease progression and aging. Since cells are sensitive to all of these extracellular cues, the ECM is increasingly recognized as an active player and potential therapeutic target in diseases such as fibrosis, artherosclerosis and cancer [5, 30–33].

The *cytoskeleton* (CSK) is a space-filling network of protein filaments that enables cells to maintain their shape and mechanical strength [34, 35]. The CSK enables cells to withstand external forces, while at the same time being dynamic and self-deforming. The mammalian CSK comprises three types of protein filaments: actin, microtubules (MTs) and intermediate filaments (IFs). Actin and MTs are polar filaments with two structurally distinct ends, which are capable of generating pushing and pulling forces by coupling polymerization to nucleotide hydrolysis. In contrast, IFs are nonpolar and more stable. All three filaments can be classified as semiflexible polymers: they remain straight under the influence of thermal fluctuations over a length scale that is comparable to their 'persistence length'. This characteristic lengthscale is much longer for MTs (a few mm) than for IFs (0.5 μm) and actin (10 μm). As a result, actin and IFs are generally considered to provide the main source

of cell stiffness, whereas the more rigid MTs may provide resistance to compression forces [36]. Purified networks of actin and IFs increase their stiffness under the influence of force. In other words, these networks strain-stiffen in response to mechanical shear or stretch [37–39]. This phenomenon allows cells to actively stiffen their actin cytoskeleton on hard substrates by contraction with myosin motors [1]. Moreover, strain-stiffening of IFs is thought to prevent excess deformation of cells and epithelial tissues [38, 39].

1.3 Role of the ECM in Mechanobiology

In this section, we will focus on the influence of physical cues provided by the ECM on cell behavior. Cells embedded in 3D interstitial matrices are influenced by various factors that are difficult to decompose, such as global (i.e. macroscopic) and local (i.e. fiber) stiffness, matrix topography, the porosity and the dimensionality. Below we will review experimental studies that have sought to disentangle these factors using biomimetic 3D ECM matrices or 2D substrates.

1.3.1 ECM Stiffness

It is now well recognized that cells cultured on top of a 2D substrate actively sense and respond to its stiffness [1, 40–42]. Many fundamental aspects of cell behavior are mechanosensitive, including adhesion, spreading, migration, gene expression and cell-cell interactions [41, 43–48]. Substrate stiffness can also regulate stem cell differentiation and compete with biochemical cues [1]. Recent experiments with stem cells on photodegradable substrates showed that stem cells even remember the mechanical history of their environment [49].

Studies of cells on 2D substrates are usually performed with nonadhesive polyacrylamide (PAA) or Polydimethylsiloxane (PDMS) gels coated with ECM proteins or ligands such as RGD peptides. Surface coupling should be chosen with care, since the distance between tethering points can influence cell fate [50] and cells can pull ligands from the surface if they are anchored too weakly [51]. The thickness of the gels should also be chosen with care, because cells can feel the stiff underlying glass/plastic substrate if the gel is too thin [52, 53]. Systematic studies showed that cells on top of PAA gels can sense over a distance of a few tens of microns [52, 53]. However, this length scale can be increased to $\sim$200 μm for fibrous networks of collagen [54] and fibrin [55]. The long range of force transmission in these ECM networks has been variously ascribed to strain-stiffening under the influence of cellular traction forces [55] or to the fibrous nature of the ECM [56]. The second explanation is supported by finite-element modeling of the transmission of traction forces in collagen [56] and fibrin [57] networks. These simulations show that cell tractions are concentrated in the relatively stiff ECM fibers, thus propagating farther than in a homogeneous elastic medium even if this elastic medium strain-stiffens [56].

Finite-element modeling and analytical theory further showed that cell-induced alignment of collagen fibers further contributes to making force transmission anomalously long-ranged [58].

Unclear is whether cells sense their environment by applying a constant stress (i.e. force) and reading out the strain (i.e. deformation) or vice versa. Theoretical models suggest that cells may readjust their contractile activity and CSK organization to maintain either an optimal strain or an optimal stress [59]. Experiments with elastic micropost array substrates indicated that epithelial cells and fibroblasts maintain a constant substrate strain [41, 60, 61]. However, recent measurements of traction forces for fibroblasts on PAA gels with a wider range of Young's moduli (6 to 110 kPa) suggest that cells switch from maintaining a constant strain on soft gels (Young's modulus below 20 kPa) to maintaining a constant stress on stiffer substrates [51]. It was proposed that the cells increasingly align their actin stress fibers to sustain a constant substrate strain as the substrate stiffness increases. At substrate rigidities above 20 kPa, the maximal contractile force that the aligned actomyosin units can generate would reach a limit. This interpretation is supported by a study of substrate-dependent stress fiber alignment [62] and a model representing the cell as a prestrained elastic disk attached to an elastic substrate via molecular bonds [63]. It is still unclear how these findings translate to the situation of a cell embedded in a 3D fibrous matrix. One study of fibroblasts inside porous collagen-glycosaminoglycan (GAG) matrices suggests that cells maintain a constant traction stress [64].

Unlike synthetic PAA and PDMS hydrogels, whose stiffness is constant up to large strains, networks of fibrin and collagen strain-stiffen as soon as the strain reaches values of a few percent [39, 65, 66]. It has been proposed that this nonlinear elastic response strongly influences cellular behavior based on studies of fibroblasts and stem cells cultured on top of thick fibrin biopolymer gels, which revealed that cell spreading was independent of the linear elastic modulus of the gels and similar to spreading on stiff PAA gels [55]. Apparently, the cells sense a stiff environment because they actively stiffen the fibrin network by exerting traction forces. Atomic force microscopy (AFM) nanoindentation as well as macroscopic shear rheology showed that cells cultured inside or on top of fibrin gels indeed cause network stiffening [55, 67]. In case of collagen gels, there is also evidence that buildup of stresses originating from cellular traction forces affect fibroblast morphology and motility [68]. Cell-induced ECM stiffening may play an important role in diseases, such as cancer and fibrosis, where it may provide a positive feedback that enhances cell contractility [33].

Summarizing, there is overwhelming evidence that mechanical properties (linear and nonlinear) of the substrate or ECM play an important role in determining cell fate. It is still an open question to what extent a cell embedded

inside a 3D fibrous ECM matrix senses the stiffness of the overall network (i.e. *global* stiffness), as on 2D substrates, or the *local* stiffness, i.e. the resistance of individual ECM fibers to bending and stretching. Furthermore, recent studies of cells on 2D hydrogels varying in their viscous but not their elastic modulus showed that cell differentiation is also sensitive to the viscous modulus [69, 70]. Moreover, cell spreading on soft substrates was shown to be strongly enhanced when the substrate (an ionically crosslinked alginate hydrogel) exhibited stress relaxation, an effect that could be recapitulated using a stochastic lattice spring model [71]. It was proposed that stress relaxation in the substrate may facilitate cell spreading by allowing cells to cluster ECM ligands. Viscous effects are indeed likely to be important since cellular time scales of traction force generation can be slower than the time scales at which the mechanical properties of cell substrates are generally measured [72].

1.3.2 Nanotopography

Structural components such as collagen [73], fibrin [74] and fibronectin [75] form hierarchically structured fibers that are radically different from the surface presented by standard 2D hydrogels. However, developments in nanotechnology and micropatterning have allowed for more advanced 2D substrates with controlled topography and adhesion areas that mimic tissue morphologies [76–78]. When the surface is patterned with nanoridges, cells align parallel to the nanoridges and migrate along them, in a process known as 'contact guidance' [76–79]. Furthermore, it was shown that cells can distinguish differences in height of a few nanometers [79–81] and can cling onto adhesion regions as small as 8 nm [82]. Cells are also sensitive to the distance between adhesion islands, as demonstrated by studies with ordered patterns of RGD-coated nanoparticles [83, 84]. Furthermore, disorder in the position of small adhesion islands can optimize cell differentiation [85]. Nanotopography is therefore a powerful design parameter in tissue engineering, as illustrated by a recent study showing that a controlled nanotopography enhances bone formation around tooth implants [86].

1.3.3 Pore Size

In vitro studies of cells embedded inside reconstituted networks composed of collagen or fibrin have shown that cell spreading and migration is hampered when the mesh size becomes smaller than the size of the nucleus [67,87,88]. The critical mesh size where cell migration is affected depends on the ability of the cells to degrade the matrix with proteolytic enzymes and on the deformability of the nucleus, which is governed by lamins [89, 90]. The pore size of collagen and fibrin networks can be controlled by tuning the protein concentration and polymerization temperature [88, 90–92]. However, these variations also affect the global and local (fiber) stiffness and network structure. The influence of pore size on cell behavior can be studied in isolation by using microfabricated

channels [93], synthetic polymer gels [94, 95] or by crosslinking the bionetwork with glutaraldehyde at a fixed polymerization condition [96]. These studies revealed that pore size controls migration speed [93, 94, 96]. Also it controls stem cell fate by controlling cell shape [95].

The fibrous nature of the ECM limits the availability of binding sites for cells. There have been several studies using model (synthetic) 3D matrices where the ligand density was varied independently of the network stiffness and pore size [94, 97, 98]. These studies suggest an increase in cell spreading and migration speed with increased ligand density. This is in contrast to 2D studies, where an optimum in both parameters is observed at intermediate ligand densities [43, 44]. However, it should be noted that the pore size of the synthetic 3D gels was in the nm-range, which is outside the physiologically relevant size regime. The thickness of the fibers in the ECM limits the size of FAs [99]. However, it was shown that cells can bend and reorient the fibers to increase the adhesion area.

We finally note that the ECM pore size can also affect cell behavior in tissues by influencing the permeability and hence interstitual flow. Fluid pressure in tissues was shown to affect cell migration and the distribution of vinculin, actin and α-actinin [100].

1.3.4 Dimensionality

When considering a cell inside a 3D fibrous ECM, it is unclear what is the effective dimensionality that the cell perceives. If the cell encounters a single fiber, the environment is perhaps effectively 1D. Indeed, the cell migration speed on thin micropatterned lines of ligands on a 2D substrate was shown to be comparable to the migration speed inside 3D cell-derived matrices, suggesting that the 1D situation is relevant *in vivo*, at least in certain contexts [101]. However, when the collagen fibers are thick due to bundling, as in dermal tissue, sarcoma cells were shown to behave as if on a 2D environment [102]. Cells embedded in reconstituted collagen networks, which consist of thinner collagen fibrils, usually interact with multiple fibers and may therefore sense a more 3D environment. The cells typically adopt a spherical or spindle-like shape instead of the flat 'pancake' shape seen on (rigid) 2D substrates [103,104]. These characteristic cell shapes are recovered when cells are sandwiched between two flat substrates, suggesting that simultaneous adhesion of the ventral and dorsal sides of the cell contributes to the 3D phenotype [105].

1.4 Integrins

Integrins are bi-directional signaling receptors. Intracellular proteins bind to the tail region of integrins, thus causing conformational changes in the head region that increases the affinity for its extracellular ligands (*inside-out signaling*). Vice versa, ligand binding triggers conformational changes that activate

intracellular signaling cascades (*outside-in signaling*). Ligand binding additionally promotes integrin clustering, which is essential for cell spreading [83]. Integrins recognize specific motifs in the ECM and also respond to physical ECM properties. In this section, we will briefly review the molecular features of integrin mechanosensing and compare the role of integrins in 2D and 3D environments.

1.4.1 Molecular Basis of Integrin Mechanosensing

Single-molecule force spectroscopy measurements using AFM or optical tweezers have shown that mechanical loading can directly influence the lifetime of integrin-ECM bonds. Some integrins, such as αIIbβ3, exhibit slip-bond behavior characterized by a decreased lifetime with increasing load [106], whereas others, such as $\alpha5\beta1$, exhibit catch-bond behavior characterized by an increased lifetime with increasing load [107, 108]. Catch-bond behavior is a common response for many adhesion molecules [109]. Theoretical modeling has shown that catch-bond clusters can in principle act as autonomous mechanosensors [16, 17]. However, the relative importance of this mechanism compared to that of other putative mechanosensors involved in connecting integrins to the nucleus and the CSK is unresolved [45].

The spatial distribution of extracellular ligands has been shown to play a role in stem cell behavior [110], lineage determination [111] and the cellular response to an applied force [112]. Clustering of integrins to form FA complexes requires a certain minimum ligand density. Various studies based on nanopatterned surfaces showed that the maximum distance between ligands where FA complexes can still form is about 80 nm [83, 113–116]. Force measurements performed on single integrin-RGD pairs showed that the force per integrin increases with reduced ligand spacing. This is somewhat counterintuitive, since one would expect load-sharing to lower the force per integrin. Perhaps the existence of a threshold ligand density to induce integrin clustering and enhance actomyosin contractility explains this observation [117].

1.4.2 Role of Integrins in 2D versus 3D Environments

Studies of cells on 2D substrates have shown that different integrins binding to the same ECM protein can lead to different phenotypes. Cells adhering to fibronectin substrates through αvβ3 versus $\alpha5\beta1$ integrins, for instance, differ in traction force generation [29, 118, 119], dynamics [120], actin CSK remodeling under influence of cyclic strain [119] and adhesion [120, 121]. These integrins activate different intracellular signaling cascades [118, 122] and interchanging the ligand binding domains reverses the signaling phenotype [123, 124]. Similarly, expression of αv$\beta6$ integrins in the presence or absence of $\alpha5\beta1$ changes traction force generation [17]. Different splice variants of $\alpha6\beta1$ with distinct cytoplasmic domains also give rise to different phenotypes due to the two distinct cytoplasmic domains [125]. Thus cells can regulate their mechanosensitivity

by modifying the integrin expression profile.

In 3D environments, integrins are required for the fibrillogenesis of various ECM proteins [126, 127]. Most research on mechanobiology in 3D matrices focused on integrins with the $\beta 1$ subunit, which binds most ECM proteins including collagen [24]. The $\beta 1$-integrins, in combinations with alterations in matrix stiffness, have been shown to promote tumor progression [5, 31, 33]. However, $\beta 1$-integrins also appear to suppress tumor metastasis in some contexts [128,129]. Inhibition or deletion of the $\beta 1$-integrins can induce metastasis via upregulated TGF-β signaling and increased expression of αV integrins has been implicated in this process [130, 131]. Interestingly, several αV integrins can bind and activate the latent TGF-β complex, which is an integral component of the ECM. For integrin $\alpha V\beta 6$ it has been demonstrated that traction forces that are transduced from the actin CSK, through integrins, alter the conformation of the integrin-bound latent TGF-β complex, thereby supporting TGF-β activation [132].

Advances in 3D traction force microscopy [133, 134] in combination with FRET-based molecular force sensors [135] are necessary tools to elucidate the mechanisms of integrin-mediated mechanosensing in 3D matrices. Microscopic characterization of the size, morphology and dynamics of cell-matrix adhesions within 3D matrices is technically challenging [136, 137]. In reconstituted collagen networks, FAs generally appear to be smaller than on (rigid) 2D substrates [136, 138]. However, in acellular porcine epithelium, which presents cells with thicker collagen bundles, sarcoma cells were shown to exhibit similar FA size and dynamics as on 2D substrates [102].

1.5 Signaling Pathways

Integrins recruit more than 150 proteins to the cell-ECM interaction sites, which are referred to as the adhesome. The adhesome includes FA adapter proteins, shuttling proteins and kinases that influence gene transcription as well as the CSK [139]. We provide a brief overview of the main signaling pathways below.

1.5.1 Mechanosensitive FA Proteins

Prominent examples of mechanosensitive proteins in the adhesome are talin [13], vinculin [135], and p130Cas [14]. In its unstretched form, talin's cryptic sites are hidden and vinculin cannot bind, but actomyosin contraction opens up talin and recruits vinculin [13]. Using a FRET-based molecular force sensor, the force threshold for vinculin recruitment was shown to be 2.5 pN [135]. Studies of vinculin-knockout cells and vinculin mutants unable to bind p130Cas have shown that vinculin is necessary for p130Cas activation in response to changes in substrate rigidity [140]. p130Cas has a central substrate domain that is intrinsically disordered and can be stretched with AFM or magnetic

tweezers [141,142]. Vinculin likely anchors p130Cas into FAs, to allow stretching of the central substrate domain [14]. Stretching can make tyrosine motifs accessible to Src kinases for phosphorylation, which are known to influence FA formation and actin dynamics [143]. In other words, p130Cas transduces cellular traction forces, due to tyrosine phosphorylation motifs that are exposed, and hereby changes actin dynamics and FA formation further downstream. Only recently, studies of p130Cas have been extended to substrates with variable stiffness such as PAA gels [140] and PDMS micropillar arrays [15]. A more extensive review on the functions of talin, vinculin and p130Cas can be found elsewhere [144].

Paxillin, zyxin and Hic-5, which are among the LIM domain proteins, have also been identified as being mechanosensitive [145]. Zyxin recruits the proteins Ena (Enabled) and VASP (Vasodilator-stimulated phosphoprotein) to FAs and to cell-cell contacts, where they promote F-actin polymerisation [146, 147]. Both zyxin and paxillin contribute to stress fiber repair, a critical process for maintaining the tensional balance within adherent cells [148]. When actin stress fibers were severed by laser ablation or damaged by mechanical strain, zyxin re-located to the newly exposed barbed ends of actin filaments at the damaged sites [149]. Interestingly, LIM proteins exhibit divergent responses to a mechanical strain. While Hic-5 and zyxin localize to stress fibers when cells cultured on 2D substrates are exposed to cyclic stretch, paxillin does not [145]. Even though cells in 3D matrices do not show similar stress fibers as on 2D substrates, zyxin and paxillin do localize at the end of protrusions that are reminiscent of FAs in cells migrating through a network of polycaprolactone fibers [99] and paxillin plays a critical role in 2D and 3D cell migration [150].

1.5.2 Rho GTPases

Following kinase-mediated phosphorylation, for example of p130Cas, many FA proteins promote Rho GTPase activity. Three members of the Rho family of small GTPases are of particular interest in the context of mechanosensing: RhoA, Rac and Cdc42. Rac and Cdc42 are primarily linked to actin polymerization at the leading edge in lamellipodia (and filopodia in the case of Cdc42). RhoA is mainly associated with the activation of actomyosin contractility, together with ROCK (Rho-associated, coiled-coil containing kinase). Rho GTPases are regulated via GEFs (guanine exchange factors) and GAPs (GTPase activating proteins) [151]. While Rho GTPases are usually considered in relation to actin, there is growing evidence that they are also coupled to IFs [152] and MTs [153].

Most studies of Rho GTPase activity have been performed using 2D cell cultures, but there are some studies in the context of 3D migration of tumor cells in collagen matrices. Rho-mediated actomyosin contractility was shown to be necessary for mammary cancer cells to orient collagen matrix perpendicular to the tumor boundary. These fibers then promote cell invasion by

contact guidance [154]. Interestingly, if the collagen matrix was artificially pre-aligned, the Rho/ROCK/MLC pathway became dispensable for invasion. ROCK also contributes to stem cell differentiation: expressing a constitutively active form of ROCK in hMSCs cultured in a 3D hydrogel was shown to induce a switch from adipogenesis (soft tissue fate) to osteogenesis (stiff tissue fate) [134], whereas ROCK inhibition with Y-27632 reduced osteogenesis.

RhoA and Rac are targeted to the plasma membrane in a mechanoresponsive manner, as demonstrated by cyclic stretch experiments with aortic smooth muscle cells on a PDMS membrane [155]. Interestingly, targeting was also microtubule-dependent. Similar stretching experiments performed on monolayers of endothelial cells that mimic the lung epithelium identified Rho GTPases as key regulators of tissue homeostasis [156], which is crucial in the lung endothelium that constantly experiences cyclic stretch.

1.5.3 Integrin-mediated Regulation of Gene Transcription

Integrin-mediated mechanosensing feeds into cell fate decisions by activating various downstream signaling cascades connected to gene expression [139]. One of the most widely studied pathways involves the mitogen-activated protein kinase (MAPK) family. The MAPK pathway is an evolutionarily conserved signaling mode that controls cell proliferation, survival and differentiation. It involves three protein families: the extracellular signal-regulated kinase (ERK) family, the p38 kinase family and the c-Jun N-terminal kinase (JNK) family. Activation of receptor tyrosine kinases (RTK) causes activation of ERK, which can subsequently phosphorylate nuclear substrates that in turn enhance or suppress gene transcription. The MAPK family has been established as a key regulator of the mechanoresponse of osteoblasts and osteoprogenitor cells [157]. Cyclic stretch or shear flows can cause activation of members of the MAPK family, which enhances osteoblast proliferation and differentiation [158]. Similar effects are seen for vascular smooth muscle cells and endothelial cells [156]. However, it is still an open question how these observations, mostly made for cells on rigid substrates, translate to more physiologically relevant environments, especially given that MAPK signaling is known to be dependent on substrate stiffness [157]. Vinculin stretching was recently shown to initiate stiffness-sensitive mitogen-activated protein kinase 1 (MAPK1) signaling in hMSCs, causing differentiation to a muscle phenotype [159].

A second network that links integrin-mediated mechanosensing to gene transcription, is the Hippo network, which functions as a tumor-suppressor pathway in vertebrates [160, 161]. Its central components are the transcriptional co-activators YAP1 (Yes-Activated Protein) and TAZ (transcriptional co-activator with PDZ-binding motif). YAP/TAZ binds to transcription factor partners, driving a transcriptional program that specifies cell growth, prolifer-

ation and cell fate decisions. In cells cultured on 2D hydrogels or micropillar substrates, YAP increasingly relocates from the cytoplasm to the nucleus when the substrate stiffness is increased [162,163]. Cell stretching can likewise cause YAP relocation to the nucleus [164,165]. It has been suggested that YAP/TAZ respond to substrate stiffness by sensing contractile actin networks, since YAP activation is dependent on myosin contractility and is therefore enhanced on stiffer substrates [166]. In addition, the actin-binding proteins Diaphanous and Cofilin [162,164] and the Rho GTPases Rac and Cdc42 have been implicated in YAP/TAZ activation [167,168]. YAP/TAZ activation on a rigid substrate promotes osteogenic differentiation of mesenchymal stem cells, whereas silencing YAP/TAZ favors the adipocyte fate regardless of substrate stiffness [162].

A third family of co-activators of gene transcription is provided by myocardin and the related transcription factors MRTF-A and MRTF-B, which mediate transcriptional regulation of the Serum Response Factor (SRF) [169]. The rigidity-dependent signaling through MRTF-A involves direct binding of MRTFA-A to the actin CSK. By binding and sequestering actin monomers, MRTFA-A prevents actin polymerization [170]. Mechanical stress exerted by actomyosin contractility (on rigid substrates) or exerted externally promotes actin polymerization and thus releases MRTF-A, which is then able to move into the nucleus and activate SRF. For fibroblasts, pulling on $\beta 1$ integrins using collagen-coated beads held in magnetic tweezers causes nuclear translocation of MRTF-A, resulting in transcriptional activation of smooth muscle actin and differentiation to myofibroblasts [171].

1.6 The Cytoskeleton (CSK)

In this section we will summarize recent findings reporting the contributions of actin, MTs and IFs to cellular mechanosensing. Although the emphasis has mostly been on the role of the actin CSK, which is responsible for traction force generation [19], there is growing evidence that crosstalk between all three cytoskeletal systems is important [172–174].

1.6.1 Actin

Cells in 2D culture typically show stress fibers, which are contractile bundles of actin and myosin II [19]. There are several different classes of stress fibers [18, 19]. Ventral stress fibers usually span almost the entire cell length and are anchored at both ends to FAs. Dorsal stress fibers are shorter and only connected to a FA at one end. Transverse arcs are present in the leading edge during cell migration and are not associated with FAs. The newly discovered actin-cap stress fibers span over, and are anchored to, the cell nucleus (see Fig. 1.2). The degree of actin crosslinking and bundling increases with increasing substrate stiffness. For fibroblasts, this allows cells to adapt their stiffness to that of the substrate [175].

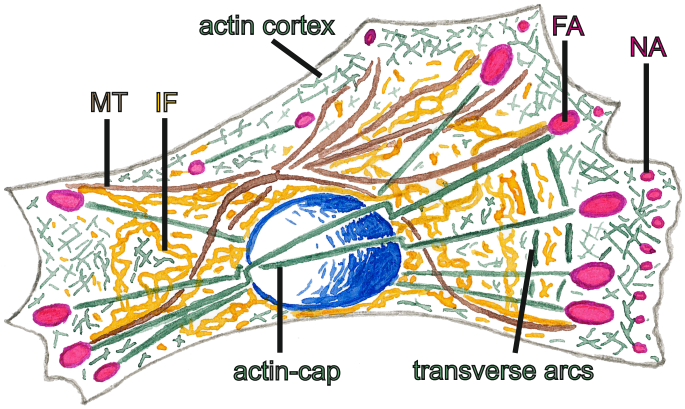

Figure 1.2: Schematic of a cell on top of a (stiff) two dimensional substrate. Focal adhesions (FAs, pink) tend to be larger than for cells inside fibrous 3D networks. Actin forms different sets of stress fibers, as indicated. FAs are connected to actin stress fibers, and some can also connect to microtubules (MT) and intermediate filaments (IFs). Newly formed Fas (nascent adhesions, NAs) are not connected to stress fibers. The NAs can mature into larger FAs upon actomyosin contraction. The cell nucleus is depicted in blue and the cell membrane in gray.

Actomyosin contractility helps to mature nascent FAs into larger and mature FAs [176] and reinforces actin anchoring via talin and vinculin [177]. In motile cells, nascent adhesions form in the lamellipodium without myosin II activity. However, without actin-myosin contractility, these adhesions will not mature and will instead turn over rapidly [176]. Actin polymerization is crucial for the formation of nascent adhesions. The traction force generated by nascent adhesions is set by the speed of actin retrograde flow. However, in FAs that are anchored to stress fibers this correlation no longer holds [176].

In reconstituted 3D ECM networks, stress fibers tend to be fewer and thinner compared to 2D, and localized near the cell membrane [104]. However, similar to cells in 2D, the formation of stress fibers is dependent on matrix stiffness [178]. For stem cells, stiffer matrices result in a higher actin concentration near the cell cortex [103]. In 3D collagen gels under dynamic compression, actin protrusions are correlated to matrix remodeling [179].

1.6.2 Microtubules (MTs)

Despite the well-known roles of MTs in cell polarity and migration [180], their role in mechanosensation has received relatively little attention.

On 2D substrates, MTs do not appear to influence the degree of cell spreading [180]. In contrast, MTs are crucial for cell spreading in 3D collagen networks [180]. In the context of 2D cell migration, MTs promote FA turnover, preventing the FAs to become so large that migration is hampered. The exact mechanism of this regulation is still poorly understood [181]. MTs may be required for delivery of a 'relaxing factor' by kinesin motors [182], or for increased FA turnover via endocytosis [183]. Other studies have shown a paxillin-dependent pathway in regulating MT depolymerization [150, 184]. Crosslinking of growing MTs to actin stress fibers is required to guide the MTs to FA sites [185, 186].

MTs also influence FAs by regulating traction forces via crosstalk with the actomyosin machinery. Both on 2D substrates [187, 188] and inside 3D collagen gels [189, 190], MT depolymerization causes increased traction forces and thereby FA maturation [191]. Interestingly, this effect was not seen for metastatic breast cancer cells [192]. Inside collagen gels, increasing the matrix stiffness by increasing the collagen concentration triggered MT depolymerization, which enhanced actomyosin contractility by releasing GEF-H1, which activates RhoA [193]. A difficulty with this assay is that changing the collagen concentration changes not only the matrix stiffness, but also its pore size and the ligand density [92, 194]. Recently a different assay was reported, where endothelial cells were cultured in collagen networks of fixed density, attached to PAA gels of varying stiffness [195]. In this case, increasing the PAA gel stiffness did not affect the growth persistence of the MTs.

1.6.3 Intermediate Filaments (IFs)

IFs form a large family of proteins that can be classified into five different types based on their self-assembly behavior [196]. Here we will focus on vimentin, which is important in mesenchymal cells like fibroblasts [197]. Through plectins, IFs can interact with actin and MTs [198], as well as with integrins containing the $\beta 3$ subunit [199]. Also, vimentin directly links $\alpha 6$ integrins with the cell nucleus *via* plectin and nesprin [200], although the function of this is unclear. In fibroblasts on 2D substrates, the association of vimentin with integrins increases the lifetime of FAs [201, 202] and enhances traction forces [203]. FA-binding of vimentin requires an intact MT network [202, 203]. Intriguingly, vimentin knockout mice only show defects under conditions of stress. They, for instance, exhibit reduced dilation of arteries in response to shear flow [197]. At the single-cell level, vimentin responds to shear flow [201]. Vimentin knockout mice also exhibit impaired wound healing, which can be traced back to impaired fibroblast migration [152, 204]. This migration defect was recently linked to reduced actomyosin contractility [152]. Vimentin increases cell stiffness and can protect the cell against compressive loads [205]. Similarly, in 3D collagen gels, the vimentin and MT network persists after dynamic compression, while the actin forms local patches to remodel the ECM [179]. Intriguingly,

on 2D substrates, the solubility of vimentin depends on the underlying substrate stiffness [174], which may contribute to stiffness adaption of cells to their substrate. In 3D matrices, vimentin-deficient fibroblasts have a dendritic morphology and they make less cell-cell contacts than wild type cells [204]. However, the implications for mechanosensing in 3D are still unknown.

1.7 The History of Traction Forces

Traction forces are the contractile forces that cells exert on the substrate or ECM to which they adhere [206]. Traction forces enable cells to probe the stiffness of their environment, in analogy to the way we probe the mechanics of an object with our hands. In addition, cells can actively remodel the extracellular matrix and influence its mechanical properties by exerting contractile forces (see Chapters 3 and 7). Experimentally, traction forces have been measured using various techniques. In the remainder of this section, the history of the development of these techniques is discussed and the technique of 'traction force microscopy' is introduced.

Traction forces were first visualized on thin silicone rubber sheets with cells seeded on top [207, 208]. Wrinkles of the rubber sheet provided a rough estimation of the cell traction forces exerted on the film [209]. Although this technique has been modified to get higher force resolution [209–212] and to include force directionality [211, 212], the complex fabrication of these sheets limited their use [208]. Instead, polyacrylamide (PAA) [213] and polydimethoxysilane (PDMS) [214] substrates have surpassed rubber sheets by virtue of the ease of preparation and their large mechanical range [213]. Furthermore, since these substrates are optically transparent, it is also easy to combine them with various imaging techniques [208]. Typically, fluorescent micro-particles are embedded in the PAA substrate and tracked using digital image analysis procedures [214, 215], typically using a 'null-force image', where the cell is removed from the surface or completely relaxed, for reference [214, 215]. This bead tracking analysis is usually done only in two dimensions [215–219], though recent studies expanded the analysis to three dimensions and identified significant normal forces [220–222]. This technique is generally referred to as '(2D) traction force microscopy' [214].

Other techniques that measure cellular traction forces include micropillar arrays, atomic force microscopy (AFM), and microneedles. Micropillars, or nanopillars, are prepared as array of pillars having a high aspect ratio so they can be bent by the cellular traction forces [223, 224]. Depending on the height, width and anisotropy of the pillars, the apparent stiffness the cell feels can be tuned [224–227]. Also, the effect of the shape of the adhesive islands can be studied [226] or cells can be confined to islands of pillars with defined shapes [227]. For single cell traction force microscopy, an AFM tip is coated with an ECM ligand such as fibronectin, which promotes cell binding [228, 229].

By actively changing the degree of bending of the AFM tip or the distance between tip and the surface, the apparent substrate stiffness can even be varied in time. With these techniques, traction forces can be accurately measured in time as the cell spreads on the surface [228–231], and has also been referred to as an 'AFM stiffness clamp', since the amount of bending of the AFM tip is related to stiffness. By actively changing the amount of bending or distance between the surface and the AFM tip, the apparent stiffness can be varied in time. A nice extension of the technique is to coat the AFM tip with a specific ligand that targets a subset of integrins [232, 233]. An alternative application of the AFM assay is to bind a cell to the AFM tip and measure its binding affinity to the surface [234] (termed 'Single-Cell Force Spectroscopy'). However, the throughput of these single-cell methods is understandably low and these techniques are experimentally challenging. Microneedles were used in some studies to measure the contractility of single cells, using the bending of the calibrated needles as a readout of the force [235]. A similar technique has also been exploited in a more three dimensional setting [236, 237], where a 3D square lattice of flexible collagen-GAG beams was used. The bending of this lattice by the adhered cells was taken as a measure of traction forces in a more physiological system. However, the pore size and beam dimensions were rather large compared to the cell size, so the cell effectively experiences a quasi 2D, or even 1D, environment.

In most tissues, the micro-environment of the cell is more three dimensional, with a much smaller pore size than seen in these *in vitro* experiments. Therefore, efforts have been made to move 3D traction force microscopy towards more physiological model systems.

One solution is to look at the collective effect of many cells on the macroscopic structure and mechanics of 3D gels. For instance, in 3D contraction assays, cells are often seeded in a three dimensional mesh work of ECM material [238–242]. This technique was pioneered for collagen by Bell in 1979 [238], where fibroblasts were seeded in collagen gels. The fibroblasts compacted the free-floating collagen gels by exerting traction forces. Though straightforward, this technique is not considered to be very quantitative, since it provides an averaged readout over a large population of cells. Also, other effects, like matrix degradation or remodeling, can affect the measurement. However, it is a straightforward method to perform a quantitative comparison between different cell types [243], to screen effects of drugs, or test the role of specific signaling pathways [244, 245]. Recently there have been efforts to establish more quantitative *3D* traction force measurements by tracking beads in 3D gels [246]. Using similar methods as in 2D traction force microscopy for analyzing bead displacements [242,246], or by tracking the fibers themselves [247,248], one can obtain the strain field in 3D. To estimate the stresses exerted by the cells, one then needs to make assumptions about the material properties of the ECM.

Until now, the matrix is generally been assumed to behave as an elastic continuum exhibiting a linear response [247, 249, 250]. However, for extracellular matrix materials, these assumptions are not expected to hold. Reconstituted networks of collagen and fibrin have been shown to significantly strain-stiffen under mechanical loading [66, 251–253]. Moreover, microrheology studies have revealed clear deviations from an affine response for collagen networks [254], consistent with theoretical predictions for fibrous networks [255]. Finally, there is also evidence that collagen networks exhibit inelastic behavior, especially when loaded at the slow rates relevant for cells [72]. Thus, for quantitative traction force measurements, more detailed and accurate mechanical models of the ECM material of interest should be used that include nonlinear elasticity, nonaffinity, and dissipative effects [249, 256].

One way to overcome this limitation is to use a synthetic material instead of the natural ECM materials, which can be safely considered as a homogeneous elastic solid. This approach was demonstrated with PEG hydrogels coated with the peptide CGRGDS [257, 258]. Another way to overcome this limitation is to measure traction forces directly by inserting calibrated micro-needles into the gels, a method that was used in collagen gels to estimate forces exerted during cell migration [259]. This approach circumvents the need for a micromechanical model of the collagen network, but limits the number of force reporters to one. One group solved the problem of measuring traction forces for cells in collagen by placing the collagen gel on top of a PAA gel seeded with fiducial markers [260]. A different route altogether is to measure traction forces on the molecular scale and *inside* the cell, by the use of engineered downstream focal adhesion proteins involved in traction force generation [135]. This approach was first demonstrated for the protein vinculin [135], which links talin to the actin cytoskeleton [261]. Here, a tension sensor was inserted into the vinculin protein, using two tagged reported proteins. When these tags are close together, they undergo fluorescence resonance energy transfer (FRET), while if they are far apart (i.e. when there is *tension* on the engineered vinculin protein) this FRET signal goes down. In other words, the FRET efficiency gives a measure of the traction force exerted by the cell if calibrated against single molecule force spectroscopy measurements. Recently, traction forces on single integrins were reported using this same technique [262].

1.8 Moving Forward from 2D to 3D

During the past few decades we have learned a lot about the molecular and physical principles of cellular mechanosensitivity from 2D cell culture studies. There is overwhelming evidence that cell fate critically depends on the stiffness of the substrate, which is therefore an important design parameter in tissue engineering. First studies of cells in reconstituted 3D collagen and fibrin matrices indicate that many results carry over from the 2D to the 3D

context. However, the ECM pore size, nanotopography, and the thickness and mechanical properties of the constituent fibers influence cell behavior in complex ways. A key challenge for future research is to design physiologically relevant assays that can unravel these effects. Another key question is what are the mechanisms by which viscous and nonlinear mechanical properties of the matrix influence cell behavior. On the molecular side, it will be interesting to understand the influence of integrin composition. By changing the fractions of catch- and slip-bond integrins, cells may modulate their sensitivity to forces and matrix mechanics. Finally, there is growing evidence that the actin CSK, which is generally considered to be the main player for mechanosensing, is coordinated with MTs and IFs. Comparatively little is currently known about the roles of the latter two cytoskeletal filament systems in mechanosensing, especially in a 3D context.

1.8.1 3D Model Systems: Fibrin and Collagen Networks

One way to create a 3D environment is to use reconstituted ECM networks. Prominent candidates are collagen and fibrin, which are both of interest in the tissue engineering field as well [263–266]. Fibrin, for instance, is already used during surgery [267], collagen has been proposed as a promising candidate for replacing cartilage [268], and both fibrin and collagen are used in burn wound dressings [269]. Also, fibrin and collagen are already used *in vitro* for studying cell biology in a tissue-mimetic, 3D environment [90, 104, 270].

Reconstituted collagen and fibrin both form a 3D fibrous network, as shown in Fig 1.3A and B. From confocal microscopy, these networks do not look strikingly different: both proteins form a homogeneous space-spanning network with similar pore size and fiber thickness [271]. Interestingly, their mechanics are very different, though, as shown in Fig. 1.3C. At low shear strains, both networks show a linear regime where their stiffness does not change with strain. At increasing strain levels, the stiffness increases with strain (termed 'strain-stiffening'), but not in the same manner. For collagen, the stiffness increases almost asymptotically, until the sample breaks at a few tens of percent strain [272]. For fibrin, the increase in stiffness follows a more complicated path, where a second plateau is seen at intermediate strain levels, followed by a new stiffening regime before eventual network rupture [66]. Interestingly, the strain level at which fibrin breaks is on the order of a few hundred percent, compared to only a $40-50\%$ for collagen gels. This illustrates the extreme extensibility of fibrin, which is indeed known to be one of the most extensible biological protein polymers [273].

Both collagen and fibrin networks can strain-stiffen by more than one order of magnitude (Fig. 1.3C). The strain-stiffening behavior in itself is by now well-known [39], having been observed for actin [274,275], vimentin [37,38,276], desmin [38] and neurofilaments [276]. This nonlinear response contrasts with the rather linear response of most synthetic polymer gels like PAA over a large

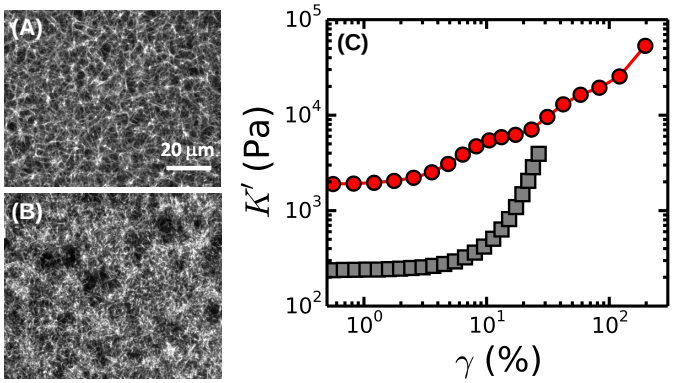

Figure 1.3: Collagen (A) and fibrin (B) both form a 3D fibrous network using physiologically relevant *in vitro* polymerization conditions (4 mg/ml for both images). (C) The mechanical properties of these two networks are, however, strikingly different (gray squares represent collagen, red circles fibrin). In (C) the differential elastic modulus K' is plotted for a 4 mg/ml collagen and an 8 mg/ml fibrin gel respectively. K' provides a quantitative measure of the stiffness of a gel in the nonlinear elastic regime. Both samples were polymerized at 37°C. The scale bar denotes 20 μm for both images.

range of strains [39]. There are two main classes of theoretical models to explain the extraordinary strain-stiffening of biopolymer networks [35, 277, 278]. The first class of models describes the fibers as semiflexible polymers, which exhibit thermal bending undulations. When a network of such filaments is strained, the thermal fluctuations are pulled out, giving rise to an entropic resistance [39, 66, 276]. The strain for the onset of stiffening is related to the excess length of the polymers between adjacent crosslinks that is stored in thermal fluctuations, and is therefore a function of the crosslink distance and the polymer persistence length. The second class of models describes the fibers instead as athermal, rigid rods. In this case, straining a network of fibers is mainly expected to cause fiber bending, because the fibers will be softer to bending than to stretching. However, as the shear strain is raised, the fibers will align along the shear direction and the network will stiffen as a consequence of a transition from bending-dominated to stretching-dominated elasticity [277, 279, 280]. Notably, the origin of strain-stiffening might not be the same for all biopolymer networks, due to the diversity in the hierarchical structure, crosslinking and network connectivity. The athermal limit is expected to apply when the fibers are thick and the persistence length is large.

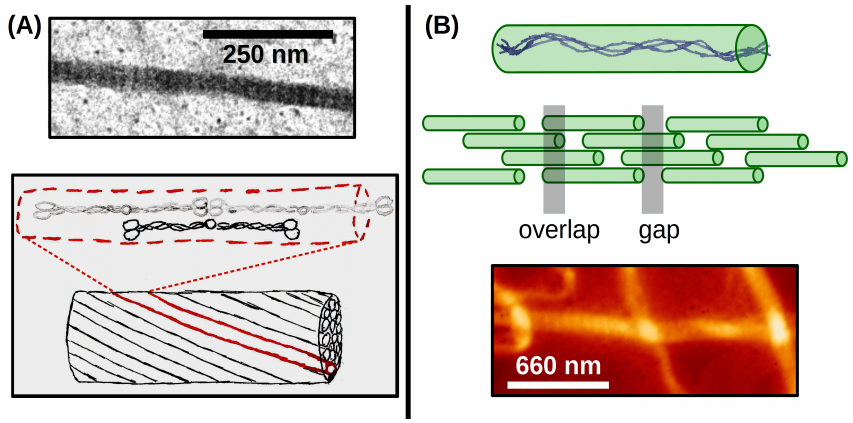

Figure 1.4: The molecular packing structure of fibrin fibers (A) and collagen fibers (B). Fibrin fibers are built out of protofibrils (red), which twist around each other to form a bundle. Protofibrils in turn are built out of fibrin monomers (black), which polymerize in a half-staggering manner that can be seen with, for instance, electron microscopy (top image in A). Collagen fibers are built up from semiflexible collagen monomers (green cylinders), which in turn are built up of three identical polypeptide chains (purple). The monomers polymerize in a quarter-staggered way, thus establishing an overlap and gap region with neighboring monomers and a 67 nm axial spacing that can be seen, for instance, with atomic force microscopy (bottom image in B).

From their dimensions (radius ∼100 nm) and their Young's modulus (E ∼ 50 MPa [251,281–288]), fibrin and collagen fibers are both expected to fall in this limit.

From this standard polymer physics perspective, it is therefore not obvious why the mechanics of these two types of biopolymer networks are so very different. However, the polymer models that we described are coarse-grained and ignore the internal structure of the polymers. Both collagen and fibrin fibers have a hierarchical molecular packing structure that arises from specific self-assembly encoded in the interactions of the protein building blocks.

Fibrin fibers are built up of protofibrils of two monomers thick, which are organized in a half-staggered arrangement as shown in Fig 1.4A. This half-staggered arrangement gives rise to an 22.5 nm axial repeat, that can be seen with AFM or electron microscopy (see top image panel (A)) [289, 290]. Protofibrils twist around each other to form thicker fibrin bundles [291]. The number of protofibrils in a bundle can be varied by changing pH [292, 293],

salt conditions [293, 294] and the concentration of thrombin (an enzyme that activates fibrin polymerization) [293, 294]. Fibrin fibers have been reported to have a high water content of about ∼80% [295, 296], resulting in a rather low protein density of about 0.2 g/cm^3 [66, 296, 297]. The typical lateral spacing between adjacent protofibrils according to X-ray scattering experiments is ∼19 nm [74, 298]. The fibrin monomers also contain domains that can unfold when subject to elongation [273, 299], which has been linked to the extreme extensibility of fibrin fibers.

Collagen fibrils are built up from semiflexible collagen monomers that are 300 nm long and 1.5 nm thick [300,301], as shown in Fig. 1.4B. The monomers are arranged in a quarter-staggered way, where they have an overlap and gap region with neighboring monomers, causing a typical 67 nm spacing termed the "D-period". This D-period can be distinguished in AFM or electron microscopy (see bottom image panel B) [302–304]. One collagen monomer spans 4.6 D-periods. Collagen monomers, as opposed to fibrin monomers, do not contain any readily unfoldable domains. The number of monomers per collagen bundle can be tuned by polymerization conditions such as temperature [90, 305, 306] or the solution pH [307–310]. Under typical assembly conditions, the number of monomers per bundle is on the order of a thousand [251,302], which is much higher than for fibrin bundles (∼hunderd), even though both protein fibers have a similar diameter (∼100 nm). The typical lateral spacing between adjacent collagen molecules is ∼4 nm [311], which is much less than the typical spacing between fibrin protofibrils. Thus, collagen fibrils are more tightly packed and are thus likely stiffer than fibrin fibers. Moreover, the difference in extensibility of fibrin and collagen may potentially be connected to the different mechanics of the molecular building blocks.

1.9 Focus of This Thesis

In this Chapter, we have discussed the importance of the ECM for mechanosensitive functions of cells. The ECM provides cells with mechanical support, structural cues, and dimensional information.

The scope of this thesis is to elucidate the physical origin of the mechanical properties of ECM networks and to relate this information to cellular mechanosensing. Various studies have shown the importance of mechanics in guiding cell behavior using simplified synthetic 2D gel substrates. However, little effort has been made until now to relate the extraordinary mechanical properties of ECM networks to mechanosensing.

In **Chapter 2**, we study the mechanical origin of the mechanics of hierarchically structured ECM networks, using fibrin as a model system. In fibrin biopolymers, whose nonlinear elastic properties are crucial for normal blood clotting, protofibrils self-assemble and bundle to form networks of semiflexible fibers. We show that the extraordinary strain-stiffening response of fibrin net-

works is a direct reflection of the hierarchical architecture of the fibrin fibers. We measure the rheology of networks of unbundled protofibrils and find excellent agreement with an affine model of extensible wormlike polymers. By direct comparison with these data, we show that physiological fibrin networks composed of thick fibers (∼80 protofibrils each) can be modeled as networks of tight protofibril bundles. We demonstrate that the tightness of coupling between protofibrils in the fibers can be tuned by the degree of enzymatic intermolecular crosslinking by the coagulation Factor XIII. Furthermore, at high stress, the protofibrils contribute independently to the network elasticity, which may reflect a decoupling of the tight bundle structure. We conclude that the shear-induced stiffening of fibrin networks is determined by the number of protofibrils in each fiber, and how tightly coupled they are.

In **Chapter 3**, we study the effect of cellular traction forces on the mechanical properties of fibrin gels. It has previously been suggested that cellular traction can cause network stiffening by exerting stresses that drive the network into the strain-stiffening regime. We show that the low strain modulus of fibrin gels seeded with cells indeed increases proportionally to cell density as long as the fibrin concentration is 2 mg/ml or less, while the strain-stiffening response remains unaltered under the addition of cells. Control measurements with the myosin inhibitor blebbistatin confirm that cellular contractility is the origin of gel stiffening. When cells are embedded in dense fibrin gels with concentrations above 2 mg/ml, the gel stiffness is unaffected, likely because the cells are prevented from spreading by being confined in the network pores. Cell-driven gel stiffening provides a convenient global measure of cellular traction force generation. Cell-induced stiffening has important implications for cellular mechanosensing, providing positive feedback for adhesion maturation and traction force generation.

In **Chapter 4**, we study the microscopic basis of the extreme extensibility of fibrin networks by performing *in situ* measurements of the molecular structure of fibrin in stretched gels using Small Angle X-ray Scattering (SAXS). In Chapter 2 we show that the elastic properties of fibrin can be described by an affine thermal bundle model, but this model fails to explain the extensibility and the stiffening response of fibrin at high strain levels. To elucidate the origin of fibrin mechanics at high strains, we conduct SAXS measurements on fibrin gels subjected to uniaxial tension. To interpret the SAXS spectra in terms of the molecular packing structure of fibrin, we compare the data with full atom simulations of protofibril stretching performed by Artem Zhmurov (Moscow Institute of Physics and Technology) and Valeri Barsegov (University of Massachusetts Lowell). First, we study fibrin gels with varying bundle size at zero strain, to elucidate the structural origin of scattering. We show that the SAXS spectra of fibrin networks are sensitive to the bundle size of the fibers. The half-staggered axial packing structure of fibrin fibers gives rise

to a series of sharp Bragg peaks, but only when the bundle size N_p is larger than 40. Strikingly, the second order reflection of the axial packing order is suppressed, which we can explain based on the symmetric structure of the fibrin monomers. The SAXS measurements furthermore reveal a partially ordered lateral packing arrangement of protofibrils within the fibers. Next, we show that forced unfolding of the γ-nodules of fibrin monomers contributes to in the extreme extensibility of fibrin networks. We show experimentally that unfolding starts at relatively low strain levels of 30%, consistent with the full atom simulations. Altogether, we now have a molecular understanding of the extensibility of fibrin gels.

In **Chapter 5**, we investigate fibrin mechanics on the micron scale using one particle optical tweezer microrheology. We developed a custom made optical tweezer setup, which we validated using viscous fluids of different viscosities and PAA gels. For fibrin gels, we tested two different bead types: one that sticks to the network and one that is made inert with covalently coupled Pluronic. We show that the inert beads can accurately report the macroscopic stiffness when taking into account a depletion layer of about $\sim$3 μm, while the sticky beads overestimate both the elastic and the viscous moduli. We studied the high frequency dependence of the linear mechanical properties, and find evidence of a power law frequency dependence with an exponent of 3/4. This exponent is theoretically expected for semi-flexible polymers and confirms the validity of the entropic network model presented in Chapter 2. We estimate the persistence length of single protofibrils to be $\sim$203 nm, which is in excellent agreement with previously reported values.

In **Chapter 6**, we switch to another ECM network often used for studying cells in a 3D environment, namely collagen type I. We measure the rheological properties of reconstituted collagen networks as a function of network architecture (tuned by varying the collagen concentration and polymerization temperature) and compare these measurements with a computational model of athermal fibrous networks developed by the group of Fred MacKintosh (VU, Amsterdam). We show that the elastic properties of collagen networks are in close agreement with multiple predictions of the model. First, we show, for the first time, that collagen gels exhibit signatures of critical behavior, which arises because of the submarginal connectivity of these gels. Second, we can predict the entire strain-stiffening response of collagen gels by taking into account a subtle change in network architecture with changing collagen concentration. Third, we show that strain-stiffening of collagen networks is governed by a shear-induced development of a negative normal stress. These results provide quantitative insight in the effect of architecture on collagen network mechanics, and provide design parameters for generating collagen systems with particular mechanical properties.

In **Chapter 7**, we embed fibroblasts inside the collagen type I networks

with the aim to test whether the cells can influence the structure and mechanical properties of the networks. First, we summarize earlier reports on cell-seeded collagen gel mechanics. With the addition of cells, we do not see any change in the rheological properties of the collagen networks, in contrast with the significant cell-driven stiffening of fibrin gels we demonstrate in Chapter 3. We rationalize these findings in terms of the minimal degree of cell spreading within the collagen gels. The rest of the Chapter is dedicated to a discussion of possible origins for this lack of cell spreading.

1.10 Acknowledgments

I would like to thank Jeroen S. van Zon for helpful feedback. Dominique M. Donato has written the 'Signaling pathways' section, while Hayri E. Balcioglu wrote most of the 'Integrins' section. This work is part of the research programme of the Foundation for Fundamental Research on Matter (FOM), which is financially supported by the Netherlands Organisation for Scientific Research (NWO). This work is further supported by NanoNextNL, a micro and nanotechnology programme of the Dutch Government and 130 partners.

2. Hierarchical Strain-Stiffening of Semiflexible Wormlike Bundles: Fibrin as Model System

Bundles of polymer filaments are responsible for the rich and unique mechanical behaviors of many biomaterials, including cells and the extracellular matrix. In fibrin biopolymers, whose nonlinear elastic properties are crucial for normal blood clotting, protofibrils self-assemble and bundle to form networks of semiflexible fibers. Here we show that the extraordinary strain-stiffening response of fibrin networks is a direct reflection of the hierarchical architecture of the fibrin fibers. We measure the rheology of networks of unbundled protofibrils and find excellent agreement with an affine model of extensible wormlike polymers. By direct comparison with these data, we show that physiological fibrin networks composed of thick fibers can be modeled as networks of tight protofibril bundles. We demonstrate that the tightness of coupling between protofibrils in the fibers can be tuned by the degree of enzymatic intermolecular crosslinking by the coagulation Factor XIII. Furthermore, at high stress, the protofibrils contribute independently to the network elasticity, which suggests a decoupling of the tight bundle structure. The hierarchical architecture of fibrin fibers can thus account for the nonlinearity and enormous elastic resilience characteristic of blood clots.

Izabela K. Piechocka, Karin A. Jansen, Chase P. Broedersz, Nicholas A. Kurniawan, Fred C. MacKintosh, Gijsje H. Koenderink

2.1 Introduction

Polymer bundles are found everywhere in nature. Inside cells, the cytoskeletal filaments are bundles of actin filaments, microtubules or intermediate filaments [35, 172]. Actin and intermediate filaments can be classified as semiflexible polymers, meaning that their thermal persistence length is comparable to their contour length [35, 278], while microtubules are often considered as rigid rods [312]. A large number of accessory proteins such as molecular motors and crosslinkers organize these polymers into higher-order structures that are tailored for specific tasks, including bundles that act as reinforcing or force-generating elements [313–315]. Polymer bundles also form the main structural element of the extracellular matrix in tissues. However, contrary to cytoskeletal proteins, extracellular matrix proteins spontaneously form bundled fibers without the need for accessory cross-linker proteins. Collagen I for instance self-assembles into rope-like, axially ordered bundles that endow tissues with a large tensile strength [316], while the plasma protein fibrin forms axially ordered bundles that reinforce blood clots [66].

Semiflexible polymer bundles have recently started to raise a lot of theoretical attention because their hierarchical structure endows them with unique mechanical properties. Biopolymers tend to be chiral and if they form bundles, the molecular packing geometry is governed by an energetic tradeoff between filament twisting and interfibril adhesion [317–319]. The bending stiffness of these bundles is highly tuneable, being sensitive to the intrinsic properties of the constituent polymers, the degree of bundling, and the strength of coupling among the polymers [320]. These bundle properties have begun to be exploited in materials science, as exemplified by fibers made of carbon nanotubes [321, 322] and responsive gels from designer supramolecular polymers [323, 324].

Several theoretical models have been developed specifically to address the molecular basis of the structure and elasticity of bundled semiflexible polymers, taking actin bundles as model system where filaments are bridged by crosslinking proteins [325–328]. By contrast, much less is known about the molecular mechanisms governing the mechanical properties of fibrin and collagen bundles. They have a more complex molecular packing structure than actin bundles, since no aid of cross-linking proteins are needed to form bundles. Moreover, fibrin and collagen tend to be much larger in size compared to actin bundles, involving hundreds or even thousands of subunits [295, 302] instead of tens of subunits [313] per cross-section.

In this chapter, we focus on the mechanical properties of fibrin bundles. The soluble precursor of fibrin networks is the protein fibrinogen, which circulates in plasma at a concentration of $2-3$ mg/ml [294]. Fibrinogen is an S-shaped hexamer comprised of two sets of three polypeptide chains, referred to as Aα, Bβ and γ [329]. The carboxy-terminal portion of each Aα-chain forms a compact αC-domain that is connected by a long and flexible chain

(the unstructured αC-connector region) to the central region of the fibrinogen molecule. Polymerization is initiated by the enzyme thrombin, which cleaves two protective fibrinopeptides (FpA and FpB) from the central E-domain, thus exposing so-called A- and B-knobs. The activated monomers spontaneously assemble into polymer bundles by a two-step process. In the first step, cleavage of FpA initiates the formation of half staggered, double-stranded protofibrils with a width of about 10 nm [294]. This is encoded in non-covalent interactions of the A- and B-knobs with complementary a- and b-holes on the ends (distal D-domains) of adjacent fibrin molecules. In the second step, cleavage of FpB releases the αC regions and thereby promotes lateral association of the protofibrils into fibers that are usually comprised of tens to hundreds of protofibrils [330]. This lateral association is promoted through interactions of the long and flexible αC-regions that project out from the surface of adjacent protofibrils [294, 331]. Factor XIII catalyzes the formation of between the α and γ polypeptide chains of the fibrinogen molecules, hereby inducing a closer packing of the protofibrils in the fibrin fiber [332].

Biophysical measurements using AFM have revealed that fibrin fibers have highly nonlinear elastic properties. They are characterized by a low linear elastic modulus and large breakage strains of $\geqslant$200% [283,333,334]. The fibers also show viscoelastic behavior and stiffen when strained [283, 334]. These nonlinear properties gives the rich mechanical response upon deformation [39, 66] and enables fibrin networks to withstand shear stresses from flowing blood and traction forces from cells *in vivo*. The mechanical properties of fibrin is very important *in vivo*, since increased or decreased in stiffness of fibrin blood clots increases the risk on thrombosis [330].

Previous attempts to explain the unique nonlinear mechanics of fibrin fibers have largely focused on deformation mechanisms at the molecular scale. Two main types of mechanisms for fibrin's elastomeric and strain-stiffening properties have been offered. The first mechanism assigns fibrin extensibility to the folded domains within the fibrin molecule, which can lengthen about 5 times by forced unfolding [335]. The main evidence for this mechanism comes from single-molecule simulations [299, 335] and AFM measurements [299]. It is still unclear how monomer unfolding will be affected when the molecules are packed into a thick fiber. IR-vibrational spectroscopy measurements on whole fibrin networks under a compressive load showed that at high strains of 100%, changes start to occur in the secondary structure content [336]. The measurements revealed a gradual conversion of alpha-helical to beta-sheet structure. This observation suggests that forced unfolding does take place and, moreover, that the fibers stiffen due to refolding into rigid beta-sheet structures. The second mechanism that has been proposed to explain fibrin elastomeric behavior assigns the fiber extensibility to the disordered αC-regions [282], which form lateral connections between protofibrils [294]. Given that these domains are

more flexible than the folded domains of the fibrin molecule, it is conceivable that the fibers behave as an elastomeric composite of rigid and flexible polymer elements. The main evidence for this mechanism comes from an apparent correlation between fiber extensibility and the length of the αC-region [337]. Unfortunately, the large and hierarchical structure of the fibrin fiber make it difficult to determine the relative contribution of these different molecular mechanisms.

Recently, we proposed that fibrin fibers can be modeled as bundles of semiflexible polymers [66]. This view makes it possible to systematically trace the contribution of each hierarchical level of structure to the mechanical properties of fibrin. However, an experimental difficulty in validating this model is that, unlike actin bundles, fibrin fibers cannot be taken apart into their constituent protofibrils and linkers, since bundling is an intrinsic property of the protofibrils. Here we show that the properties of the bundles can nevertheless be dissected by comparing the mechanical properties of fibrin networks prepared with different levels of bundling. To modulate the degree of bundling, we exploit the known sensitivity of fibrin polymerization to salt and pH conditions [292,338,339]. We prepare networks with bundle sizes that range between 2 up to $\sim$360, varying the bundle size by more than two orders of magnitude. We demonstrate that the nonlinear rheology of networks close to the protofibril limit is in excellent quantitative agreement with theoretical predictions for networks of semiflexible polymers, allowing us to extract the thermal persistence length and enthalpic stretch modulus of protofibrils. We next show that the mechanics of networks of thick fibers can be quantitatively explained by modeling the fibers as bundles of the semiflexible protofibrils. Furthermore, we find that the coupling strength between the protofibrils can be tuned by FXIII-mediated molecular crosslinking. Our findings validate the bundle model for fibrin bundles, which gives a powerful framework to integrate the mechanical properties of fibrin on different scales. Our experimental approach of considering the hierarchical bundle structure is more broadly applicable to other natural and bio-inspired fibrous materials.

2.2 Materials and Methods

2.2.1 Fibrin Polymerization

To obtain fibrin clots close to the protofibril limit (traditionally referred to as 'fine clots' [340]), human fibrinogen (FIB3, Enzyme Research Laboratories, Swansea, UK) was dialyzed for 2 days at 4 °C against a buffer of ionic strength 0.45 (achieved by 50 mM of TRIS-HCl and 400 mM NaCl) and pH 8.5, as described previously [292, 338, 339]. The pH was adjusted with NaOH. The dialyzed fibrinogen was centrifuged for about 20 minutes at 9000 rpm to remove any aggregates. The concentration was determined by measuring the absorbance at 280 nm with correction for scattering at 320 nm [292]. Fine

fibrin clots were polymerized by adding 0.5 U/ml human thrombin (Enzyme Research Laboratories) in fine clot buffer (50 mM of TRIS-HCl and 400 mM NaCl, pH 8.5) in the presence of 3.2 mM $CaCl_2$ at 37 °C.

Data from fine clots were compared to data networks of bundled protofibrils, referred to as 'coarse clots'. FIB3 fibrinogen was diluted in a buffer of near physiological pH and ionic strength (20 mM HEPES, 150 mM NaCl, 5 mM $CaCl_2$, pH 7.4). Polymerization was initiated by adding 0.5 U/ml thrombin and incubating the samples at 37 °C. Fibrinogen stock solution contains the coagulation factor XIII, an enzyme that catalyzes the formation of covalent intermolecular bonds [332, 341]. Consequently, fibrin networks contained a constant molar ratio of FXIII to fibrinogen at all fibrinogen concentrations (0.1−8 mg/ml) and they were always fully crosslinked, as shown by sodium dodecyl sulfate polyacrylamide gel electrophoresis (SDS-PAGE) analysis (see Fig. 2.10 in the supplementary information (SI)). Data for crosslinked coarse clots were taken from our earlier study [66]. Data for coarse clots with reduced levels of crosslinking were obtained by adding 1,3-Dimethyl-4,5-diphenyl-2-[(2-oxopropyl)thio]imidazolium, trifluorosulfonic acid salt (D004) before thrombin addition, which is a specific inhibitor of FXIII [342]. D004 was obtained from Zedira (Darmstadt, Germany) and dissolved in dimethylsulfoxide (DMSO) to a concentration of 20 mM. We used D004 concentrations between 0 and 200 μM. Since DMSO can affect fibrin assembly [343], we used a fixed DMSO concentration of 1%v/v for all tests, including controls, involving FXIII inhibition.

For thick coarse clots of fibrin fibers with 366 protofibrils, FIB3 fibrinogen was filtered through a 0.2 μm filter and injected at 2.7 mg/ml into a superdex 200 column, which was equilibrated with fibrin buffer (20 mM HEPES, 150 mM NaCl, pH 7.4), at room temperature. The flowrate was 0.5 ml/min (pressure ∼0.12 MPa). The fraction corresponding to the second peak, containing fibrinogen monomers [344], was collected. This fraction was concentrated to ∼15 mg/ml, using MacroSep centrifuge tubes (Pall Corporation) at 811 rcf. Tubes were washed with buffer before use. Concentration was determined in the same way as for fine clots. The fibrinogen monomer fraction was snap-frozen and stored at -80°C. It was checked that there was still FXIII crosslinking, using SDS-PAGE analysis (*not shown*). Both α-polymer and γ-γ-crosslinking were present.

2.2.2 Rheology

Rheology measurements were performed with a stress-controlled rheometer (Physica MCR 501; Anton Paar, Graz, Austria). Directly after adding thrombin, the fibrinogen solutions were quickly transferred to the rheometer plate, which was equiped with a steel cone and plate (20, 30 or 40 mm diameter, 1° cone angle). The rheometer was preheated to 37 °C. Solvent evaporation was prevented by coating the sample edges with mineral oil. The time evolution of the linear shear modulus, G^*, was monitored during fibrin polymerization

by applying a small-amplitude oscillatory strain with amplitude $\gamma = 0.5\%$ and frequency $\omega = 3.14$ rad/s and measuring the stress response, $\sigma(\omega) = G^*\gamma(\omega)$. The shear modulus is a complex quantity, $G^* = G' + iG''$, having an in-phase elastic component, G', and an out-of-phase viscous component, G''. Networks of fine clots reached a constant shear modulus (G_0) after about 1 hour, while coarse clots took longer (up to 4 hours).

To probe the nonlinear mechanical response, we used a differential measurement protocol, which captures the stress-stiffening response of biopolymer networks more accurately than large amplitude oscillatory shear measurements [345]. Briefly, small amplitude stress oscillations of amplitude $\delta\sigma = 0.1\sigma$ and frequency 0.1 Hz are superimposed on a steady shear stress, σ. The tangent shear modulus, which is the local tangent of the stress-strain curve, follows from the oscillatory strain response, $K^*(\sigma) = \delta\sigma/\delta\gamma$. In the linear response regime, K' equals the linear plateau modulus, G_0. The networks were nearly perfectly elastic and did not exhibit any significant creep until the shear stress was close to the breakage point. Moreover, the stiffening curves were repeatable as long as the stress did not exceed the rupture stress. Unless noted otherwise, the rheology data represent the mean ± standard deviation from at least three independent experiments.

2.2.3 Imaging

To measure the diameter of the fibers, we performed transmission electron microscopy (TEM) using a Verios electron microscope (FEI Europe B.V, Eindhoven, the Netherlands). About 20 μl of freshly prepared fibrinogen and thrombin was quickly deposited as a thin layer on EM grids (TED PELLA, Van Loenen Instruments, Zaandam, the Netherlands) and polymerized at 37 °C in a humid atmosphere. After complete polymerization (1 hour for fine clots, 4 hours for coarse clots), the grids were washed several times with MilliQ and air-dried. Samples were imaged the same day at 20 kV. Fiber diameters were measured manually. We counted more than 200 fibers, combining data for networks polymerized at concentrations between 0.5 and 2 mg/ml.

To visualize the architecture of fibrin networks in their native, hydrated state, we performed confocal fluorescence microscopy using a Nikon Eclipse Ti inverted microscope equipped with a 100xoil immersion objective (NA 1.49), a 488-nm laser (Coherent, Utrecht, The Netherlands) for illumination, and a photomultiplier tube detector (A1; Nikon, Amsterdam, the Netherlands). Alexa488 labeled fibrinogen was purchased from Life Technologies (Bleiswijk, the Netherlands), dissolved in either fine clot buffer or coarse clot buffer (without $CaCl_2$) and mixed with unlabeled fibrinogen in a 1:10 molar ratio. Samples were prepared in sealed glass chambers and polymerized at 37 °C for 1 hour (fine clots) or 4 hours (coarse clots) before imaging. The images are maximum intensity projection over stacks of 10 μm thick in z.

2.2.4 Turbidity

To measure the mass-length ratio, μ, and the number of protofibrils, N_p, of fibrin fibers in their hydrated state, we performed turbidity measurements using a Cary300 UV-Vis spectrophotometer (Agilent Technologies, Amstelveen, Netherlands). Fibrin gels were polymerized directly in disposable cuvettes (UV-Cuvette micro, Plastibrand, Germany), which were closed off by caps to prevent evaporation. To remove any air bubbles, cuvettes with 350 μl fibrinogen solution were degassed in vacuum for ∼8 min, before starting polymerization at 37°C by the addition of thrombin.

Once the samples were fully polymerized, the optical density, OD, was measured as a function of wavelength, λ, between 350 and 900 nm. To extract the fiber dimensions from the turbidity, $\tau = ODln(10)$, we analyzed the data according to a theoretical model proposed by Carr *et al* [296] and later extended by Yeromonahos and co-workers [295]. Assuming that the networks can be modeled as isotropic networks of rigid cylindrical fibers with a large length-to-diameter ratio, the turbidity τ can be expressed in the form:

$$\tau\lambda^5 = A\mu(\lambda^2 - Ba^2) \tag{2.1}$$

Here λ is wavelength in cm, μ is the mass-length ratio in Da/cm and a is the fiber radius in cm. A and B in eq. 2.1 are constants and are equal to $(88/15)c_p\pi^3 n_s(dn/dc_p)^2/N_A$ and $(184/231)\ \pi^2 n_s^2$ respectively. Here, N_A is Avogadro's number, n_s is the refractive index of the solvent, dn/dc_p is the specific refractive index increment ($dn/dc_p = 0.17594\ cm^3g^1$ for fibrin [296]), and c_p is the protein concentration expressed in $g\ ml^{-1}$. Thus, from eq. 2.1, $\tau\lambda^5$ is expected to be linear in λ^2 with a slope that is proportional to μ and with a y-intercept that is related to both μ and a. Note that this expression includes a small correction [346] of the original formulas in ref. [295]. Given that individual protofibrils have a known mass-length ratio $\mu_0 = 1.44 \times 10^{11}$ $Da\ cm^{-1}$ [347], the number of protofibrils in a fiber, N_p, follows from the turbidity analysis as $N_p = \mu/\mu_0$. We observed a linear dependence for both coarse and fine clots between 650 and 800 nm, and thus this range was chosen to fit the data. Turbidity data represent an average over three independent measurements per condition. Data for crosslinked coarse clots (i.e. without D004) were taken from a previous study [66], but re-analysed according to the model of Yeromonahos *et. al.* [295], instead of Carr *et. al.* [296]. Since fine clots scatter rather weak, we could only obtain reliable results for concentrations above 2 mg/ml, where the OD ensured reliable read-out and analysis ($OD > 0.01$).

2.2.5 Crosslinking Analysis by SDS-PAGE

The extent of covalent crosslinking of the γ and α chains of fibrin was analyzed by reducing SDS-PAGE analysis. Coarse fibrin gels over a range of concen-

trations (0.5−8 mg/ml), as well as coarse and fine fibrin gels in the presence of varying amount of D004 (0−200 μM, 1% DMSO final concentration) at a fixed fibrin concentration of 2 mg/ml, were tested. Fully polymerized fibrin gels were dissolved by adding SDS-PAGE sample buffer (Sigma Aldrich, Zwijndrecht, the Netherlands) and heating at 95°C. Samples were loaded on 8% polyacrylamide gels (homemade). The final gels were stained with InstantBlue (Gentaur, Eersel, the Netherlands).

2.3 Theoretical Framework

We have previously shown by optical tweezer microrheology that fibrin fibers exhibit transverse thermal fluctuations with a frequency spectrum characteristic of semiflexible polymers [66]. This observation implies that the elasticity of fibrin networks is entropic in origin and can be described by models for semiflexible polymers. These models approximate a polymer by a smooth linear contour that resists bending with a quantity, κ, called the bending modulus [278]. The rigidity of semiflexible polymers can be quantified by the persistence length l_p, which represents the decay length of angular correlations along the polymer contour. The persistence length is related to the bending modulus by $\kappa = k_B T l_p$, where k_B is Boltzmann's constant and T is temperature. A polymer is called semiflexible when l_p is comparable to the contour length. Because semiflexible polymers bend in response to thermal forces, their response to an applied pulling force is entropic in origin. Pulling straightens out the thermally-induced bends and thereby causes a reduction in the conformational entropy of the polymer [348].

The elastic modulus of a network of crosslinked semiflexible polymers depends on network connectivity [278]. When the network is well-connected, it will tend to deform in an affine (i.e. uniform) manner. In this case, all filaments experience the same deformation and they are predominantly stretched, while bending plays no role. The network elasticity can thus be calculated analytically from an orientational average over the force-extension response of each filament [39, 348]. In contrast, when the network connectivity is low, it may be more energetically favorable for the filaments to bend, rather than stretch, in response to an applied shear stress, resulting in nonaffine deformations [278]. Since it is much more challenging to analytically predict the elastic modulus in this case, the nonaffine regime has mostly been explored by computer simulations. Nonaffinity is always expected to decrease the elastic modulus compared to the affine limit, since it increases the number of degrees of freedom in the system.

In this Chapter, we will compare our experimental data to analytical predictions assuming an affine network response. In this case, the plateau elastic modulus in the linear elastic regime, G_0, can be expressed in terms of the total fiber length per unit volume, ρ, l_p, and a second length scale l_c that represents

the distance between crosslinks [348]:

$$G_0 = 6\rho k_B T l_p^2 / l_c^3 \tag{2.2}$$

where ρ is the total fiber length per unit volume. The cross-link distance, l_c, can be estimated using scaling theories for semiflexible polymers. Crosslinking is expected to occur either at the scale of the mesh size, $\xi = (\rho)^{-1/2}$, or at the scale of the somewhat larger entanglement length, l_e, which scales as $(l_p)^{1/5}\rho^{-2/5}$ [276, 348].

Once the shear stress exceeds a certain critical value, networks of semiflexible polymers will strain-stiffen as a consequence of the entropic resistance of the filaments to stretching. This onset shear stress, σ_0, characterizing the onset of nonlinearity, can be expressed as [348]:

$$\sigma_0 = \rho k_B T l_p / l_c^2 \tag{2.3}$$

In case of inextensible polymers, the entropic model predicts a power-law stiffening response according to $K' \sim \sigma^{3/2}$, which fits well for actin and neurofilaments [276, 349]. However, for fibrin networks, we [66] and others [39] previously observed a more complex stiffening response, with a transition from entropic stiffening to an enthalpic regime governed by the stretch modulus of the fibers. For fibers with a stretch modulus κ_s, the elastic modulus is expected to reach a plateau value that lies between $K' = 1/15\rho\kappa_s$ if the network is still isotropic, and $K' = 1/8\rho\kappa_s$, once the shear strain is large enough to orient half of the filaments along the diagonal [66]. Full expressions for the stress-dependent modulus can be calculated numerically [39].

When the filaments comprising the network are themselves bundles of semiflexible bundles, the elasticity of the network becomes a function of the degree of bundling. In case of fibrin, the fibers are bundles of N_p protofibrils. We take *'F'* to denote the bundle of protofibrils (i.e. fibers) and *'pf'* for single protofibrils. Thus ρ^{pf} is the length density of protofibrils, and the corresponding length density of fibers can be expressed as: $\rho^{pf} = \rho^F / N_p$. The persistence length of a bundled protofibril can be expressed as [320]:

$$l_p^F = N_p^x l_p^{pf} \tag{2.4}$$

where x is a coupling exponent that describes the strength of the linkage between the protofibrils in a bundle [313] and l_p^{pf} as the persistence length of a protofibril. This exponent x can range from 1, corresponding to loose coupling, to 2, corresponding to tight coupling. Combining eq. 2.2 with eq. 2.4, the plateau modulus and onset of stiffening of a network of bundles can be written as:

$$G_0 = 6k_B T (l_p^{pf})^{7/5} (\rho^F)^{11/5} N_p^{7x/5} \tag{2.5}$$

Since G_0 can be measured using rheology and $\rho^F = \rho^{pf}/N_p$ is known, x can be directly calculated using eq. 2.5.

2.4 Results

2.4.1 Varying Bundle Size

Under physiological conditions, fibrinogen self-assembles into an hierarchical structure, first forming double-stranded protofibrils, which bundle into thick fibers. Confocal microscopy of these 'coarse' fibrin gels show an open network made up of thick fibers, where the pore size is on the order of several microns [66] (Fig. 2.1A). TEM images of fibrin networks deposited and dried on EM grids reveal that the fibers have a diameter in the range of 50−100 nm (Fig. 2.1C and Fig. 2.12A in the SI). Similar results were obtained by SEM of fixed 3D fibrin networks (see Fig. 2.11 in the SI).

The aim of this chapter is to elucidate the contribution of each hierarchical structural level to the mechanical properties of fibrin. Even though fibrin fibers cannot be taken apart into their constituent protofibrils and linkers, due to the fact that bundling is an intrinsic property of the protofibrils, we can exploit the known sensitivity of fibrin polymerization to salt and pH to vary the bundle size [292, 338, 339]. We assembled fibrin networks under conditions where lateral assembly of protofibrils is almost completely inhibited. This so-called *fine* clot limit is favored in a buffer with high pH (8.5) and high ionic strength (0.45). Confocal imaging reveals that fine clots indeed form a dense network with a pore size too small to clearly visualize (Fig. 2.1B). This is consistent with estimating the pore size using $\xi \simeq 1/(\rho)^{1/2}$ [276, 348], which predicts a mesh size of a few hundreds of nanometers. TEM images show that indeed the fine clots are made out of very thin fibers (Fig. 2.1D). Similar results were obtained with SEM (see Fig. 2.11 in the SI). The diameters of the fine fibers range from 15−30 nm (Fig. 2.12B in the SI). Based on structural and experimental data, a diameter in the range of 10−20 nm is expected for single protofibrils [290,338,339,350,351]. This indicates that fine clots contain single protofibrils as well as bundles of 2 or 3 protofibrils. Indeed, some fibers in the TEM images show evidence of $N_p = 2$, since fiber twisting can be distinguished.

EM microscopy requires sample drying and surface immobilization, which can lead to experimental artifacts and affect the accuracy of the diameter determination. Therefore, we also estimated the number of protofibrils (N_p) based on light scattering from fibrin networks in their hydrated state. For fine fibrin clots, we find an N_p close to 2, independent of protein concentration (see Fig. 2.13 in the SI). This observation suggests that minimal bundling occurs, consistent with the EM and confocal images. By contrast, turbidimetry reveals that the average bundle size in fibrin networks prepared under near-physiological conditions is close to 87 when the networks are formed at fibrin

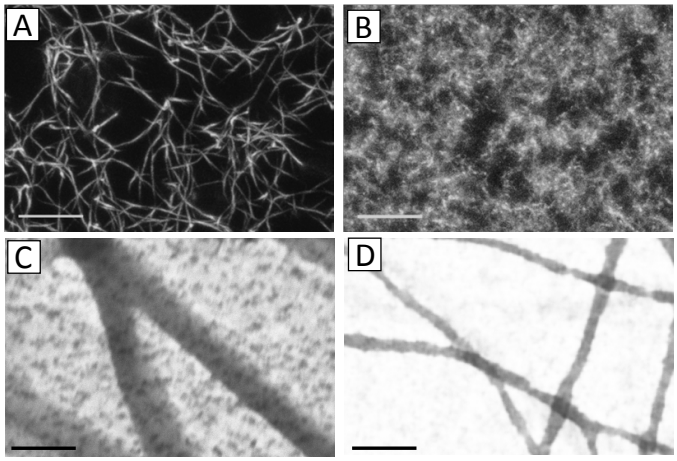

Figure 2.1: Microstructure of (A,C) networks of bundled protofibrils under physiological ("coarse clot") conditions, and (B,C) networks prepared under high salt/pH ("fine clot") conditions. Panels (A) and (B) show confocal fluorescence microscopy images of 1 mg/ml fibrin gels (scale bars 20 μm). Panels (C) and (D) show TEM images revealing the fiber diameters (scale bars 200 nm).

concentrations between 0.1−3 mg/ml, and thereafter decreases to ∼20 at 8 mg/ml (see Fig. 2.13 in the SI.) Note that these values result from a reanalysis of our previously published turbidity data [66] using a recent, more accurate scattering model [295].

2.4.2 Rheology of Fine Fibrin Clots

To enable a quantitative interpretation of the rheology of physiological fibrin networks as a function of protofibril bundling, we first study the rheological properties of the fine fibrin clots, which show minimal bundling. We probed the nonlinear elastic response of the networks by applying a stepwise increasing constant shear stress while superposing a small oscillatory stress to probe the tangent shear moduli, K' and K''. All networks strongly stress-stiffen once the shear stress exceeds a certain critical value, σ_0, as shown in Fig. 2.2A. Depending on concentration, they can stiffen up to 100-fold before they break. The corresponding strain at rupture reaches large values of close to 200%, in line with the known elastomeric properties of fibrin [333].

The linear modulus measured at small strains, G_0, increases strongly when the protein concentration is raised from 0.5 to 6 mg/ml. More specifically, G_0 increases as a power law with an exponent of 2 (solid squares in Fig.

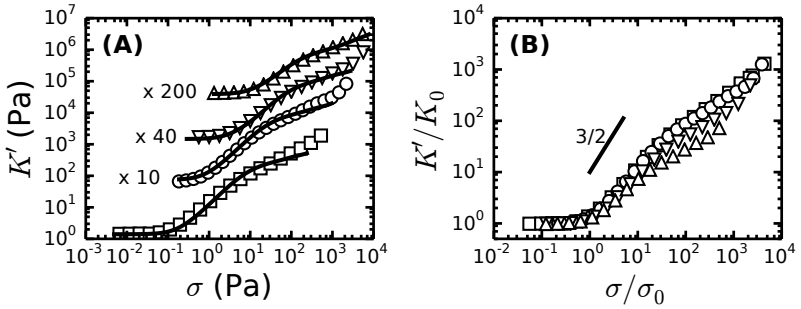

Figure 2.2: Stress-stiffening of fine fibrin clots at different concentrations: c_p = 0.5 (squares), 1 (circles), 3 (triangles up) and 6 mg/ml (triangles down). In (A), the solid lines represent affine thermal model for extensible chains. The K values have been shifted vertically for clarity, as indicated. (B) Normalized stress-stiffening curves. Fine clots exhibit a clear deviation from the predicted 3/2 scaling (short solid line) for inextensible polymers.

2.3A), which is consistent with analytical models for networks of semiflexible polymers described in section 2.3. This model predicts an exponent of 11/5 (solid line in Fig. 2.3A). For reference, we note that our data agree well with prior measurements on fibrin networks prepared under similar fine clot conditions [292, 352] (Fig. 2.3A in the SI).

Past an onset stress σ_0, K' increases in a complex fashion. Thermal models of crosslinked inextensible semiflexible polymers predict a strong increase in stiffness with stress, $K \sim \sigma^{3/2}$, above σ_0 [348]. However, fine fibrin networks show a weaker stiffening with stress and is dependent on fibrin concentration (Fig. 2.2B). A similar weak stiffening with stress was previously seen for fish fibrin and vimentin, where this effect was attributed to filament backbone stretching, which is an enthalpic effect [39, 276].

To test whether backbone stretching can also account for the stress response of the fine fibrin networks, we fitted the stiffening curves to the full theoretical prediction [39] using three fit parameters: the persistence length l_p, characteristic distance between crosslinks l_c, and stretch modulus κ_s. As shown in Fig. 2.2A, the theory (solid lines) are indeed able to capture both the onset of strain-stiffening, which originates from chain entropy, and the inflection at intermediate stress, which stems from backbone stretching. However, at large stresses, the model systematically underestimates the measured clot stiffness. The model accounts for shear-induced alignment of fibrin fibers under stress, but assumes that the stretch modulus of the fibers is indepen-

dent of strain. The systematic discrepancy of the data with the theory at high stresses strongly suggests that the protofibrils themselves stiffen under extension. However, the close agreement between theory and experiment at low and intermediate stresses does suggest that the limited bundled protofibril networks can be modeled as extensible semiflexible polymers.

From the fit of the rheology data to the extensible wormlike chain model (Fig. 2.2), we get a value of 120 nm for l_p for fine fibrin clots, which is independent of fibrinogen concentration (Fig. 2.15 in SI). Next, we examined whether we obtain physically meaningful values for the fit parameters l_p, $\kappa_{stretch}$ and l_c.

We obtain a value of 150 nm for the average l_p of the filaments forming the fine fibrin networks, independent of c_p (Fig. 2.19). Given an average N_p of 2, this corresponds to $l_p^{pf} = 75$ nm, consistent with the supposition that the protofibrils are semiflexible polymers. This value is smaller than estimates from light scattering experiments (200 nm) [353] and analysis of EM images of fish fibrin (500 nm) [39, 354], but is close to values reported in recent light scattering and small-angle X-ray scattering experiments (120 nm) [355].

The protofibril stretch moduli that we obtain from the fits to the extensible wormlike chain model lie between 80 and 150 pN, assuming we have minimal bundling in the fine clot case ($N_p = 2$) (closed symbols in Fig. 2.16A in SI). This protofibril stretch modulus is in the range of the stretch modulus inferred from macroscopic rheology of fish fibrin, which should give single protofibril networks (50−100 pN) [39]. If we assume that the protofibrils behave as homogeneously elastic cylinders of diameter 10 nm, we find a Young's modulus E of 1 up to 1.9 MPa, which is close to the range of 1.7−15 MPa measured by bending and stretching of individual fibers [281–283]. Fibrin protofibrils are somewhat softer than intermediate filaments, for which $E = 9$ MPa [276], and three orders of magnitude softer than actin filaments, for which $E = 1 - 3$ GPa [356].

In addition to the stretch modulus, we determined the crosslink distance, l_c, which decreases from 0.25 μm at 0.5 mg/ml (1.5 μM) fibrin to 0.05 μm at 6 mg/ml (17 μM) (symbols in Fig. 2.3B). To test whether these values are reasonable, we estimate l_c using scaling theory for semiflexible polymers. Cross-linking is expected to occur at either the scale of the mesh size, $\xi \simeq (\rho)^{-1/2}$, or at the scale of the somewhat larger entanglement length, l_e, which scales as $(l_p)^{1/5}(\rho)^{-2/5}$ [276,348]. Here, ρ is the fiber density in terms of length per volume, which can be computed from the mass concentration, c_p, and μ. Remarkably, the fitted values of l_c closely agree with the calculated values of $l_e \sim (l_p)^{1/5}(\rho)^{-2/5}$, if we assume a prefactor of 0.75 (Fig. 2.3B, solid line) [357]. Furthermore, these fitted values are close to the lower bound expected in case of dense crosslinking, $l_c \simeq \rho^{-1/2}$, using the same prefactor (Fig. 2.14B dashed line).

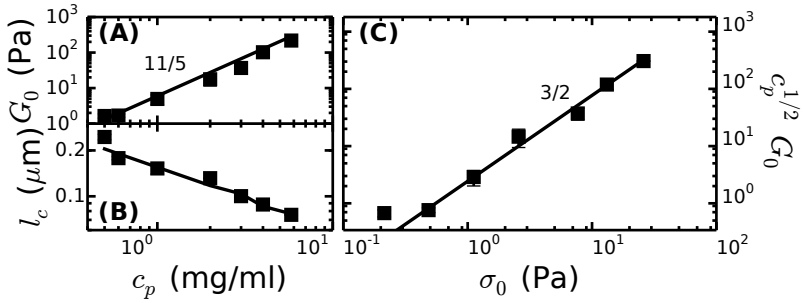

Figure 2.3: Comparison of rheology of fine clots (squares) with the affine thermal model (lines). (a) Plateau modulus compared with the predicted 11/5 power-law (solid line). (b) Cross-link distance compared with theory assuming $l_c = l_e$ (solid line), assuming a prefactor of 0.75. (c) The dependence of $c_p^{1/2} G_0$ on σ_0 depicts a 3/2 relation.

As a further test of the applicability of this model for fine clots, we examined the relationship between the linear modulus G_0 and the onset of stiffening σ_0, for which the thermal affine model provides a clear prediction (eq. 2.2 and eq. 2.3). Thus, we expect $c_p^{1/2} G_0 \sim \sigma_0^{3/2}$, independent of the degree of cross-linking [357]. Our data are indeed consistent with this prediction (Fig. 2.3C). Together with the fact that we obtain physically meaningful values of l_c and κ_s, this strongly supports our conclusion that affine entropic stretching underlies the elastic response of fine clots.

2.4.3 Hierarchical Bundle Limit: Physiological Fibrin Coarse Clots

Under physiological blood clotting conditions, fibrin protofibrils laterally aggregate to form bundles [294]. To mimic these conditions, we formed fibrin networks at near-physiological pH (7.4) and ionic strength (0.17 mM). Previously [66], we found that the stiffness of these gels increased with protein concentration (Fig. 2.4A) with an exponent close to 11/5, as predicted for semiflexible polymers. To interpret these data, we hypothesized that the networks are composed of fibers that can be modeled as bundles of protofibrils. To test this hypothesis, we varied the bundle size by comparing bundled protofibril networks ('coarse clots') to the fine clot limit, where bundling is suppressed.

Bundling into fibers of N_p protofibrils will reduce the number of distinct fibers in the network, which we can express in terms of the fiber length-per-volume, $\rho^F = \rho^{pf}/N_p$. Moreover, bundling will increase the bending stiffness of the fibers. The persistence length of a fiber can be related to the protofibril

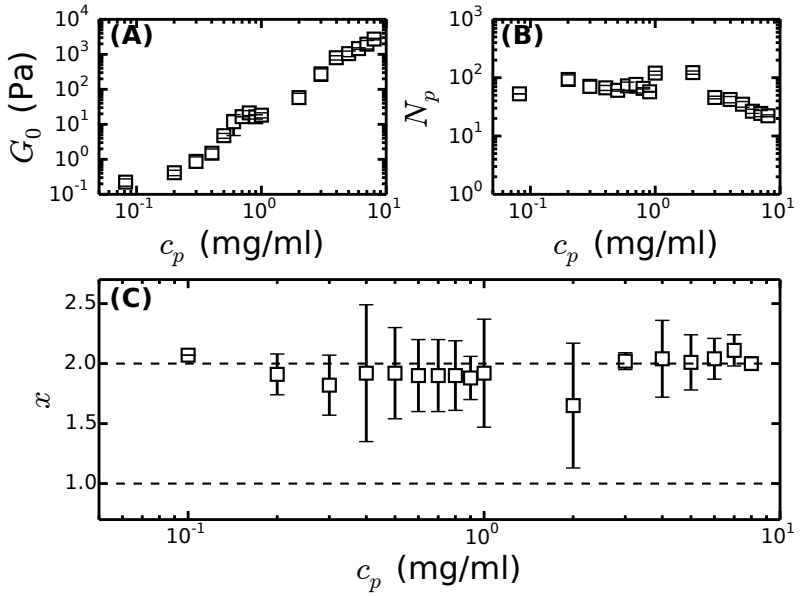

Figure 2.4: Bundle coupling inferred from the linear elastic modulus of physiological fibrin networks. (A) Plateau modulus of fibrin networks, taken from our previous work [66]. (B) Bundle size obtained by reanalyzing existing turbidity data [66] using an updated scattering model [295]. (C) Coupling strength expressed in terms of the exponent x, which is calculated using eq. 2.5, and the data in (A) and (B), assuming $l_p^{pf} = 75$ nm. The dotted lines indicates the two limits for x, where 1 denotes a loose coupling and 2 a tight coupling of protofibril bundles.

persistence length as $l_p^F = N^x l_p^{pf}$, where x is an exponent that characterizes the coupling strength [313]. In the case that protofibrils are tightly coupled, the relative shear among protofibrils is prevented; we expect $x = 2$. On the other hand, when the protofibrils can bend independently inside the bundle, then the bundle is considered loose where we expect $x = 1$. We can calculate x for fibrin fibers of coarse clots from eq. 2.5, using the measured plateau modulus (Fig. 2.4A) and bundle size (Fig. 2.4B) using $l_p^{pf} = 75$ nm calculated from rheology of fine clots. We find values that are consistent with a tight coupling (i.e. $x = 2$), independent of fibrin concentration (Fig. 2.4C).

We can plot the linear modulus of fibrin networks of varying bundle sizes together with the linear modulus of fine clots. We expect $G_0 \sim (\rho^F)^{11/5} l_p^{7/5} \sim (\rho^F)^{11/5} (N_p^x l_p^{pf})^{7/5}$. As shown in Fig. 2.5A, we obtain excellent consistency

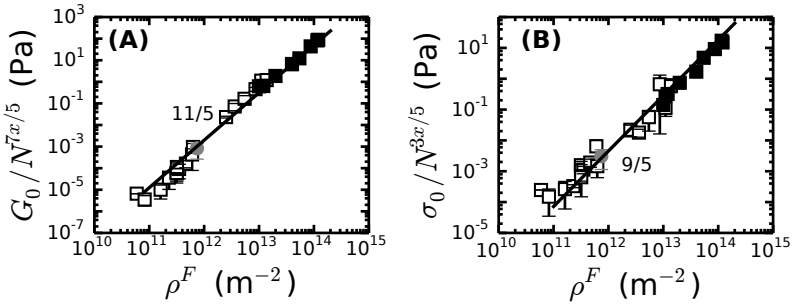

Figure 2.5: The plateau modulus (A) and the stress for the onset of stiffening (B) of fibrin networks are well explained by the semiflexible wormlike bundle model. This is shown by rescaling fine fibrin networks (solid squares, $N_p \sim 2$) and coarse fibrin networks (open squares for $N_p \sim 80$, gray circle for $N_p = 366$) by their dependence on N_p. For fine clots, we assume a loose coupling ($x = 1$), a tight coupling for coarse clots ($x = 2$, see Fig. 2.4C) and intermediate coupling for very thick fibrin fibers ($N_p = 366$, $x = 1.3$).

between fine and coarse clot data sets, using $x = 2$ for coarse and $x = 1$ for fine. Moreover, both data sets agree well with the theoretical model assuming an affine network deformation (solid line). We also rescaled the onset stress of coarse and fine clots, for which we expect $\sigma_0 \sim (\rho^F)^{9/5}(N_p^x l_p^{pf})^{3/5}$. We found good agreement of coarse and fine clot data with the affine model (solid line). Furthermore, we note that the rescalings in Fig. 2.5A and B also holds for larger bundle sizes. Indeed, fibrin bundles of ∼350 protofibrils, obtained by further purification of the fibrinogen stock (see materials and methods), still follow the affine thermal model (open symbols in Fig. 2.5).

We next compared the stress-stiffening behavior of coarse and fine fibrin networks, where network elasticity originates from axial (enthalpic) stretching. The hypothesis is that the protofibrils will stretch in parallel, which we can check by rescaling K' and σ by the length density of protofibrils ρ^{pf}. We found that coarse and fine fibrin networks have an identical stiffening response upon normalization for average force per protofibril levels of ∼1 pN, as shown in Fig. 2.6. This behavior strongly suggests that, just as for fine clots, the elasticity of coarse clots is controlled by a combination of entropic and enthalpic fiber stretching of the individual protofibrils inside the bundle. This universal response, which is independent of the degree of bundling or the protein concentration, indicates that at high stresses, the protofibrils contribute independently to the network elasticity. Thus the (enthalpic) stretch modulus

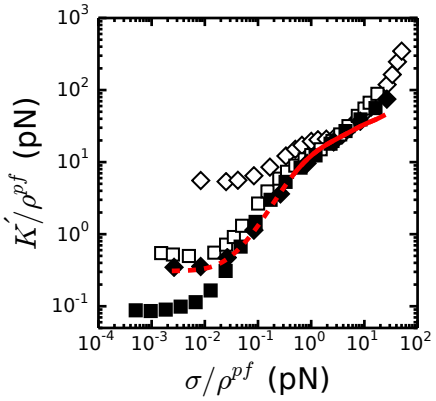

Figure 2.6: Direct comparison of the high-strain (enthalpic) elastic response of coarse (open symbols) and fine clot (closed symbols) networks. Data are shown for two protein concentrations c_p = 0.5 (squares) and 3 (diamonds) mg/ml, were coarse is represented by open symbols and fine by closed symbols. The affine thermal model prediction for extensible wormlike chains for 3 mg/ml fine fibrin (red dashed line) is shown, where the enthalpic regime is indicated by the solid line.

of fibrin fibers is linear in the number of constituent protofibrils. Interestingly, this behavior may also reflect a decoupling of the tight bundle structure that is expected theoretically for short-wavelength deformations [320]: tight bundle behavior is expected for long wavelength bending, which will dominate in the low stress/strain regime, while increasingly loose bundle behavior is expected for shorter wavelength bends that become dominant under high axial loads. Thus, the collapse of coarse and fine clot data in Fig. 2.6 likely reflects the different length scales probed at varying levels of stress.

We have shown that the protofibril stretch modulus is in the range 80 and 150 pN (see Fig. 2.16A in SI). We can compare this with values calculated from coarse clots data using the modulus at the enthalpic regime: $K_s = f\rho^{pf}\kappa_s$, where f is a factor dependent on the alignment of the network [66]. For an isotropic network $f = 1/15$, while for an highly aligned network $f = 1/8$. Both these limits are plotted in Fig. 2.16A in the SI. The stretch modulus for protofibrils is close to the aligned limit for coarse clots, indicating that the network of coarse clots is highly aligned at the enthalpic stretching regime. Indeed, the strain levels corresponding to the enthalpic regime falls within the range of 10−30% strain (Fig. 2.16B in SI), making it likely that the network is aligned at this regime.

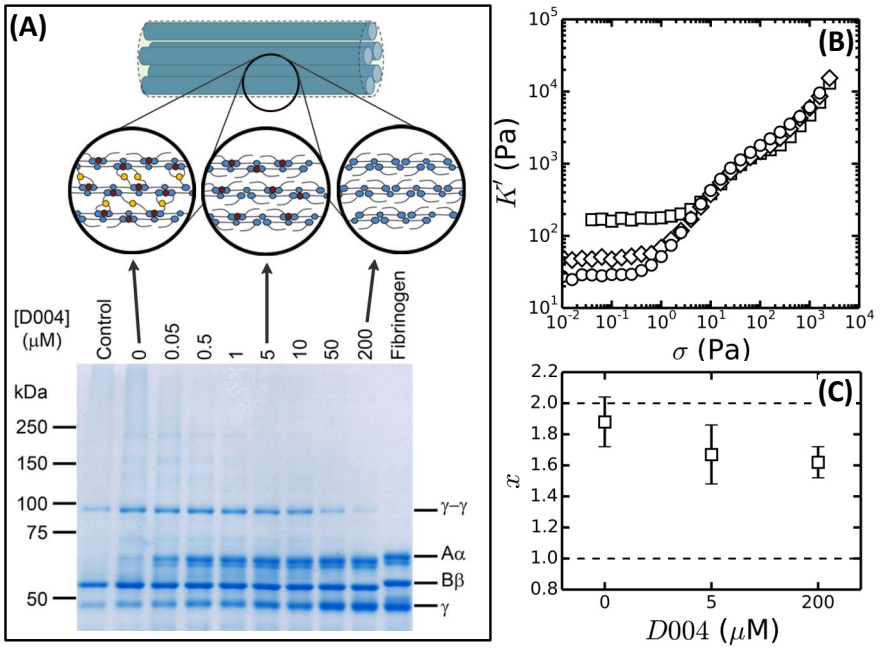

Figure 2.7: Influence of FXIII-mediated crosslinking on bundle stiffness. (A) Reducing SDS-PAGE gel of 2 mg/ml fibrin gels formed in the presence of different concentrations of the FXIII-inhibitor D004. The control consists of a 2 mg/ml fibrin gel without DMSO. Crosslinks between protofibrils (α-α-crosslinking) is depicted schematically in yellow, while γ-γ-crosslinking is shown in red. (B) Stress-stiffening curves for 2 mg/ml fibrin gels with 0 μM (squares), 5 μM (diamonds) or 200 μM (circles) D004. (C) Corresponsing coupling factor x calculated from eq. 2.5. Crosslink inhibition makes the bundles less tight. The two limits ($x = 2$ for a tight bundle and $x = 1$ for a loose bundle) are indicated by a dotted line.

If protofibril stretching is strictly linear, a weak increase is expected due to shear-induced fiber alignment. Strikingly, the model prediction in Fig. 2.6 (solid red line) systematically underestimates the actual stiffness of both fine and coarse clots at large stress. This discrepancy suggests that the fibrin fibers are intrinsically nonlinear. This hypothesis is indeed supported by direct force-extension measurements on individual fibers, which showed substantial intrinsic molecular nonlinearity at large tensile strains [282, 283, 334].

2.4.4 Varying Bundle Tightness

We have shown evidence that physiological fibrin clots (coarse clots) can be modeled as tightly coupled protofibrils over a range of bundle sizes. The stiffness of a wormlike bundle is expected to be strongly dependent on the coupling strength between the constituent polymers. In this section, we will show that the tightness of protofibril bundles can be varied by varying crosslinking between protofibrils.

Previous studies have shown that lateral association of protofibrils is promoted by crosslinking of α-chains protruding from the protofibril surfaces, as sketched in Fig. 2.7A [294, 358, 359]. Crosslinking is mediated by the enzyme FXIII, which creates covalent peptide bonds between specific sites on the α-chains. FXIII additionally creates crosslinks between α- and γ-chains, as well as crosslinks between γ-chains within protofibrils [360, 361]. Based on this evidence, we hypothesize that FXIII-mediated crosslinking may control the tightness of the bundle.

To check this hypothesis, we controlled crosslinking of FXIII by adding a site-specific inhibitor D004 in the range of 0 μM and 200 μM. As shown by SDS-PAGE (Fig. 2.7A), we can inhibit crosslinking in a graded manner. At 0 μM D004, there is both α-crosslinking (distinguishable by the disappearance of the Aα-band) and γ-γ-crosslinking (bands indicated), as sketched in the left-most cartoon. When we add 5 μM D004, there is no detectable α-chain crosslinking (neither $(\alpha)_N$ polymers or α_N-γ_M crosslinks), consistent with prior reports [332,360], and the amount of γ-γ-crosslinking has reduced to about 50%. There is complete inhibition of crosslinking at 200 μM D004 (see Fig. 2.17 in the SI for the quantification).

Next we investigated the change of mechanics upon FXIII inhibition, where we selected 0, 5 and 200 μM D004 (respectively squares, diamonds and circles in Fig. 2.7B). Complete inhibition of α-crosslinking at 5 μM D004, causes a drop in linear elastic modulus by a factor $\sim$4. Full inhibition of FXIII further reduced linear modulus up to a factor 6 compared to the control, consistent with previous reports [332, 360, 362, 363]. According to the proposed semiflexible bundle model, the small-strain regime is determined by entropic elasticity, and should thus be sensitive to the bending rigidity of the fibers. A smaller elastic modulus indicates a looser, more flexible bundle. Using eq. 2.5, we calculated the bundle coupling exponent, x, directly from the rheology and turbidity data (Fig. 2.9B). This factor decreases from near 2 to 1.6 (Fig. 2.7C). Interestingly, x is still much larger than 1 in the absence of crosslinking. This means that, even in the absence of covalent crosslinks, protofibril bundles are still rather tightly coupled. Similarly, decrease in gel stiffness on reduced internal fiber crosslinking have been observed for other systems, such as actin bundled with fascin [325] and nanotubes bundles coupled by covalent crosslinks [321].

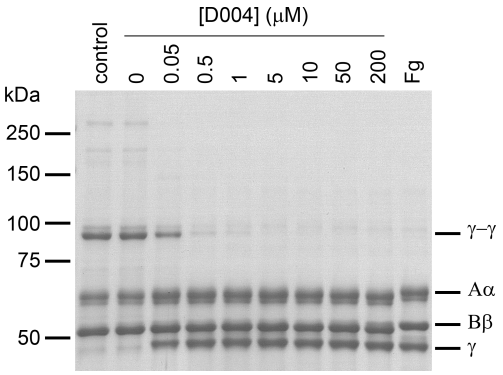

Figure 2.8: Reducing SDS-PAGE gel for 2 mg/ml fine fibrin networks formed in the presence of different concentrations of the FXIII inhibitor D004, as indicated. Fg is fine fibrinogen without thrombin and calcium. The control consists of fine fibrin without the presence of DMSO.

Strikingly, after the onset of strain-stiffening, K' overlaps for all three D004 concentrations. This is consistent with the semiflexible bundle model we presented earlier, where the high-strain regime is determined by independent stretching of the protofibrils. Since inhibition of FXIII crosslinking not only affects inter-protofibril crosslinking, but maybe also intra-protofibril crosslinking and thus change the protofibril stretch modulus, we checked this by polymerizing fine fibrin gel with varying levels of D004. As shown in Fig. 2.8, SDS-PAGE revealed a gradual decrease of γ-γ- and α-chain crosslinking with D004. Inhibition of α-chain crosslinking was complete at 0.05 μM D004, while γ-γ was inhibited completely at 1 μM (see Fig. 2.18 in SI for the quantification). This is lower compared to coarse clots, where γ-γ is inhibited at 200μM D004. However, the addition of D004 does not change the stretch modulus of protofibrils, even at concentrations where γ-γ-crosslinking is completely inhibited (Fig. 2.9A).

We conclude that decreasing FXIII crosslinking by D004 decreases the tightness of coarse clot fibers. This lowers the linear modulus by lowering the fiber bending rigidity, but does not change the enthalpic response of the networks at high stress.

2.5 Discussion and Conclusion

Polymer bundles are present in many biological systems: from cytoskeletal components to extracellular matrix in tissues. The size of these bundles can vary from a few monomers to thousands in a fiber. In the case of fibrin net-

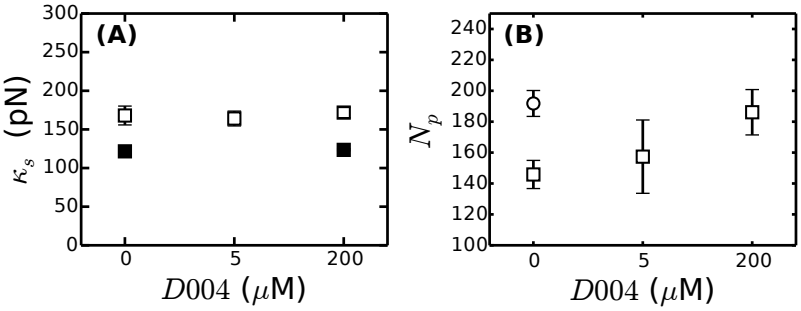

Figure 2.9: (A) The stretch modulus of fibrin protofibrils does not change when crosslinking by FXIII is inhibited by D004, assuming aligned networks in the enthalpic stretch regime. All networks are with 1% final DMSO concentration. (B) Influence of crosslink inhibition by D004 on in the bundle size N_p of coarse fibrin based on turbidity measurements. Open squares are for 2 mg/ml coarse fibrin with 1% DMSO final concentration, while the open circle represent the 0% DMSO control, while closed squares are for fine fibrin.

works, the size of the fibers can be tuned by changing pH and salt conditions. Recently, we proposed that fibrin fibers can be modeled as bundles of semiflexible polymers [66]. In this chapter, we have shown we can dissect the properties of the bundles by comparing the mechanical properties of fibrin networks prepared with different levels of bundling.

We varied the bundle size from 2 up to 366, thus changing bundle size by more than two orders of magnitude. We demonstrated that the nonlinear rheology of networks close to the protofibril limit are in excellent quantitative agreement with theoretical predictions for networks of semiflexible polymers (Fig. 2.2A and 2.3). Comparing these 'fine' networks with networks prepared with an higher degree of bundling ('coarse' networks) revealed a master curve when rescaled by the number of protofibrils in a bundle (N_p) and the tightness of the bundle (x) (Fig. 2.5). This rescaling is based on the assumption we have a loose coupling between protofibrils in the fine clot case. Given the small number for N_p for the fine clot limit, we think this is a reasonable assumption. The persistence length provided by the model was on average 150 nm, which means, given $N_p = 2$ for fine clots, a persistence length of 75 nm for the protofibrils. This value is consistent with our interpretation of the fine clots as networks of semiflexible polymers. Also, this value is close to the l_p found in recent simultaneous light scattering and small-angle X-ray scattering experiments on polymerizing fibrinogen (120 nm) [355]. However,

this value of l_p^{pf} is somewhat smaller compared to values estimated from light scattering (200 nm) [353], and values reported for protofibrils of fish fibrinogen (500 nm) [39, 354]. Based on $l_p^{pf} = 75$ nm and tight coupling, we expect l_p to vary between 30 and 560 μm for coarse clots, since N_p varies between from 20 to 86 (Fig. 2.4B). In the future, the persistence length of protofibrils, and coarse clots of known N_p and x, should be directly measured, for instance by stretch experiments with AFM or optical tweezer techniques.

We note that in a previous publication [66] we assumed loose coupling for the coarse clot limit. This assumption was based on optical tweezer measurement, which showed significant thermal fluctuations for coarse fibrin networks. However, in the current work, we directly calculated the coupling strength, x, by combining rheology and turbidity results. Here we find for coarse clots a tight coupling. For thicker coarse clots ($N_p = 366$), the calculated tightness decreases to 1.3. The decrease in tightness with fiber diameter could be related to a decrease in protein density: fibrin fibers can be considered as fractals [364], were the protein density within fibrin fibers decreases with increasing fiber diameter.

We have shown that the origin of fibrin mechanics is due to the hierarchical structure fibrin fibers. In particular, when we rescale the nonlinear mechanics to the total protofibril length per volume, ρ^{pf}, when the rescaled mechanical properties of fine and coarse clots overlap, the origin of their mechanics should be the same in origin. We proposed this mechanism is protofibril stretching in parallel. We have shown that the stiffening of both coarse and fine clots follow the wormlike chain model up to about 10 pN. From hereon, the stiffening is not explained by shear-induced fiber alignment alone: the wormlike chain model includes this effect (Fig. 2.6, solid red line). In other words, at large stress, the wormlike chain model systematically underestimates the stiffness of both fine and coarse clots. We proposed that this marked discrepancy indicates that the fibrin protofibrils are intrinsically nonlinear. Here we will discuss in more detail the possible origin of the nonlinearity of protofibrils.

Several different interpretations for this nonlinearity have been proposed. One interpretation is that the supramolecular structure of the fibers is responsible for fiber stiffening [39, 283]. The protofibrils are coupled by long and rather flexible carboxy-terminal extensions of the Aα-chains (αC domain) that protrude from the protofibrils [359], which may give rise to nonlinearities when fully stretched at high strain. Support for this idea comes from force-extension measurements on fibers assembled from fibrin of different species, which demonstrated that a longer Aα-chain length correlates with greater extensibility [337]. Also, a computational study indicated through molecular dynamics simulations that the αC domain plays a crucial role in fibrin fiber mechanics [365]. However, we observe intrinsic nonlinearity also in fine clots, which have limited bundling. Furthermore, the protofibril stretch mod-

ulus derived from coarse clots is comparable to the stretch modulus calculated from fine clots, where there is limited α-α-crosslinking. This argues against a supramolecular origin of nonlinearity, and instead suggests an alternative interpretation were the nonlinearity is intrinsic to the protofibrils themselves. One potential source of protofibril nonlinearity is forced monomer unfolding. Molecular simulations show that domains within fibrinogen monomers start to unfold at 75-150 pN forces, which is accompanied by a conversion of the alpha-helical domains into stiffer beta-sheet structures [335]. It is a priori difficult to predict how this unfolding behavior will be modified once fibrin monomers are incorporated in a protofibril or thick fiber. However, Fourier transform infrared spectroscopy [336] and direct staining of stretched networks with the beta-sheet specific dye Congo Red [366] showed convincing evidence of a strain-induced conversion of alpha-helical into beta-sheet secondary structure. Single protein unfolding measurements indicate typical forces of 90 pN to unfold fibrin monomers [299], which is comparable to the largest forces per monomer that can be applied during shear rheometry without network breakage ($\sim$100 pN). To directly resolve the microscopic origin of protofibril stiffening under shear, it will be important to perform *in situ* measurements of fibrin secondary structure in combination with shear rheometry using, for instance, vibrational spectroscopy or X-ray scattering techniques (see also Chapter 4).

We have shown that FXIII crosslinking can vary the tightness of a bundle and, consequently, the low strain stiffness of the fibrin network. However, the decrease of intra-protofibril crosslinking could also have effects on the persistence length of protofibrils, which could affect the calculation of x in Fig. 2.7C. Instead of measuring the persistence length directly, we calculated the stretch modulus of protofibrils based on the rheology data for 0 and 200 μM D004 (Fig. 2.19 in SI and Fig. 2.9A). Even though γ-γ-crosslinking is inhibited at 200 μM D004 (Fig. 2.8), the stretch modulus of these protofibrils not change with increasing D004 levels (Fig. 2.9A). This indicates that intra-protofibril γ-γ-crosslinking does not contribute to the stretch modulus of single protofibrils. Similarly, for coarse clots with varying levels of D004, the calculated protofibril stretch modulus also does not vary with D004 concentration.

In this chapter, we have shown that both small and very large bundles of protofibrils give rise to a rich mechanical behavior under the influence of increasing shear stress. This behavior cannot be captured by thermal models of crosslinked inextensible semiflexible polymers, which predicts a stronger dependence on stress ($K' \sim \sigma^{3/2}$). However, a bundled architecture within the fibers, where strain-stiffening arise from filament backbone stretching, accurately describes both the fine and coarse clot limit. Furthermore, we also show that this model holds when the intra-fiber crosslinking is varied. This has important implications for understanding the origins of fibrin mechanics. Furthermore, these results can inspire material design with more complex me-

chanical properties.

2.6 Acknowledgments

I like to thank Izabela Piechocka and Nicholas Kurniawan for doing part of the experiments and fruitful discussions. I would also like to thank John Weisel, Rustem Litvinov and Chandrasekaran Nagaswami for giving me the opportunity to learn SEM on biological samples in their group and helpful discussions. This work is part of the research programme of the Foundation for Fundamental Research on Matter (FOM), which is financially supported by the Netherlands Organisation for Scientific Research (NWO). This work is further supported by NanoNextNL, a micro- and nanotechnology programme of the Dutch Government and 130 partners.

2.7 Supplementary Information

Methods

Scanning Electron Microscopy (SEM) was performed on fibrin gels using the Verios (FEI Europe B.V, Eindhoven, the Netherlands). Fibrin gels were polymerized in 20 μl dialyzing buttons (Hampton Research, Aliso Viejo, United States) in a humid atmosphere. After polymerization, the gels were washed 3x by cacodylate buffer (50 mM sodium cacodylate, 0.15 M natrium chloride, pH 7.4), followed by 2 hours or overnight fixation with 2% glutaradehyde in cacodylate buffer. After fixation, samples were washed 3x with cacodylate buffer and then dehydrated by increasing percentages of ethanol. After complete dehydration (100% ethanol), samples were washed with 50% hexamethyldisilazane (HMDS) in ethanol and twice with 100% HMDS. Samples were left overnight to evaporate residual HMDS under the hood. After complete HMDS evaporation, samples were put on stubs equipped with carbon tape and sputter coated with an 154 Ångstrom Gold/Palladium. Samples were imaged at 10 kV using secondary electrons.

Supplementary Figures

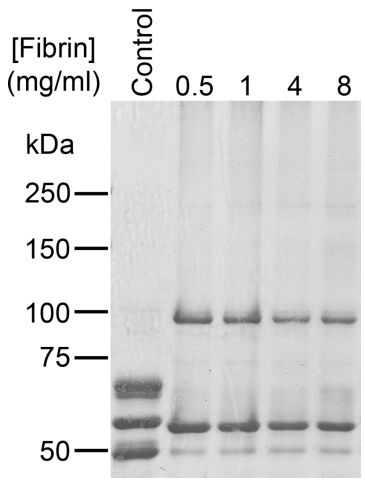

Figure 2.10: SDS-PAGE analysis of coarse fibrin gels under increasing protein concentration in mg/ml, as indicated. Control consists of fibrinogen without thrombin or calcium.

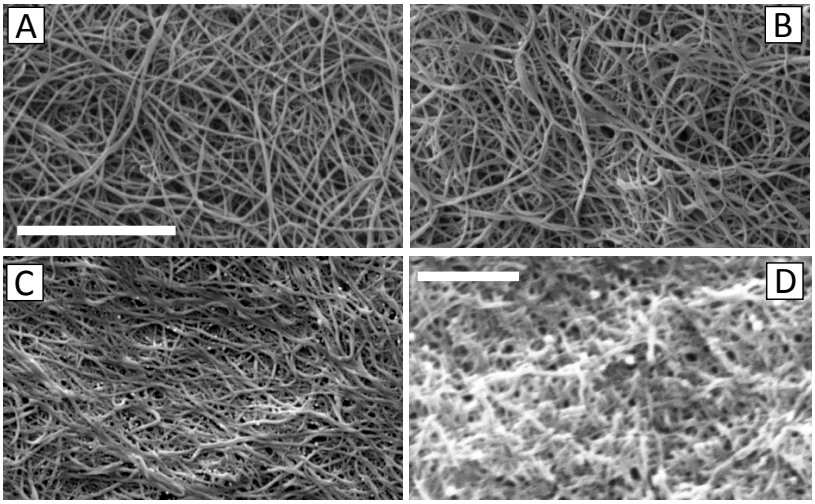

Figure 2.11: SEM on fibrin clots.(A-C) Coarse fibrin clots at 1, 3 and 7 mg/ml respectively. Scale bar represents 5 μm for (A-C). (D) Fine fibrin clot at 1 mg/ml. Scale bar denotes 400 nm.

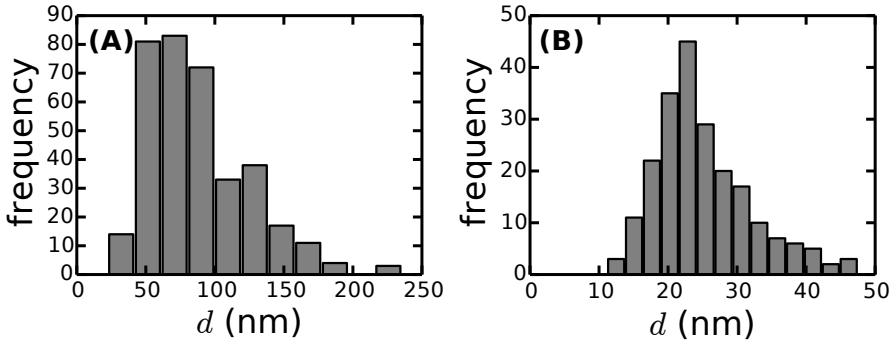

Figure 2.12: Histogram of fiber diameters determined from TEM images of fibers prepared under (A) coarse clot conditions, which promote protofibril bundling, and (B) fine clot conditions, which suppress protofibril bundling. In both, more than 200 fibers where taken into account, and data from 0.5 up to 2 mg/ml were combined.

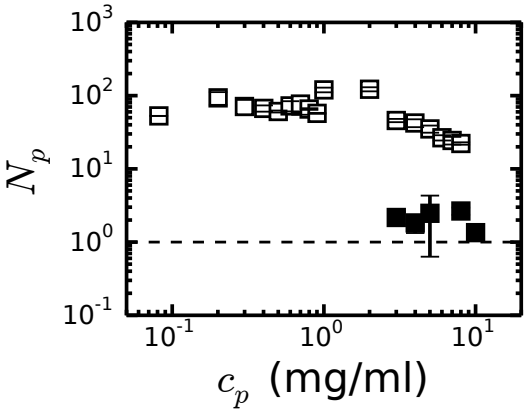

Figure 2.13: Number of protofibrils of fibrin fibers polymerized under coarse (open squares) and fine (filled squares) clot conditions, based on turbidity measurements. The limit of $N_p = 1$ is indicated.

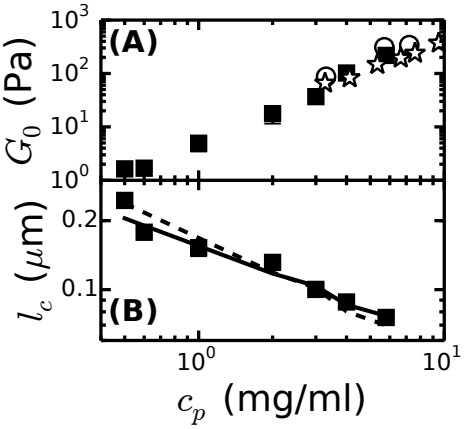

Figure 2.14: (A) The linear, small-strain, modulus for fibrin clots polymerized under fine clot conditions, which show minimal bundling (black squares), compared with previous measurements (open circles [292] and open stars [352]). (B) Cross-link distance compared with theory assuming $l_c \simeq l_e = l_p^{1/5}\rho^{-2/5}$ (solid line) or $l_c \simeq \rho^{-1/2}$ (dashed line), using a prefactor of 0.75 for both theoretical estimations.

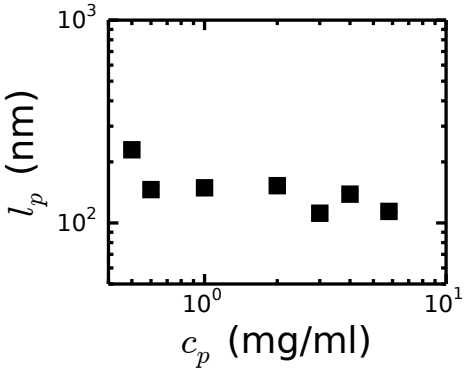

Figure 2.15: The persistence length from fitting the full prediction to the fine clot rheology data. The fiber persistence length does not vary with concentration.

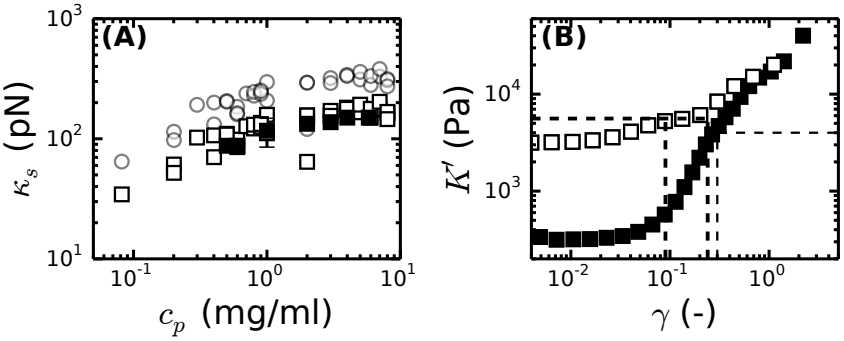

Figure 2.16: (A) The protofibril stretch modulus derived from coarse and fine fibrin clot rheology data. Black squares are fine clots, open squares are coarse clots in the aligned limit ($K_s = 1/16\rho^{pf}\kappa_s$) [66] and open gray circles are coarse clots in the isotropic limit ($K_s = 1/8\rho^{pf}\kappa_s$) [66]. (B) The differential elastic modulus for 8 mg/ml fine (closed black squares) and coarse clots (open black squares) plotted against strain. For coarse clots, the region where κ_s is determined is indicated in dashed lines. For fine clots, the inflection point is indicated by dashed lines, indicating the beginning of the enthalpic stretching regime. The stretch modulus is determined by fitting the non-linear mechanical properties by the full theoretic prediction (see Fig. 2.2 A).

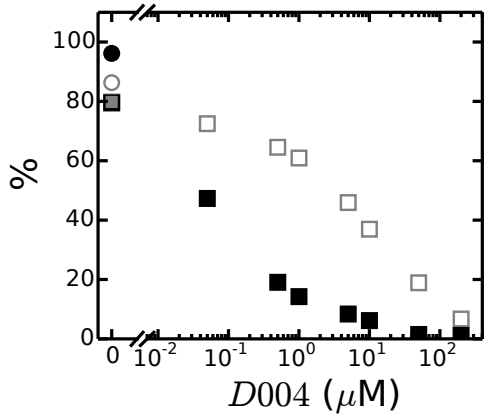

Figure 2.17: Percentage of crosslinked α-chain (closed squares) and crosslinked γ-chain (open grey squares) in 2 mg/ml fibrin coarse clots under the presence of FXIII inhibitor D004. Circles correspond to the 2 mg/ml fibrin control with no DMSO present.

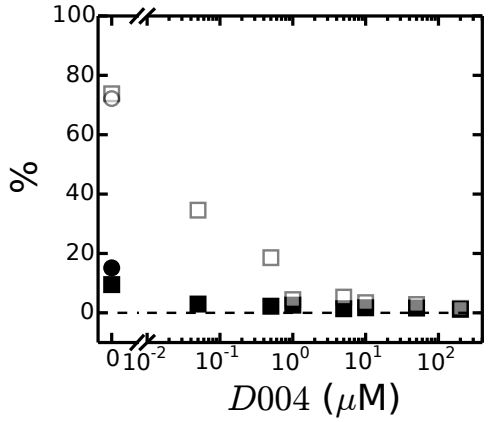

Figure 2.18: Percentage of crosslinked α-chain (closed squares) and crosslinked γ-chain (open grey squares) in 2 mg/ml fibrin fine clots under the presence of FXIII inhibitor D004. Circles correspond to the 2 mg/ml fine fibrin control with no DMSO present.

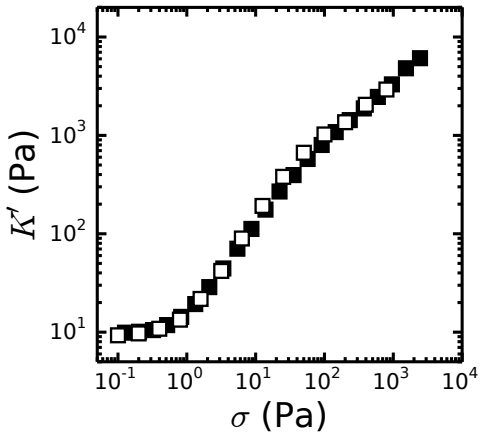

Figure 2.19: Nonlinear rheology of fine fibrin clots (2 mg/ml), in the presence (open squares) and absence (closed squares) of 200 μM D004.

3. Cells actively stiffen fibrin gels by contractile stress

During wound healing and angiogenesis, fibrin serves as a provisional extracellular matrix. We use a model system of fibroblasts embedded in fibrin gels to study how cell-mediated contraction may influence the macroscopic mechanical properties of their extracellular matrix during such processes. We demonstrate by macroscopic shear rheology that the cells increase the elastic modulus of the fibrin gels, but only in dilute (up to 2 mg/ml) gels. Microscopy observations show that this stiffening sets in when the cells spread and apply traction forces on the fibrin fibers. We further show that the stiffening response mimics the effect of an external stress applied by mechanical shear. We propose that stiffening is a consequence of active cell contraction, which provokes a nonlinear elastic response of the fibrin matrix. Cell-induced stiffening is limited to at most a factor 4, even though fibrin gels can in principle stiffen much more before breaking. We discuss this observation in light of recent models of fibrin gel elasticity, including the model discussed in chapter 2. We conclude that the fibroblasts pull out thermal bending undulations of the fibers, which requires relatively low strains, from the fibrin network, but do not axially stretch the fibers. Our findings are relevant for understanding the role of matrix contraction by cells during wound healing and cancer development, and may provide new design parameters for materials to guide morphogenesis in tissue engineering.

K.A. Jansen, R.G. Bacabac, I. K. Piechocka, G.H. Koenderink

3.1 Introduction

The mechanical behavior of animal cells is controlled by a network of stiff protein filaments known as the cytoskeleton. The cytoskeleton is a remarkable material that is maintained out of equilibrium by a variety of molecular processes using chemical energy [367]. An important contribution comes from molecular motors, which use energy resulting from ATP hydrolysis to move along actin filaments and microtubules [368]. There is strong evidence that myosin II motors, which interact with actin filaments, actively increase cell stiffness by generating contractile prestress [228, 230, 369–371]. Measurements on purified actin networks have shown that these networks strongly stiffen when either an external or an internal stress is applied [372, 373]. Cells can exploit this nonlinear stress response to modify their stiffness rapidly in response to changes in the stiffness of the extracellular environment [175, 230, 231, 371]. Conversely, the stiffness of the extracellular environment can change in response to activity of the cells, since the contractile actin-myosin cytoskeleton is physically connected to the extracellular matrix via integrin transmembrane receptors organized in adhesion complexes [374–376]. Cells thus partly transmit their internally generated forces to the extracellular matrix. These so-called traction forces are typically in the nanoNewton-range [33, 64, 237, 377–379]. By pulling on the matrix, cells can actively sense changes in ECM rigidity, on which they base decisions regarding spreading, migration, proliferation, gene expression, and even differentiation [1, 40, 213, 380, 381] (see also section 1.3.1 Chapter 1). This mechanoresponsiveness plays a crucial role in normal tissue development and function [45, 382], whereas misregulation of the balance between cell traction and ECM stiffness contributes to cancer progression, fibrotic disease, and artherosclerosis [4, 33, 383].

In connective tissues, cells reside within an extracellular matrix (ECM) that is mainly composed of collagen fibers [26]. Active cell contraction results in patterning and contraction of the collagen network during tissue morphogenesis and wound healing [238, 384–386]. During wound healing, cells are initially recruited to a provisional ECM composed of the blood clotting protein fibrin [387], which is likewise contracted and patterned by active cell contraction [241, 388]. Similar to actin networks, fibrin and collagen networks stiffen in response to an applied stress [39, 66, 389, 390]. Therefore, we anticipate – in analogy to the actin cytoskeleton, which is stiffened by myosin contractility – that extracellular networks can be driven into a nonlinear stress-stiffened regime by cellular contraction. There are indeed several reports of cell-induced stiffening of ECM gels that suggest an active, myosin-dependent origin. A classic example of cell-mediated ECM stiffening is provided by the phenomenon of clot retraction in the initial stage of blood clotting, where platelets actively contract and stiffen the fibrin blood clot [391, 392]. More recently, fibroblasts and mesenchymal stem cells were also shown to cause fibrin gel stiffening, and

it was hypothesized that active cell contraction drives the gel into a nonlinear, stress-stiffened regime [55]. Similarly, active stiffening by cellular contraction has been reported for collagen networks [393–395]. However, the precise physical mechanisms of cellular control over the mechanical properties of the ECM remain unclear, since systematic measurements comparing the linear and nonlinear rheology of ECM networks in the presence and absence of cells are lacking.

Here we use a model system of fibroblasts embedded in fibrin gels to study how the contractile activity of cells affects the macroscopic mechanical properties of their environment. We measure the linear and nonlinear rheological properties of the cell-populated fibrin networks and correlate these with the dynamics of cell spreading and fibrin gel contraction. We demonstrate that the cells stiffen the fibrin gels while they spread, by applying traction forces that drive the gels into a stiff nonlinear elastic regime. Since fibrin serves as a provisional matrix in wound healing and angiogenesis, and is also involved in pathological states such as tumor invasion, our results are relevant for interpreting the mechanical role of cells in fibrin remodeling during wound repair, angiogenesis, and tumor growth [241, 396, 397]. Moreover, the system studied here is relevant in the contexts of tissue regeneration [241, 398, 399], surgery and tissue repair [400].

3.2 Materials and Methods

3.2.1 Fibrin Gel Preparation and Cell Seeding

Human CCL-224 fibroblasts (a gift from Prof. J. Boonstra, Biology Department, Utrecht Universiteit, NL) were cultured to near-confluency in 75-cm^2 tissue culture flasks (Nunc, Roskilde, Denmark) in a-Modified Eagle's Medium (α-MEM, Gibco, Paisely, UK) supplemented with 10% fetal bovine serum (FBS, Gibco) and antibiotics (10 mg/ml penicillin/streptomycin, Sigma-Aldrich, Zwijndrecht, NL). Cultures were incubated at 37°C and 5% CO_2 in a humidified incubator and subcultured at confluency. Cells were harvested by trypsinization with a 0.1% EDTA/0.25% trypsin solution. The cells were pelleted by centrifugation and resuspended in a CO_2-independent medium composed of αMEM medium supplemented with 20 mM Hepes, 2% FBS, and 0.1% pen/strep. This stock suspension was used within one hour. The cell number density was determined using a microscope counting chamber (Hemacytometer, Optik Labor, Lancing, UK), and cells were diluted with CO_2-independent medium to a final number density of $4{\cdot}10^6$ cells/ml.

To prepare cell-populated gels, fibrinogen was first polymerized in fibrin assembly (FA) buffer and then overlaid with cell culture medium. Cells were pelleted by centrifugation and resuspended in FA buffer (20 mM Hepes, 150 mM NaCl, 5 mM $CaCl^2$, pH 7.4). The cells were centrifuged for a few minutes, resuspended in FA buffer and directly mixed with human fibrinogen (Enzyme

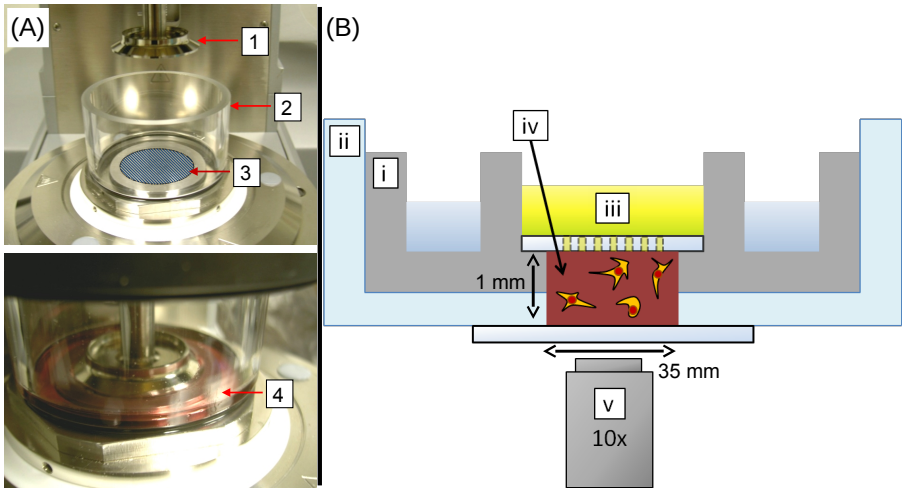

Figure 3.1: Experimental assays. (A) The viscoelastic properties of cell-populated fibrin gels were measured with a stress-controlled rheometer (top). The top plate is a cone (1) of 40 mm in diameter and 1° angle. The fibrin solution was pipette on the bottom plate (3), the top plate was quickly lowered (bottom image), and the fibrin was allowed to polymerized *in situ* at 37°C. The gel was immersed in cell culture medium supplemented with serum (4), using a perspex ring (2). (B) Schematic representation of the custom-designed microscope holder used for observing cells spreading in fibrin gels (not drawn to scale). The sample (iv) was confined in a stainless steel well (i) topped with a glass plate with holes to enable medium (iii) exchange. The entire geometry was contained in a glass bottom dish (ii). Cell spreading was observed by bright field microscopy using a 10x air microscope objective (v).

Research Laboratories, Swansea, UK) to attain a final density of 500 cells/μl unless stated otherwise. Polymerization and crosslinking of fibrinogen was initiated by adding 0.5 U/mL human α-thrombin (Enzyme Research Laboratories) final concentration. Fibrin's γ- and α-chains were fully crosslinked by FXIIIa present in the stock, according to SDS-PAGE analysis [66]. Fibrin gels were prepared at concentrations ranging from 0.1 to 6 mg/ml, where 1 mg/ml is equivalent to a molar concentration of 2.94 μM. Fibrin fibers form in a two-stage process, where fibrin monomers first form double-stranded protofibrils which then laterally associate into fibers. The fibers prepared under our conditions have a constant diameter close to 100 nm and a mass/length ratio of about $1 \cdot 10^{13}$ Da/cm (corresponding to 86 protofibrils per fiber), as

determined by wavelength-dependent turbidity measurements [66].

(-)-Blebbistatin (Sigma-Aldrich) was dissolved in methanol to a final concentration of 5 mM and stored at -20°C. The drug was tested in a final concentration range of 2 to 100 μM. Controls in which we added methanol without blebbistatin in cell culture medium showed no effect on cell morphology at these concentrations. In contrast, there was a clear reduction of cell spreading in culture with increasing blebbistatin concentration (data not shown).

3.2.2 Rheology

Rheology tests were performed with a stress-controlled rheometer (Physica MCR 501, Anton Paar, Graz, Austria). Fibrinogen solutions with or without cells were polymerized at 37°C between the steel cone and plate (40 mm diameter, 1°). After 10 minutes, the fibrin gel was overlaid with 8 mL of αMEM supplemented with 2% FBS, 20 mM Hepes, and 0.1% antibiotics (see Fig. 3.1A). We verified that the rheology measurements are minimally affected by the oxygen/metabolite gradient between the edge and center of the cone-plate geometry, by quantifying cell viability by microscopy (Supplementary Information, materials and methods section and Fig. 3.10). The time evolution of the linear shear modulus, G^*, during fibrin polymerization and cell spreading was monitored by applying a small-amplitude oscillatory strain with amplitude $\gamma = 0.5\%$ and frequency $\omega = 3.14$ rad/s and measuring the stress response, $\sigma(\omega) = G^*\gamma(\omega)$. The shear modulus is a complex quantity, $G^* = G' + iG''$, having an in-phase elastic component, G', and an out-of-phase viscous component, G''. The gels were axially constrained by strong adherence to the rheometer plates throughout the experiment. Networks reached a constant shear modulus after 3 hours in the absence of cells and 4 hours in the presence of cells. The frequency-dependent rheology of fully polymerized networks was probed across a frequency range of $0.06-38$ rad/s using an oscillatory strain of 0.5% amplitude. The high-strain regime was probed by applying a steady prestress, σ, and superposing a small stress oscillation of amplitude $\delta\sigma = 0.1\sigma$. The tangent modulus follows from the oscillatory strain response, $K^*(\sigma) = \delta\sigma/\delta\gamma$. K' was independent of frequency and of waiting time in the pre-stressed state, indicating negligible viscous flow [345]. Unless noted otherwise, rheology data are expressed as mean $\pm$ standard deviation from at least three independent experiments. Statistical analysis was performed using the Student's t-test; $p < 0.1$ was considered significant.

3.2.3 Microscopy

To visualize cell spreading inside fibrin gels, we observed cell-populated fibrin gels on a Nikon inverted microscope, using an incubation chamber and objective heater to maintain a temperature of 37°C (TokaiHit, Shizuoka-ken, Japan). The cell-seeded gels were prepared in a custom-made holder, consisting of a stainless steel well for maintaining a humid atmosphere and a glass

disc with 500 μm-diameter holes to permit medium exchange, as sketched in Fig. 3.1B. Bright field images of spreading cells were taken with a 10x (N.A. 0.3) air objective using an EM-CCD camera (Roper Coolsnap, Photometrics, Tucson, US) at a rate of 1 frame/min and exposure time of 200 ms. Cell viability was maintained by blocking infrared and UV light with a bandpass filter and by controlling light exposure with a light shutter synchronized with image frame grabbing.

Traction *strains* applied by spreading cells were visualized by time-lapse imaging of 1 μm diameter polystyrene beads adhered to the fibrin network in bright field at a rate of 1 frame/min. The particle displacements were tracked at 15 nm resolution using a tracking program written in Labview 7.1 (National Instruments Corporation, Utrecht, NL) that identifies particles by a pattern matching routine [401].

Fluorescent fibrin gels for confocal microscopy were prepared by mixing unlabeled fibrinogen with 24 mole% of Alexa488-labeled fibrinogen (Invitrogen, Breda, NL). The networks were imaged using a scanning confocal microscopy on an inverted Eclipse Ti microscope (Nikon). Fluorescence images were obtained by illumination with a 488 Ar laser (Melles Griot, Albuquerque, NM) and DIC images were recorded at the same time. Images were taken at least 50 μm from the surface. Z-stacks were taken with a piezo-driven immersion objective (either 100x (N.A. 1.49) oil or 40x (N.A. 1.3) oil objective, Nikon). During a time-sequence, an image was taken every 10 min at 5 to 10 regions in the sample. Image stacks were projected along the z-axis (for z-stacks) or time-axis (for time-lapse movies) in ImageJ (http://rsbweb.nih.gov/ij/).

3.3 Results

3.3.1 Cell Spreading and Traction Force Generation

We constructed a biomimetic tissue model by dispersing fibroblasts inside a crosslinked fibrin network. The cells were suspended in a solution of initially monomeric fibrinogen and were entrapped in the network during thrombin-triggered fibrin polymerization. To ensure that we look only at effects of cell traction forces, we focus on a time window of 7 hours after cell seeding. This time is sufficiently long for cells to spread and apply traction forces to the gels, but not long enough for matrix remodeling by chemical effects such as proteolytic degradation, matrix synthesis, or matrix crosslinking, which require time scales of over 24 hours [398, 402–405].

To monitor the time dependence of matrix formation, we observed the networks with confocal fluorescence microscopy. Matrix formation started immediately upon thrombin addition and warming to 37°C, resulting in a space-filling network of fibrin fibers within several minutes (see Fig. 3.11 in SI). To monitor the dynamics of cell spreading, we observed the cells with bright field microscopy (Fig. 3.2). The entrapped cells initially remained round, indicative

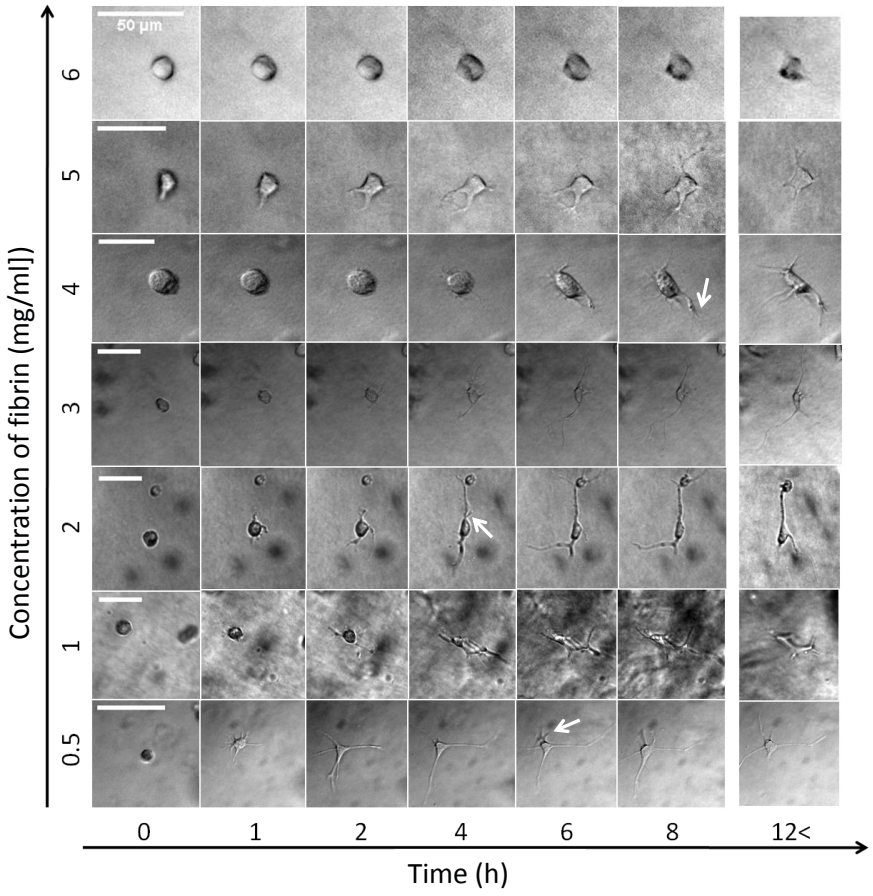

Figure 3.2: Morphological changes of cells during spreading in fibrin gels of different densities. Representative bright field images of fibroblasts at several stages during cell spreading (time axis on bottom) in fibrin gels of concentrations ranging from 0.5 to 6 mg/ml (concentration axis on the left). Scale bars denote 50 μm. Arrows point to examples of pseudopodia.

of negligible attachment to the matrix (first column, 0 h). However, within 2 hours, the cell shapes started to change as the cells attached to the matrix and spread.

Though there was some variation in the time needed for different cells within the same gel to spread, all cells in a given gel were fully spread within 4−6 hours. The shape change of the cells was most pronounced in dilute (0.5−2 mg/ml) fibrin gels. The cell body became elongated and extended several thin pseudopodial processes into the surrounding matrix with lengths up to 50 μm; in the focal plane we typically observed between 2 and 6 such protrusions. This multipolar morphology is characteristic of cells residing inside fibrin or collagen gels and resembles cell morphologies inside tissues, while being strikingly different from the flat, fan-like morphology of the same cells plated on flat substrates [104, 138, 406, 407]. Time lapse imaging revealed that the pseudopodial processes underwent cycles of extension and retraction (Movie S1 in the Supporting Material *online*, see section 3.7.2). The lifetime of pseudopodia was usually 1−3 hours. Nearly all protrusions had multiple side-branches; some of these were highly dynamic and grew and retracted on time scales of minutes, whereas others were stable for hours (for examples see white arrows in Fig. 3.2). Fibroblasts in denser (3−6 mg/ml) fibrin gels had a markedly different morphology, exhibiting only short and thin protrusions (Fig. 3.2 and Movie S2 *online*). The overall cell diameter remained close to the original diameter, which was typically less than 25 μm. This was more noticeable when zooming in with a 40x objective (see Fig. 3.12 in SI).

To test whether cell spreading resulted in matrix remodeling, we performed three-dimensional imaging of fluorescently labeled fibrin networks using confocal microscopy. In the absence of cells, fibrin networks were homogeneous and isotropic over the entire range of fibrin concentrations. As an example, Fig. 3.3A shows the maximum intensity projection of a confocal z-stack for a 1 mg/ml fibrin network. When cells are present during fibrin polymerization, the networks are locally restructured around the cells. Fig. 3.3B shows an example maximum intensity projection taken after overnight incubation of a cell (near the center of the image) inside a 1 mg/ml fibrin network (Movie S3 *online* shows the entire z-stack with the fibrin image merged with the bright field image of the cell). There are several signatures of cellular contraction: the fibrin network is highly condensed adjacent to the cell body and fibrin fibers within a distance of about 30−40 μm from the cell surface are radially oriented towards the cell. Local condensation and alignment of matrix fibers around cells, especially near pseudopodial protrusions, is indeed commonly reported in 3D-matrices [104, 408–410]. The network becomes noticeably more heterogeneous when the cell density is increased from 125 to 500 and 850 cells/μl (Fig. 3.13(A-D) in the SI). However, the estimated volume fraction of cells was always below 1%, so the network structure on larger length scales

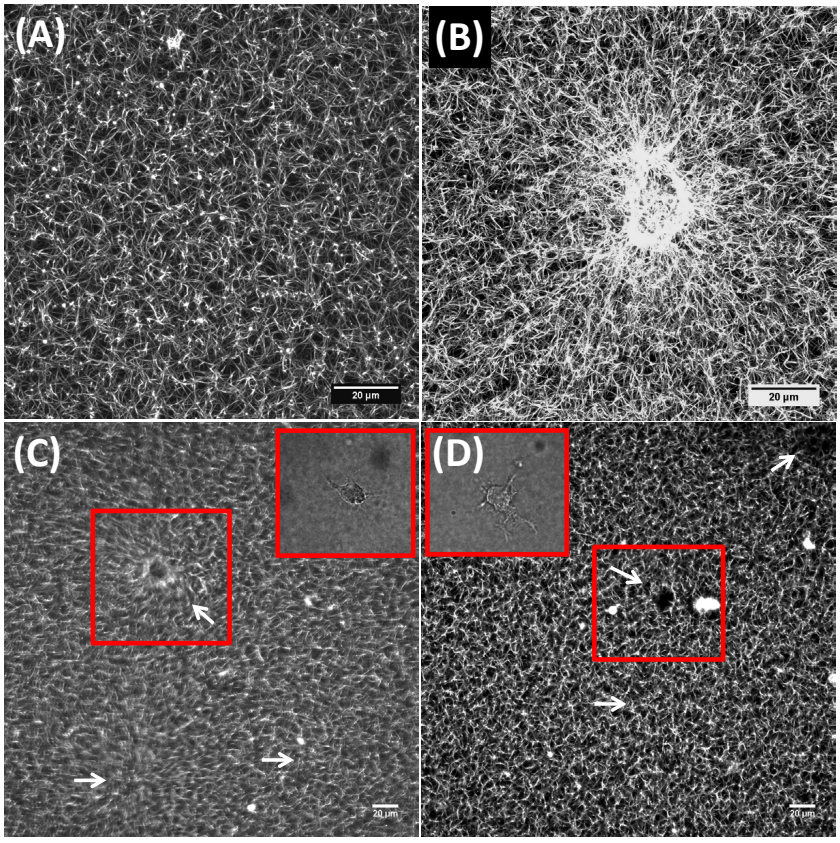

Figure 3.3: Spreading cells locally remodel the surrounding fibrin network by recruiting and aligning fibrin fibers. (A) Maximum intensity projection of a confocal z-stack of 40 μm of a fluorescently labeled 1 mg/ml fibrin network without cells. (B) Maximum intensity projection of a 40 μm confocal z-stack of a cell-populated 1 mg/ml fibrin network, showing alignment and recruitment of fibrin fibers around the cell located near the center of the image. Movie S3 (*online*) shows the corresponding z-stack, combining fluorescence images of the fibrin networks with bright field images of the cell. (C and D) Time projections of time-lapse movies (taken at a fixed confocal xy-plane) of cell-populated fibrin gels with fibrin concentrations of 2 mg/ml (C) and 3 mg/ml (D) obtained during fibrin polymerization and subsequent cell spreading. White arrows point to the presence of a cell (which can be seen by DIC microscopy, see insets). Boxes indicate cells that are in focus during the time sequence. The corresponding time lapse movies are shown in Movie S6 and S7 (*online*), combined with PIV analysis. Maximum intensity projections were obtained from z-stacks of 40 images over a total depth of 40 μm (A and B), while the time projections are obtained from 47 images (C, total time 7.5 hours) or 54 images (D, total time 9 hours).

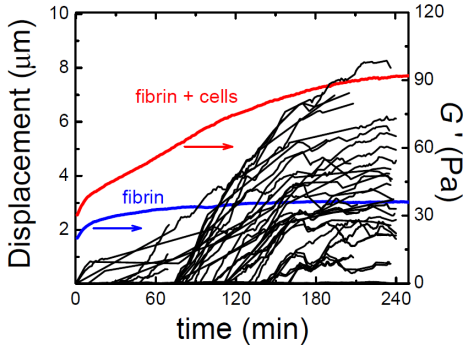

Figure 3.4: Examples of the increase in traction strain and macroscopic elastic modulus of a cell-populated fibrin gel over time, during fibrin polymerization and subsequent cell spreading. The traction strain was quantified by measuring the displacements of fiducial markers (1 μm diameter beads) embedded in the fibrin networks towards a spreading cell (black lines). The elastic modulus, G', was measured by macroscopic rheology (red line). The fibrin concentration was 1 mg/ml and the cell density was 500/μL. For reference, the blue curve shows G' for a fibrin gel without cells.

(tens to hundreds of microns) remained homogeneous. Image analysis of the fiber orientations shows that the networks also remained mostly isotropic (Fig. 3.13F).

Time-lapse movies of polymerizing networks show that cells exert contractile forces on the network that reach up to distances of at least 100 μm away from the cell surface (see Movie S6 *online* and the time-projection in Fig. 3.3C, where the cells are indicated by white arrows). Strikingly, these large network deformations are only seen in dilute networks (2 mg/ml fibrin or less). In denser gels, network deformation is negligible over a time span of at least 7.5 hours (Movie S7 *online* and the time projection in Fig. 3.3D, for a 3 mg/ml gel).

To quantify network deformation during cell adhesion and spreading, we tracked the positions of fiducial markers (1 μm spheres) attached to the network in the vicinity of spreading cells. As shown by Movie S4 (*online*) of a cell spreading in a 1 mg/ml fibrin gel, cells are initially round but start to spread and deform after about 1 hour. As the cell spreads, it pulls the surrounding probe particles inwards. The bead displacements were quantified by tracking their centroid positions over time (Fig. 3.4, black lines, each corresponding to a different particle). After about 1 hour of culture, the majority of the particles

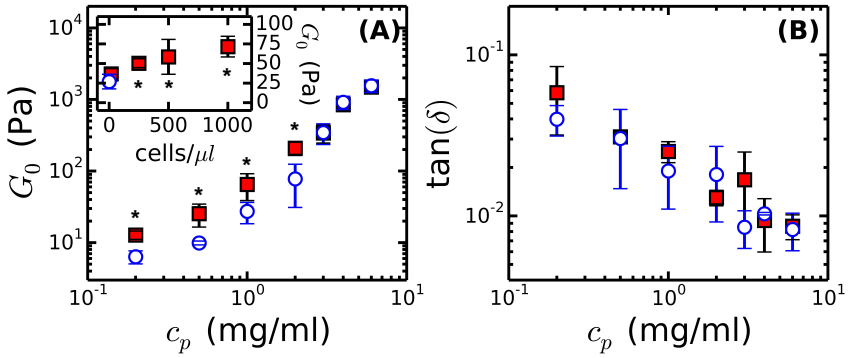

Figure 3.5: Linear viscoelastic shear moduli of fibrin gels with and without cells (at $\omega = 1$ rad/s). (A) The elastic modulus, G', is shown as a function of fibrin concentration for fibrin gels without cells (open circles) and with 500 cells /μl (closed squares). *Inset*: G' of 1 mg/ml fibrin gels as a function of cell density; the open circle corresponds to the cell-free case. (B) Loss tangent, G''/G', corresponding to the data shown in (A). Asterisks denote statistically significant differences ($p \leq 0.1$) compared to the unseeded (cell-free) case.

started to be pulled toward the spreading cell. After about 3 hours, the motion of the probe particles ceased, indicating the onset of mechanical equilibrium between the cell traction forces and the elastic resistance of the fibrin gel [411]. This time scale is consistent with the time lapse movies of spreading cells (Fig. 3.2), which showed that cell spreading was complete within 4 to 6 hours. After 6 hours, only local rearrangements of the fibrin network occurred, as shown by Particle Image Velocimetry (PIV) analysis of the time-lapse movies of polymerizing cell-seeded fibrin gels ($<$ 3 mg/ml, see supporting information and Movie S6 *online*). To test whether cells are still metabolically active once bead movement ceases, we added the peptide GRGDS to the cell culture medium (see SI). This peptide disrupts cell attachment to the fibrin network by competing for the integrin receptor $\alpha V\beta 3$ [408, 412]. Around 1 hour after addition of GRGDS to the medium, we observe a sudden recoil of the particles surrounding the cells (Movie S5 *online*), showing that tension is suddenly released and implying that cells indeed actively maintain tension. Strikingly, cells in denser ($\geq$ 3 mg/ml) gels spread without noticeably deforming the surrounding fibrin network in a timescale of 7.5 hours (Movie S7 *online*).

3.3.2 Rheology of Cell-populated Fibrin Gels

Since fibrin gels are known to stiffen strongly when subject to an external load, we hypothesized that active cell contraction may increase the elastic modulus of fibrin gels [39, 66, 389]. To test this hypothesis, we measured the linear elastic modulus, G', of fibrinogen solutions with and without cells during polymerization by macroscopic shear rheology. In the absence of cells, G' immediately started to increase and reached a plateau after about 3 hours (blue line in Fig. 3.4). This increase reflects fast polymerization of fibrin into a space-filling elastic network, followed by a slower process of covalent crosslinking by FXIIIa [341, 413]. In the presence of cells, we also observed an immediate increase of G', but it took 4 h to reach a constant value of G' and the increase of G' was biphasic, with an inflection around 2 h (red line in Fig. 3.4). The first phase of network stiffening likely corresponds to the same network formation process that occurs in the absence of cells. The second phase of network stiffening approximately coincides with the onset of cell spreading (black lines in Fig. 3.4). We note, though, that the onset of cell spreading varied from 30−70 min, probably due to variations in the delay between cell harvesting and the start of the experiments and to the fact that cells need ∼1 hour to re-express integrins after trypsinization [414]. A similar biphasic stiffening response was observed in fibrin gels and plasma clots containing contractile platelets [270]. Over the entire range of fibrin concentrations (0.2−6 mg/ml) studied, mechanical equilibrium (i.e., a constant G') was reached within 4−6 h. This time scale is consistent with the bead tracking data and the time-lapse images of spreading cells shown earlier. However, the morphology of cells inside the rheometer might differ from that seen in the cell spreading assays due to strain shielding at small strains, as was seen in collagen gels [415].

In steady state, the fibrin networks behaved as near-perfect elastic solids, with a frequency-independent elastic modulus (Fig. 3.14 in SI) and a very small loss tangent, G''/G', which decreased about ten-fold, from ∼0.05 to 0.006, when the fibrin concentration was increased from 0.2 to 6 mg/ml (Fig. 3.5B). This solid-like behavior is caused by the presence of covalent bonds between fibrin monomers within and between fibers created by the enzymatic activity of FXIIIa [66]. In the absence of cells, the elastic plateau modulus, G_0, increased nearly quadratically with fibrinogen concentration over the range of 0.5−6 mg/ml (blue circles in Fig. 3.5A). In the presence of cells, G' was three-fold higher than for the cell-free gels when the fibrin concentration was 2 mg/ml or less (red squares in Fig. 3.5A; differences are statistically significant for fibrin concentrations with $p<0.1$ below 2 mg/ml and $p<0.01$ at 2 mg/ml). However, at fibrin concentrations above 2 mg/ml, the cells did not significantly influence the elastic modulus. The viscous modulus, G'', increased by about the same factor as G' (Fig. 3.15 in SI). As a result, the loss tangent of gels with cells (solid squares) was indistinguishable from that of gels without cells

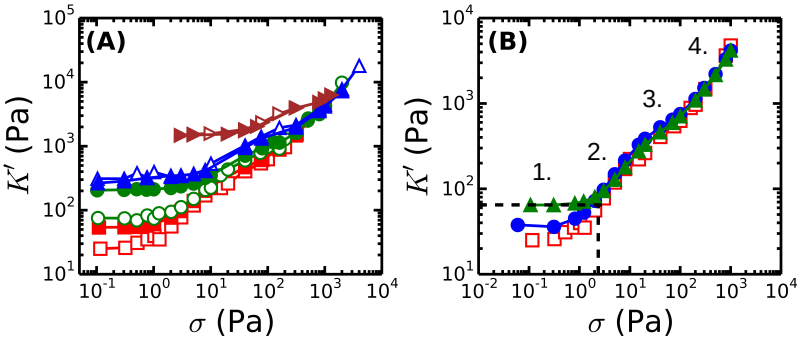

Figure 3.6: Stress-stiffening response of fibrin gels with and without cells. (A) Tangent elastic modulus, K', as a function of external (macroscopic) shear stress, σ, for fibrin gels with different concentrations: 1 mg/ml (red squares), 2 mg/ml (green circles), 3 mg/ml (blue triangles up), 6 mg/ml (brown triangles right), where open symbols are without cells and solid symbols is with cells (500 cells/μl). (B) K' as a function of σ for a fibrin gel (1 mg/ml) containing cells at different densities: 0 cells/μl (red open squares), 125 cells/μl (blue circles) and 850 cells/μl (green triangles). By comparing the stiffening curves of cell-seeded and cell-free gels, we estimate the cell-induced prestress (vertical dotted line) as the σ-value where the apparent linear modulus of the cell-populated gel matches the K'-value on the stiffening curve of the acellular gel (horizontal dotted line). The curves show a linear elastic regime (labeled 1) followed by a nonlinear response with three regimes with a distinct σ-dependence (labeled 2 to 4), see main text for details).

(open circles).

To test whether the stiffening effect depends on cell density, we measured G_0 for fibrin gels of 1 mg/ml and 4 mg/ml. At 1 mg/ml (inset of Fig. 3.5A), the cells indeed increased G_0 in a dose-dependent manner (solid squares), giving an increase relative to the cell-free gel (open circle) ranging from a factor 1.4 at 16 cells/μl (not significant, p=0.18) to a factor 2.7 at 1000 cells/μl (significant with p<0.1). At 4 mg/ml (Fig. 3.16 in SI), cells also increase G_0, but only at densities of 5000 cells/μl, corresponding to a volume fraction of about 4%.

To test whether the stiffening of the fibrin gels in the presence of cells is caused by cell-mediated contractile prestress rather than by cells acting as crosslinkers, we compared the nonlinear rheology of fibrin networks with and without cells using a prestress method. We subjected gels to a macroscopic shear stress, σ, and measured the differential shear modulus, $K'(\sigma)$, with a small superposed oscillatory stress. If cells stiffen gels by exerting contractile

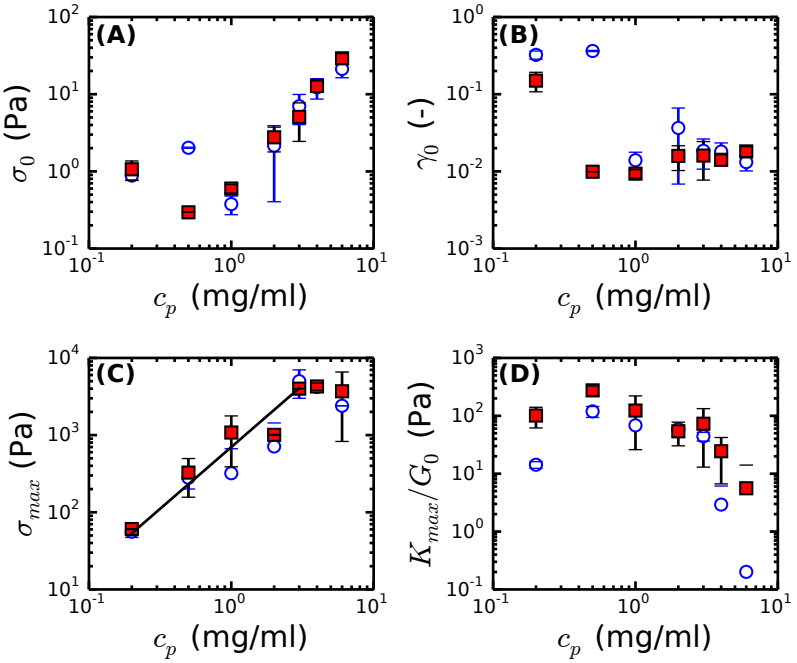

Figure 3.7: The onset stress (A) and the onset strain (B) of strain-stiffening, the maximum shear stress (C) and the maximum extend of strain-stiffening before breakage (K_{max}/G_0, (D)), plotted against fibrin concentration. Open circles correspond to unseeded gels, while closed squares correspond to gels with 500 cells/μl. The line in (C) shows a power-law fit with an exponent of 1.6 $\pm$0.14.

prestress, we expect convergence of the elastic moduli of cell-seeded and unseeded gels as soon as σ exceeds the contractile prestress [373]. If, in contrast, cells act merely as crosslinkers, we expect that the cell-seeded gels will be stiffer than unseeded gels independent of σ. In the absence of cells, $K'(\sigma)$ increased with stress until the gels broke at a maximum stress level, σ_{max}, as illustrated for gels of 1 mg/ml (open squares), 2 mg/ml (open circles), and 6 mg/ml (open triangles) fibrin in Fig. 3.6A. The maximum extent of strain-stiffening before breakage, as quantified by the ratio K_{max}/G_0, was close to a value of 100 for gels of 0.2−3 mg/ml and decreased to 10 for gels of 6 mg/ml fibrin (open circles in Fig. 3.7D). The nonlinear elastic response in the presence of cells (solid symbols in Fig. 3.6A) was qualitatively similar to the behavior of unseeded gels. The gels again had a linear regime for stress levels below an onset stress,

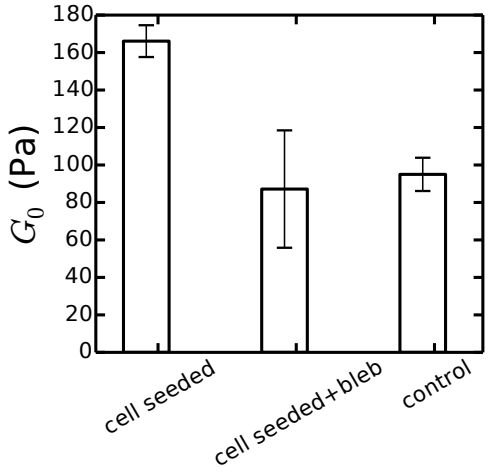

Figure 3.8: Fibrin gel stiffness with and without cells in the presence or absence of blebbistatin. Blebbistatin was added in the medium from the start to a final concentration of 100 μM. In case of the control sample (no cells), we added methanol without blebbistatin. For the cell seeded case there was no methanol added to the medium. However, tests in 2D culture showed no effect on cell spreading at this methanol concentration. Data points are averages of 4 separate measurements for the control and of two separate measurements for the other two cases.

σ_0, and stiffened at larger stress levels until the breakage stress, σ_{max}, was reached. For dense gels ($\geq$3 mg/ml fibrin), the entire stress dependence of the response of cell-seeded and acellular gels was indistinguishable (triangles). However, for dilute gels ($\leq$2 mg/ml fibrin) the cells caused a clear increase of the linear elastic modulus while leaving the high-stress response unchanged. The maximum shear stress, σ_{max}, supported by the gels was unchanged by the presence of cells (Fig. 3.7C), and the maximum elastic modulus, K_{max}, was likewise unchanged. Consequently, the relative degree of stress-stiffening before breakage, K_{max}/G_0, was about 3-fold lower for cell-seeded gels than for acellular gels (Fig. 3.7D). When we increased the cell density, we observed an even more pronounced increase of the linear modulus, but the high-stress response still remained unchanged (Fig 3.6B). These observations strongly support our hypothesis that cells stiffen the gels by an active mechanism, involving contractile prestress. Indeed, tests with blebbistatin, which specifically inhibits myosin II contractile activity [416], show that myosin activity is a requirement for cell-induced stiffening (Fig. 3.8).

The increased stiffness of the cell-seeded gels coincided with a postponement of the onset of stress-stiffening (Fig. 3.7A). In the absence of cells, the stress at the onset of strain stiffening, σ_0, increased more than tenfold when the fibrin concentration was raised from 0.6 to 6 mg/ml (open circles in Fig. 3.7A). The corresponding onset strain, γ_0, was 30% for the most dilute gels (0.2 and 0.5 mg/ml) and only 1−3% for the more concentrated gels (open circles in Fig. 3.7B). The cells increased σ_0 and decreased γ_0 for gels with fibrin concentrations below 2 mg/ml ($p<0.06$). Similar to the cell-free gels, there appeared to be two distinct concentration regimes for γ_0, with $\gamma_0 \simeq 10$ % for 0.2 and 0.5 mg/ml fibrin and $\gamma_0 \simeq 1$ % at higher fibrin concentrations.

3.4 Discussion

3.4.1 Cells Stiffen Fibrin Gels by Generating Contractile Prestress

We showed that fibroblasts seeded inside extracellular matrices prepared from purified human fibrinogen cause macroscopic matrix stiffening. The extent of stiffening increases with increasing cell density, reaching a maximum of 3-fold stiffening over cell-free gels at 1000 cells/μl. At higher cell densities, cells caused macroscopic contraction and detachment from the rheometer plates. Stiffening was apparent only in dilute fibrin scaffolds of 2 mg/ml or less. These findings are consistent with several prior studies, showing comparable degrees of stiffening in case of fibroblasts and mesenchymal stem cells (factor 2−4 stiffening, at a similar cell density as ours [55]) and platelets (factor 10 stiffening, but at a 100-fold larger cell density compared to our study [270, 417]). A similar extent of cell-induced stiffening was also reported for frog embryonic tissue [418]. In these earlier studies, it was already hypothesized that the stiffening effect may be caused by active contractility of the cells, which may drive the gel into a nonlinear, stress-stiffened state. In our work, we systematically tested this hypothesis. Here we showed by rheology measurements in the presence of the myosin inhibitor blebbistatin that cell-induced gel stiffening indeed requires myosin-driven contractility.

We observed a clear correlation between the onset of gel stiffening and the onset of cell spreading. Time-dependent rheometry showed that the cells started to stiffen the fibrin gels ca. 1−3 hours after cell seeding, which coincided with the moment where microscopy showed that cells started to attach to the gels and spread. Fibrin network formation was largely complete within the first hour (Fig. 3.11 in SI), well before the cells began to spread. In the process of spreading, the cells applied inward (traction) forces to the fibrin fibers and caused fibrin gel compaction, but only near the cell edges. This compaction was only seen in dilute (≤ 2 mg/ml) fibrin gels. Once the cells were fully spread (ca. 6 hours after seeding), they maintained active tension in the surrounding

fibrin network. This was apparent from the abrupt release of tension when GRGDS was added to block the RGD binding integrins [408, 411, 412]. The elastic modulus of the cell-seeded gels reached a constant value once the cells were well-spread.

Cell-induced gel stiffening could in principle arise either from active traction forces, which prestress the network [419–421] or from a passive crosslinking effect of the cells [420, 422]. We consider the latter explanation unlikely, since the cells take up less than 1% of the total sample volume, based on an average cell diameter of 25 μm. Moreover, the close correspondence of the time dependence of cell spreading and gel stiffening strongly suggests that cell traction forces are related to gel stiffening. This interpretation is further supported by tests with blebbistatin, showing that myosin inhibition prevents gel stiffening (Fig. 3.8). A direct comparison of the nonlinear elastic behavior of cell-seeded and cell-free gels also supports an active mechanism. The cell-seeded gels have a higher elastic modulus than acellular gels at low shear stress, but an identical elastic modulus at high shear stress. Furthermore, the cell-seeded gels have a smaller onset strain than cell-free gels. These observations indicate that the cells generate an internal prestress that brings the fibrin gels in a nonlinear stress-stiffened state. The stiffness of the cell-seeded gels is controlled by a sum of the active prestress and the externally applied shear stress. Fig. 3.6B illustrates the concept, by comparing stress-stiffening curves of a cell-seeded fibrin gel (green triangles) with that of a cell-free gel (red squares). The cell-seeded gel has an initial modulus (horizontal dotted line) that corresponds to the modulus of the cell-free gel under an external shear stress of about 2 Pa (vertical dotted line). At shear stresses larger than 2 Pa, the cell-seeded gel starts to stiffen and its nonlinear modulus coincides with that of the cell-free gel. The maximal modulus reached before breakage is the same for the cellular and acellular gels. Since the cellular gel starts out in a prestressed, stiffened state, the total degree of gel stiffening caused by the external stress (given by the ratio K_{max}/G_0) is less than for the acellular gel. We note that these observations are qualitatively consistent with prior large amplitude oscillatory shear measurements of fibrin gels and plasma clots containing platelets [270]. The platelets, similar to the fibroblasts studied here, increased G_0 (by a factor of 5) while having no effect on gel stiffness at large levels of shear stress. Moreover, similar to the fibroblasts studied here, the platelets postponed the onset of strain-stiffening to larger values of σ_0 and reduced the maximum extent of strain-stiffening before gel breakage.

The external shear stress where the nonlinear modulus of the acellular gel matches the linear modulus of the cellular gel can provide an estimate of the global prestress in the cellular gels generated by the cells [373]. The prestress thus estimated increases roughly linearly with increasing cell density, going from 1 Pa for 16 cells/μl to 3 Pa at 1000 cells/μl in gels of a constant (1

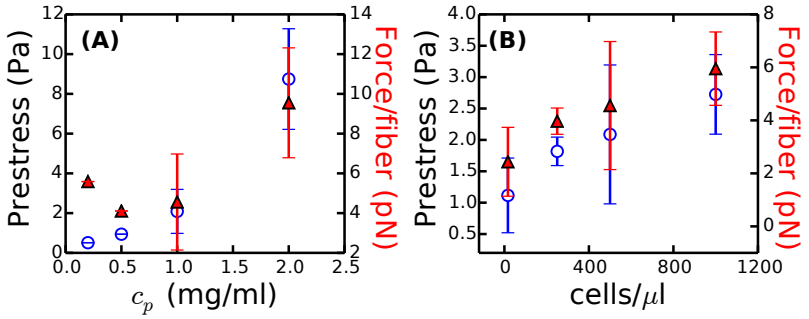

Figure 3.9: Cell-mediated prestress (left axis, open circles) determined by comparing the stress-stiffening response of cellular and acellular gels according to the procedure shown in Fig. 3.6B, and corresponding calculated average force per fibrin fiber (right axis, solid triangles). (A) Prestress as a function of cell density in gels of fixed fibrin concentration (1 mg/ml). (B) Prestress as a function of fibrin concentration at a fixed cell density (500 cells/μl).

mg/ml) fibrin concentration (open circles in Fig. 3.9A). At fixed cell density (500 cells/μl), the prestress increases from 0.5 Pa to 9 Pa as the fibrin concentration is increased from 0.2 to 2 mg/ml (Fig. 3.9B). However, at fibrin concentrations of 3 mg/ml and higher, there is no measurable prestress, since the elastic moduli of cellular and acellular gels are indistinguishable. This does not necessarily imply that the prestress is zero, since the prestress may be less than the onset stress needed to induce strain-stiffening ($\sigma_0 = 7$ Pa at 3 mg/ml). However, bright field imaging did show that the cells are less well-spread in dense (3−6 mg/ml) fibrin gels than in dilute (0.2−2 mg/ml) gels. Cells in denser gels are less elongated and generate much shorter protrusions than in more dilute gels (Fig. 3.2 and Fig. 3.12 in SI). On 2D gels, well-spread cells tend to exert higher traction forces than less-spread cells [1, 377, 379], which raises the possibility that cells in dense fibrin gels exert smaller traction forces than in dilute gels. Recent work suggests that matrix-embedded cells mainly generate traction along their pseudopodial protrusions [423, 424]. The reduced tendency of the cells to form pseudopods in dense gels may therefore also contribute to a smaller overall prestress. However, a direct measurement of traction forces on a microscopic scale in the fibrin network immediately adjacent to the cells will be needed to verify this hypothesis [257].

From the prestress values, we can estimate an average traction force experienced by each fibrin fiber by dividing the prestress by the total filament length density, ρ. We find an average force per fiber between 2 and 10 pN,

depending on cell density and fibrin concentration (solid triangles in Fig. 3.9A and B). These values are considerably lower than traction forces reported by other techniques and in a variety of ECM materials [64, 237, 247, 257]. This is expected, since the numbers reported here are ensemble averages over the entire cell population. In the local vicinity of cells, we expect higher force levels than in the regions in-between cells. Interestingly, the reduced cell spreading in denser fibrin gels is in apparent contradiction with studies of cell spreading on planar (2D) elastic substrates, where increased substrate stiffness tends to promote cell spreading [40,175,213,377]. However, in 3D matrices several other factors can influence cell spreading behavior, such as differences in local stiffness, ligand density, porosity, and three-dimensionality of cell surface receptor engagement (see Chapter 1 for an extensive review). Changing the fibrin concentration changes not only the stiffness, but also the matrix porosity. The average mesh size determined by confocal microscopy decreases as a square root in fibrin concentration, going from 10 μm at 0.1 mg/ml fibrin to 2 μm at 6 mg/ml fibrin [66]. The small mesh size of the denser gels may constrain the cell body and also impede the extension of pseudopods. In the future, it will be interesting to find alternative ways to modify the matrix rigidity without changing the network architecture.

3.4.2 Mechanistic Origin of Fibrin Gel Stiffening

The nonlinear elastic modulus of the fibrin gels has a remarkably complex dependence on stress, with four distinct phases, as indicated in Fig. 3.6B. We recently showed that these four phases reflect the hierarchical structure of fibrin networks [66]. At small stress, excess length between crosslink points stemming from thermal bending fluctuations are pulled out, giving rise to an initial linear regime (regime 1) followed by an entropic stiffening response (regime 2). Despite their large diameter ($\sim$100 nm), the fibers do exhibit significant thermal fluctuations because they are composed of semiflexible protofibrils that are bundled by flexible linker chains. Due to this bundle-like architecture, the fibers exhibit still significant thermal fluctuations and show a $\omega^{3/4}$ dependence as expected for semi-flexible polymer chains (see Chapter 5). However, it is likely that for fibrin gels prepared under conditions where the fibers are thicker or the mesh size is larger, entropy no longer plays an important role. In these cases, we instead expect nonaffinity to govern the low-stress response [425].

As the stress is raised further, the fibers themselves are axially stretched, causing a small regime of constant elastic modulus (regime 3) followed by another strain-stiffening regime (regime 4). The stiffening at large stress suggests that the fibers themselves have an inherently nonlinear force-extension response. Direct force-extension measurements using atomic force microscopy have indeed demonstrated strain-stiffening on the level of individual fibrin fibers, though the exact molecular origin is still under debate. Possible explanations are stretching of flexible αC-linker regions that connect the pro-

tofibrils within a fiber [66, 282] or forced-unfolding of the fibrin monomers [299, 335, 389, 426]. Remarkably, the cells only influence regimes 1 and 2 of the nonlinear response of the fibrin gels. In regimes 3 and 4, where the fibrin fibers themselves are axially stretched, the stiffening curves for cell-populated gels are identical to those of cell-free gels (Fig. 3.6A and B). This observation indicates that stress/strain applied by the cells are sufficient to stretch out thermal undulations of the fibrin fibers between crosslink points, thereby increasing the elastic modulus in regime 1 and shifting the onset of regime 2 to a larger onset stress. However, the cells are apparently unable to stretch out the backbone of the fibrin fibers. Indeed, the forces reported in Fig. 3.9 are insufficient for causing forced unfolding of fibrin monomers, which requires forces on the order of 100 pN [426]. Strain-stiffening of individual fibrin fibers requires large strains on the order of 100% [282]. We cannot exclude that backbone stretching occurs locally in a few highly strained fibrin fibers, but we can exclude that it occurs on a macroscopic scale.

The cell-induced stiffening of the fibrin gels is an analogue of rheological measurements of reconstituted actin-myosin gels [372, 373]. Contractile prestress generated by myosin II motors was shown to produce identical stiffening as an external stress applied by shearing actin networks [373]. The active prestress reached values equivalent to an external stress of 14 Pa. The average force per actin filaments (which may be calculated from the known mass concentration and mass per length ratio of actin fibers [427]) was 0.3 pN. Consistent with the fact that cells contain many myosin II motor molecules, the average force in the actin-myosin networks is an order of magnitude lower than the forces we find for cell-mediated matrix stiffening.

3.4.3 Implications of Cell-induced Stiffening

In recent years, various quantitative techniques (collectively known as 'traction force microscopy', see section 1.7 in Chapter 1) have been developed to measure traction forces exerted by cells on 2D substrates [378, 379, 428] and inside 3D hydrogels [247,257,423]. The basic idea is to measure the strain field in the substrate by tracking the displacements of fiducial markers and to convert strains into traction forces by using an appropriate elastic model for the substrate. This conversion requires certain assumptions, such as continuum elasticity and linearity. These assumptions are reasonable for typical synthetic hydrogels such as polyacrylamide, but are invalid in physiologically relevant fibrous materials such as collagen or fibrin networks [56, 57]. Our results show that cells are able to induce active stiffening of fibrin matrices, which should be taken into account in future attempts to perform traction force microscopy in 3D matrices.

Cell-induced stiffening also has implications for understanding tissue behavior during tissue development and homeostasis. By locally pulling on the matrix, cells can sense and respond to mechanical changes of the ECM. How-

ever, at the same time they also actively change the stiffness and tension in the ECM, thus creating a mechanical feedback loop [429]. This effect may explain recent findings showing that fibroblasts and human mesenchymal stem cells plated on soft fibrin gels behaved the same as on stiff 2D substrates, suggesting that the cells respond to the gel's high-strain modulus [55]. Cell-induced matrix stiffening may also result in a feedback loop enhancing cellular contractility, development of stress fibers and growth of adhesions [33]. Furthermore, the nonlinear elastic response of the ECM on cell contractility will likely influence the mechanical interactions among cells during tissue morphogenesis, a phenomenon which has been seen [46, 238, 384] as well as theoretically [430–433]. Studies of cells cultured in/on linearly elastic materials have shown that stem cell fate can be controlled by changing matrix stiffness [1, 89], which implies that scaffold stiffness is a key design parameter for biomaterial scaffolds for tissue repair. Owing to its natural function in angiogenesis and wound repair, fibrin is particularly popular for applications in tissue engineering of cartilage, cardiac muscle, skin wound healing, nerve, and vascular tissue [400,434]. Given that matrix stiffness is an important design parameter, cell-induced stiffening is thus an important factor.

3.5 Conclusion

Here we have shown that fibroblasts stiffen tissue-like fibrin matrices by applying contractile forces against the extracellular matrix that brings it into a stress-stiffened regime. By correlating observations of cell spreading with rheological measurements, we discovered that stiffening starts as the cells start to spread and apply contractile tension. Once the cells are well-spread, they maintain an isometric contractile force on the fibrin matrix. Control tests with an actin-myosin inhibitor correlated contractile force with stiffening of fibrin gels. We found that both cell spreading and fibrin gel stiffening were sensitive to the matrix density. Cells assumed well-spread, elongated shapes with long protrusions in gels of low fibrin concentrations and spread progressively less in denser fibrin gel, remaining round with small protrusions in the densest gel tested (6 mg/ml). By directly comparing nonlinear rheology measurements on cell-seeded and cell-free gels, we conclude that cells generate traction forces that are sufficient to pull out large wavelength thermal undulations of the fibrin fibers, but insufficient to axially stretch the fibrin fibers. The mechanical properties of fibrin blood clots during wound healing, fibrosis, and cancer development are probably controlled at least in part by the nonlinear elastic response of the clots to the active internal forces generated by embedded cells.

3.6 Acknowledgments

I would like to thank the design and mechanical workshop at AMOLF for realizing the cell spreading geometry used to follow cell spreading in time. I also

like to thank Rommel Bacabac for doing some of the cell-seeded experiments. I also thank Prof. J. Boonstra for his gift of the fibroblasts, Oscar Stassen and Elly Hol for performing qPCR, William Thielicke for sending documentation on the program PIVlab, and José Alvarado for help with OrientationJ analysis. This work is part of the research programme of the Foundation for Fundamental Research on Matter (FOM), which is financially supported by the Netherlands Organisation for Scientific Research (NWO). This work is further supported by NanoNextNL, a micro and nanotechnology programme of the Dutch Government and 130 partners.

3.7 Supplementary Information

3.7.1 Supplementary Materials and Methods

Materials

To test the involvement of integrins in cell spreading and traction force generation, we added the integrin-binding peptide GRGDS (AnaSpec Inc., Seraing, Belgium) to a 3 mg/ml fibrin matrix with fibroblasts, once the cells were well-spread. This peptide should compete with integrin binding sites on fibrin [408,411,412]. GRGDS was dissolved in 5% acetic acid at a concentration of 2 mM and stored at -20°C. GRGDS was freshly diluted with CO2-independent medium to a concentration of 20 μM and added to cell-populated gels after completion of cell spreading by exchanging this medium with the medium on top of the glass disc. The final GRGDS concentration was 10 μM, sufficient for maximal inhibition of integrin binding [408, 411, 412].

qPCR protocol

Cells were allowed to spread for 6 hours within gels of 1 mg/ml fibrin (denoted as '3D') at a cell density of 500/μl. Medium was removed and replaced by 0.05% trypsin/EDTA (Invitrogen). The gels were incubated for ∼10 min at 37°C to dissolve the gels. The solutions were then spun down and the pellets were quick-frozen and stored at -80°C. Cells cultured in tissue culture flasks (denoted as '2D') were trypsinized and collected by centrifugation. Cell pellets were quick-frozen and stored at -80°C. Quantitative real time PCR (qPCR) analysis was performed as described elsewhere [435]. Briefly, RNA was isolated from cells grown in 2D or 3D culture using TRIsure (Bioline) and precipitated in 2-propanol for 1 hour room temperature. 500 ng of RNA was DNaseI treated and used as a template to generate cDNA following the manufacturer's instructions (Quantitect-Qiagen, Venlo, the Netherlands) with a mixture of oligo dT and random primers at 42°C during 30 min. The resulting cDNA (10 μl) was diluted 1:20 and served as a template in real-time quantitative PCR assays (SYBR Green PCR Master Mix (ABI)). Quantification and normalization procedures are described in detail elsewhere [436]. Briefly, the expression of the genes rnapolii, hprt, gapdh and ef1a were used to normalize the detected integrin expression. Primers were designed for the PCR product to be intron spanning using NCBI's Primer Blast [437]. qPCR was performed for integrin β3 with primers FW: CCCCACCACAGGCAATCAAA, and RV: AGCGTCAGCACGTGTTTGTA, and for integrin αV with primers FW: CAAGGGAACCCTTCCTCGGA, and RV: GGAGAAACAGTGCTCGTCGG.

Rheology

For rheology measurements of (cell seeded) fibrin gels, a steel cone and plate (40 mm diameter, 1° cone angle, 'CP40-1') was used. After 10 minutes, the fibrin gel was overlaid with 8 mL of αMEM supplemented with 2% FBS, 20 mM HEPES, and 0.1% antibiotics, as sketched in Fig. 3.1A. Since the medium is only touching the edges of the geometry, there will be a gradient of nutrients and oxygen from the sample edge to the center. To assess whether this gradient influences cell viability, we imaged cells within fibrin networks in a custom-made glass sample chamber that mimics the cone-plate geometry of the rheometer. Based on cell morphology, we counted the number of spread, round and dead cells (Fig. 3.10). We found that up to about 10 mm inwards (corresponding to half the radius of the geometry), the cells are spread. At 8−9 mm inwards, the fraction of round cells starts to go up. At about 12 mm inwards, cells start to die, mostly likely due to an oxygen and metabolite gradient. Thus, clearly, cells do not behave the same in the center as near the edge. It should be noted, however, that in a cone-plate geometry, the outer edges contribute much more strongly to the measured mechanics than the center of the sample. Also in the region where the cells do spread, more than 80% of the sample volume is located. We also note that even if the CP40-1 geometry is not ideal for cell survival, it does create a three-dimensional scaffold for the cells and is therefore a reasonable compromise between cell survival and three-dimensionality, with the effect of dead cells on fibrin gel mechanics being minimal. We also checked that the presence of medium around the rheometer plates did not influence the viscoelastic behavior.

PIV analysis

Particle Image Velocimetry (PIV) analysis was performed based on fluorescence confocal microscopy time-lapse movies of 2 and 3 mg/ml fibrin gels recorded during cell spreading. We used an existing PIV routine in Matlab (PIVlab_GUI.m, downloaded from http://www.mathworks.nl). Briefly, 1064x1064 pixels images were highpass filtered using a filter size of 15 to 30 pixels before analysis. PIVlab uses a method called 'multiple pass' to increase accuracy. The search window area at step one was 64 pixels with 32 pixel overlap, at step two 32 with 18 pixels overlap and at step three 20 with 10 pixels overlap. The last step is chosen to be slightly bigger than the observed mesh size. For finding of the peak of the correlation matrix, a Gaussian 2x3 point sub-pixel estimator was used. The final accuracy was estimated to be 1 to 2 μm, corresponding to a few pixels [438].

Alignment Analysis

To analyze the response of fibrin fiber orientations to the presence of cells, we analyzed confocal images of cell-free and cell-populated fibrin networks using the ImageJ plugin OrientationJ, developed by Daniel Sage at the Biomedical

Image Group (BIG), EPFL, Switzerland and freely available at bigwww.epfl.ch (last visited 26 August 2013). Specifically, we analyzed maximum intensity projections of z-scans taken over a depth of 40 μm (1 μm step size). Briefly, OrientationJ evaluates the local orientation and coherency of every image pixel and computes a distribution of angles. A Gaussian window of 2 or 3 pixels and a Gaussian gradient was used to determine the local derivative [439]. Using these orientation images, we calculated the nematic order parameter. Given a collection of orientation measurements, ψ, in the range (-90°, 90°], the nematic order parameter is computed from the second-order tensor order-parameter S_2 [440]:

$$S_2 = \begin{bmatrix} \langle \cos 2\psi \rangle & \langle \sin 2\psi \rangle \\ \langle \sin 2\psi \rangle & -\langle \cos 2\psi \rangle \end{bmatrix} \tag{3.1}$$

Angle brackets $\langle \cdot \rangle$ denote averages over all orientation measurements. The tensor S_2 is symmetric and traceless. Solving the eigenvalue problem for S_2 yields two eigenvalues,

$$\lambda_{1,2} = \pm \sqrt{\langle \cos 2\psi \rangle^2 + \langle \sin 2\psi \rangle^2} = \pm S \tag{3.2}$$

which yield the (two-dimensional) scalar order-parameter S familiar for liquid crystals. This order parameter quantifies the width of the distribution of orientation measurements. It is zero for a uniform distribution of orientations, and approaches one for a sharply-peaked distribution. We find that in practice S is between 0.1 and 0.2 for isotropic networks.

3.7.2 Movies

For the supplementary movies, we refer the reader to:
http://www.biophysj.org/biophysj/supplemental/S0006-3495(13)01136-3

3.7.3 Supplementary Figures

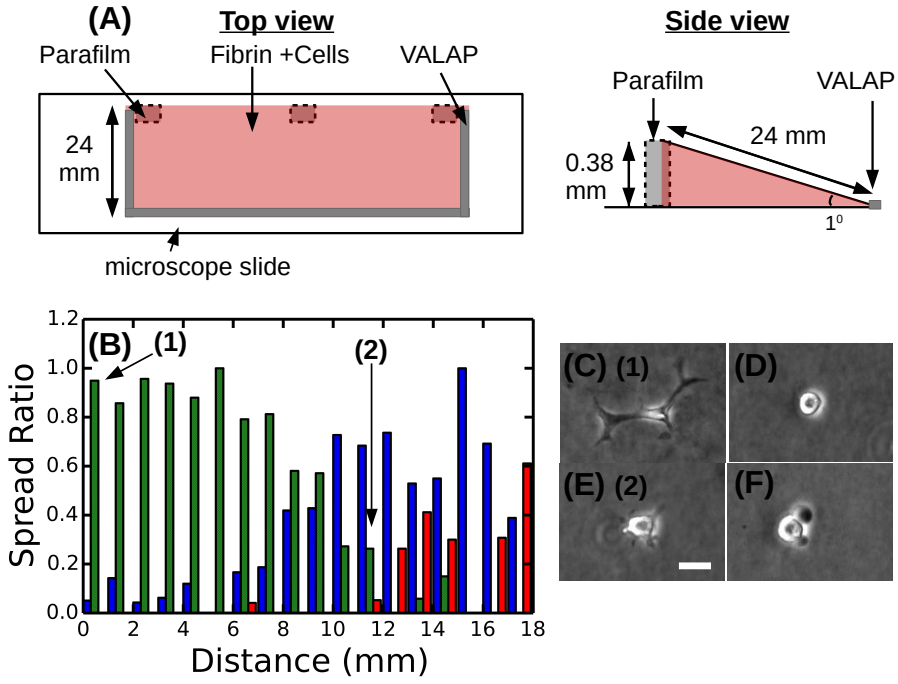

Figure 3.10: Morphologies of cells in a 2 mg/ml fibrin gels after 7 hours in a sample geometry that mimics the rheometer cone-plate geometry. (A) Schematic showing how the CP40-1 geometry is mimicked using glass coverslips (not drawn to scale). After filling the geometry with a solution of activated fibrinogen and cells, the sides were sealed with VALAP and the geometry was placed in a petridish with medium after 10 minutes polymerization. Cells were observed in the middle of the glass slide. (B) Relative counts of spread (green), round (blue) and dead cells (red) as a function of distance from the edge, as determined from cell morphology. (C-F) Examples of cell morphologies observed with a 10x air objective using phase contract. (C) and (E) represent 'spread' morphologies seen at spot 1 and 2 in (B). (D) Example of a round cell. (F) Example of a dead cell. The scale bar is 20 μm for all images.

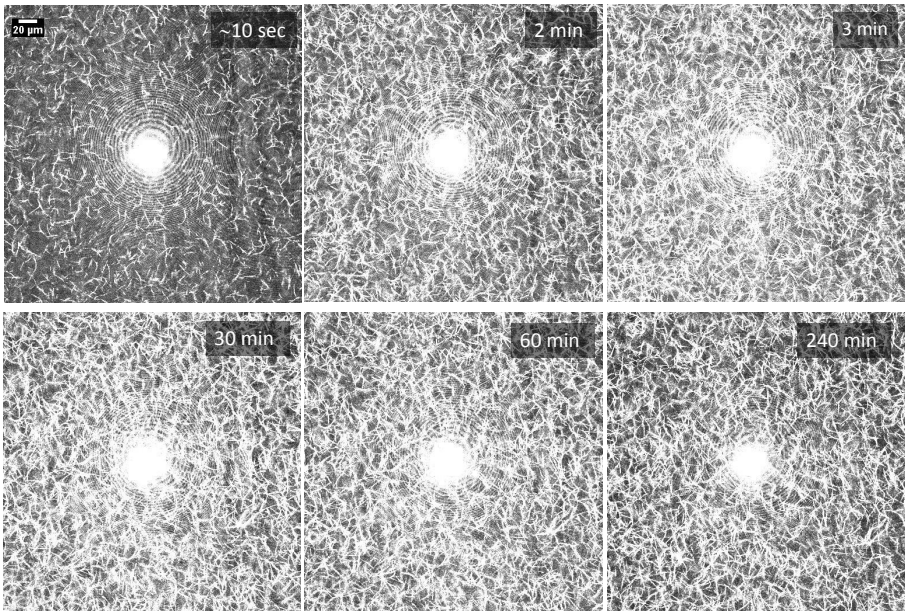

Figure 3.11: Time lapse images showing polymerization of a cell-free fibrin gel recorded by label-free confocal reflection microscopy (1 mg/ml). The scale bar denotes 20 μm. Images were taken using a 40x oil objective and 457 nm laser light. Time elapsed since the addition of thrombin is indicated in each panel. The bright spot in the center is an artifact of the imaging technique. Images recorded after the ∼10 second time point are over-saturated because the laser and detector settings were optimized to capture the earliest time point.

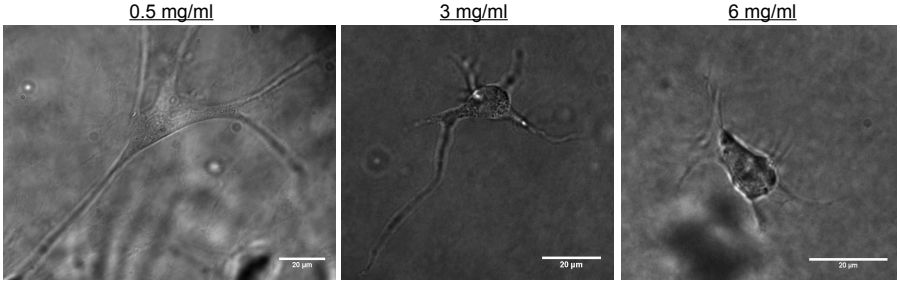

Figure 3.12: Cells in fibrin gels of different concentrations (see labels) imaged using a 40x (N.A. 1.0) oil immersion objective. Images were taken after overnight incubation. The scale bars are 20 μm.

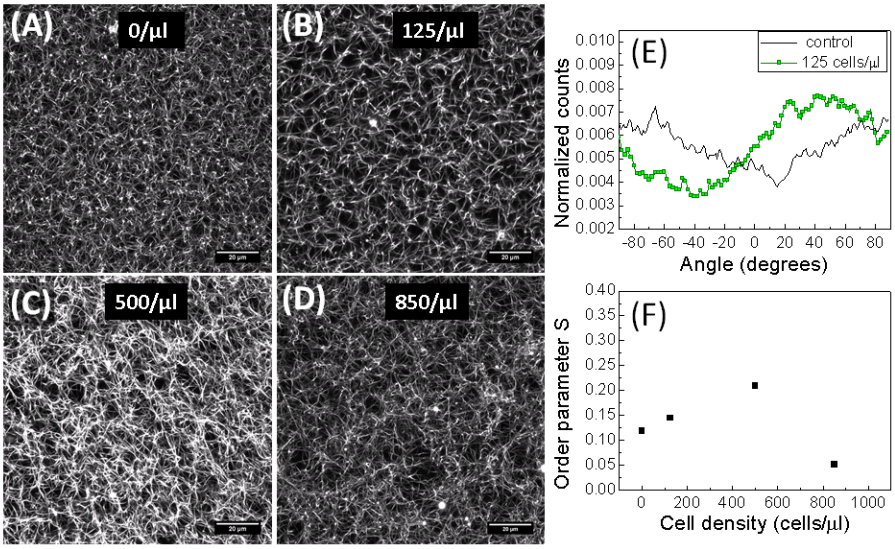

Figure 3.13: The effect of increasing cell density (see labels) on fibrin network structure. (A-D) All images are maximum intensity projections of confocal fluorescence microscopy stacks of 40 images spanning 40 μm in height. The cell density was varied from 0 to 850 cells/μl (see labels). Scale bars are 20 μm. (E) Pixel orientation histogram for images (A) (control, black line) and (B) (green line squares). Images were analyzed using OrientationJ. (F) Nematic order parameter of images (A-D). S can range between 0 for an isotropic system and 1 for a perfectly aligned system, but in practice we find values of 0.1−0.2 for isotropic networks. Only the networks with 500 cells/μl is slightly anisotropic ($S = 0.21$).

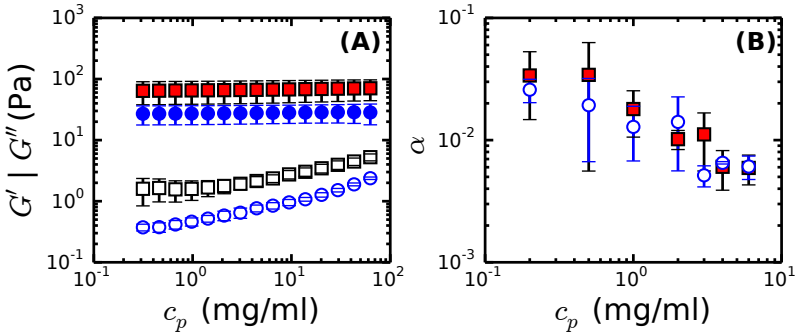

Figure 3.14: Frequency dependence of the linear rheology of fibrin gels with cells (squares) and without cells (blue circles). (A) Linear elastic modulus (solid symbols) and viscous modulus (open symbols) of a fibrin network (1 mg/ml) with and without cells (500/μl). (B) Power law exponent, α, of the frequency dependent elastic modulus for fibrin networks with and without cells (500/μl) as a function of fibrin concentration.

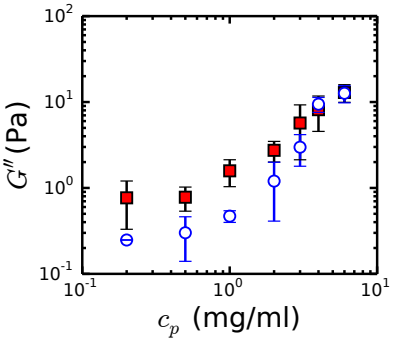

Figure 3.15: The viscous (loss) modulus G'' of cell-seeded (500/μl) fibrin gels (red solid squares) and unseeded fibrin gels (blue open circles) as a function of fibrin concentration.

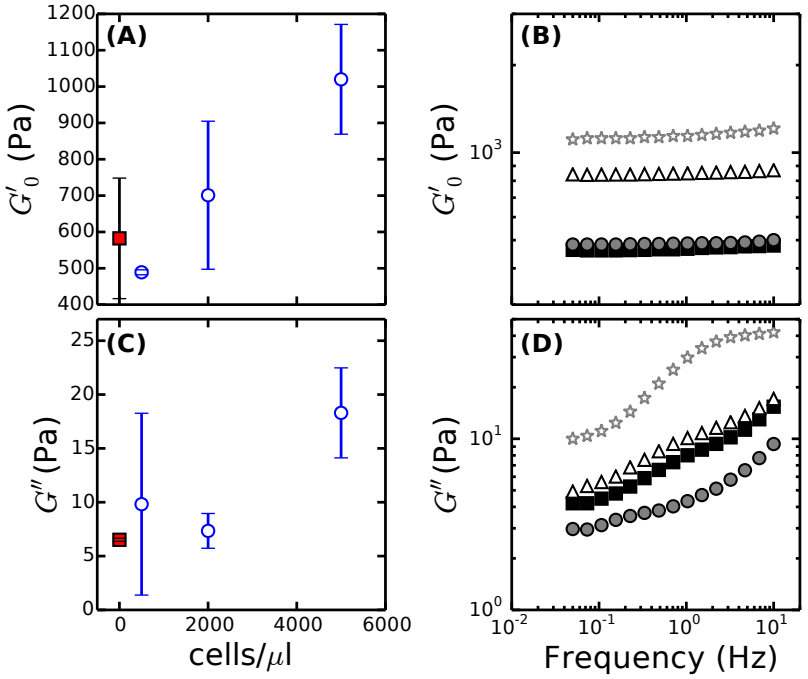

Figure 3.16: (A-B) The elastic (storage) plateau modulus, G'_0, and viscous (loss) modulus G''_0 of cell-seeded fibrin gels (red solid squares) and unseeded fibrin gels (blue open circles) as a function of cell density for a 4 mg/ml fibrin gel. (C-D) The frequency dependence of cell-seeded fibrin gels (gray filled circles 500 cells/μl, open black triangles 2000 cells/μl, gray open stars 5000 cells/μl) and unseeded fibrin gels (black filled squares) as a function of cell density for a 4 mg/ml fibrin gel. The frequency dependence is unaffected, except at 5000 cells/μl. Perhaps the volume fraction of cells is large enough here to influence the overall rheology.

4. Fibrinogen Unfolding During Fibrin Gel Stretching

Fibrin is a transient extracellular matrix that forms upon vascular injury as a first step towards wound healing. Fibrin fibers can be extended several times their own length without rupture, though the origin of this extraordinary extensibility is still poorly understood. In this chapter, we study the origin of fibrin extensibility by using small-angle X-ray scattering (SAXS) in combination with tensile tests. SAXS measurements provide insight into both the axial and lateral molecular packing structure of the fibers. We show that the degree of axial and radial packing order is dependent on fibrin bundle size, which we relate to the mesh size of the network that puts an upper bound on the range of crystalline order. By comparing our SAXS measurements with full-atom simulations of protofibrils, we show that the second order reflection of the half-staggering axial repeat distance is suppressed due to the symmetric structure of the fibrinogen monomer. Upon stretching, however, several new peaks appear, including the second order reflection. At high strains of ∼100%, the peaks indicative of axial order disappear, showing that stretching causes forced molecular unfolding. To trace the molecular origin of these changes, we compare our SAXS results with predicted SAXS spectra based on full-atom simulations of stretched protofibrils. Taken together, our experiments and simulations directly show that protofibril elongation is mediated by 1) elongation of the alpha-helical coiled-coil regions and 2) γ-nodule unfolding, which starts at 30% strain. These results are important to understand the reduced extensibility in case of disease-related fibrinogen mutations and the influence of FXIIIa crosslinking on fibrin fiber extensibility.

K.A. Jansen, A. Zhmurov, G. Portale, D.H. Merino, R.I. Litvinov, B.E. Vos, V. Tutwiler, I.K. Piechocka, N.A. Kurniawan, W. Bras, J.W. Weisel, V. Barsegov, G.H. Koenderink

4.1 Introduction

The formation of a fibrin network during blood clotting is one of the first step towards wound healing [330]. The fibrin network serves as a plug to stop bleeding and provides a scaffold for cells that mediate wound healing. Fibrin formation is initiated by enzymatic conversion of the soluble plasma protein fibrinogen to its activated form, referred to as fibrin [441]. The fibrinogen monomer is comprised of two identical subunits, each of which is formed by three polypeptide chains denoted Aα, Bβ and γ. These chains fold into a trinodular structure that is around 46 nm in length and 4.5 nm in diameter [350]. The central E-region is formed by the N-terminal portions of all the chains, while the terminal D-regions are formed by the C-terminal portions. The D-regions consist of a number of structurally distinct domains, including the β and γ-nodules [442]. The middle portions of the Aα, Bβ and γ chains form rod-like α-helical coiled-coil connectors between the E- and D-regions. The C-terminal ends of the Aα-chains known as the αC regions form globular αC-domains that are tethered to the molecule with the flexible αC-connectors [359]. Thrombin triggers fibrin clot formation by sequentially removing two sets of fibrinopeptides known as FpA and FpB from the N-termini of the Aα and Bβ chains. Removal of the FpA peptides exposes A-knobs in the E-region that are complementary to 'a' holes in the D-regions, thus causing half-staggered self-assembly into two-stranded protofibrils [443]. Subsequent removal of the FpB peptides exposes B-knobs in the E-region that are complementary to 'b' holes in the D-regions. Both B:b interactions and interactions between the *alpha*C-domains of adjacent protofibrils are thought to contribute to protofibril bundling [330, 358, 444, 445]. Under near-physiological ('*coarse clot*') conditions, purified fibrin forms fibers that are bundles of several tens of protofibrils [66]. In contrast, at high pH and ionic strength, protofibril bundling is inhibited and so-called '*fine clots*' are formed (see Chapter 2). The fibers are mechanical reinforced by activated Factor XIII (FXIII), which forms covalent bonds between the γ and α chains [446].

The mechanical properties of fibrin significantly affect the biological functions of fibrin [447, 448]. Blood clotting requires that fibrin networks are sufficiently elastic and strong that they can withstand the mechanical forces applied by flowing blood [449, 450] and the contractile forces applied by platelets [420, 451]. Moreover, fibrin networks need to provide appropriate mechanical resistance to the contractile forces applied by cells during wound healing [67, 270]. Yet, abnormally stiff networks formed in case of excessive crosslinking can also be disadvantageous since they are not easily lysed and cause thrombotic diseases [343]. Both whole plasma clots and purified fibrin networks exhibit remarkable elastic properties: they stiffen strongly and can be reversibly sheared or stretched up to strains in excess of 100% [66,366,389,413]. Mechanical measurements on single isolated fibers have shown that the fibers

themselves also stiffen when stretched [282], and that they can be stretched up to four-fold their original length without breaking [283, 333, 334].

The physical basis of the exceptional nonlinear elastic behavior of fibrin is still under debate. Fibrin networks are structured across multiple scales, from the molecular (monomer) scale, to the protofibril, the fiber, and finally the network scale. It is difficult to disentangle the distinct contribution of each of these scales to the overall macroscopic response. At the network scale, the elastic properties of fibrin have been modeled by polymer theories, which treat fibrin fibers as uniform semiflexible polymers with a certain stretch and bend rigidity [39]. These models indeed predict a strain-stiffening response. However, the extreme extensibility of fibrin networks can only be understood when the internal structure of the constituent fibers is explicitly modeled.

There are two main models to explain the extensibility of fibrin fibers. The first model relies on forced unfolding of the fibrin monomers. All-atom Molecular Dynamics (MD) simulations of the force-extension behavior of single fibrin molecules showed that stretching causes molecular elongation by an interplay between unwinding of the α-helical coiled-coil connectors and unfolding of the γ-chain nodules [299, 335]. The simulations further predicted that the coiled-coil connectors undergo an α-helix to β-strand conversion, resembling the stretch-response of coiled-coil domains in intermediate filaments and myosin [452, 453]. Each coiled-coil consists of 111 or 112 amino-acid residues of the Aα-, Bβ-, and γ-chains, and can thus contribute a 23-nm molecular extension as it goes from a folded length of 17 nm to an unfolded length of 40 nm, as supported by molecular simulations and AFM measurements [426]. Unfolding the γ-chain nodules can contribute another 160 nm molecular extension [299]. However, it is unclear how intermolecular contacts between fibrin molecules packed together in a fiber will influence the unfolding process. This question is difficult to address in view of the large size and complexity of the fibers. Furthermore, it is unclear what force levels fibrin molecules will experience locally within a strained network, especially in dilute networks that are known to experience inhomogeneous (nonaffine) deformations [413, 454].

The second model to explain the extensibility of fibrin fibers has focused on their bundle-like supramolecular structure, which consists of relatively rigid protofibrils coupled by long and rather flexible carboxy-terminal extensions of the Aα-chains that protrude from the protofibrils [359]. Computational modeling of this composite structure showed that stretching of the unstructured αC-connector region of the α-chain can in principle explain the extensibility and strain-stiffening of fibrin fibers [365]. Experimental support for this model comes from force-extension measurements on fibers assembled from fibrin of different species, which demonstrated that a longer αC-chain region correlates with greater extensibility [337]. However, there is also some experimental evidence against a supramolecular origin of nonlinearity. As shown in Chapter

2, we have evidence from rheology studies that fine clots, which mostly lack a bundle organization, show the same elastomeric response as coarse clots. This observation does not change when α-α-crosslinking is inhibited. The extensibility and strain-stiffening behavior thus occur independent of the αC-chain regions and is apparently intrinsic to the protofibrils themselves, lending support to the molecular unfolding model.

A few studies have sought to directly test the molecular mechanism that underlies the elastomeric response of whole fibrin networks by combining macroscopic mechanical testing with *in situ* structural measurements. There are some clear hints from Small Angle X-Scattering (SAXS) studies on stretched fibrin films and gels that molecular unfolding does occur at high tensile strains. The scattering peak corresponding to the half-staggered axial repeat distance (22.5 nm) of fibrin was shown to increase in width and decrease in height at increasing strains, indicating increased disorder [389,455,456]. One study even showed disappearance of the peak at a tensile strain of 100% strain [389]. More direct evidence for force-induced changes in secondary structure comes from vibrational spectroscopy measurements, which confirmed the predicted α-helix to β-strand conversion of the coiled-coil regions in stretched and compressed fibrin gels [336]. Further qualitative evidence for this structural transition has come from staining with the β-sheet-specific dye Congo Red [366]. However, the generality of these observations is unclear and the details of the unfolding pathway, such as onset strain and sequence of domain unfolding, are unknown.

Here we aimed to test directly whether forced unfolding of fibrin molecules occurs during macroscopic fibrin network stretching, and if so, to identify the unfolding pathway. To this end, we probed the molecular packing structure of fibrin gels that were reconstituted *in vitro* by *in situ* SAXS measurements during gel stretching with a uniaxial tensile tester. SAXS is widely used for structural characterization of soft matter on small length scales ($\sim$1-100 nm) [457]. This range of scales nicely matches the typical length scales associated with the molecular packing structure of fibrin as well as other protein fibers like collagen [458] and silk [459]. Moreover, SAXS is non-invasive and can probe structural information in a label-free manner. These features make SAXS an ideal method to study changes in molecular structure taking place in macroscopic samples during deformation. However, it is not straightforward to identify changes in molecular structure from SAXS data for complex systems such as fibrin.

Long-range order in the molecular packing arrangement of fibrin monomers in the fibers gives rise to Bragg diffractions, which show up as peaks at characteristic distances in the SAXS spectra [295,298,460,461]. Changes in molecular structure can be inferred from changes in the positions, heights, and widths of these Bragg peaks provided that a model is available of the molecular packing structure. Unfortunately, modeling of scattering from fibrin is complicated due

to the complexity of its molecular packing structure. Fibrin fibers are known to exhibit long-range axial packing order resulting from half-staggered overlap of the fibrin monomers since early SAXS measurements dating back to [460] as well as electron microscopy (EM) studies [289]. Intriguingly, third and higher-order reflections of the 22.5 nm axial repeat distance are usually visible, but the second order reflection is almost always lacking in SAXS spectra [298,460,461]. The origin of this peak suppression is unclear. For fibrin samples with thin fibers, also the first order reflection of the half-staggering distance is not clearly visible [456]. Furthermore, the cross-sectional packing structure of fibrin fibers is still poorly understood. Some X-ray scattering and EM studies concluded that there is no ordered, lateral packing in fibrin fibers [460, 462], while others found evidence of lateral crystallinity [298, 463, 464].

Here we provide SAXS data for fibrin gels obtained during stretching, together with a molecular interpretation based on a direct comparison of our data with full atom simulations of fibrin protofibrils from our co-workers, Artem Zhmurov (Moscow Institute of Physics and Technology), and Valeri Barsegov (University of Massachusetts Lowell). To understand the influence of the molecular packing structure of fibrin fibers on the SAXS spectra, we first performed SAXS measurements on unstretched fibrin gels with varying bundle sizes. We show that the axial molecular packing structure of fibrin can explain the suppression of the second order reflection of the 22.5 nm axial repeat. Further, we find that the Bragg peaks corresponding to axial order are much more pronounced for thicker fibers and that the peak width is correlated to the mesh size of the network. The SAXS spectra confirm a recent model describing the radial packing structure of fibrin fibers as partially ordered [295]. When the fibrin gels are subjected to uniaxial stretch, we find clear evidence for forced molecular unfolding. The second order reflection of the 22.5 nm axial repeat distance appears when the strain reaches ∼30%, which coincides with unfolding of the γ-nodules in simulations of single protofibril stretching. Furthermore, peaks corresponsing to axial packing order become broader and less intense with increasing strain, indicative of increased disorder. At strains of ∼90-100%, the peaks disappear, but only for slow pulling rates. By combining SAXS experiments with MD simulations, we can now understand the molecular basis of fibrin's extensibility and strain-stiffening response. Forced unfolding may also help explain recent findings that mechanical stretch protects fibrin fibers against fibrinolysis [465–467].

4.2 Materials and Methods

4.2.1 Fibrin Polymerization

Human fibrinogen depleted of Von Willebrand Factor (VWF), fibronectin and plasminogen (FIB3) as well as human αthrombin were purchased from Enzyme Research Laboratories (Swansea, UK). The fibrin networks were in all

cases covalently crosslinked by fibrinoligase (FXIIIa), which is present in the fibrinogen stock, resulting in a constant molar ratio of FXIIIa with respect to fibrinogen. Experiments were performed on so-called 'coarse clots', which were formed in near-physiological condiations, at 37°C and in fibrin buffer containing 20 mM Hepes, 150 mM NaCl and 5 mM $CaCl_2$ at pH 7.4. Fibrin formation was initiated by adding 0.5 U/mL thrombin (final concentration) and allowed to proceed for at least 4 hours before experiments. Fibrin′s γ- and α-chains were fully crosslinked according to SDS-PAGE analysis over the entire fibrin concentration range that was tested (4 to 8 mg/ml).

To test how the influence of fiber bundle size (expressed in terms of the average number of protofibrils per fiber, N_p) influences the SAXS spectra, we also prepared samples under conditions designed to either increase or decrease N_p.

To increase N_p, we used two different strategies. The first strategy used FIB3 fibrinogen that was first dialyzed into fibrin buffer (without $CaCl_2$) for 2 days. The protein concentration after dialysis was determined by measuring the absorbance at a wavelength of 280 nm with correction for scattering at 320 nm [292]. This resulted in a larger number of protofibrils in a bundle compared to the non-dialyzed case: $N_p = 120$ compared to $N_p = 84$ at $c_p =$ 1 mg/ml, as determined by turbidimetry. Since we did not measure N_p at the concentration used for the SAXS experiments, we assumed $N_p \sim 100$ for the 8 mg/ml samples. The second strategy, which increased N_p further, was inspired by a recent study showing that removal of fibrinogen oligomers, which are generally present in solutions of purified plasma fibrinogen, results in an increase in protofibril lateral association [344]. Briefly, FIB3 fibrinogen was filtered through a 0.2 μm filter and injected at a concentration of 2.7 mg/ml onto a Superdex 200 gel filtration column, which was equilibrated with fibrin buffer (20 mM HEPES, 150 mM NaCl, pH 7.4), at room temperature. The flow rate was 0.5 ml/min (at a pressure of ∼0.12 MPa). The fibrinogen monomer fraction corresponding to the second peak [344] was collected and concentrated to ∼15 mg/ml by centrifugation in MacroSep centrifuge tubes (Pall Corporation) at 811 rcf. The tubes were washed with buffer before use. The fibrinogen monomer fraction was snap-frozen and stored at -80°C. This strategy gave $N_p = 366$ at $c_p = 1$ mg/ml, as measured by turbidimetry. Since we did not measure N_p at the concentration used for SAXS measurements ($c_p = 4$ mg/ml), we will assume $N_p \sim 366$ for the 4 mg/ml samples. Fibrin gels from dialyzed or gel-filtered fibrinogen were allowed to polymerize for 4 hours at 37°C in fibrin buffer supplemented with 5 mM $CaCl_2$.

To decrease N_p relative to the 'coarse clot' conditions, we created so-called 'fine clots' [292, 338, 339]. Briefly, fine clots were generated by dialyzing FIB3 fibrinogen for at least 2 days at 4 °C against fine clot buffer (50 mM TRIS-HCl, 400 mM NaCl, pH adjusted to 8.5 with NaOH). The final fibrinogen

concentration was determined by measuring the solution absorbance at 280 nm with correction for scattering at 320 nm [292]. Fine fibrin clots were polymerized for 1 hour at 37 °C by adding 0.5 U/ml thrombin in fine clot buffer with 3.2 mM $CaCl_2$. This procedure resulted in a dense network with thin fibrin fibers with $N_p = 2$, independent of fibrinogen concentration (see also Chapter 2).

4.2.2 Small Angle X-ray Scattering (SAXS) and Tensile Tests

Small Angle X-ray Scattering (SAXS) was performed at the DUBBLE Beamline (BM26B) of the European Synchrotron Radiation Facility (ESRF, Grenoble, France) [468]. The range of wavevectors, q, was calibrated using silver behenate powder as a standard (see Fig. 4.4). The sample-to-detector (P1M) distance was 2.8−3 m and the energy of the beam was 12 keV. Measurements of fibrin gels inside glass capillaries (i.e. 0% strain, 'capillary measurements') were performed using 2 mm borosilicate glass capillaries with 0.01 mm wall thickness (cat.nr. 4007620, Hilgenberg, Germany). Capillaries filled with buffer were taken as background. Since there can be variations in capillary thickness, we ensured that a background was taken for every capillary and on every spot we measured, before we polymerized the fibrin gels in the same capillaries. The beam dimensions on the sample were 900x700 μm.

For stretching experiments, a Linkam tensile tester (TST350, Linkam Scientific Instruments, UK) was installed in the beam path. The tensile tester was equipped with a 20 N force transducer with 0.001 N force resolution. The samples were subjected to a stepwise increasing strain ramp, with a pulling speed of 7 (5 samples), 10 (6 samples) or 50 (3 samples) μm/s. After each strain interval, we measured for 20 s at 5 or 6 different positions in the sample. For fine clot samples, we measured for 30 s up to 2 min per spot due to low scattering signal. No visual damage was observed, nor abrupt changes in the force level, during the SAXS measurements. The beam dimensions on the sample were ∼400x700 μm. Dog-bone shaped fibrin gels were created with two pieces of Velcro (∼6.5x6 mm) in home-made Teflon molds with a sample length of 22 mm. These molds were cleaned with 70% ethanol, treated with a thin layer of mineral oil to facilitate removal of the fibrin gels from the mold, and preheated to 37°C before use. The Velcro pieces were also cleaned in 70% ethanol. The sample volume was 850 μl and the initial sample dimensions were 5.2 mm in width and 2.8 mm in thickness. About half of the Velcro area was clamped in the tensile tester. The initial slack in the gel was pulled out before the strain measurement was started and sample buffer was added every other strain step to prevent drying.

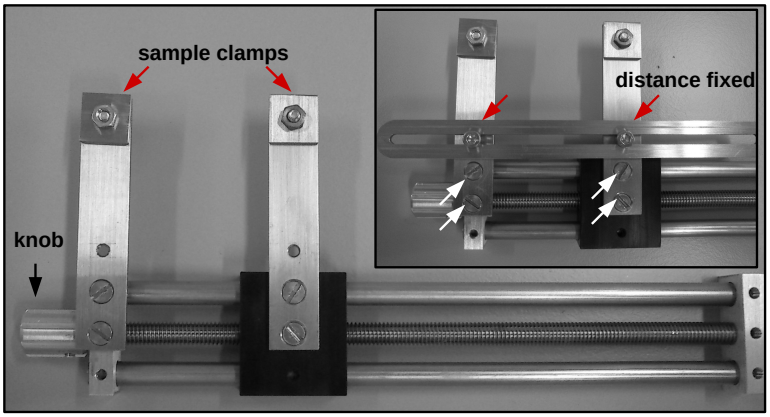

Figure 4.1: A manual sample stretcher developed in-house. The sample was clamped as indicated and manually stretched, where one knob turn translated into 1 mm stretching. When the desired distance was reached, the distance was locked (inset, red arrows) and the sample was detached from the stretcher (inset, white arrows) and transported to a fixative solution to fix the sample at that stretched distance. The total length of the stretcher was about 170 mm.

4.2.3 Imaging and Analysis of Fiber Alignment

To determine the degree of fiber alignment at increasing strain levels, a manual stretcher was developed in-house (Fig. 4.1). Alexa488 labeled fibrinogen was purchased from Life Technologies (Bleiswijk, the Netherlands), dissolved in coarse clot buffer (without $CaCl_2$) and mixed with unlabeled fibrinogen in a 1:30 down to 1:80 molar ratio. Dog-bone shaped fibrin samples of 8 mg/ml (dialyzed coarse clots) with Velcro pieces at their ends were clamped in a similar fashion as for the SAXS measurements. The pulling speeds used in SAXS experiments were approximated ($\sim$5$-$40 μm/s). Buffer was applied to the sample every mm of straining. When the desired strain level was reached, the stretched distance was locked (Fig. 4.1 *inset*) and the sample was fixed in a 2.5% glutaraldehyde solution in fibrin buffer for at least 3 hours and up to overnight. During this time, the sample was protected from light to prevent photobleaching. The fixed samples were cut into smaller pieces with a sharp surgery knife and transported by a tweezer to a glass-bottom petridish (Mattek Corporation, USA). Buffer was added to prevent drying. The fibrin network was imaged on a confocal fluorescence microscope using a Nikon Eclipse Ti inverted microscope equipped with a 100xoil immersion objective (NA 1.49), a 488-nm laser (Coherent, Utrecht, The Netherlands) for illumination, and a

photomultiplier tube detector (A1; Nikon, Amsterdam, the Netherlands). Z-stacks of 10 μm thick, taking an image every 0.125 μm, were collected 10 μ into the sample. Confocal reflectance microscopy on unstretched (and unlabeled) fibrin samples polymerized inside sealed glass flowchambers was performed on the same setup, using a 488-nm laser for illumination.

We quantified the alignment by using the ImageJ plugin OrientationJ [439] on filtered maximum intensity projections of varying strain levels (using 10 μm thick z-stacks and a bandpass filter to reduce noise). Briefly, OrientationJ evaluates the local orientation and coherency of every image pixel and computes a distribution of angles. A Gaussian window of 2 or 3 pixels and a Gaussian gradient was used to determine the local intensity derivative in x and y [439]. Using these orientation images, we calculated the nematic order parameter. Given a collection of orientation measurements, ψ, in the range (-90°, 90°], the nematic order parameter is computed from the second-order tensor order-parameter S_2 [440]:

$$S_2 = \begin{bmatrix} \langle \cos 2\psi \rangle & \langle \sin 2\psi \rangle \\ \langle \sin 2\psi \rangle & -\langle \cos 2\psi \rangle \end{bmatrix} \tag{4.1}$$

Angle brackets $\langle \cdot \rangle$ denote averages over all orientation measurements. The tensor S_2 is symmetric and traceless. Solving the eigenvalue problem for S_2 yields two eigenvalues,

$$\lambda_{1,2} = \pm \sqrt{\langle \cos 2\psi \rangle^2 + \langle \sin 2\psi \rangle^2} = \pm S \tag{4.2}$$

which yield the (two-dimensional) scalar order-parameter S familiar for liquid crystals. This order parameter quantifies the width of the distribution of orientation measurements. It is zero for a uniform distribution of orientations, and approaches one for a sharply-peaked distribution. We find that in practice S is between 0.1 and 0.2 for isotropic networks, taking into account the coherency of every image pixel.

4.2.4 Modeling

The structure of fibrin protofibrils

To interpret the SAXS spectra, we will compare our data to an *in silico* model of fibrin oligomers and protofibrils developed by our collaborators, Artem Zhmurov (Moscow Institute of Physics and Technology), and Valeri Barsegov (University of Massachusetts Lowell). The modeling procedure is described in full detail elsewhere [299, 469], and will be briefly recapitulated here. The starting point was the crystal structure of full-length human fibrinogen (PDB code 3GHG) [329]). The αC-region (Aα221-610), which does not appear in the crystal structure and is unlikely to contribute to the SAXS scattering, was not included in the structure, unless stated otherwise. There are several unresolved portions of the molecule in the crystal structure data: residues 1-26, 1-57, and

1-13 at the N-termini of the Aα, Bβ and γ chains, respectively; and residues 201-610, 459-461, and 395-411 at the C-termini of the Aα, Bβ and γ-chains, respectively. These regions do not possess stable secondary/tertiary structures detectable by X-ray crystallography. Hence, they were reconstructed computationally using the VMD software package [470]. The complete structure was energy-minimized by a steepest descent algorithm to remove steric clashes.

A computational procedure was developed to reconstruct double-stranded oligomers denoted as FOn-m, where n and m are the number of fibrin monomers in the upper and lower strands, respectively. Fibrin oligomers from FO2-1 up to FO4-4 were constructed by this procedure. The procedure entailed the following steps:

i) Fibrin monomers were first connected head-to-tail through the D-D interface to form single-stranded oligomers. The monomers were placed such that the D-D interface resembled the PDB structure of the double-D region 1N86 [471] and 1FZG [472];

ii) The Kabsch algorithm for structure alignment [473] was used to position the double-D fragment such that the globular parts overlapped with the corresponding regions in the two abutting fibrin molecules;

iii) The C-terminal parts of the γ-chains in the aligned fibrin monomers were crosslinked *in silico* to mimic FXIII-mediated crosslinking. Specifically, two covalent bonds were created, one linking residues γGln398 and γLys406 in one γ chain with residues γLys406 and γGln398, respectively, in the other γ chain;

v) A double-stranded oligomer was created by adding a lower strand with a third monomer to the upper strand containing the crosslinked dimer in a half-staggered manner. Initial placement was achieved by Monte-Carlo docking simulations, employing translational and rotational moves;

(vi) The knobs 'A' and 'B' were inserted into the respective holes 'a' and 'b' and an energy minimization simulation run was performed. Next, 100 ns-long equilibration in full-atomic resolution was performed using the solvent accessible surface area (SASA) implicit solvent model [474]. In these simulations, the knob-hole bonds were stabilized by using a weak harmonic potential.

(vii) The thus generated oligomer FO2-1 was energy-minimized and equilibrated.

(viii) Oligomers up to FO4-4 were generated by repeating steps (i) through (vii).

To investigate the structural changes in fibrin protofibrils upon stretching, all-atom Molecular Dynamics (MD) simulations were performed in implicit solvent. The FO4-4 oligomer was selected as the model system for these pulling simulations. The geometry of the *in silico* pulling experiments is shown in Fig 4.2. The oligomer was truncated in the two coiled-coil regions to mimic the long oligomer structure. Since there are six polypeptide chains cut at both

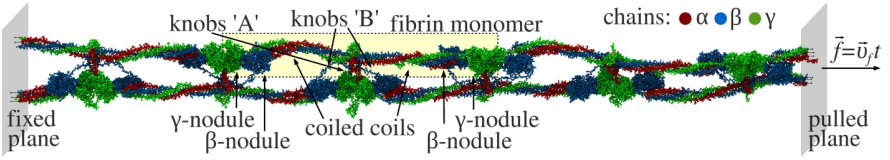

Figure 4.2: Dynamic force spectroscopy *in silico*. To mimic AFM pulling experiments, the left end of the fibrin oligomer FO4-4 was constrained (fixed plane) and a ramped force $f = v_t t$ (where v_t is the pulling speed) was applied to the right end (pulled plane). The oligomer was truncated in the two coiled-coil regions to mimic the long oligomer structure and to ensure that the force was applied evenly to all six polypeptide chains within each monomer.

sides, the force is thus applied evenly to all chains. Earlier simulations of our collaborators of forced unfolding of single fibrin molecules showed that, in the course of their forced unfolding, the fibrin monomers also rotate around the longitudinal axis [299, 335]. For this reason, the amino acid residues tagged by the external pulling force should be allowed to move freely. To ensure this condition, the following simulation approach was developed. Two parallel planes were defined, perpendicular to the axis of the protofibril. The plane at one end of the molecule was constrained (fixed plane), while the other plane (pulled plane) was assumed to be connected to a cantilever tip (virtual bead) by a harmonic spring, mimicking a typical AFM pulling experiments. The end of this spring moved with a constant (cantilever) velocity, thus applying a dynamic force-ramp with a pulling force $f = v_t t$ that increased with the force-loading rate $v_t t$. In each fibrin oligomer, residues αAsp114, βSer144, and γSer86 in the upper strand and residues αGln131, βAsn164, and γSer105 in the lower strand in the leftmost monomers were constrained. The mechanical force was applied to residues αArg118, βLys148, and γLeu90 in the upper strand and residues αIle127, βAsn160 and γLeu101 in the lower strand in the rightmost monomer.

Reconstruction of long protofibrils

The oligomers constructed *in silico* are much shorter than the(coarse) fibrin fibers in the experiments, where the length between branch points is typically of order $\sim$1 μm or $\sim$23 fibrin monomers based on the typical mesh size of coarse fibrin networks. To enable a direct comparison of the measured SAXS profiles with computational predictions, our collaborators therefore computationally reconstructed protofibrils with a length of $\sim$1 μm. Since the fibrin protofibrils twist around their long axis, simple translation and replication of

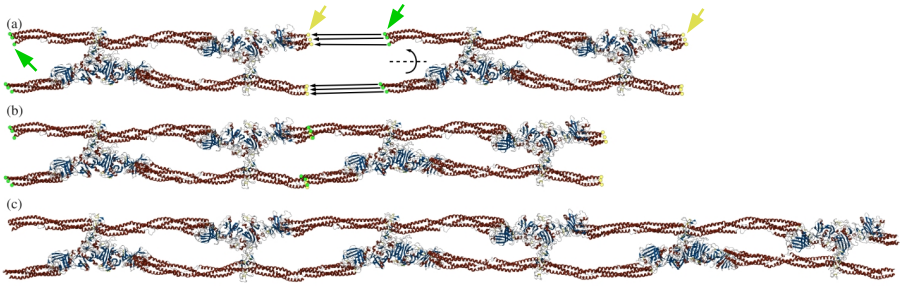

Figure 4.3: *In silico* reconstruction of a long fibrin protofibril from short oligomers for computational predictions of SAXS spectra. (a) First, two short oligomer constructs are brought close together by translation and rotation around the protofibril axis until the amino acid residues of the left construct (green dots and arrows) match with the residues on the right construct (yellow dots and arrows). (b) Next, the structures are combined. (c) A third oligomer is added in a similar manner. This is an iterative step that can be repeated until the protofibril is of the required length.

the oligomer structure would result in gaps between repeated structural fragments (FO4-4). Instead, the following procedure was developed. First, the oligomers were truncated so that the amino acid residues at one end were the same as the amino acids at the other end (green and yellow dots in Fig. 4.3). Two copies of the fragment were brought together so that the Cα-atoms of matching amino acids were as close as possible. To this end, the replicated fragment was translated and rotated around its long axis (Fig. 4.3), leading to a protofibril fragment that was twice the length of the initial fragment, FO4-4. This procedure was repeated until the protofibril was $\sim$23 fibrin monomers long.

Prediction of SAXS spectra based on simulated structures

Consider a system of N independent scattering particles forming a fibrin fiber, where each i-th scatterer has a scattering strength f_i. The total scattering intensity I as a function of the wavevector q is given by:

$$I_f(q) = I_e(q) \sum_i \sum_j f_i f_j \cos(q r_{ij}) \tag{4.3}$$

where $\overrightarrow{r_{ij}}$ is the vector connecting the i-th and j-th scatterers and r_{ij} is the projection of $\overrightarrow{r_{ij}}$ on the direction perpendicular to the primary wave. $I_e = (I_0 e^2/mc^2)(1+\cos^2(2\theta))/(2d^2)$ is the scattered intensity by a single electron

at a distance d from the detector when the incoming wave has an intensity I_0 [457, 475]. e^2/mc^2 is the classical electron radius [457]. The wavevector is related to the scattering angle 2θ according to:

$$q = |\vec{q}| = 4\pi \sin(\theta)/\lambda \tag{4.4}$$

where λ is the wavelength of the incoming light. In case of identical scatterers (such that $f_i = f$ for all $i = 1, 2, ..., N$), we can write a scalar version of eq. 4.3:

$$I_f(q) = I_e^*(q) \sum_i \sum_j \cos(qr_{ij}) \tag{4.5}$$

where $I_e^* = f^2 I_e$. To simplify the calculations, the distribution of inter-atomic distances, $p(r)$, was used, using as input the atomic structure of the oligomers obtained from the MD simulations. The scattering pattern of a single protofibril can then be calculated (in the large N limit) as:

$$I_f(q) = I_e^*(q) \int_0^{r_{max}} \frac{p(r)\sin(qr)}{qr} dr \tag{4.6}$$

where r_{max} is the maximum inter-atomic distance. For a network of protofibrils we need to integrate the scattered intensity over all fiber orientations. In case of an isotropic 3D fibrin network, we obtain:

$$I^{3D}(q) =< I(q) >^{3D} = I_e^*(q) \tag{4.7}$$

Our confocal microscopy experiments demonstrate that a small percentage ($\sim$11%) of fibrin fibers was already aligned even at zero strain (Fig. 4.17), consistent with prior observations [389]. We thus assumed that the scattered intensity of unstretched gels is a superposition of intensities for aligned fibers, $I_f(q)$, and unaligned fibers, $I^{3D}(q)$, according to:

$$I_{tot}(q) = p_a I_f(q) + p_u I(q)^{3D} \tag{4.8}$$

where $p_a = 0.11$ and $p_u = 1 - pa = 0.89$ according to the confocal data and previous publications [389]. To compute spectra of strained gels, we used previously published SEM data on strain-dependent fibrin fiber alignment ($p_a(\varepsilon) = \langle \cos(2\theta) \rangle$ [389], where ε is strain) shown in [389], as input. Upon stretching, two processes occur in parallel: (i) unaligned fibrin fibers will start to align, i.e. p_a increases and p_u decreases; and (ii) already aligned fibers will be stretched and they may exhibit forced unfolding. Hence, stretched gels can be decomposed into 3 fiber populations: (a) a fraction p_u of still unaligned fibers, (b) a fraction of aligned but not stretched fibers, and (c) aligned and stretched fibers. Thus, the expression for I_{tot} of strained gels becomes:

$$I_{tot}(q,\varepsilon) = p_u(\varepsilon)I^{3D}(q) + p_a(0)I_a(q,\varepsilon) + \int_0^{\varepsilon} \frac{dp_a(\varepsilon - s)}{ds} I_a(q,s)ds \qquad (4.9)$$

Or in discrete form:

$$\begin{aligned} I_{tot}(q,\varepsilon) \quad = \quad & p_u(\varepsilon)I^{3D}(q) + p_a(0)I_a(q,\varepsilon) + \\ & \sum_{s=0,\delta\varepsilon,2\delta\varepsilon,\ldots}^{\varepsilon-\delta\varepsilon} [p_a(\varepsilon - s) - p_a(\varepsilon - s - \delta\varepsilon)]I_a(q,s) \end{aligned} \qquad (4.10)$$

where $I_a(q,\varepsilon) = I_f(q,\varepsilon)$, $I_u(q) =< I(q) >_{3D}$, and $\delta\varepsilon$ is the strain increment. The total scattering intensity at strain ε is a combination of scattering from fibers that are unaligned ($p_u(\varepsilon)I^{3D}(q)$), fibers that are aligned *and* stretched $p_a(0)I_a(q,\varepsilon)$, and a group of fibers that are in varying degrees stretched and oriented with the strain direction ($\sum_{s=0,\delta\varepsilon,2\delta\varepsilon,\ldots}^{\varepsilon-\delta\varepsilon}[p_a(\varepsilon-s)-p_a(\varepsilon-s-\delta\varepsilon)]I_a(q,\varepsilon)$) In this third term, the summation is perform).ed over aligned and stretched fibers that differ in the extent of their stretching/unfolding and the $p(r,\varepsilon)$ (and consequently $I(q,\varepsilon)$) distribution was taken from the simulated atomic structures of stretched fibrin protofibrils. To calculate the spectra for different strains, say for $\varepsilon = 0\%$, 5%, 10%, ..., 150% with strain increment $\delta\varepsilon = 5\%$, eq. 4.10 is used iteratively. For example, to compute the spectrum for a gel at 15% strain, we need the spectrum for 0% strain, etc. Given that the pulling simulations are limited to short fibrin protofibrils of $\sim$10$-$50 fibrin monomers, the structural models were replicated along the protofibril axis, which coincides with the uniaxial direction of force application. Finally, to account for spectral line-broadening as a consequence of a widening distribution of stretched and unfolded fibrin monomers, we convolved the calculated spectra with a Gaussian function, G, using the following convolution integral:

$$\int_0^{q_{max}} I_{tot}(q',\varepsilon)G(q - q')dq' \qquad (4.11)$$

The width of $G(x)$ was estimated from the distribution of molecular elongations and a variety of stretched and unfolded structures from multiple forced unfolding runs and was fixed at 0.03 nm^{-1}.

4.3 Interpretation of Scattering of Fibrin Networks

X-ray and neutron scattering can provide information about the periodic molecular packing of ordered materials, as illustrated by measurements on a powdered crystal in Fig. 4.4. The length scales that one can probe are related to the wavelength λ of the incoming X-rays by $q = 4\pi\sin(\theta)/\lambda$ [457, 476], where

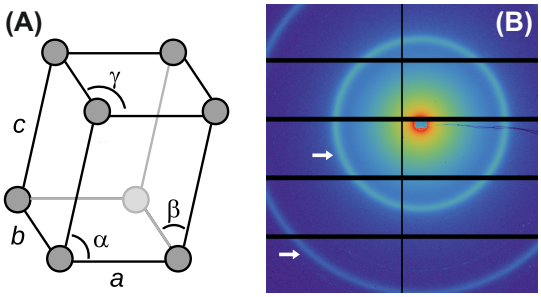

Figure 4.4: Example of a SAXS measurement on a powdered crystal used for calibration of the wavevector range. (A) Silver behenate has a unit cell of $a = 4.15$ Å, $b = 4.71$ Å, $c = 53.56$ Å, $\alpha = 89.47^\circ$, $\beta = 87.62^\circ$ and $\gamma = 76.33^\circ$ [477]. (B) In powder diffraction, the crystals are isotropically oriented, giving rise to concentric circles that correspond to the typical distances of the unit cell. The arrows point out the first and second order reflections of the typical distance c in (A), corresponding to $q = 0.117$ Å^{-1} and $q = 0.235$ Å^{-1} respectively. The grid pattern is due to the detector, which is built up of 10 separate panels. To protect the detector against damage by the intense incoming beam, a beam stop is added (black square). The intensity at the beam stop is measured by a photo-diode (note thin wire on the right hand side).

2θ is the angle between the incident and scattered X-rays. In small-angle X-ray scattering (SAXS), the X-rays scattered at low angles (typically at angles smaller than ∼2 degrees) are collected using a specimen-to-detector separation of several meters. The scattering vector q is directly related to distances d_s in the sample by $|q| = 2\pi/d_s$. Thus, by setting the angle range, the length scale region of interest can be selected. In practice, this is achieved by changing the sample-to-detector distance. For our SAXS experiments, we used silver behenate powder to check the q-range. This powder contains crystals with a triclinic unit cell, as shown in Fig. 4.4A [477]. Since the crystals are isotropically oriented in the powder, the scattering pattern consists of concentric rings, which correspond to Bragg reflections from the typical distances of the unit cell (Fig. 4.4B).

In Chapter 2, we showed that fibrin fibers can be considered as hierarchically structured bundles of protofibrils, which themselves are composed of half-staggered fibrin monomers. The fibers branch to form a three dimensional connected network. This network is homogeneous at large scales, but inhomogeneous at scales approaching the mesh size. To model the scattering intensity of such networks, the mesh work can be considered as a collection of fractal

blobs of size ξ_{blob} with fractal dimension D_m, where each blob contains n fiber segments (where $n \gg 1$)(see top schematic in Fig. 4.5). At the micron scale, the segments are approximately cylinders of average length l and diameter d. While d is equal to the fiber diameter, l is related to the fiber persistence length rather than the network mesh size. Based on these assumptions, a model was proposed to predict the light scattering intensity of fibrous networks [478,479]:

$$I = K_{op} c_p M \cdot S(q) \cdot A(q) \cdot B(q) \tag{4.12}$$

where c_p is the fibrinogen weight concentration, M is the blob molecular weight, and K_{op} is an optical constant: $K_{op} = (4\pi^2/N_A\lambda_0^4)n^2(\partial n/\partial c)^2$ and is equal to $2.68 \cdot 10^{-7}$ cm^2/g^2 [479]. Although this model was originally developed to describe light scattering data, the general form of this expression also applies to neutron and X-ray scattering data and has been validated by small angle measurements for wave vectors down to $q \sim 10^{-3}$ nm^{-1} and for fibrin concentrations up to 40 mg/ml [480]. The q-dependent quantities in 4.12 are $S(q)$, which is the structure factor describing the spatial correlation between blobs, $A(q)$, which is the structure factor of the fiber segments, and $B(q)$, which is the form factor of a single segment. These quantities can be calculated using the following equations [478,479]:

$$S(q) = 1 - \beta e^{-(\gamma \xi_{blob} q)^2} \tag{4.13}$$

$$A(q) = \frac{1}{\left(1 + \left(\frac{q\xi_{blob}}{\pi}\right)\right)^{(D_m/2)}} + \frac{l}{\xi_{blob}} \tag{4.14}$$

$$B(q) = \frac{1}{\left(1 + q^2 d^2 \sqrt{\frac{l}{32d}}\right)^{\alpha_s/2}} \tag{4.15}$$

D_m is the mass fractal dimension of the blobs, α_s is related to the surface fractal dimension of the fiber segments by $D_s = 6 - \alpha_s \simeq 2$, and the parameters $\beta \simeq 1$ and $\gamma \simeq 0.28$ [478]. Here, the form factor of the fiber segments, $B(q)$, only accounts for the overall cylindrical shape. In case of coarse clots, the fiber segments have a complex molecular packing structure, being a bundle of protofibrils that themselves are double-stranded filaments of fibrin monomers. To account for this internal molecular packing structure, the factor $B(q)$ in Eq. 4.13 should be a replaced by a structure factor to describe the lateral packing arrangement of the protofibrils multiplied with the form factor of a protofibril (either a cylinder approximation or the scattering intensity $I_f(q)$ that we calculate here from full atom MD simulations of protofibrils).

Fig. 4.5 shows the expected scattering intensity as a function of wavevector (black line) for a coarse clot using typical parameters ($\xi_{blob} = 10$ μm, $l = 0.5$

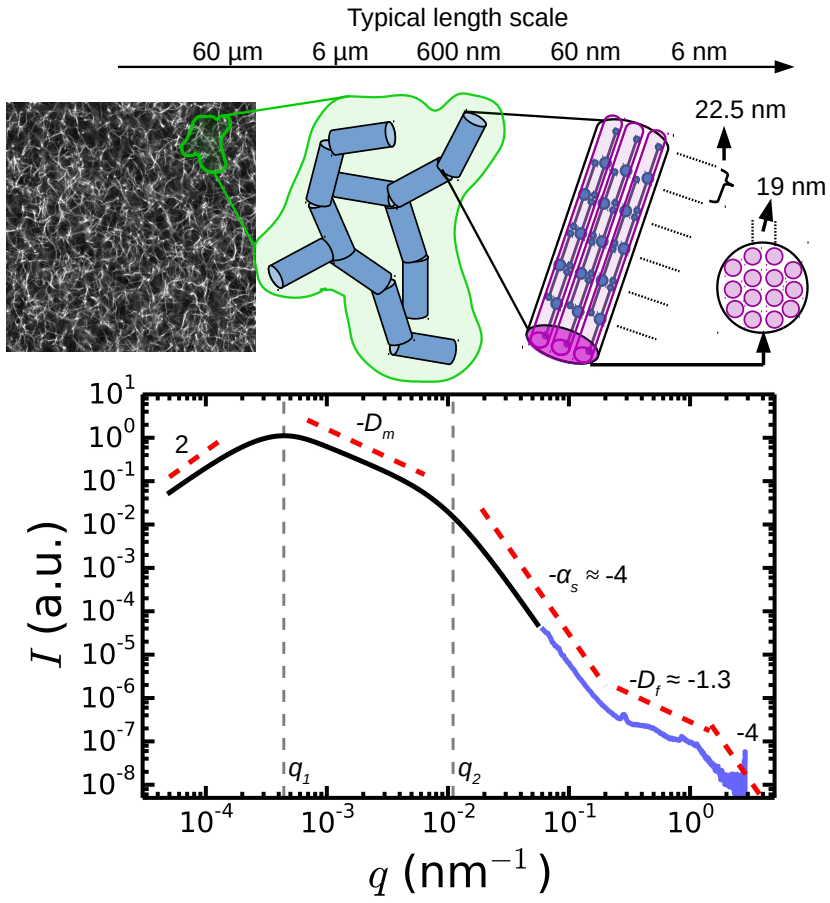

Figure 4.5: Typical length scales in fibrin networks visible by light, X-ray and neutron scattering. Light scattering probes length scales ranging from the fiber to the network scale (black curve in graph), where the fibrin network (confocal image on the top left, 100x100μm) can be considered as a collection of blobs (green in top schematic) of fiber segments (blue in top schematic) with fractal dimension D_m [478, 479]. X-ray and neutron scattering can probe higher q-values (blue curve in graph), where the molecular length scales inside the fibers are probed, such as the axial half-staggering distance among the fibrin fiber (22.5 nm), and the typical spacing between the protofibrils in a fiber cross-section (∼19 nm [74], purple in top schematic). The black scattering curve has been calculated using the model presented in eq. 4.12 using parameters expected for coarse fibrin networks ($\xi_{blob} = 10$ μm, $l = 0.5$ μm, $d = 0.2$ μm, $D_m = 1.3$ and $\alpha_s = 4$). The blue curve represents an actual SAXS measurement on a 4 mg/ml coarse fibrin network ($N_p \sim 366$). Curves are shifted along the y-axis (note arbitrary units).

μm, $d = 0.2$ μm, $D_m = 1.3$ and $\alpha_s = 4$). For small wave-numbers, $q < q_1$, the network can be considered as a homogeneous system. The scattering intensity exhibits a peak at a q-value q_1, which is related to the long-range order in the network [481] and is proportional to the average size of the blobs according to $q_1 \simeq 4.4/\xi_{blob}$ [478]. In the wavevector range where $q_1 < q < q_2$, the scattering intensity is determined by the fractal structure within the blobs, provided that q is larger than ξ_{blob}^{-1} but smaller than d^{-1} or l^{-1}. In this case $I \propto q^{-D_m}$. Prior experiments have shown that D_m depends on fibrinogen concentration: for dilute fibrin networks (≤ 1.5 mg/ml), D_m is close to 1.3 [478], while it can increase to 2.8 for high fibrin concentration (~ 40 mg/ml) [480]. Additionally, D_m was shown to be dependent on the network architecture, varying between 1 and 2.2 for a range of assembly conditions [482–487]. For larger wave numbers, where $q > q_2$, we enter a Porod regime, which reflects scattering from the interface between the fibers and the solvent. Here, the surface fractal dimension of the fiber segments dominates the scattering intensity. Depending on the surface roughness, the slope α_s is either 4 (completely smooth or sharp interface) or -3 (completely rough). Previous studies revealed α_s values close to -4 for coarse clots [478, 479]. The onset of this Porod regime is set by the diameter of the fiber segments according to $q_2 \simeq 2.2/d$ [295, 478, 479].

The q-range we are focusing on in this Chapter ranges from $q \sim 6 \cdot 10^{-2}$ nm^{-1} to $q \sim 3$ nm^{-1}, which corresponds to length scales ranging from ~ 105 nm down to ~ 2 nm. In this regime, we probe length scales corresponding to the molecular packing inside the fibrin fibers. When a fiber is oriented vertically in the X-ray beam, the X-rays scatter parallel to the fiber axis, giving rise to a *meridional* scattering pattern [458] that is sensitive to the half-staggered packing along the fibril axis. In contrast, the X-rays scattered at right angles to the fiber axis produce an *equatorial* pattern, which reveals the radial packing order of protofibrils within the fiber. If the fiber is rotated with respect to the detector, the pattern on the detector will be rotated accordingly. For an isotropic network of fibers, the meridional and equatorial pattern will therefore be superimposed. Since the patterns represent an average from all fibers encountered by the X-ray beam, both SAXS patterns will appear as a series of concentric circles.

The axial molecular packing structure of fibrin fibers is known to be highly ordered. Electron microscopy and AFM images have clearly revealed a half-staggered arrangement with a periodicity corresponding to half the monomer size, i.e. 22.5 nm [289, 290, 443]. Previous SAXS studies revealed sharp Bragg peaks, indicative of a large coherence length, at the expected first order q-value [298, 389, 455, 460, 463, 480] and higher-order reflections of this same distance [298, 455, 460, 462, 463]. Strikingly, the second order was either very faint or absent. It is unknown why this is the case.

The cross-sectional packing of protofibrils inside the fibrin fiber is thought

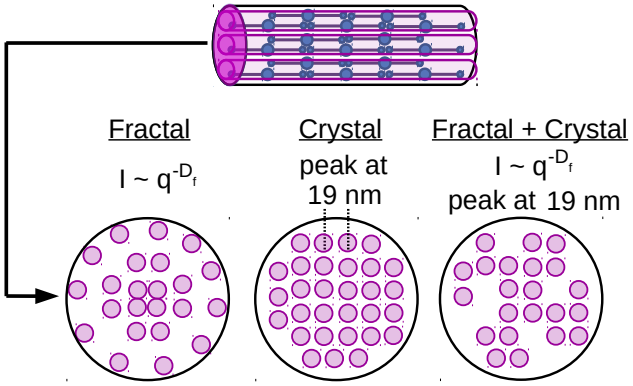

Figure 4.6: There are two opposing models for the radial packing structure of the protofibrils within a fibrin fiber. One model describes fibrin fibers as fractals with fractal dimension $D_f = 1.3$ [364], while the other claims fibrin molecules are packed in a crystalline array with unit cell 19 x 19 x 46 nm [74]. Recently, Yeromanahos *et al* [295] unified these models, describing fibrin fibers as crystalline but with pores where protofibrils are missing, leading to a superposition of the crystalline structure and the disordered, fractal structure.

to be less ordered than the axial packing, but there is disagreement about the degree of disorder. One EM study showed that even within a given preparation, the lateral packing order may vary from fiber to fiber [289]. As shown in Fig. 4.6, there are two rather different structural models proposed for the cross-sectional packing. The first model [74] is based on prior SAXS data [298] and proposes that protofibrils are packed in an ordered lattice with a tetragonal unit cell measuring a x c x c = 18.4 x 18.4 x 46 nm, where 18.4 nm corresponds to twice the distance between protofibrils and 46 nm to the length of one fibrinogen monomer. Thus, this model predicts the presence of a Bragg peak at a q-vector corresponding to a repeat distance of 18.4 nm, with a width that corresponds to the fiber diameter if the packing is perfectly crystalline. Indeed some measurements by SAXS [461, 464], neutron diffraction [480, 488] and energy-dispersive X-ray diffraction [463, 464] revealed broad Bragg peaks, indicating a small crystal size and partial disorder. However, other SAXS studies found no evidence for lateral crystalline order [462]. The second model for protofibril packing instead treats fibrin fibers as disordered, fractal assemblies of protofibrils (Fig. 4.6). This model was inspired by AFM bending experiments and fluorescence intensity measurements, showing that fibrin fibers can be considered as mass fractals [364] with fractal dimension of 1.3. This means

that with increasing fiber diameter d, the number of molecules per cross-section increases as d^{D_f} with $D_f = 1.3$ instead of the quadratic increase expected for an ordered fiber. In other words, thinner fibers are predicted to be less *dense* than thicker fibers. This view is qualitatively consistent with light scattering studies, showing that fibrin fibers are highly porous and contain more than 70% water [295, 462]. This model predicts that the scattering intensity will scale as q^{-D_f} [489]. Recently, a reconciliation of these two models has been proposed by considering the lateral packing as crystalline, but with a large number of holes where protofibrils are missing (right most model in Fig. 4.6). This arrangement results in a superposition of a fractal-like scattering and a broad peak due to locally crystalline regions [295, 490].

At the highest q-values shown in Fig 4.5, when $q \gtrsim 1$ nm^{-1}, we enter a second Porod regime related to the intra-fiber surfaces [480] (Fig. 4.5), where we expect to see a q^{-4} dependence. The onset of this regime is related to the radius of one protofibril ($q = 2\pi/r_{pf} \sim 1$ nm^{-1}, using $r_{pf} = 5$ nm [294]).

4.4 Results

4.4.1 Internal Structure of Fibrin at Zero Strain

We aimed to study the strain-induced changes of the molecular packing structure of fibrin fibers in gels subjected to a macroscopic uniaxial stretch. As a first step, we compared unstrained fibrin networks prepared with varying fibrin bundle size, expressed in terms of the number of protofibrils in a fibrin bundle, N_p. We varied the bundle size over a wide range of $N_p = 2$ up to $\sim$360. The 2D SAXS patterns were isotropic in all cases, as expected for a random fibrous network, as shown in Fig. 4.7. The patterns show concentric rings whose intensity increases with increasing fibrin bundle size. This effect is more clearly, and quantitatively, shown in Fig. 4.8A, in the form of the 1D SAXS spectra obtained by a radial integration of the 2D scattering patterns, taking the beamstop as center. Note that the curves are shifted along the y-axis for clarity.

The spectrum for the sample containing the thickest fibers ($N_p \simeq$360) exhibits a clear peak at $q = 0.285$ nm^{-1} (top blue curve labeled '1' in Fig. 4.8A). This peak corresponds to a repeat distance of 22.2 nm and can thus be assigned as the first order reflection of the half-staggered axial packing distance [389]. When the bundle size is decreased to $\sim$100 protofibrils per bundle, this same peak is still present, but with a reduced intensity (black line labeled '2' in Fig. 4.8A). For networks of 8 mg/ml fibrin, where the average bundle size is $\sim$20, the first order reflection no longer visible (gray curve labeled '4' in Fig. 4.8A)). Interestingly, a small peak re-appears when the fibrin concentration is reduced to 4 mg/ml (gray curve labeled '3' in Fig. 4.8A)). When the bundle size is dropped to 2, corresponding to the fine clot limit, the first order reflection is not visible at all (red bottom curve labeled '5' in Fig. 4.8A). We

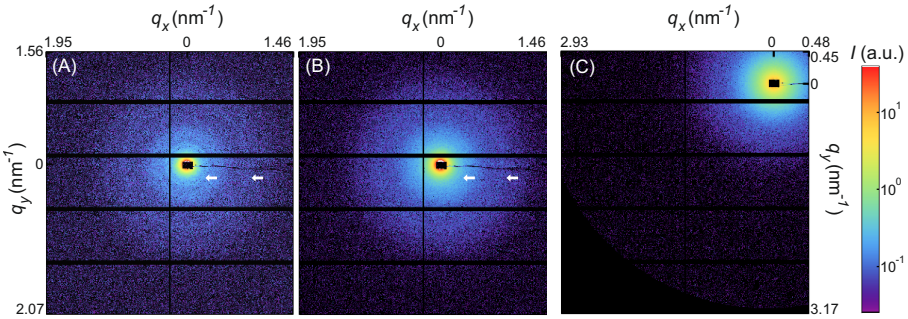

Figure 4.7: The dependence of 2D SAXS patterns on fibrin fiber thickness. (A) SAXS pattern (background subtracted) of a 4 mg/ml fibrin gel with thick fibers (bundle size $N_p \simeq$366), (B) 8 mg/ml fibrin gel with $N_p \sim$ 100 and (C) 8 mg/ml fine fibrin gel with $N_p = 2$. (A) and (B) share the same y-axis, while (C) is taken with a slightly different q-range by translating the detector in x and y, but keeping the same distance between the detector and sample. In (A) and (B), the first and third order reflections of the half-staggered axial packing periodicity of fibrin (22.5 nm) are highlighted by white arrows. In (C) these peaks are not distinguishable from the background. Intensity is in arbitrary units (see color bar).

conclude that the intensity and width of the peak corresponding to the first order reflection of the axial repeat distance is dependent on the bundle size. This result is in agreement with earlier work, where the first order reflection was observed for coarse fibrin clots [295, 298, 389, 456, 463, 464, 488], but not for fine clots [456]. The peak position corresponds to a repeat distance of 22.2 nm for all bundle sizes, consistent with SEM and AFM studies showing a 22.5 nm repeat [289, 290] and earlier SAXS studies showing 22 nm [389].

Prior SAXS studies of coarse clots revealed, in addition to the first order reflection, also several higher order reflections [295, 298, 488]. This observation is indicative of a long-ranged half-staggered packing order along the fibril axis. Given that the first order peak is observed at $q = 0.28$ nm^{-1}, the second, third and fourth order reflections are expected at $q = 0.57$, $q = 0.855$, $q = 1.14$ nm^{-1}, respectively (see vertical dashed lines in Fig. 4.8A). Interestingly, the third and fourth order reflections are evident in all samples, even for those samples where the first order reflection is absent. However, the third and fourth order peaks do get more pronounced with increased bundle size. Intriguingly, the second order reflection is absent for all fibrin samples. The absence of a second order reflection was also noted in prior SAXS studies [295, 460, 461], but the origin of peak suppression has remained unclear.

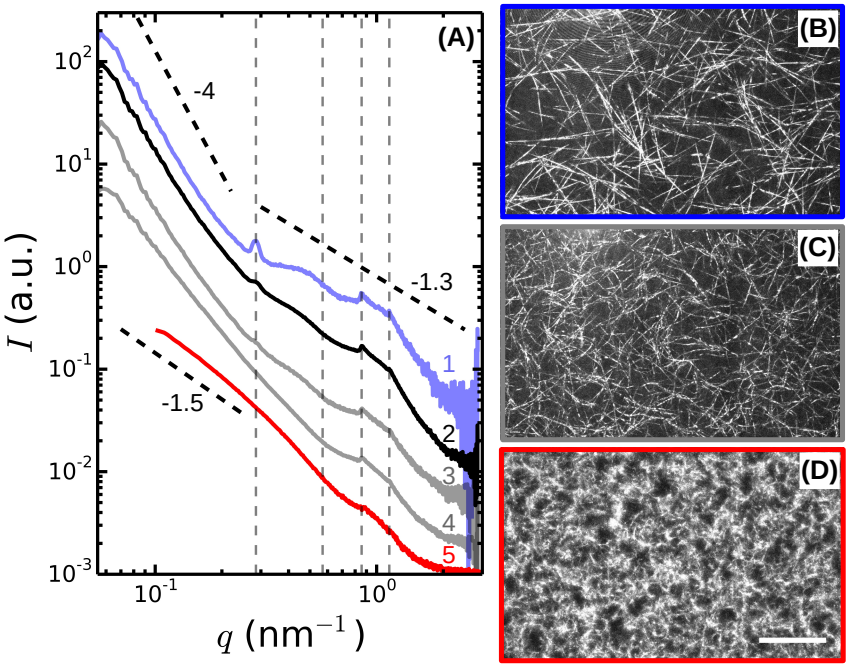

Figure 4.8: The dependence of 1D SAXS spectra on fibrin fiber thickness obtained by radial integration of the 2D SAXS patterns. (A) SAXS spectra of fibrin gels prepared under different conditions: 1) 4 mg/ml fibrin gel with bundle size of $N_p \sim 366$ (blue), 2) 8 mg/ml coarse fibrin gel with $N_p \sim 100$ (black), 3) 4 mg/ml coarse fibrin gel with bundle size $N_p = 44$ (gray), 4) 8 mg/ml coarse fibrin gel with bundle size $N_p = 23$ (gray), and 5) 8 mg/ml fine fibrin gel with bundle size $N_p = 2$ (red). The intensity curves are shifted along the y-axis for clarity. The black dotted lines are power laws with exponents -4 (expected in the Porod regime), -1.3 (expected from the fractal radial packing structure of the fibrin fibers) and -1.5 (observed exponent for fine clots at low q). Vertical dotted gray lines indicate the expected positions of the first, second, third and fourth order reflection of the axial half-staggered packing distance (22.5 nm). (B) and (C) are confocal reflectance images of 1 mg/ml fibrin clots with (B) thick fibrin fibers of $N_p = 366$ and (C) fibrin fibers of $N_p = 86$. (C) Confocal fluorescence micrograph of a 1 mg/ml fine fibrin gel, where $N_p = 2$. For all images, a maximum intensity projection is shown over a total depth of 20 μm. The scale bar is 20 μm for all images.

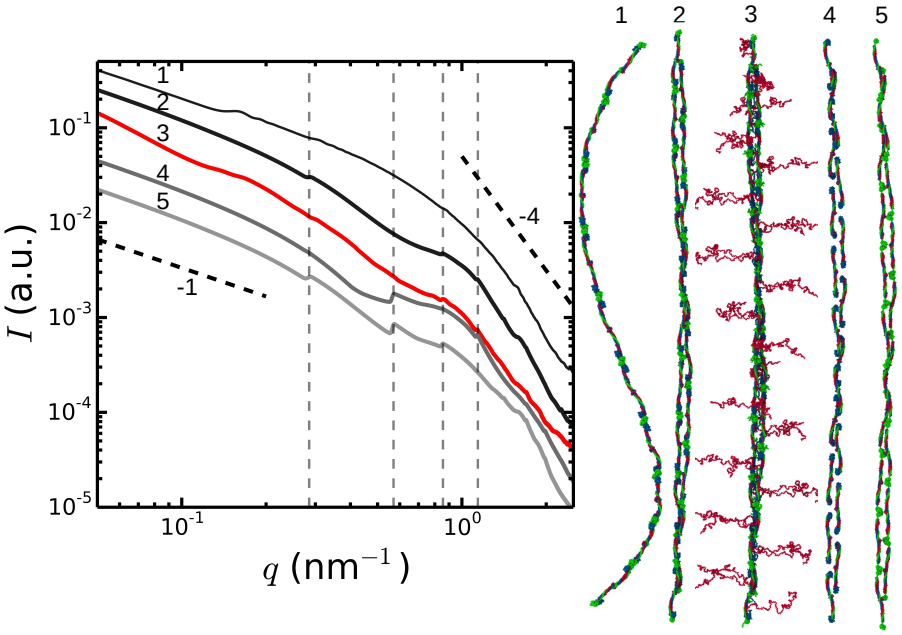

Figure 4.9: The dependence of simulated SAXS patterns on internal protofibril structure. 1) One strand of a protofibril, where the fibrin monomers adhere end-to-end through the D:D interface. 2) A double-stranded protofibril with twist (i.e. after equilibration of the protofibril structure), but omitting the αC regions. 3) The same protofibril as 2), but now with αC regions added as random coils (shown in red). 4) The same structure as 2), but with the γ-nodules removed. 5) The same structure as 2), but now with the β-nodules removed. The two black dashed lines indicate a power law dependencies of -1 at low q-numbers (expected for cylinders, see 4.10 in SI) and -4 at high q-numbers (corresponding to the Porod regime).

To understand why the second order reflection is suppressed, we compared the measured spectra with predicted spectra based on full atom MD simulations of fibrin protofibrils (FO10-9). The expected scattering intensity for a dilute solution of protofibrils is shown in Fig. 4.9 (curve 2), where the gray dashed lines indicate the expected positions of the first, second, third and fourth order reflections of the half-staggering distance. Just like in the experiments, the second order reflection is absent in the simulated protofibril spectrum. To track down the origin of this peak suppression, we systemati-

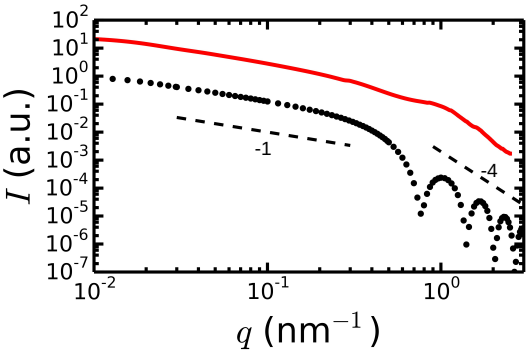

Figure 4.10: The calculated form factor of a cylinder (black dots) with length $5 \cdot 46$ nm and diameter 10 nm, compared with the simulated scattering of protofibrils (FO6-5, red line) in solution. Curves are shifted along the y-axis for clarity. The dashed lines indicate power laws with exponents of -1 (Guinier regime) and -4 (Porod regime).

cally remove certain parts of the protofibril to investigate their contribution to the scattering pattern. The second order reflection is suppressed both with (spectrum nr. 3) and without (spectrum nr. 2) the αC domains. The presence of the αC domains does influence the other reflections corresponding to the half-staggering distance, causing a reduced peak intensity and increased width. Interestingly, when we remove either the β or the γ-nodules, the second order reflection appears. As an extra control, we also looked at single-stranded protofibrils, composed of a string of monomers adhered end-to-end through the D:D interface (nr. 1 in Fig. 4.9). In this case, a new peak appears at $q = 0.157$ nm^{-1}, corresponding to a typical distance of 40 nm. This distance corresponds to the distance between the centers of mass of the two end regions: A fibrinogen monomer has a length of 46 nm length and two end-regions each with size of 6 nm [491,492]. The distance between the centers of mass of the two end regions is thus 40 nm. For the double stranded protofibrils, this peak is suppressed. We conclude that the second order reflection is not present in SAXS spectra of fibrin gels due to destructive interference originating from the symmetric nature of the fibrinogen molecule. When this symmetry is perturbed by the removal of the β or γ nodule, the second order reflection appears. As we will show later on in this chapter, this feature provides an unambiguous way to detect the onset of forced unfolding of the β or γ nodules.

The overall decrease of the simulated scattering intensity of the protofibril solutions with q exhibits two distinct power regimes, one with an exponent close to -1 at low q, and one with an exponent close to -4 at high q. We

can rationalize this q-dependence by calculating the expected form factor for a protofibril approximated as a cylinder [476]:

$$P(q) = \int_0^{\pi/2} \Big[\frac{2J_1(qR\sin x)}{qR\sin x}\frac{\sin(qL\cos x/2)}{qL\cos x/2}\Big]^2 \sin x dx \qquad (4.16)$$

Here R and L are the radius and length of the cylinder respectively, and J_1 is the first order Bessel function. For protofibrils, $R = r_{pf} = 5$ nm [294] and we use $L = 5 \cdot 46$ nm to compare with the simulations of protofibrils with a length of ∼5 monomers. As shown in Fig. 4.10, the simulated SAXS spectra indeed have a similar dependence on q as expected for cylinders of the radius and length of the protofibrils, with a q^{-1} decrease of $I(q)$ at low q and a Porod regime where $I(q)$ decreases as q^{-4} at high q. However, we do not see oscillations in intensity at high q for the simulations. These oscillations are only expected for dilute solutions of monodisperse cylinders and when the cylinders have an internally uniform electron density. Protofibrils are not homogeneous, however, in electron density (one of the reasons why we see Bragg peaks in the first place) and they contain water pockets [74].

The q-dependence at low q scales as a power law with an exponent of -1 in case of the simulations, as well as in the case of the form factor of a cylinder (Fig. 4.10).

In the measurements for fine fibrin clots, we observe a stronger q-dependence (power exponent of ∼-1.5) at low q than the q^{-1} dependence expected from single protofibrils (and cylinders) in solution. This apparent discrepancy is due to the fact that in the experiments we have fibrous networks, whereas the simulations are performed on (single) protofibrils. Light scattering on coarse fibrin networks showed a dependence of $I(q)$ on bundle size and on the mass fractal dimension D_m characterizing the network structure [478, 479] (see Fig. 4.5). For fine clots, the limit where the scattering intensity is dependent on the network fractal dimension D_m is $q_2 = 0.11$, which is based on the average diameter of the fine clot fibers of 20 nm (see section 4.3 and Fig. 4.5). Thus, for $q < q_2$, we expect that the scattering intensity scales as q^{-D_m}. Experimentally, we find D_m close to 1.5. This interpretation should be tested independently with light scattering experiments. Note that we do not expect to see the *Fiber-Solvent* Porod regime for fine clots, since for $q > q_2$ we are already in the regime where we expect to see the internal features of the fibers. However, we still do expect a Porod regime at higher q-values ($q \gtrsim 1$ nm^{-1}), which are experimentally not accessible for our fine clot system due to the low scattering intensity of these samples.

We see a clear influence of bundle size on our SAXS measurements of fibrin gels (see Fig. 4.8). Specifically, we observe a change in the power law exponent of $I(q)$ at low q-values ($q \lesssim 0.2$ nm^{-1}). For coarse networks with bundle sizes N_p of 100 or more (curves 1 up to 4), the intensity decreases steeply with q

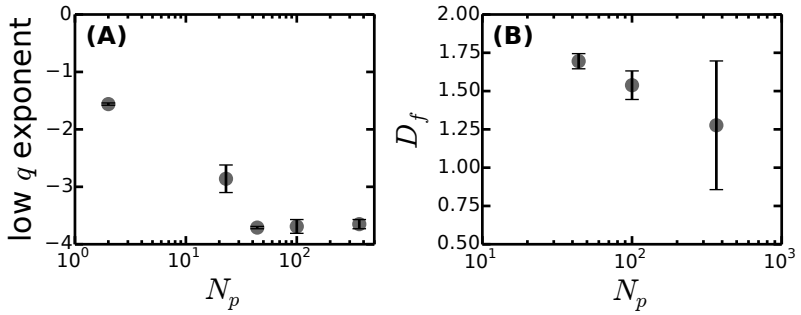

Figure 4.11: Power law exponents characterizing the q-dependence of the SAXS scattering intensity of coarse clots at low and high q. (A) Power law exponent of $I(q)$ in the low q regime ($q < 0.2$ nm^{-1}) as a function of bundle size. The exponent is close to -1.5 for fine clots ($N_p = 2$) and closer to the Porod limit of -4 for coarse clots. (B) The fractal dimension D_f characterizing the radial (cross-sectional) molecular packing structure of fibers in coarse fibrin clots of 4 mg/ml, obtained by scaling out the overall power-law decrease of $I(q)$ with q in the range of $0.2 \lesssim q \lesssim 1$ nm^{-1}) (see 4.12A). The bundle sizes N_p on the x-axis were measured at 4 mg/ml for the $N_p \geq 40$ sample, and estimated based on values measured at $c_p = 1$ mg/ml for the other two samples.

according to a power law with an exponent close to -4. In contrast, for the fine clots (curve 5), the intensity decreases much more weakly according to a power law with an exponent close to -1.5. The difference in power law slopes is statistically significant ($p<0.02$). Figure 4.11A presents a summary of these exponents. We can rationalize this bundle size dependence in the context of the different scattering regimes expected for fibrous networks as sketched in Fig. 4.5. For the coarse clots, the low q regime corresponds with the 'Fiber-Solvent Porod Region', which is the first regime above q_2 in Fig. 4.5. In this Porod regime, scattering is dominated by the interface between fibers and solvent [295, 347, 480]. Since the average fiber diameter is on the order of 100 nm, we expect the Porod regime to set in at $q_2 \sim 0.02$ nm^{-1}). In the Porod regime, we expect a power law exponent close to -4, consistent with our SAXS measurements (curves 1 to 4 in Fig. 4.8). As discussed above, for the fine clots, we expect to be in a different scattering regime, dominated the mass fractal dimension of the blobs. This prediction should be tested with light scattering experiments.

At higher q-values (in the range of $0.2 \lesssim q \lesssim 1$ nm^{-1}), we probe length scales corresponding to the periodicity of the axial packing (discussed above)

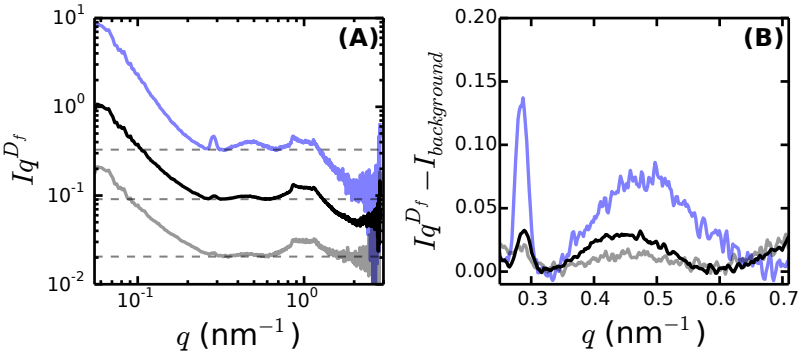

Figure 4.12: The scattering intensity measured for coarse fibrin networks with thick fibers multiplied by the fractal dimension (D_f) of the mass distribution within the fibers to better reveal the Bragg peaks originating from axial and lateral molecular ordering. (A) Rescaled SAXS curves for coarse gels of varying bundle size, shifted along the y-axis for clarity. (B) Magnified view of a small region of the rescaled SAXS curves, where the background level $I_{background}$ (horizontal striped lines in panel A) was subtracted. In (B), the gray curve was multiplied by a factor 10, while black curve was multiplied by a factor 4. For (A) and (B), the blue line corresponds to a 4 mg/ml fibrin gel with bundle size of $N_p \sim 366$, the black line corresponds to a 8 mg/ml coarse fibrin gel with $N_p \sim 100$, and the gray line corresponds to a 4 mg/ml coarse fibrin gel with $N_p = 44$.

but also the radial packing. As discussed in section 4.3, the radial packing structure of fibrin fibers is poorly understood. Two opposing models have been proposed, one modeling the mass distribution inside fibrin fibers as a fractal [364], while the other models fibers as crystalline packings of protofibrils [74] (see Fig. 4.6). If fibrin fibers can be considered as fractals, we expect that the scattering intensity should scale with q according to a power law with an exponent given by the fractal dimension [489]. In contrast, if fibrin fibers can be considered as crystalline, we expect a peak at a q-value that is inversely proportional to the average spacing between neighboring protofibrils. One earlier SAXS study reported an average radial repeat distance of 18.4 nm, which corresponds to twice the distance between protofibrils. As shown in Fig. 4.8A, the measured scattering curves for coarse fibrin samples can be considered as a superposition of an overall power-law decrease with superimposed peaks. The exponent characterizing the overall power-law decrease of $I(q)$ is close to -1.3 (indicated by the black dashed line between 0.2 and 1 nm^{-1}). This observation is consistent with several prior sets of SAXS measurements [295, 461, 490] and

also with the proposal made by Yeramonahos and co-workers [295, 490] that fibrin fibers are partially crystalline.

To better test whether the SAXS curves can be described by a superposition of a power law and Bragg peaks, we multiply the measured scattering intensity with q^{D_f}, adjusting D_f such that the curves are flat between 0.2 and 1 nm^{-1}. As shown in Fig. 4.12, we can indeed find values for D_f for which the curves are flat in this q-region. The best-fit values for D_f systematically decrease with increasing bundle size, as shown in Fig. 4.11B): we find $D_f = 1.7 \pm 0.05$ for $N_p = 44$, $D_f = 1.5 \pm 0.4$ for $N_p \sim 100$, and $D_f = 1.3 \pm 0.4$ for $N_p \sim 360$. The fractal dimensions we find by SAXS are consistent with previously reported D_f values of 1.7 and 1.3 [295, 364].

Multiplication of the scattering curves by D_f clearly reveals the Bragg peak at 0.29 nm^{-1} corresponding to the axial half-staggered order, but it also clearly shows a second, much broader peak centered around 0.47 nm^{-1}. This peak is only observed for coarse fibrin systems, with bundle sizes $N_p > 40$. The position of the peak is independent of the bundle size, as shown in 4.11A (open squares) (See Fig. 4.26 in the SI for fitting of the peaks). The peak position corresponds to a typical distance of about 13 nm. This distance does not correspond to the half-staggered axial order. Instead, it likely reflects the lateral repeat distance between protofibrils. Previous studies in which lateral order was examined reported somewhat larger repeat distances of around 19 nm [298, 461, 463, 464, 488]. However, it has been shown in light scattering studies that the packing density, and therefore the average spacing between protofibrils, is rather variable, depending on assembly conditions such as fibrinogen concentration, FXIII concentration, and buffer conditions [295, 332, 490]. Therefore, we believe that the peak does originate from lateral order. The large width of the peak suggests that this ordering is only short-ranged.

Indeed, the fiber diameter poses a strict upper limit on the range of order that can be expected. In a perfectly crystalline system, the size of the crystal is quantified by the Scherrer length, which sets the full width at half maximum of a Bragg's peak, Δq, according to: $L_{scherrer} = 2\pi/\Delta q$ [493]. We use this expression for the Scherrer length to estimate an apparent crystal size. When we plot the Scherrer length obtained by performing Gaussian peak fits to the broad peak corresponding to the lateral ordering, we find that it is independent of N_p (open squares in 4.12B). This suggests that the extent of (crystalline) cross-sectional ordering is not limited by the fiber diameter, but rather by intrinsic disorder. The presence of intrinsic disorder is consistent with the observation of a fractal dimension, and also with prior quantitative electron microscopy data [289].

For comparison, we also analyze the Scherrer length as extracted from the width of the peak corresponding to the first order reflection of the half-staggering axial repeat. As shown in Fig. 4.12B (black solid circles), in this

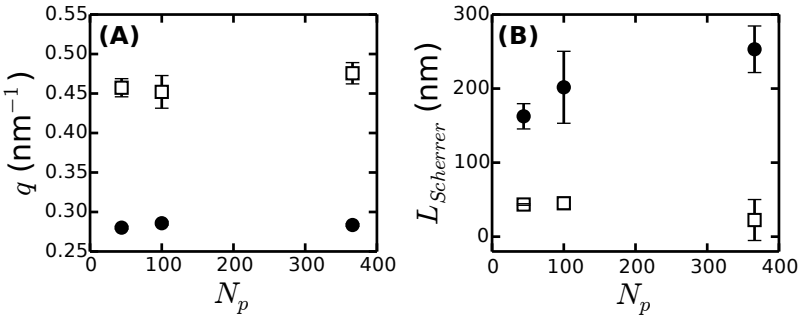

Figure 4.13: (A) The q-positions of the first sharp peak corresponding to the first order reflection from the axial packing structure of fibrin fibers (black solid circles), and of the broad peak that is attributed to the radial packing order (open squares). (B) The Scherrer length computed from the full width at half maximum of the peaks corresponding to axial order (black solid circles) and radial order (open squares).

case $L_{scherrer}$ does show an increase with increasing bundle size, meaning that the axial order becomes higher as the fibers become thicker. We expect that the range of axial ordering is limited by the crystal size, which should in turn be related to the length of fiber segments between two branch points [494]. For a fixed fibrin concentration, we expect that the mesh size increases with increasing degree of bundling, as illustrated by the confocal images in Fig. 4.8B,C and D. Assuming that the networks are homogeneous and isotropic, the average mesh size ξ can be estimated from the concentration using, $\xi \simeq \sqrt{1/\rho}$, where ρ is the total fiber length per volume [66]. For a bundle size $N_p = 366$ at 8 mg/ml fibrin, we expect an average mesh size of 1.5 μm. For the $N_p = 100$, $c_p = 8$ mg/ml and the $N_p = 44$, $c_p = 4$ mg/ml samples, the average mesh size should be about 0.5 μm. The increase of $L_{scherrer}$ with increasing N_p seen in Fig. 4.12B can thus be explained by a corresponding increase of the mesh size.

The effect of branching on the peak width is also nicely illustrated by simulations of the scattering pattern from protofibrils of varying length (see Fig. 4.14). When the length is decreased, the overall scattering curve does not change, but the peak corresponding to the first order reflection broadens. As an alternative test, we compared simulated SAXS spectra of single protofibrils (curve nr. 1 in Fig. 4.15 with spectra for mini-networks of 2 or 3 crossed protofibrils (curves nr. 2 and 3). Strikingly, the peak corresponding to the first order reflection shifts from $q \simeq 0.28$ nm^{-1}, corresponding to 22.5 nm, to $q \simeq 0.306$ nm^{-1}, corresponding to 20.5 nm when a branch is added. At the same

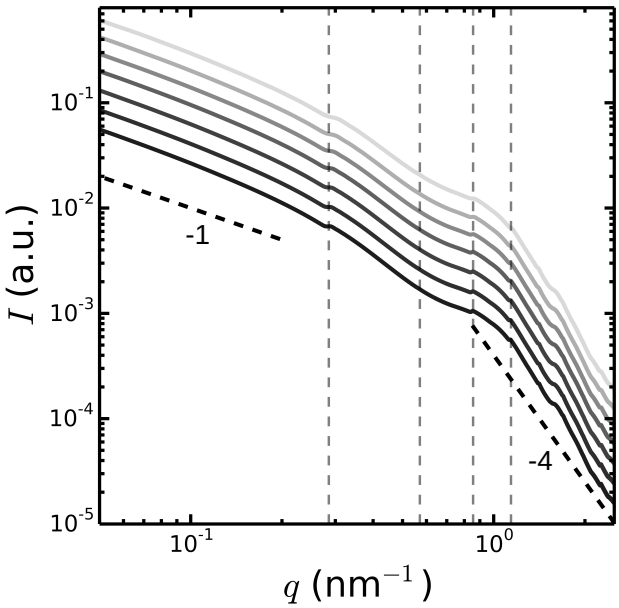

Figure 4.14: The dependence of simulated SAXS patterns for single protofibrils on protofibril length. For the curves in increasing shades of gray, the length increases by half a monomer length going from: FO4-3 to FO5-4, FO6-5, FO7-6, FO8-7, FO9-8 and finally FO10-9. The expected locations of the first, second, third and fourth order reflections of the half-staggering axial repeat distance are depicted by vertical dashed gray lines. The dashed black lines are power laws with an exponent of -1 in the Guinier regime at low q and an exponent of -4 in the Porod regime at high q.

time, the peak broadens. This observation is consistent with the decreasing Scherrer length with decreasing mesh size we observe experimentally.

In summary, we have shown that the SAXS spectra of fibrin networks are sensitive to the bundle size of the fibers. The half-staggered axial arrangement of fibrin monomers within the fibers gives rise to a sharp reflection at $q = 0.285$ nm^{-1} and several higher-order reflections. However, this reflection is only visible when the bundle size N_p is larger than 40. The larger the bundle size, the more intense and narrow the first order peak. We argue that the peak width is related to the typical length of fiber segments between branch points, which increases as fibrin assembles into thicker fibers. Strikingly, the

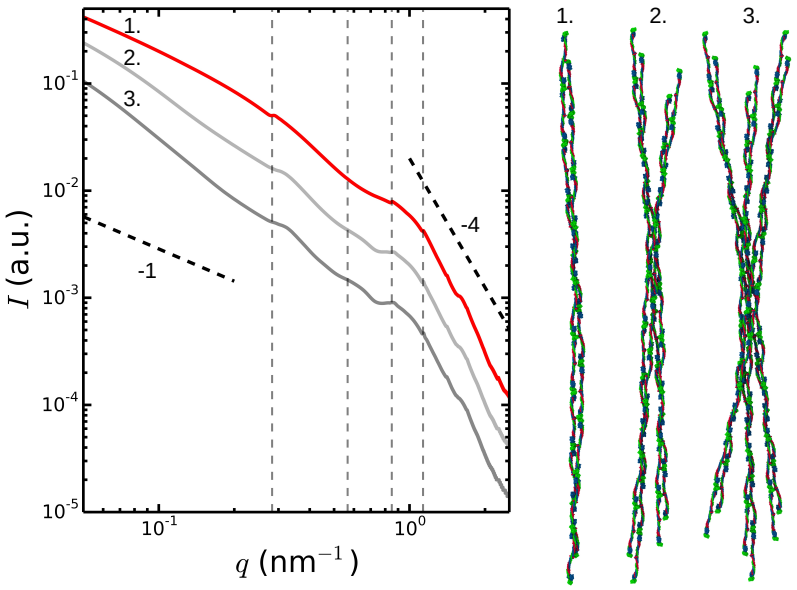

Figure 4.15: The dependence of simulated SAXS patterns on protofibril branching. 1) Unbranched protofibril control, FO10-9 (red line). 2) Two protofibrils (FO10-9) that cross each other at an angle of ∼15°, forming a mini network (light gray line). 3) Three protofibrils (FO10-9) crossing (dark gray line). The expected locations of the first, second, third and fourth order reflections of the half-staggering axial repeat distance are depicted by dashed gray lines for reference.

second order reflection of the axial packing order is absent for all samples that we tested. With the help of simulations of protofibrils by Artem Zhumorov and Valeri Barsegov (Fig. 4.9), we can rationalize this finding based on the symmetric structure of the fibrin monomers. Furthermore, the simulations show that the disordered αC-regions emanating from the protofibrils should broaden the peaks. Regarding the radial packing structure of the (coarse) fibers, our SAXS measurements support a recent model proposing a partially ordered arrangement of protofibrils within the fiber [295,490]. We find evidence of a disordered arrangement characterized by a fractal dimension D_f in the range of 1.1 up to 1.7 (depending on bundle size) together with a broad peak stemming from a characteristic spacing between protofibrils of 13 nm.

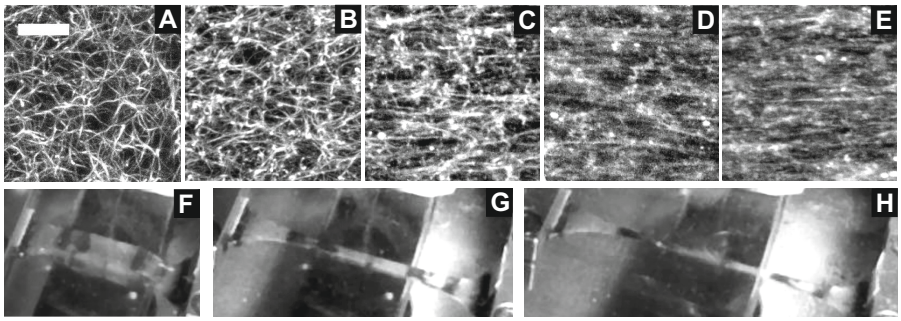

Figure 4.16: Alignment of a coarse fibrin network ($N_p \sim 100$, 8 mg/ml) under the influence of an increasing uniaxial tensile strain. Maximum intensity projections of 10 μm deep confocal z-stacks for (A) 0%, (B) 15%, (C) 20%, (D) 40% and (E) 65% strain. Scale bar denotes 10μm for (A-E) and images are rotated to have approximately the same strain direction. Photographs of a fibrin gel in the Linkam tensile tester used for SAXS measurements at applied strains of (F) 0%, (G) 85% and (H) 120%. The black bands are graphite marks used to monitor the strain. The black structures at the two ends of the gel are pieces of Velcro that are embedded in the gel so that the gel ends can be clamped.

4.4.2 SAXS of Stretched Fibrin Networks

Alignment

In section 4.4.1 we have shown that SAXS spectra of fibrin networks exhibit a series of distinct peaks that can be explained in terms of the characteristic half-staggering axial repeat distance of the molecular packing structure of the fibers. We also showed that the intensity and width of these peaks as well as the slope of the overall decrease of $I(q)$ at low q are dependent on fiber thickness. Next we aimed to investigate potential changes in the internal structure of fibrin under elongation.

Fibrin samples were polymerized in a bone-shaped Teflon mold with Velcro as anchor points. The Velcro pieces on each end of the gel were clamped in a Linkam Tensile tester. We were able to stretch the samples up to typically about 120% strain before the gel ruptured, often near one of the anchoring points (Fig. 4.16(F-H)). We observed that under influence of extension, the sample thinned and expelled water, consistent with a previous study [389] (panel F-H). Moreover, the applied tensile strain caused the fibrin network to align.

The degree of fiber alignment was quantified by imaging fixated stretched

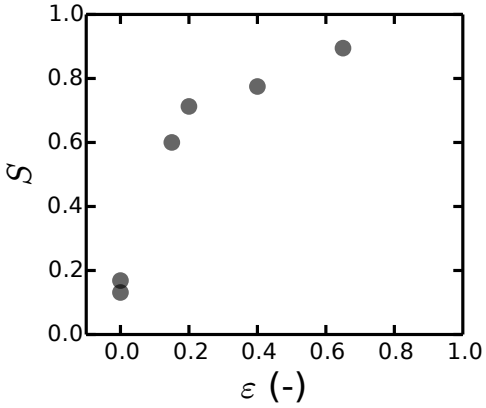

Figure 4.17: The 2D order parameter, S, for coarse fibrin gels ($N_p \sim 100$, 8 mg/ml) under increasing extensional strain determined by image analysis of maximum intensity projections of 3D confocal z-stacks (Fig. 4.16(A-E)). Each data point represents an individual measurement on a different fibrin gel that has been stretched and fixated at a given strain.

fibrin samples under varying strain levels (Fig. 4.16(A-E)). At 0% strain, the fibers showed no obvious preferential alignment (Fig. 4.16A), while at increasing levels of strain, the fibers progressively aligned more. To quantify this effect, we performed image analysis using the OrientationJ plugin [439] for ImageJ on maximum intensity projections of 10 μm thick z-stacks to determine the 2D order parameter S (defined in eq. 4.2). S is 0 for perfectly isotropic systems and 1 for completely aligned networks. In practice, we typically find $S \sim 0.1 - 0.2$ for isotropic systems, as shown in Chapter 3 and in Fig. 4.17 (0% strain). S rapidly increases from $\sim$0.15 at 0% strain to 0.7 at 20% strain. At 65% strain, almost the entire network is aligned as seen in the maximum intensity projection (Fig. 4.16E), which results in a high S-value of 0.89 (Fig. 4.17). The increase in order parameter with extensional strain is steeper than determined in an earlier study, albeit using a different definition for the order parameter, where the order parameter increases over a range of $\sim$300% strain [389]. There are several caveats with the alignment analysis by confocal microscopy. First we note that from the confocal images the fibers seem to get thinner and come close together with strain, which makes it difficult to track individual fibers. Second, the 2D maximum intensity projection likely increases the order parameter artificially, if fibers that are still in the process of re-orientating in the z-direction are projected to the same plane. Therefore, we expect quantitatively more accurate results from a three-dimensional

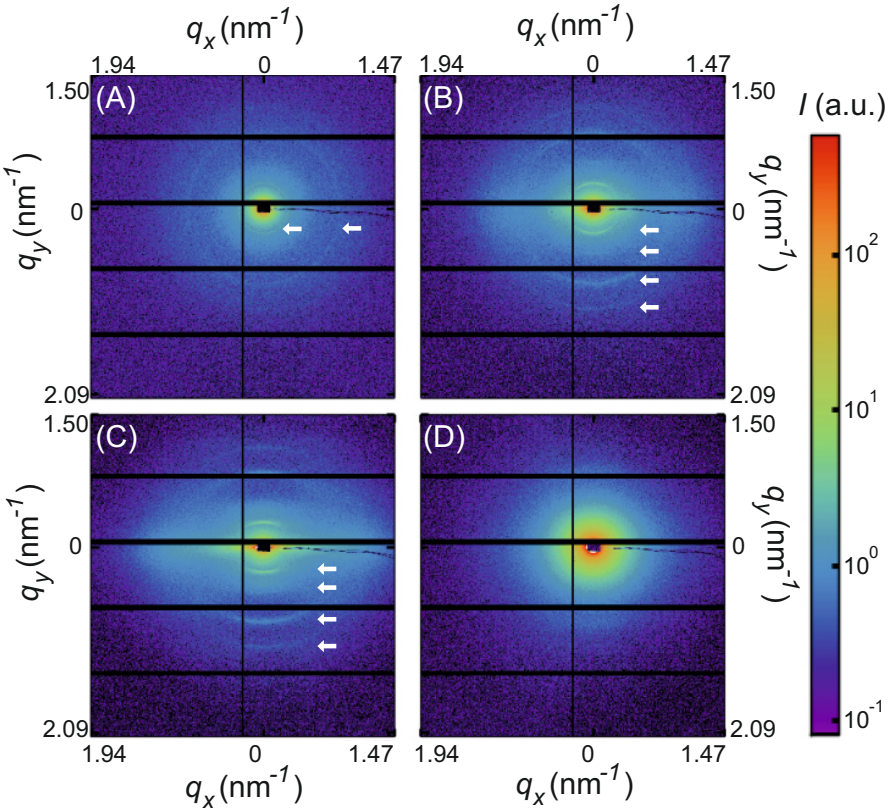

Figure 4.18: Scattering patterns of 8 mg/ml coarse fibrin gels ($N_p \sim 100$) for (A) 0%, (B) 50%, (C) 90% and (D) 110% strain. The stretching speed was 7 μm/s between intervals. The peaks are pointed out by white arrows. The color bar on the right displays the intensity axis (in arbitrary units). (A-C) were recorded directly (∼2 min) after stretch, while (D) was recorded after ∼6 minutes of stress relaxation.

analysis of the angle distribution of the fibers, which we have started to do using the image toolbox SOAX [495]. In any case, our 2D analysis predicts significant fiber alignment with strain. Next we investigated how the SAXS pattern changes for networks under varying degrees of extensional strain.

The 2D SAXS patterns radically changed when fibrin samples were stretched, as shown in Fig. 4.18. At 0% strain, the scattering pattern showed the same features as patterns measured for fibrin samples in capillaries, being isotropic and showing peaks originating from the half-staggered axial packing order. This observation indicates that the network structure is initially isotropic and that the gels were not perturbed much during sample handling, consistent with the confocal images. When the strain was increased however, the scattering pattern became more and more anisotropic, indicating progressive alignment of the fibrin network with increasing strain. Also, certain peaks initially appeared in the meriodional (strain) direction at intermediate levels of strain (Fig. 4.18B and C) and disappeared (Fig. 4.18D) when the strain was further increased. To quantify this behavior in detail, we performed a partial radial integration over a $\pm 15^\circ$ (total 30°) angle in the strain direction. We thus obtain the *meridional* scattering pattern originating from X-rays scattered parallel to the axis of the fibers aligned along the strain direction. The meridional scattering is thus sensitive to strain-induced changes in the half-staggered packing along the fibril axis.

The SAXS spectra obtained at 0% strain look identical to the spectra we measured for fibrin networks in capillaries (section 4.4.1). Upon stretching, we observe marked changes in the spectra. Strikingly, these changes depend on the pulling rate, which was either 50 μm/s (Fig. 4.19), or 10 μm/s (Fig. 4.20), or 7 μm/s (Fig. 4.21). At the fastest pulling rate of 50 μm/s (Fig. 4.19), we initially see peaks appearing with increasing strain (light gray to black). The first order peak corresponding to the half-staggered molecular packing distance is not visible at 0% strain, but appears when the strain reaches ~60%, though only after several minutes (compare panel A measured after 2 minutes with panel B measured after 6 minutes). Apparently, the fibrin networks are not directly in a steady state at this high pulling rate. This is supported by the force-extension measurements by the Linkam tensile tester, which show significant stress relaxation at this pulling rate (Fig. 4.27 in the SI). The first order peak is accompanied by a new, broad peak around $q = 0.45$ nm^{-1} and a smaller peak at $q = 1.06$ nm^{-1}. With increasing strain, also the third and fourth order reflections of the axial half-staggering distance get more pronounced (dashed gray lines). At 80% strain, the peak at $q = 0.45$ shifts to slightly lower q-values ($q = 0.436$ nm^{-1}), which means that it shifts to larger distances. Also, two new, smaller peaks appear, one at $q = 0.535$ (close to the expected location of the second order reflection of the half-staggering axial distance) and the other at $q = 1.54$ (arrows in panel B).

Interestingly, when the pulling speed was decreased to 10 μm/s (Fig. 4.20), peaks appeared at similar q-values as observed at the higher pulling rate, but they appeared at smaller strain levels and/or after a smaller relaxation time.

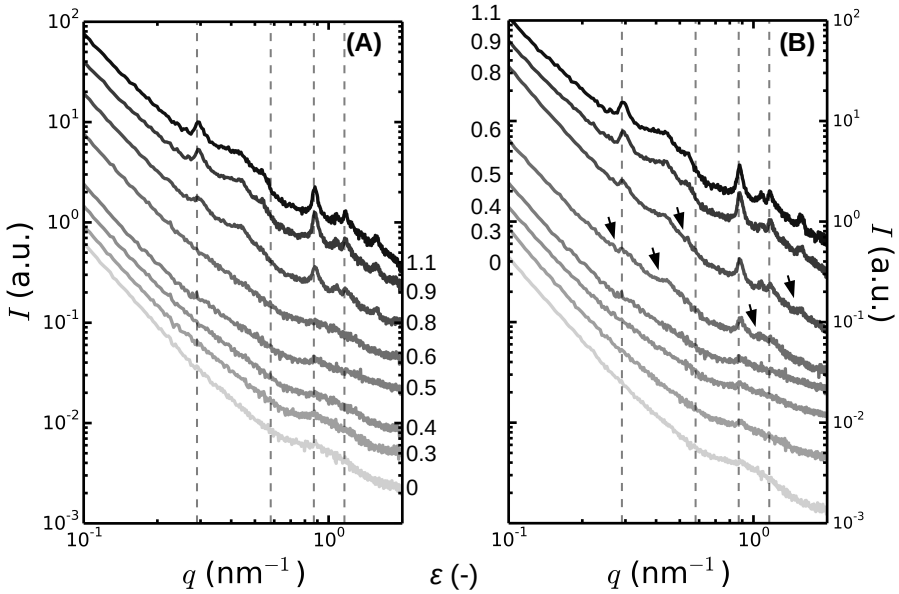

Figure 4.19: Scattering intensity in the axial (meridional) direction for a coarse fibrin network (8 mg/ml, $N_p = 23$) that is stretched at a pulling rate of 50 μm/s. (A) Scattering intensity recorded ∼2 min after stretching and (B) ∼6 minutes after stretching. Vertical dotted lines indicate the locations of the first, second, third and fourth order reflections of the axial half-staggering repeat distance. The strain level, ε, corresponding to each curve is indicated. The black arrows in (B) indicate peaks that appear with increasing strain levels.

For instance, the first order reflection of the half-staggered distance appeared at 60% strain already after 2 minutes instead of 6 min. Also, a new peak appeared at $q \sim 0.52$ nm^{-1} at a strain level of only 30%. Consistent with these findings, force-extension measurements showed significantly less stress relaxation (Fig. 4.27 in the SI). Another marked difference compared to the 50 μm/s pulling speed case, is that the peaks corresponding to the axial half-staggering distance decrease in height at high strain levels, and eventually even mostly disappear at the highest strain of ∼120%.

At an even lower pulling speed of 7 μm/s, we again observed the appearance of peaks at similar q-values as in the 10 μm/s case: The peak at $q \sim 0.52$ nm^{-1} again appeared already at a strain of 30%. At slightly higher strains, a shoulder was observed in some cases on the low q-side of the peak corresponding

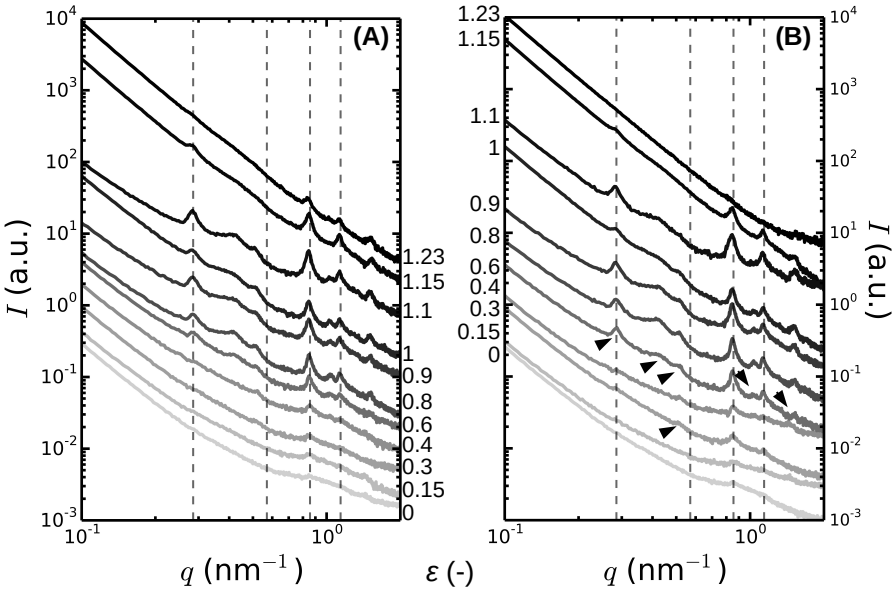

Figure 4.20: Scattering intensity in the axial (meriodional) direction for a coarse fibrin networks (8 mg/ml, $N_p = 23$) that is stretched at a pulling rate of 10 μm/s. (A) Scattering intensity recorded ∼2 min after stretching and (B) ∼6 minutes after stretching. Vertical dotted lines indicate the locations of the first, second, third and fourth order reflections of the axial half-staggering repeat distance. The strain level, ε, corresponding to each curve is indicated. The scattering curves are shifted along the y-axis for clarity.

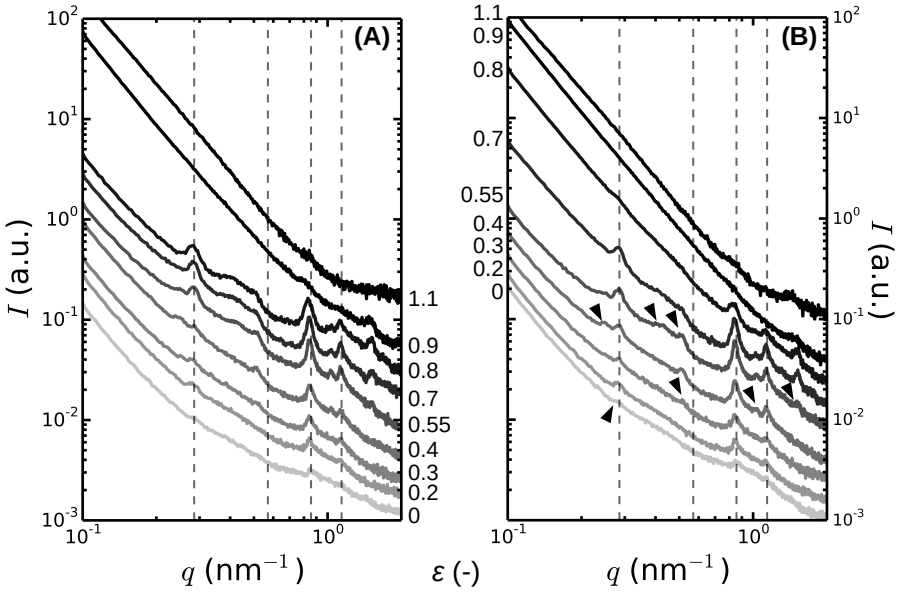

Figure 4.21: Scattering intensity in the axial direction for a coarse fibrin network (8 mg/ml, $N_p = 23$) that is stretched at a pulling rate of 7 μm/s. (A) Scattering intensity recorded ∼2 min after stretching and (B) ∼6 minutes after stretching. Vertical dotted lines indicate the locations of the first, second, third and fourth order reflections of the axial half-staggering repeat distance. The strain level, ε, corresponding to each curve is indicated. The scattering curves are shifted along the y-axis for clarity.

to the first order reflection of the axial half-staggering distance at $q \sim 0.247$ nm^{-1} (indicating the presence of a new repeat distance that is larger than 22 nm). Interestingly, at this low pulling speed, the peaks corresponding to the half-staggered axial packing order completely disappeared at a strain of 90%, whereas at a pulling rate of 10 μm/s this happened at a significantly higher strain of ∼120%. We note that we observed similar strain-dependent changes in the Bragg peaks for networks with larger bundle sizes ($N_p \sim 100$) stretched at the same speed of 7 μm/s (Fig. 4.28 in SI), though in this case the peaks originating from the axial packing order disappeared at a larger strain level (∼120%), suggesting that structural relaxation may be slower for thicker fibers.

The observation that peaks corresponding to the half-staggered axial packing order appear with increasing tensile strain can be rationalized in terms of the strain-induced alignment. The progressive alignment of the fibers along the vertical direction makes it possible to distinguish the Bragg peaks in the meriodional direction. The appearance of new peaks unrelated to the half-staggered packing as well as the disappearance of peaks with increasing strain indicate that straining in addition causes structural changes in the internal axial packing structure. From section 4.4.1 we know that the second order reflection of the axial half-staggering distance only appears when either the β- or γ-nodule unfolds. Interestingly, we never observed the second order reflection of the half-staggering distance at the expected location (second vertical dashed line). Upon straining, we observe the appearance of a new peak at q-number that is close to the position of the second order reflection (see second vertical dashed line), but at a somewhat lower q-value. Potentially, this peak may be attributed to the second order reflection of a (partially) unfolded half-staggering axial distance of $22+\delta d$. Here δd varies between 2 and 6 nm to account for the higher order peaks at $q = 0.45$ nm^{-1}, $q \sim 0.247$ nm^{-1} and $q = 0.52$ nm^{-1}. To test whether this is a reasonable interpretation, we compared our scattering intensity plots with simulated scattering intensity profiles of protofibrils pulled *in silico*. These full atom simulations were done by Artem Zhmurov (Moscow Institute of Physics and Technology) and Valeri Barsegov (University of Massachusetts Lowell).

The simulations show that under the influence of increasing extensional strain, the two strands of the protofibril move closer together as the initial 'slack' in the protofibril is pulled out, as shown in Fig. 4.22A. Already at strains below 30%, there is some elongation of the protofibril, without significant unfolding. At 30% strain however, the forces are high enough to partially unfold one of the γ-nodules inside the protofibril (see also the zoom-in in panel B), giving rise to an 3−4 nm extension. This γ-nodule unfolds more and more with increasing strain. At the same time, the alpha-helical coiled coils formed by the α, β and γ chains exhibit varying degrees of unfolding and transfor-

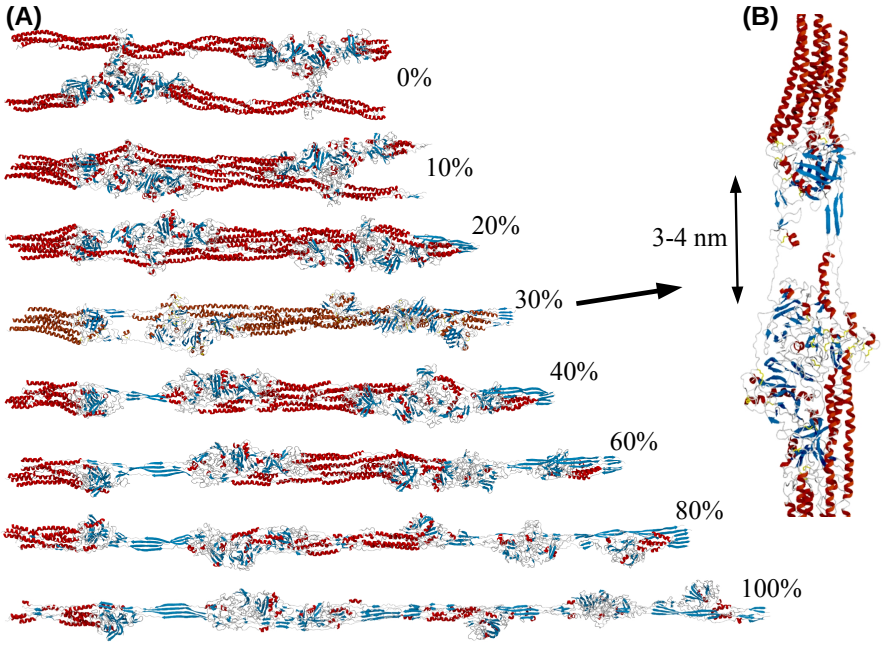

Figure 4.22: Structural changes during protofibril stretching predicted using full atom simulations. (A) Representative images of (part of) a protofibril during stretching. The strain level is indicated. (B) Zoom-in of the unfolding event at 30% elongation, where the γ-nodule of one of the protofibril subunits unfolds, giving rise to a 3−4 nm extension. Red denotes α-helical secondary structure, blue arrows denote β-sheet secondary structure, and gray denotes random coils. These data were kindly provided by Artem Zhmurov.

mation to beta-sheet structure. These pulling experiments were performed for several short protofibrils (FO2-2 up to FO5-5). While the exact unfolding pathway varied, the main features were all shared, namely that unfolding of one of the γ-nodules started at 30% strain, while the alpha-helical coiled coils transformed into β-sheet structures. This picture is consistent with vibrational spectroscopy measurements and staining tests with the β-sheet-specific dye Congo Red on stretched fibrin gels, which also showed an increased β-sheet content when fibrin networks were strained [336, 366].

The structures shown in Fig. 4.22 were used to compute the X-ray scattering intensity. Fig. 4.29 in the SI shows the simulated intensities for single (partially) unfolded protofibrils in solution. The first order reflection of the

half-staggering distance migrates to smaller q-values (i.e. larger distances), as one might expect, with increasing strain levels, together with the corresponding higher order reflections. However, these scattering intensity graphs cannot be directly compared with our SAXS experiments, since we start from an isotropic sample. With increasing strain, the network aligns more and more to the strain direction, as shown in Fig. 4.16 and Fig. 4.17. Thus, we need to account for fiber alignment and inhomogeneous strain distributions in the network (see section 4.2.4). We achieve this by assuming that the scattered intensity of stretched gels is a superposition of intensities for aligned fibers and unaligned fibers. The aligned fibers include fibers that just got oriented along the strain direction and are still unstrained, as well as fibers under varying levels of strain, depending on the macroscopically applied strain level. The total scattering intensity is calculated according to eq. 4.10. As a last step, to account for spectral line-broadening as a consequence of a widening distribution of stretched and unfolded fibrin monomers, the scattering intensity plots are convolved with a Gaussian function with a width of 0.03 nm^{-1}.

Fig. 4.23 shows predicted scattering intensity plots for two stretching simulations of isotropic solutions of protofibrils comprising a mixture of folded and (partially) unfolded protofibrils as a function of extensional strain. Interestingly, the first order reflection does not move much with strain, though it does broaden with increasing strain and decreases in height. The third and fourth order reflections of the half-staggering axial repeat distance are also present for all strain levels, though the height decreases with increasing strain. The scattering intensities below 30% strain show the influence of protofibril stretching and alignment without (significant) unfolding. At 15% strain, a peak appears between the third and fourth order reflections at $q \sim 0.992$ nm^{-1}, which coincides with a slight shift of the first order and third order reflections to lower q-numbers (arrows in Fig. 4.23). These three peaks are related to an elongation of the 22 nm half-staggering axial repeat distance by 15%. We note that at strains around 15%, the second order reflection of the half-staggering axial repeat distance is not yet apparent and there is no significant unfolding yet.

Once the strain reaches 30%, one of the γ-nodules in the elongated protofibrils starts to unfold, giving rise to the appearance of the second order reflection in the SAXS spectra due to symmetry breaking (as discussed in section 4.4.1). The location of the second order reflection is notably at smaller q-values than expected based on the rest length of the half-staggering axial repeat distance ($q = 0.285$ nm^{-1} for 22 nm), indicating that indeed the γ-nodules of protofibrils that are already under tension start to unfold first. The second order reflection peak shifts to lower q-numbers as the strain is further increased. This observation is consistent with our experimental data obtained at the slowest pulling speed of 7 μm/s, where a peak appeared when the strain reached 30% strain, at a q-value close to, but smaller than, the expected sec-

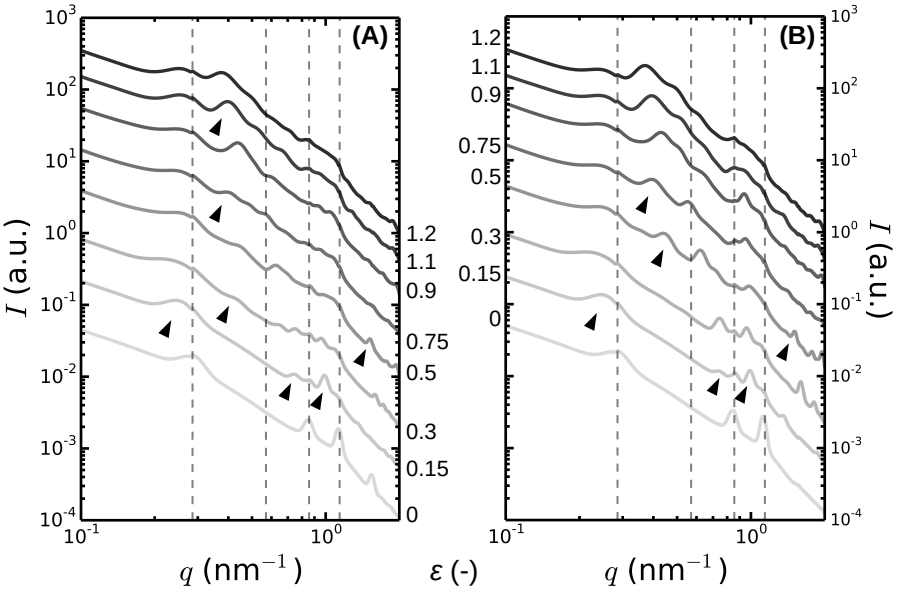

Figure 4.23: Predicted scattering intensity obtained from *in silico* pulling experiments on a mixture of full atom structures at various levels of alignment and unfolding using eq. 4.10 and a Gaussian convolution as described in section 4.2.4. (A) and (B) show the simulated scattering intensity using two different protofibril pulling runs. Vertical dotted lines indicate the locations of the first, second, third and fourth order reflections of the axial half-staggering repeat distance (22 nm). The strain level, ε, is indicated. The data for these scattering intensity plots were kindly provided by Artem Zhmurov.

ond order reflection position. Moreover, we observed also experimentally that the position of this peak shifted to lower q numbers as the strain was further increased.

In summary, the simulations predict that a variety of new peaks should appear once the strain reaches 30%, as a consequence of γ-nodule unfolding. These peaks are expected to be located at q-values in-between the positions of the first and second order reflections originating from the rest length of the half-staggering axial repeat distance (22 nm). These peaks can thus be taken as a clear signature of γ-nodule unfolding. The peaks that we observed in-between the expected locations of the third and fourth order reflections (from the rest length of the half-staggering axial repeat distance (22 nm)), together

with the shoulder that appears on the low-q side of the first order peak, are related to an extension of the 22 half-staggering axial packing distance, but should not be directly taken as a signature of protofibril unfolding.

Lateral Packing Changes at High Strain

So far, we have focused on the change of the axial molecular packing structure of the fibrin fibers with increasing extensional strain. We have shown that unfolding starts at strains above 30% at low pulling speeds ($<$10 μm/s), while at the highest pulling speed the unfolding is delayed (50 μm/s). Next, we investigated how the lateral packing structure of the fibrin fibers changes under influence of extensional strain. To analyze the change in lateral packing order, we averaged the scattering intensity orthogonal to the strain direction by a line of 10 pixels in width to obtain the *equatorial* scattering pattern originating from X-rays scattered perpendicular to the axis of the fibers aligned along the strain direction.

As discussed in detail in section 4.3, the lateral packing structure of the fibrin fibers is thought to be less ordered than along the axial direction. There are two main models from the literature that describe the lateral packing of protofibrils in a fibrin bundle, as shown in Fig. 4.6. One model describes the fibrin fiber as mass fractals with a fractal dimension of $D_f \sim 1.3$ [364], with no internal crystal structure. This would give rise to a q^{-D_f} dependence for the scattering intensity. The other model describes the fibrin fiber as a ordered lattice with a tetragonal unit cell measuring a x c x c = 18.4 x 18.4 x 46 nm, where 18.4 nm corresponds to twice the distance between protofibrils and 46 nm to the length of one fibrinogen monomer [74, 298]. This model would give rise to a peak around 18.4 nm. Recently, a combination of these two models has been proposed, where the lateral packing is crystalline, but with a large number of protofibrils missing ('holes'). This arrangement results in a superposition of a fractal-like scattering and a broad peak due to locally crystalline regions [295, 490]. In section 4.4.1, we have confirmed this superposition for coarse fibrin networks, though we observed a broad peak at a lower distance ($\sim$13 nm) than expected and the fractal dimension varied between $1.3 - 1.7$ depending on bundle size.

At 0% strain, the equatorial scattering curve (light gray curve in Fig. 4.24) looks similar to the isotropic averages for fibrin gels in capillaries presented in section 4.4.1 and to the meriodional averages obtained for gels at 0% shown in section 4.4.2. At high q, we see the third and fourth order reflections of the half-staggering axial packing. When the fibrin network is strained (light gray to black), we observe subtle changes in the scattering curves. We do not see any peak at the predicted 18.4 nm distance predicted from the crystal structure proposed by Yang *et al.* [74] (dotted vertical lines). However, the data do show a broad peak at $q \sim 1.0$ nm^{-1}. At low strains, this broad peak coincides with the expected positions of the third and fourth order reflections of the

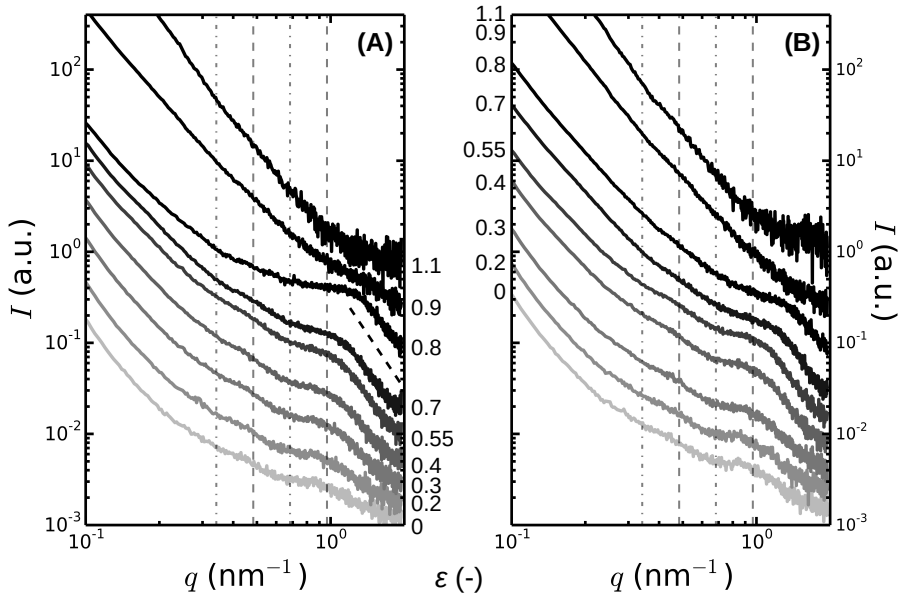

Figure 4.24: Scattering intensity in the lateral (equatorial) direction for coarse fibrin networks (8 mg/ml, $N_p = 23$) stretched at a pulling rate of 7 μm/s. (A) Scattering intensity recorded ∼2 min after stretching and (B) ∼6 minutes after stretching. Vertical dotted lines indicate where first and second order peaks are expected based on the repeat distance of 18.4 nm proposed by Yang *et al.* [74, 298]. The observed peak attributed to the lateral packing (13 nm), and it second order reflection, are indicated by the vertical gray dashed lines. The strain level, ε, is indicated. The black dashed line at high q in (A) denotes a power law with exponent -4 (Porod). The scattering curves are shifted along the y-axis for clarity.

half-staggering axial packing distance ($q = 0.86$ nm^{-1} and $q = 1.14$ nm^{-1}). However, the contribution of the axial packing decreases with increasing strain due to fiber alignment. This means that we expect the third and fourth order reflections from the axial half-staggering repeat distance to disappear with increasing strain. Thus, the peaks observed at higher strains should be attributable to the lateral packing structure of the fibrin fibers. In the capillary measurements we observed a broad peak at $q \sim 0.47$ nm^{-1} that we attributed to a partially crystalline lateral packing structure with a 13 nm repeat distance (dashed vertical lines). For the strained gel, we also observe a broad peak at approximately this distance for some samples, which persists for a broad range of strains (Fig. 4.31). We interpret the broad peak at $q \sim 1.0$ nm^{-1} as the second order reflection of this peak. The peak at 1.0 nm^{-1} does not move with increasing strain values, until the strain reaches values of $\gtrsim$80%, where significant unfolding takes place. At these high strain levels, the second order reflection of the lateral repeat distance (13 nm) shifts to higher q-numbers. Also, the Porod regime at high q (black dashed line), which is related to the solvent-protofibril interfaces as explained in Fig. 4.5, is moved out to higher q-values. This observation indicates that the protofibrils themselves become thinner once significant unfolding occurs. This interpretation is consistent with the predicted structures shown in Fig. 4.22, where protofibrils become significantly thinner at strains of ∼80%, once a significant portion of the γ-nodule is unfolded.

We note that we observe similar equatorial scattering curves also for the other pulling rates, as shown in Fig. 4.31 in the SI, where the peaks attributed to lateral order disappear at the same strains (∼120%) where the peaks attributed to the axial packing order disappear.

Plastic Deformation

So far we have shown that our experiments confirm predictions from simulations that protofibril unfolding starts at 30% strain. A key experimental signature is the appearance of a Bragg peak corresponding to the second order reflection of the (elongated) half-staggering axial repeat distance. We further showed that the lateral packing does not change much with strain, except at high extension where the axial order has mostly disappeared. In this section we investigate how reversible these changes are by stretching coarse fibrin networks to different levels of strain, and returning to a lower strain level, as shown in Fig. 4.25.

At a strain of 45%, we observe the first order reflection of the half-staggering axial distance (22 nm), as well as the third and fourth order reflections (vertical dashed lines). Also, there is a peak close to the second order reflection that we attribute to the second order reflection of the elongated half-staggering axial repeat distance. At this strain level and pulling speed (7 μm/s), the protofibrils have partially unfolded γ-nodules.

When the strain is increased further to 60%, the fibrin fibers are more aligned (Fig. 4.16 and Fig. 4.17), leading to an increase of the intensity of the first, third and fourth order reflections of the half-staggering axial distance (Fig. 4.21), and the scattering curve shows more obvious signs of unfolding (peaks in-between the first and second order reflection of the axial half-staggering distance, indicated by the first two vertical lines). Interestingly, when the strain is returned back to 45%, the scattering curve suggests that the fibers remember the strain direction, since the first, third and fourth order reflections have a higher intensity compared to the original state of the network at 45% strain. The second order reflection is still present upon returning to 45%, though it has a large shoulder to lower q-values. These observations are supported by the scattering intensity in the equatorial direction, where the first and second order reflections of the lateral packing distance between protofibrils (13 nm) are better visible compared to the original state of the network at 45% strain.

When the strain is increased from 45 to 90%, there is significant protofibril unfolding, since the peak corresponding to the first order of the axial half-staggering distance completely disappears. Interestingly, when the sample is relaxed back to 45%, the first order re-appears together with its higher order reflections (third and fourth order) but the second order is not present. This implies that there is complete refolding, even though the sample is still under 45% strain. One possible explanation is that protofibrils, in combination with unfolding, also slide along each other to relieve tension [413]. The equatorial scattering now shows a broad shoulder at q-numbers where we expect to see peaks originating from lateral ordering. We attribute this to significant fiber alignment (as also indicated by the peaks of the axial packing) and a broad disorder in the lateral packing distance. The observation that the first order reflection re-appears after sample relaxation is consistent with prior SAXS observations on fibrin films [455], though in that case the maximum strain levels were lower ($\sim$40% strain) and the waiting time was hours instead of minutes. When we strain the sample to 110% and then return back to 45%, the structure does not refold back completely, as indicated by the reduced height of the first, third and fourth order reflections of the axial half-staggering distance compared to the control case (thick gray line). This idea is supported by the equatorial scattering intensity, which shows that the onset of the protofibril Porod regime is delayed, which indicates thinner protofibrils compared to the control (0% strained to 45% at a strain rate of 7 μm/s).

4.5 Discussion

We have investigated the origin of the remarkable extensibility of fibrin networks by performing *in situ* SAXS measurements on fibrin gels subject to uniaxial tension in combination with full-atom simulations of the force-extension

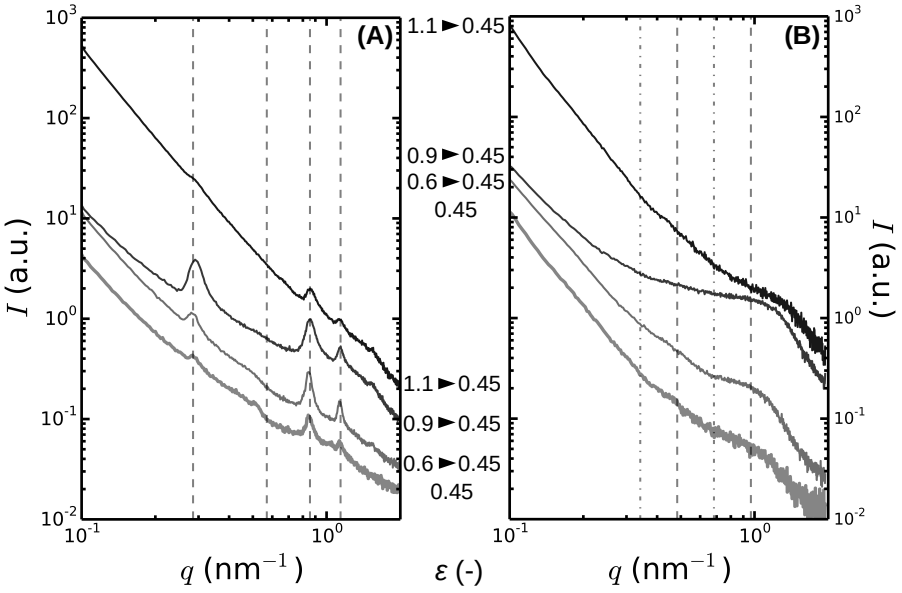

Figure 4.25: Scattering intensity in the axial (meridional) (A) and the cross-sectional (equatorial) (B) direction for a coarse fibrin network (8 mg/ml, $N_p = 23$) stretched at a pulling rate of 7 μm/s, recorded $\sim$2 min after stretching. The fibrin gel is pulled to the indicated strain level (0.45, 0.6, 0.9 or 1.1) before relaxing it back to a strain level of 0.45. The vertical dashed lines in (A) indicate the locations of the first, second, third and fourth order reflections of the axial half-staggering distance. The dotted vertical lines in (B) denote the predicted locations of the peaks originating a crystalline lateral packing of the protofibrils assuming a unit cell measuring 18.4 x 18.4 x 46 nm ($q = 0.341$ nm^{-1} and higher order reflections) [74]. The dashed vertical lines in (B) denote the observed peaks attributed to the lateral packing ($q = 0.483$ nm^{-1} and higher order reflections). The scattering curves are shifted along the y-axis for clarity.

behavior of fibrin protofibrils (performed by Artem Zhmurov and Valeri Barsegov). We showed that fibrin network elongation is accompanied by forced γ-nodule unfolding when the strain exceeds 30%. This process gives rise to a peak in the scattering intensity located in-between the expected location of the first and second order reflections originating from the rest length of the half-staggering axial repeat distance (22 nm). We showed that these peaks can be taken as a clear signature of γ-nodule unfolding. We also observed peaks in the scattering intensity in-between the expected locations of the third and fourth order reflections (from the rest length of the half-staggering axial repeat distance (22 nm)), together with a shoulder on the low-q side of the first order peak. We showed that these peaks are likely related to an extension of the alpha-helical coiled coil regions of the protofibrils, and should not be taken as a signature of protofibril unfolding.

Depending on strain rate, complete unfolding occurs at strains close to 90% or higher. This is in line with a previous publication, which showed that the first order reflection of the half-staggering distance (22 nm) vanished at 100% elongation [389]. However, this strain is larger than strains reported for fibrin films ($\sim$40%) [456]. We note that for fibrin films the second order reflection of the half-staggering distance was also observed at 0% strain [455, 456], which is suggestive of mechanical perturbations during sample preparation. This hampers a quantitative comparison of the strain required for unfolding between our results and the prior SAXS data for fibrin films.

To compare the simulated scattering intensity of stretched protofibrils with our SAXS experiments, we used previous published data on fibrin network alignment [389]. This is not ideal, since fibrin alignment is likely to depend on the pulling rate as well as on the mesh size of the fibrin network. To quantify fiber alignment for our own networks, we have performed confocal microscopy on fibrin networks that were fixed after stretching to various levels of strain (Fig. 4.16) and we analyzed the fiber alignment using maximum intensity projections of 10 μm thick z-stacks. This analysis is likely to provide artificially high values for the order parameter, since all fibers are forced onto one plane. We expect quantitatively more accurate results from a three-dimensional analysis of the angle distribution of the fibers, which we have started to do using the image toolbox SOAX [495]. In principle, we can also use 3D fiber tracking data directly as input to simulate the scattering intensity. This is still work in progress.

We convolved the scattering intensity calculated from simulated protofibril structures with a Gaussian function with a width of 0.03 nm^{-1}. This width was chosen to fit the experiments. To check whether this width is reasonable, we compare this width to the broadening from the experimental setup. In experiments, the scattering intensity data are broadened by misalignment and energy spread of the incident beam. This broadening is estimated to be 2$-$3

Å [496], corresponding to a broadening of about $0.003-0.004$ nm^{-1}. This experimental broadening is about $7-10$ times smaller than the value used to calculate SAXS curves from simulations. This indicates that the modeled SAXS curves can be further improved in the future. However, qualitatively the simulations do indicate which scattering peaks to expect from protofibril stretching and unfolding, and at what q-values, and the simulation predictions are all confirmed experimentally.

In the experiments we used coarse (bundled) fibrin gels ($N_p = 23$ and $N_p \sim 100$), whereas the simulations were performed for protofibrils ($N_p = 1$). Thus, the comparison between experiment and simulations is not entirely fair. To address this issue, we also performed SAXS experiments on stretched fine fibrin gels, which have minimal bundling (see Chapter 2, $N_p = 2$). We observed qualitatively the same features as for the coarse fibrin networks, as shown in Fig. 4.30 in the SI, though the scattering intensity was reduced. We did not observe a peak corresponding to lateral ordering, as one might expect in the absence of significant protofibril bundling (panel B).

4.6 Conclusion

In this Chapter, we have shown SAXS data for fibrin gels under elongation, supported by full-atom simulations on stretched protofibrils (from our co-workers, Artem Zhmurov and Valeri Barsegov) to interpret strain-induced changes in molecular structure. First, we investigated the effect of lateral packing on the scattering patterns by varying the bundle size at 0% strain. We showed that the axially symmetric molecular packing structure of fibrin can explain the suppression of the second order reflection of the 22 nm axial repeat. If the symmetry is perturbed by unfolding of the γ or β-nodule, the second order appears. We further showed that the Bragg peaks corresponding to axial order are much more pronounced for thicker fibers and that the peak width is correlated to the mesh size of the network. Further, we found indications of a partially ordered lateral packing structure of the fibers with a characteristic repeat distance of 13 nm, independent of bundle size. When the fibrin gels were subjected to uniaxial stretch, we observed clear evidence for forced molecular unfolding. At an applied strain of 30%, peaks appear between the first and second order reflections of the 22 nm axial repeat distance. Predicted SAXS curves based on simulations of stretched protofibrils showed that these peaks are an unambiguous signature of γ-nodule unfolding. Furthermore, both simulations and experiments showed that the peaks originating from axial order become broader and less intense with increasing strain, indicative of increased disorder. At strains of $\sim 90-100\%$, the peaks disappeared in the experiments, but only for small pulling rates. This loss of axial order coincided with a loss of lateral order. By combining SAXS experiments with MD simulations, we can now understand the molecular basis of fibrin's exten-

sibility and strain-stiffening response. Forced unfolding may also help explain intriguing recent findings that mechanical stretch protects fibrin fibers against fibrinolysis [465–467]. Moreover, forced unfolding may potentially unmask cryptic binding sites for cells and extracellular matrix molecules, in a similar manner as in fibronectin [497] and could be exploited to design molecular switches [498].

4.7 Acknowledgments

I would like to thank Artem Zhmurov and Valeri Barsegov for sharing their full-atom simulations on pulled protofibrils. I also like to thank the people of the Dubble beam-line in Grenoble for excellent assistance with the SAXS measurements and helpful discussion: Giuseppe Portale, Daniel Merino and Wim Bras. Also, I like to thank Han Meijer (University Eindhoven, the Netherlands) for borrowing of their tensile tester and help on the design of the dog-bone molds. I am grateful for useful discussions with John Weisel and Rustem Litvinov (uPenn, Philadelphia) and in particular for the idea of combining confocal microscopy with fibrin fixation. Also I like to thank Bart Vos and Baldomero Alonso Latorre for help with the data analysis. Last but not least, I would like to thank everyone who went on SAXS beam-time with me to help with the experiments: Gijsje Koenderink, Izabela Piechocka, Nicholas Kurniawan, Corianne van den Akker, Andre Scholich, Bart Vos and Valeri Tutwiler. This work is part of the research programme of the Foundation for Fundamental Research on Matter (FOM), which is financially supported by the Netherlands Organisation for Scientific Research (NWO). This work is further supported by NanoNextNL, a micro and nanotechnology programme of the Dutch Government and 130 partners.

4.8 Supplementary Information

Supplementary Figures

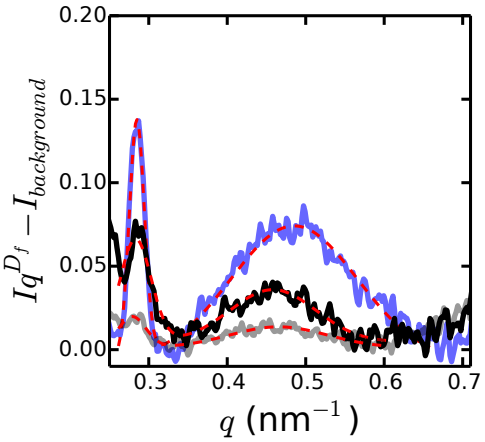

Figure 4.26: Three fitting examples of two Gaussians per sample. The fits are depicted in red dashed lines. The blue line depicts a 4 mg/ml fibrin gel with bundle size of $N_p \sim 366$, the black line is a 8 mg/ml coarse fibrin gel with $N_p \sim 100$ and the gray line is a 4 mg/ml coarse fibrin gel with bundle size $N_p = 44$. Gray is enhanced by a factor 10, while black is magnified by a factor 6.

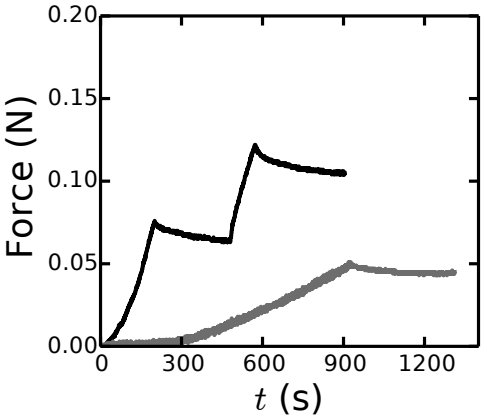

Figure 4.27: Example tensile test curves measured on coarse fibrin gels ($N_p = 23$, 8 mg/ml) for pulling rates of 50 μm/s (black) and 10 μm/s (gray). The strain levels for 50 μm/s were 40% (first peak) and 60% (second peak), while for the 10 μm/s only the 50% strain level is shown. There is significantly more force relaxation in the 50 μm/s case compared to the 10 μm/s case.

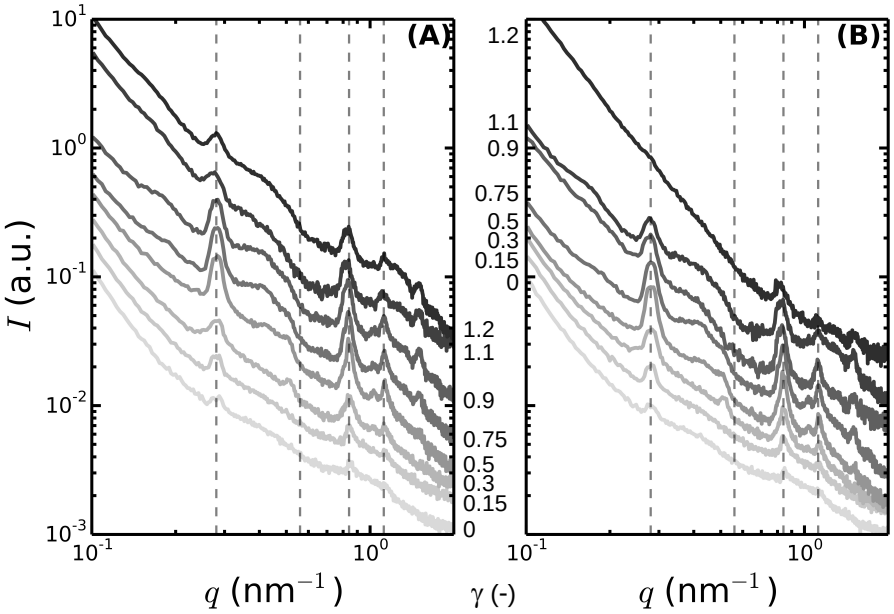

Figure 4.28: Scattering patterns of coarse fibrin gels ($N_p \sim 100$, 8 mg/ml) for varying strain levels (A) 2 minutes after stretching and (B) 6 minutes after stretching. Vertical dotted lines indicate the locations of the first, second, third and fourth order reflections of the half-staggering distance. The strain levels are indicated. Scattering curves are shifted along the y-axis for clarity.

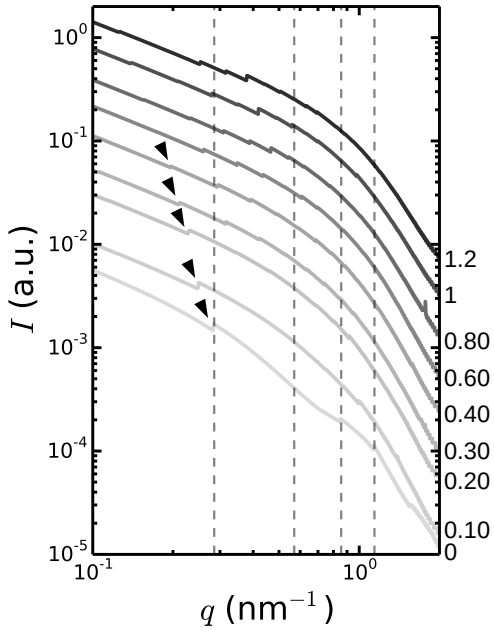

Figure 4.29: Simulated scattering intensity for dilute solutions of (partially) unfolded protofibrils as depicted in Fig. 4.22, without convolution with a Gaussian function. Black arrows highlight the strain-induced migration of the first order reflection of the half-staggering axial packing distance to lower q-values. Vertical dotted lines indicate the locations of the first, second, third and fourth order reflections of the axial half-staggering repeat distance. The strain level is indicated. The simulated scattering curves are shifted along the y-axis for clarity.

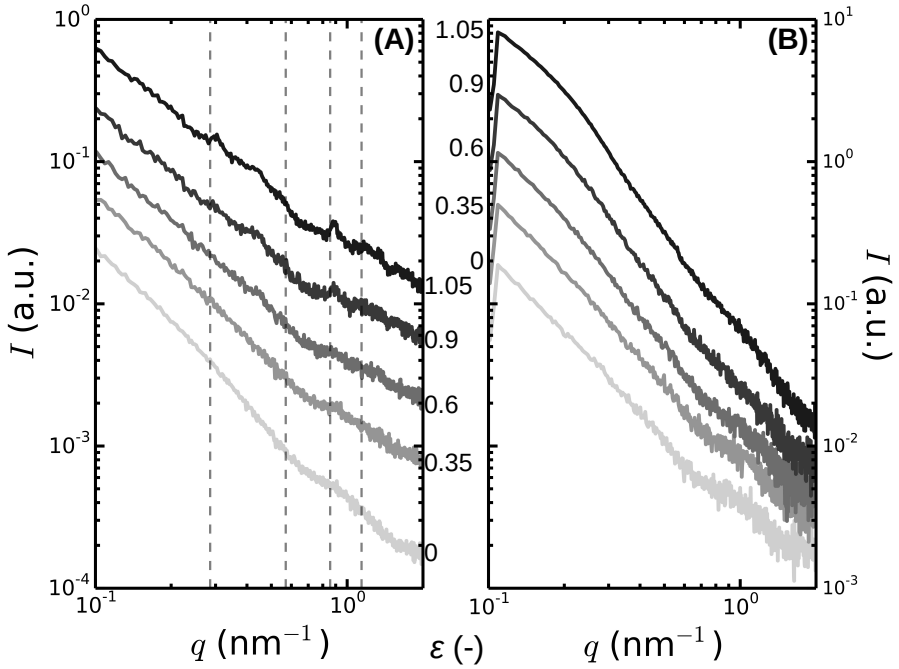

Figure 4.30: Scattering intensity in the axial (A) and lateral (B) direction for fine fibrin networks ($N_p = 2$, 8 mg/ml) pulled at 20 μm/s. (A) Scattering intensity directly (∼2 min) after stretching and (B) ∼6 minutes after stretching. Vertical dotted lines indicate the locations of the first, second, third and fourth order reflections of the axial half-staggering repeat distance. The strain level, ε, is indicated. The scattering curves are shifted along the y-axis for clarity.

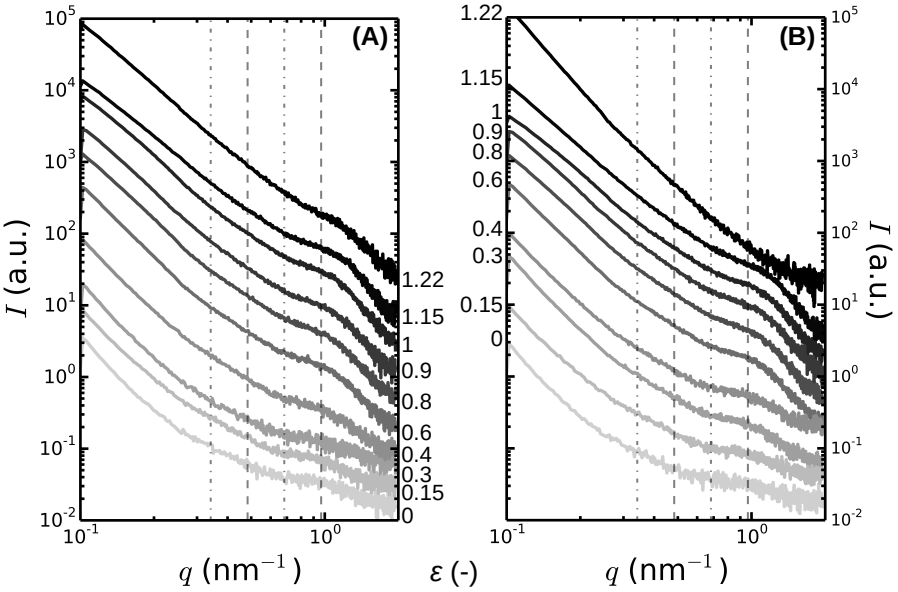

Figure 4.31: Scattering intensity in the lateral direction for coarse fibrin networks ($N_p = 23$, 8 mg/ml) pulled at 10 μm/s. (A) Scattering intensity directly ($\sim$2 min) after stretching and (B) $\sim$6 minutes after stretching. Vertical dotted lines indicate to 18.4 nm, and its second order reflection, expected for the model presented by Yang *et. al.* [74, 298]. The observed peak attributed to the lateral packing (13 nm), and it second order, is indicated in vertical gray dashed lines. The strain level, ε, is indicated. The scattering curves are shifted along the y-axis for clarity.

5. Microscopic View of Fibrin Blood Clots

Mechanical interactions of cells with their tissue environment through cellular adhesions have been shown to regulate many cell processes, including cell migration and cell division. On the scale of the cell, local mechanical properties of the fibrous extracellular matrix at the micron scale are likely to be more important than the global mechanical properties. In this chapter, we develop a customized optical tweezer microrheology setup that allows us to probe the local mechanical properties of fibrin networks at the cellular scale by measuring the thermally driven fluctuations of micron-sized probe beads embedded in the material of interest. We first validate the technique by comparing microrheological measurements on viscous fluids of varying viscosities and polyacrylamide gels with macroscopic shear rheometry. Next, we test the technique on fibrin networks whose architecture is varied by tuning the fibrin concentration and self-assembly conditions. We show that the surface chemistry of the probe beads crucially affects the micromechanical properties of fine fibrin networks: Without surface passivation, beads accumulate fibrin on their surface and overestimate the shear modulus of the network, while a covalent Pluronic coating creates a depletion layer of about 3 μm thick and leads to an underestimation of the network modulus. Using the high-frequency response of the passivated beads, we determine the persistence length of protofibrils to be 203 $\pm$ 75 nm, which is in excellent agreement with prior findings. Finally, we study fibrin networks with a large pore size ($\sim$10 μm), for which we recover the bulk modulus within a factor 3. We conclude that optical tweezer microrheology is a powerful tool to obtain information about the local micromechanical properties of extracellular matrix networks at the scale relevant to cells, as well as the network and fiber response.

Karin A. Jansen, Andre Scholich, Gijsje H. Koenderink

5.1 Introduction

Mechanical interactions between cells and the extracellular matrix play a vital role in the regulation of cell behavior and tissue morphogenesis in health and disease [3, 4, 499]. Cells probe their mechanical environment by exerting traction forces [206]. Studies of cells on top of 2D substrates showed that the stiffness of the substrate has a strong influence on cell spreading, differentiation, migration, gene expression and cell-cell signaling [41, 43–48] (see also Chapter 1 section 1.3.1). Recently, the viscous properties of the substrate were shown to also influence cell behavior [72, 500]. In 3D environments that more closely mimic the extracellular matrix in tissues, it was shown that local mechanical interactions at the micron-scale regulate cell migration [310] as well as cell division [501]. Cells can also locally change the architecture and mechanics of the ECM, as shown in Chapter 3. Cells probe the mechanical properties of their environments on the scale of the size of the protrusions that interact with the matrix fibers, so at the scale of several microns [99, 423, 502, 503].

The mechanics of ECM gels are highly complex: They tend to stiffen under the influence of stress in complex ways [39,66,272] (see also section 1.8.1). This is very different from most synthetic materials, like polyacrylamide (PAA), which have a constant stiffness out to very large strains [39]. Cellular traction forces have been measured on top of two dimensional PAA substrates [504,505] and inside three dimensional hydrogels [257] by applying linear continuum elastic theories to calculate forces from measured bead displacements (see also section 1.7). In the context of 3D extracellular matrices, this method is far from trivial, since the pore size is typically on the order of microns (instead of nanometers) [271], the ECM network typically strain-stiffens [39], and viscous dissipation of the network occurs on cellular timescales [72]. Therefore, quantitative information is needed about the local micromechanical properties of ECM networks to interpret cellular traction forces [247, 249, 503, 506].

One way to measure local mechanical properties is to use nanoindentation [55, 507]. However, this is a surface technique that does not give information about the mechanics inside a 3D gel. Others have used microrheology techniques, such as multiple particle tracking using time-lapse video microscopy [508–511], optical tweezer microrheology [512] or magnetic microrheology [513]. However, most of these microrheology studies focused on the mechanical properties of cells [511,514,515] and isolated intracellular networks like actin [333, 373, 427, 516–522]. Only a few studies so far addressed the microrheological properties of extracellular matrices using either optical tweezers [523–528], magnetic tweezers [403,529–532] or video particle tracking [533]. Most of these studies focused on the low frequency regime though, and did not investigate the influence of the bead's surface chemistry.

There are two main classes of microrheological techniques: Active microrheology, using optical or magnetic tweezers, and passive microrheology, using

video particle tracking. These techniques are often used to determine the mechanical properties in the low frequency regime. However, when optical tweezers are combined with interferometric detection using quadrant photodiodes, one can obtain also high frequency information over a range up to 100 kHz [515,534]. The advantage of such a high bandwidth is that one can obtain in a single measurement both the network response (at low frequencies) and the dynamics of the individual polymers (at high frequencies) [427, 535, 536].

Microrheology of fibrous protein networks brings several complications, however. The bead size is an important parameter to consider. If the bead is smaller than the mesh size, then the passive fluctuations will give information about the mesh size and not the mechanical properties of the network [523]. Also, the bead surface chemistry is an important consideration. This parameter has mainly been studied in the context of actin networks [516, 537], where it was shown that inert beads report a lower modulus and a higher frequency dependence compared to bulk rheology. In contrast, sticky beads tend to overestimate the modulus, but give the correct frequency dependence. One study claims that sticky beads are necessary to report the correct moduli, even when the bead size is $\sim$10 times larger than the average mesh size [538].

Here, we develop an optical tweezer based setup to perform high bandwidth microrheology on fibrous protein networks. We validate the method using viscous fluids of calibrated viscosity, as well as small pore size PAA gels, which have a significant elastic component. We then show that we can probe the local viscoelastic moduli of fibrin networks. For this we employ two different bead types: One set of beads that stick to the network (plain polystyrene beads) and one set of passivated beads that are inert (polystyrene beads covalently coated with Pluronic). We show that both bead types provide the correct concentration dependence of the elastic modulus G', but the sticky beads overestimate G', while the inert beads underestimate G'. We can explain this over- and under estimation in terms of a change in local fibrin concentration at the bead's surface. At high frequencies for the inert beads, we observe clear evidence of entropic elasticity for G'', with a characteristic $\omega^{3/4}$ frequency dependence, while at low frequency the data agree with macrorheology. This observation confirms the model proposed in chapter 2, where we concluded based on macrorheometry data that the linear elastic modulus of fibrin networks must be entropic in origin. We can now apply the microrheology technique to probe the influence of cells on their local tissue environment, for instance during cell-mediated stiffening [67, 524, 525, 528]. Also, it could even be combined with simultaneous intracellular microrheology to probe the response of the cell [539]. Optical microrheology is also highly suited for on-line monitoring of blood clotting and fibrinolysis (nano-thromboelastography [540]).

5.2 Materials and Methods

5.2.1 Sample Preparation

So-called 'fine' and 'coarse' fibrin gels crosslinked by fibrinoligase (FXIIIa) were made as described in Chapter 2, using reagents from Sigma and human fibrinogen and thrombin from Enzyme Research Laboratories (Swansea, UK). Coarse clots were made using fibrinogen dialyzed into the fibrin buffer (without $CaCl_2$, see Chapter 2) before use. The fibrin concentration was varied between 0.4 up to 2 mg/ml. Fine and coarse fibrin gels were allowed to polymerize for at least 1 or 4 hours at 37°C respectively. For optical tweezer measurements, beads at a (final) volume fraction of less than 1% were added just before the addition of thrombin, and the gels were polymerized inside sealed glass chambers. For confocal microscopy, Alexa488 labelled fibrinogen was purchased from Life Technologies (Bleiswijk, the Netherlands), dissolved in either fine clot buffer or coarse clot buffer (without $CaCl_2$, see Chapter 2) and mixed with unlabeled fibrinogen in a 1:20 molar ratio.

Polyacrylamide (PAA) gels were formed by mixing the following ingredients: BIS-acrylamide (40% w/v) was mixed with acrylamide (30% w/v) and water. The solution was degassed by 10 minutes centrifugation. Then ammonium persulfate (APS, 10% w/v) and Tetramethylethylenediamine (TEMED) were added to induce polymerization. The final conditions were (v/v) 1.1% BIS-acrylamide, 1.1% acrylamide, 0.5% APS and 0.15% TEMED. The PAA gels were polymerized at room temperature (22°C) for $\sim$ 4 hours or, in case of rheology measurements, until a plateau in the linear viscoelastic moduli was reached. For optical tweezer measurements, beads were added before APS and the gels were polymerized inside sealed glass chambers. To ensure a homogeneous bead distribution, the glass chambers were rotated for the first $\sim$ 20 minutes of polymerization. To check that the overall stiffness does not change by the presence of beads, we measured the rheological properties of bead-seeded gels by adding the beads just before APS and TEMED. After 15 min, when the sample was still fluid, the sample was gently transported to the rheometer plate to ensure an homogeneous bead distribution inside the sample.

5.2.2 Bead Preparation

Polystyrene beads (1.5 μm diameter) were purchased from Polysciences (Eppelheim, Germany) and stored at 4°C. Silica beads (1 μm diameter) were purchased from G. Kisker GbR (Steinfurt, Germany) and stored at 4°C. In some cases, home-made silica beads were used. These beads were prepared according to a protocol introduced by Stöber *et. al.* [541] and modified by Zhang *et. al.* [542]. In short, tetraethyl orthosilicate (TEOS), ammonia (30%) and absolute ehtanol were used. Two solutions were made. Solution 1 contained 46

ml of ethanol and 10 ml of ammonia, while solution 2 contained 7 ml of TEOS and 28 ml of ethanol. Solution 2 was added drop by drop to solution 1 under rapid mixing to get 1.2 μm diameter beads, as determined by transmission electron microscopy by Dominique Thies-Weesie at the University of Utrecht. The polydispersity was measured to be 3.4% (see Fig. 5.15 in the supplementary information (SI)). The silica beads were stored in 100% ethanol at room temperature. All the three bead types were washed with water by repeated centrifugation and resuspension before use.

In this Chapter, we investigate the effect of bead chemistry on the measured mechanical properties in fibrin networks. For this purpose, we render 1.5 μm polystyrene beads inert by coating them covalently with Pluronic using a protocol introduced by Kim *et. al.* [543]. In short, 15 μl bead suspension was added in a LoBind Eppendorf tube (VWR, Amsterdam, the Netherlands) and sonicated for 5 min. Beads were pelleted by centrifugation for 5 min at 16.1×1000 g to remove the supernatant. The beads were resuspended in 100 μl F-127 Pluronic solution (1% w/w). After 10 min incubation, 40 μl Toluene is added and incubated for 3 hours. This allowed the beads to swell such that the Pluronic chains are inserted. During this time, the tubes are in a rotating wheel (20 rmp). The Toluene is removed by heating the tubes to 98°C in a water bath in the fume hood for 10 min. The excess Pluronic was removed by centrifuging at 16.1×1000 g for 5 min. The final bead solution was stored in fine fibrin buffer (50 mM TRIS-HCL, 400 mM NaCL, pH 8.5) or water at room temperature. The beads were stable for at least two years.

5.2.3 Macrorheology

Rheology measurements were performed with a stress-controlled rheometer (Physica MCR 501; Anton Paar, Graz, Austria). Directly after adding thrombin, the fibrinogen solutions were quickly transferred to the rheometer plate, which was equipped with a steel cone and plate (40 mm diameter, 1° cone angle). The rheometer was preheated to 37 °C for experiments with fibrin, or kept at 22 °C in the case of PAA. Solvent evaporation was prevented by coating the fibrin sample edges with mineral oil. For PAA, water was added in the wells. The time evolution of the linear shear modulus, G^*, was monitored during fibrin polymerization by applying a small-amplitude oscillatory strain with amplitude $\gamma = 0.5\%$ and frequency $\omega = 3.14$ rad/s and measuring the stress response, $\sigma(\omega) = G^*\gamma(\omega)$. The shear modulus is a complex quantity, $G^* = G' + iG''$, having an in-phase elastic component, *G'*, and an out-of-phase viscous component, *G"*. Networks of fine fibrin clots and also PAA reached a constant shear modulus (G_0) after about 1 hour. After polymerization, a frequency test was performed by applying 0.5% strain and varying the frequency from 10 to about 0.05 Hz. These frequency tests were compared with microrheology measurements obtained with the optical tweezer setup.

5.2.4 Imaging

To check the local environment around the beads, we perform confocal microscopy on fibrin networks with (coated or not coated) beads and without beads (control). For this we use a confocal fluorescence microscopy on a Nikon Eclipse Ti inverted microscope equipped with a 100xoil immersion objective (NA 1.49), a 488-nm laser (Coherent, Utrecht, The Netherlands) for illumination, and a photomultiplier tube detector (A1; Nikon, Amsterdam, the Netherlands). Alexa488 labeled fibrinogen was purchased from Life Technologies (Bleiswijk, the Netherlands), dissolved in fine clot buffer (without $CaCl_2$) and mixed with unlabeled fibrinogen in a 1:20 molar ratio. Samples were prepared in sealed glass chambers and polymerized at 37 °C for 1 hour (fine clots) or 4 hours (coarse clots) before imaging. The images are summations over stacks of 5−10 μm thick in z, taken 10 μm away from the surface with 0.125 μm step size.

5.2.5 Optical Tweezer Measurements

Setup

The optical tweezer is build in-house on a Nikon Eclipse Ti inverted microscope, which is depicted schematically in Fig. 5.1A. A 1064 nm wavelength continuous laser (YLM-5-1064-LP, IPG Photonics, Germany) is guided via an optical fiber to the back of the microscope, which is placed on a vibration-isolating optical table. The beam goes through a beam expander (ELQ-25-2.5x-1064, Thor Labs) before it is guided through two acousto-optical deflectors (AODs) (DTSXY-400-1064, AA Opto Electronics). The first reflection exiting from the AODs is selected with a pinhole. The pair of AODs gives us control over both the x and y direction of the laser beam and move the laser trap in the sample via a computer via two computer-controlled variable frequency drivers (AAMCS, France). The laser power within the sample can be varied by either changing the laser power directly at the laser driver, or by changing the transmission efficiencies of the AODs.

Probe beads within the sample are optically trapped using a 100x oil objective (NA 1.4, Nikon). The laser light exiting the sample is collected using an oil condenser (NA 1.4, Nikon, japan, HNA-oil) and projected onto the back-focal plane of the condenser on a quadrant photodiode (QPD) (YAG-44-4AH Excelitas Technologies). The QPD gain is controlled using a field-programmable gate array (FPGA board, NI PXIe- 1073, national instruments, Netherlands) via a custom written program termed 'MicroRheology'. The gain was varied between 1 and 7 depending on the laser power and bead size used. The QPD electronics calculates (analogue) the displacements in $x(t)$ and $y(t)$ from the differences in voltages in the four quadrants of the QPD, as shown in Fig. 5.1B. This interferometric paticle position detection method results in nanometer spatial and ~ 10 μs temporal resolution [544]. The $x(t)$, $y(t)$ and

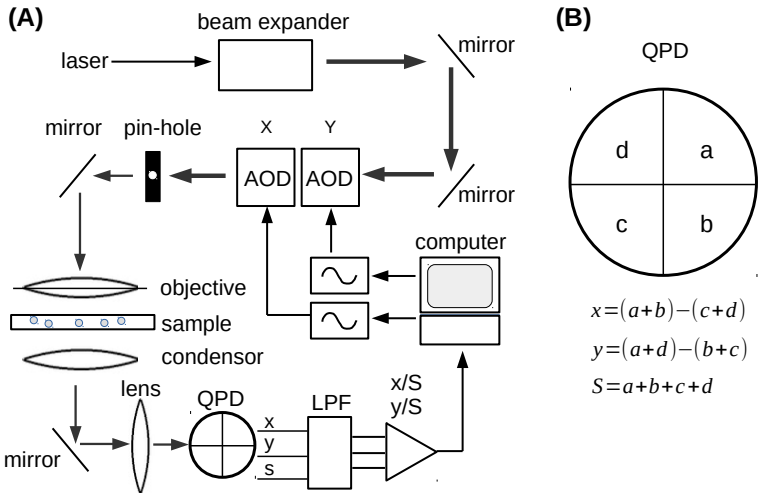

Figure 5.1: (A) Schematic diagram of the optical tweezer measurement setup as described in section 5.2.5. (B) Schematic diagram of the quandrant photo diode (QPD) detector and its operations to calculate fluctuations in x and y in the sample plane. The x and y signals are normalized by the sum-signal S.

sum signal is filtered by a low-pass filter (LTC1564, Linear Technology) with cutoff 150 kHz. The signal of the QPD is normalized to the sum signal before analysis to account for noise in the laser intensity. The recording of the position signal was typically 60 sec in fibrin gels, oversampling by recording at a sampling frequency of 200 kHz. Such oversampling avoids aliasing artifacts in data acquisition [545]. The data is analyzed with an home-made program written by Marco Seynen termed 'MicroRheology', which is written in C# using Microsoft Visual Studio 2010.

Data Analysis

We developed a customized optical tweezer setup for determining the microrheological properties of biopolymer networks. For this purpose, we sparsely seed our networks with beads and measure the constrained thermal fluctuations in the x and y direction. If a Brownian particle embedded in a material is in thermal equilibrium and there are no other forces acting on it, then the fluctuation-dissipation theorem holds [546] and the position fluctuations u of this particle are related to the response function of the material [547]:

$$A''(\omega)_\alpha = \frac{\omega}{2k_BT} S_\alpha(\omega) \tag{5.1}$$

In this formula, α is either the direction x or y, and S_α is the integral over the equilibrium fluctuation spectrum:

$$S_\alpha(\omega) = \int < u_\alpha(t) u_\alpha(0) > e^{i\omega t} dt \tag{5.2}$$

A'' is the imaginary part of the response function. The real part A' is related to A'' via the Krames-Kronig integral [547]:

$$A'(\omega)_\alpha = \frac{2}{\pi} \int_0^\infty \frac{\xi A''(\xi)_\alpha}{\xi^2 - \omega^2} d\xi \tag{5.3}$$

We refer to A^* as the *apparent* complex response function ($A^* = A' + iA''$), since the fluctuations are recorded in the presence of an harmonic confining potential, namely the laser trap. The rheological complex response function, B^*, is determined by correcting the apparent response function for the contribution of the laser trap with trapstiffness k_α [534, 547]:

$$B^*(\omega)_\alpha = \frac{A^*(\omega)_\alpha}{1 - k_\alpha A^*(\omega)_\alpha} \tag{5.4}$$

If we assume the material is an isotropic and incompressible medium, then the complex shear modulus G^* is related to B^* via the generalized Stokes equation [547–549]:

$$G^*(\omega) = \frac{1}{6\pi R B^*(\omega)} \tag{5.5}$$

were R is the bead radius. This equation is in principle only valid for incompressible media (i.e. Poisson ratio $\nu = 1/2$). However, if the medium is compressible, G^* can be at most 25% off, given that ν is still between 0 and $1/2$ as typical for biopolymer networks [548]. For fibrin, values close to 0.5 have been suggested for ν in the linear elastic regime relevant for passive microrheology [366]. Interestingly, at high deformations, fibrin gels show evidence of negative compressibility [389]. The importance of compressibility effects is frequency-dependent, since at high frequencies, the network is viscously coupled to the fluid, whereas at low frequency, the system becomes compressible [548]. The crossover frequency f_{cros}, above which viscous coupling dominates, can be estimated from a two-fluid model as [548]:

$$f_{cros} \simeq \frac{G}{\mu} \frac{\xi^2}{R^2} \simeq 200 \text{ Hz} \tag{5.6}$$

Using parameter values typical for fine fibrin gels, with $G = 10$ Pa, $\mu = 0.001$ Pa·s, $\xi = 100$ nm and $R = 0.75$ μm, we find f_{cros} ∼200 Hz. This means that, above ∼200 Hz, we can consider fine fibrin gels as incompressible.

To determine the linear viscoelastic properties of fibrin and PAA gels, at least 10 beads per conditions are measured at a fixed distance of 10μm above the glass surface, unless stated otherwise. The geometric mean is shown per sample, since the average is more sensitive to outliers with high modulus (see Fig. 5.16 in SI). To allow a comparison of G' and G'' from micro- and macrorheology measurements, we averaged the modulus between 5 and 6 Hz. The number of samples per condition for the fibrin gels are summarized in Table 5.2 in the SI. For fibrin, the reported G'' are corrected for the solvent contribution ($G'' = \mu 2\pi f$, with viscosity $\mu = 0.001$ Pa·s).

To validate our home-made setup and analysis, we measured the apparent and rheological response functions for viscous fluids of known viscosities (water and water-glycerol mixtures), while varying the trapstiffness by varying laser power. For a viscous fluid, the apparent complex response function A^* reported by an immersed bead held by a trap of stiffness k is calculated as [534]:

$$A^*(\omega) = \frac{1}{k - i\omega\gamma(\omega)} \tag{5.7}$$

where γ is the drag of the particle. For a spherical particle, this is Stokes drag $\gamma = 6\pi\mu R$, where μ is the viscosity of the surrounding medium. The rheological response function is then calculated using eq. 5.4.

Calibration

For a trapped particle in an viscous fluid, the Fourier transform of the thermal fluctuations takes the shape of an Lorentzian [545, 547, 550, 551]:

$$S(f) = \frac{k_b T}{\gamma\pi^2(f_c^2 + f^2)} \tag{5.8}$$

Here $k_B T$ is the thermal energy and f_c is termed the corner frequency [545, 547, 550]. The low frequency response is governed by the laser trap, according to $S(f) = 4\gamma k_B T/\kappa$, while at high frequency the response is governed by the thermal fluctuations of the bead. The corner frequency is the boundary between these two regimes and is proportional to the strength of the trap:

$$k = 2\pi f_c \gamma \tag{5.9}$$

For calibration, 10 up to 15 spherical particles in buffer solution (in case of fibrin) or water (in case of PAA) were measured and the average k-values in both x and y was used to analyze data obtained in fibrin and PAA networks.

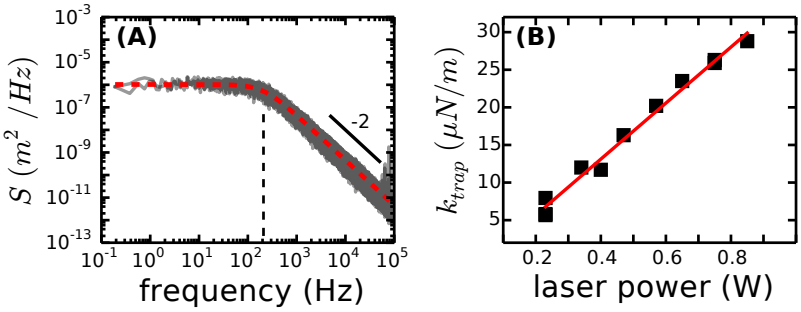

Figure 5.2: (A) The Power Spectral Density (S) of an one μm silica bead in water. Data is depicted in gray, while the red dashed line is the Lorenzian function (eq. 5.8) used to calibrate the trap. The vertical black dashed line denotes the corner frequency f_c. (B) The average trapstiffness in x and y, k_{trap}, can be tuned by varying the laser power of the laser driver. The red line is a linear fit. The laser power in the sample is about 0.05 times lower compared to values shown in (B).

5.3 Results

5.3.1 Setup Validation

Calibration and Viscous Fluids

We developed an optical tweezer setup to measure local mechanical properties of fibrous networks. To validate this setup, we first measured 1 μm diameter silica beads in water. The beads were sparsely seeded inside a flow chamber with a height of $\sim$300 μm. The beads were trapped 10 μm away from the bottom surface. The Brownian displacement fluctuations of a single bead inside the laser trap were recorded via the QPD. The Fourier transform of these fluctuations gives the power spectral density function (S), which shows a plateau at low frequencies and a -2 slope at high frequencies (Fig. 5.2A). This result is consistent with eq. 5.8 and earlier reports [547, 552]. The transition from a plateau to a -2 slope is characterized by the corner frequency f_c. Using this corner frequency, the trap stiffness of the laser can be determined with eq. 5.9.

The trap stiffness was linearly dependent on laser power (Fig. 5.2B). This linear dependence is indeed expected and is consistent with earlier reports [547, 552]. In addition, we expect that the trap stiffness shows a depth dependence due to the high numerical aperture (NA) of the used objective and the refractive index mismatch between the immersion oil and the aqueous

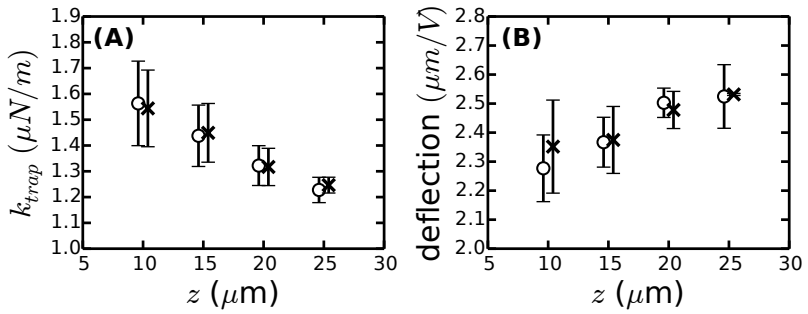

Figure 5.3: The dependence of the trapstiffness (A) and the QPD deflection (B) on focus depth in the sample. Crosses refer to the x-direction, while open circles denote the y-direction. The symbols are shifted along the x-axis for clarity in both (A) and (B), the sample depth z is 10, 15, 20 and 25 μm. For $z = 25$ μm only 2 beads were measured, while for the other heights 5−11 beads were measured (see Table 5.1 in SI for statistics).

samples [553, 554]. Indeed, the trap stiffness decreased linearly with increasing focus depth for depths between 10 and 25 μm, as shown in Fig. 5.3A, consistent with earlier reports [553, 554]. The trapstiffness in the x and y direction have the same magnitude for all sample depths z, showing that the laser spot is symmetric.

The QPD deflection in x and y was calibrated using the plateau level at low frequencies in Fig. 5.2 using eq. 5.8 and the fit in Fig. 5.2A [550]:

$$S_{fit} = \frac{C}{f_c^2 + f^2} \tag{5.10}$$

$$\text{deflection} = \sqrt{\frac{S}{S_{fit}}} = \sqrt{\frac{k_b T}{\gamma \pi^2 C}} \tag{5.11}$$

Here S_{fit} is the fitting function with C and f_c as fitting variables. The deflection converts the voltage outputs from the QPD to μms and the values reported here are in the same range as previous reports [555]. The deflection shows a slight increase with sample depth, as shown in Fig. 5.3B.

The depth dependence of the trap stiffness and deflection shown in Fig. 5.3 emphasize the importance of using a consistent focus depths for optical tweezer microrheology. In the following controls, we make sure we are always at a depth of 10 μm away from the bottom surface. This height is sufficiently far away

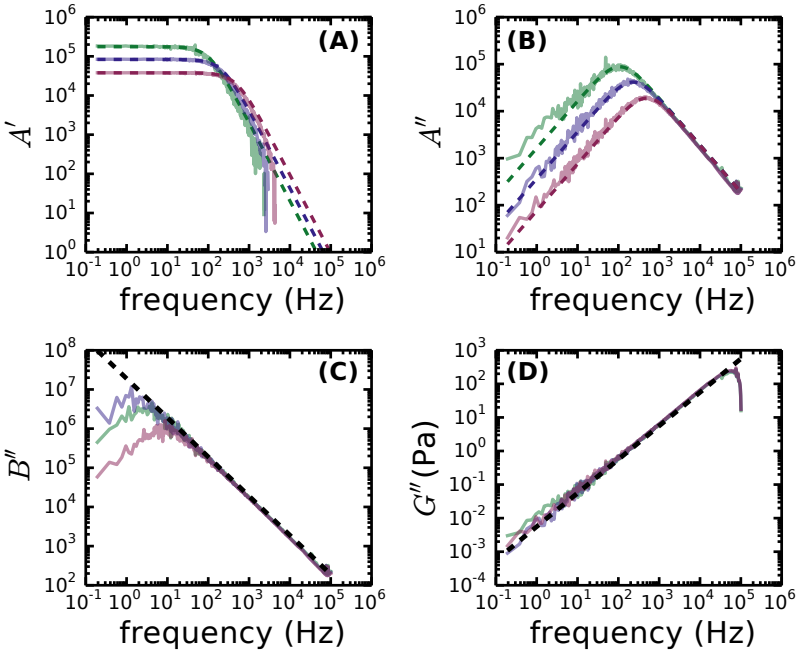

Figure 5.4: The response functions of 1μm silica beads in water, for varying laser powers. (A) The real part and (B) imaginary part of the apparent response function. (C) The imaginary rheological response function. (D) The viscous modulus. The trap stiffness is varied from $5.67{\cdot}10^{-6}$ (green), to $1.20{\cdot}10^{-5}$ (blue) and $2.63{\cdot}10^{-5}$ N/m (purple) by tuning the laser power. The dotted lines are the theoretical predictions.

from the top and bottom surfaces of the flow cell to prevent wall effects such as hydrodynamic drag, long-range surface forces, or optical reflections [556, 557].

To further validate our optical tweezer microrheology setup, we compared the calculated and measured response functions of beads in water, which has a viscosity of μ= 1 mPa·s at room temperature. To calculate the elastic and viscous properties of the medium, first the complex apparent response function is calculated using eq. 5.7. As shown in Fig. 5.4A and B, the apparent response function depends on the trapstiffness at frequencies below $\sim$ 500 Hz, while at higher frequencies all response functions overlap. This is indeed expected, since the apparent response function is not yet corrected for the laser contribution. The measured apparent response function for varying trapstiffness overlap well with the calculated response function from the known viscosity and trapstiff-

ness over the whole frequency range, except at the lowest frequencies ($\leq$5 Hz). Low frequenciy results from optical tweezer microrheology indeed commonly suffer from noise due to sample and laser drift. Note that the A' data are cut-off about one decade earlier than the A'' data; this is a consequence of the Kramers-Kronig transformation needed to infer A' from the measured A'' and the finite frequency range over which A'' is known.

The rheological response function can be calculated from the apparent response function by correcting for the contribution of the trap trap, using eq. 5.4. As shown in Fig. 5.4C, the imaginary part of the rheological response function for beads in water is now independent of trapstiffness and are in close agreement with the theoretical prediction (shown in black) except again at low frequencies. As shown in Fig. 5.4D, the measured G''-values for water closely agree with the theoretical prediction of $G'' = 2\pi\mu f$ for all trap stiffnesses. Only at frequencies below 5 Hz, the experiments overestimate G''. We obtain similar results for a 50% v/v glycerol-water mixture (μ=5.9 mPa·s at room temperature [558, 559]) (see Fig. 5.17 in SI). We can thus accurately capture the viscous properties of fluids of varying viscosities at frequencies higher than 5 Hz.

Polyacrylamide (PAA) gels

We established that we can accurately measure the viscous properties of fluids of varying viscosities at frequencies above 5 Hz. Next, we investigated a model system with both an elastic and viscous component, namely PAA. We prepared PAA gels with low stiffness to approach the stiffness of fine fibrin gels (i.e. G' on the order of 10 Pa or less). The pore size of these PAA gels should be on the order of a hundred nanometers or less [560, 561] and is thus much smaller compared to the bead size used here (1.5 μm). Macrorheology measurements showed that the viscous and elastic moduli of the PAA gels were of the order of several Pascals, as shown in Fig. 5.5 (red and blue symbols). The moduli determined by optical tweezer microrheology (gray lines) are very similar to the values obtained by macrorheology in the overlapping frequency range (0.5−10 Hz). For instance, macrorheology gives $G' = 5.4 \pm 1$ Pa and $G'' = 2.17 \pm 0.26$ Pa at frequency 5 Hz, while optical tweezer microrheology gives $G' = 8.3 \pm 4.4$ Pa and $G'' = 2.5 \pm 1.3$ Pa in the range of 5−6 Hz. We note that noise peaks at frequencies of ∼100 Hz reflect vibrations originating from the laser driver. These noise peaks are more pronounced in elastic samples, like PAA gels, than in viscous samples like water and water-glycerol fluids.

The macroscopic rheology measurements can only access the elastic plateau regime for G'. Optical tweezer microrheology, in contrast, reveal a slight frequency dependence of G' for low frequencies (i.e. $f \lesssim 50$ Hz) (Fig. 5.5A, solid line with a power law exponent of 0.2) and a steeper frequency dependence at higher frequencies (solid line with a power law exponent of 0.5). This frequency dependence is consistent with a previous report [548] which showed

that dilute PAA gels can be described by the Rouse model [562,563]. We note that for long linear polymer chains with narrow molecular weight distribution, the low frequency response is governed by a flow regime and an entanglement regime, while the high frequency response describes the transition towards the glass state as well as the glass state with modulus G_g^* [564]. More concentrated PAA gels ($\simeq$2 % w/w) showed exponents close to 1 [548,565] and could be described by a rheological model that combines an continuous relaxation spectrum model and fractional derivatives for the higher frequencies [565]:

$$G^*(\omega) = G_f^* + G_g^* = \int_0^\infty H(\lambda)\frac{i\omega\lambda}{1+i\omega\lambda}\frac{d\lambda}{\lambda} + G_1\frac{(i\omega\lambda_1)^a}{1+(i\omega\lambda_1)^a} \tag{5.12}$$

where $H(\lambda)$ is the continuous relaxation spectrum and λ is the relaxation time. λ_{max} is the maximum relaxation time, below which the sample flows. $H = n_f G_N^0(\frac{\lambda}{\lambda_{max}})^{n_f}$ when $\lambda < \lambda_{max}$ and 0 otherwise, where -n_f is the slope of G'' at very low frequencies ($< 10^{-2}$ Hz, not accessible in our setup) and G_N^0 is the linear storage modulus at the plateau. G_f^* describes the low frequency response from flow to the glass transition state. $1/\lambda_1$ is the typical crossover frequency between glass and solid state in the mechanical response (at high frequencies) and is related to the microstructure of the PAA [565]. G_1 is the high frequency modulus at $f = 1/\lambda_1$. The exponent a is below 1 for PAA and was reported to decrease with acrylamide concentration. This model was shown to work up to frequencies of 500 Hz [565].

Both the model presented in [565] (eq. 5.12) and the Rouse model state that, for intermediate to high frequencies, both G' and G'' should scale with the same power law exponent a. In particular, the Rouse model states that this exponent should be 0.5. Since we see a power law exponent of 0.5 for G', we expect to see a power law exponent close to 0.5 for G'' as well. We find a power law exponent of 0.62 $\pm$ 0.02 at low frequencies ($f \lesssim 10$ Hz) for G'', and a smaller exponent of 0.45 $\pm$ 0.03 by microrheology at higher frequencies (fitted between 10 Hz $< f <$ 50 Hz). The onset of the regime where G' and G'' have a similar slope is dependent on the gel concentration [565,566]. We estimated this onset by using the model presented in [565] using:

$$f_T = \frac{1}{2\pi\lambda_1}\left(\frac{G_N^0}{G_1 cos(\pi a/2)}\right)^{1/a} \tag{5.13}$$

Using values typical for our PAA gel ($a = 0.5$, $G_1 = 100$ Pa, G_n^0 =10 Pa and $\lambda_1 \sim 10^{-4}$ s), we estimated f_T to be around 10 Hz. This estimate is in line with prior measurements [565], where f_T increases with increasing acrylamide concentration ($f_T \sim c^{1.6}$) for gels with a similar BIS-acrylamide content as our gels. This cross-over frequency is also consistent with the power law dependences of G' and G'' shown in Fig. 5.5.

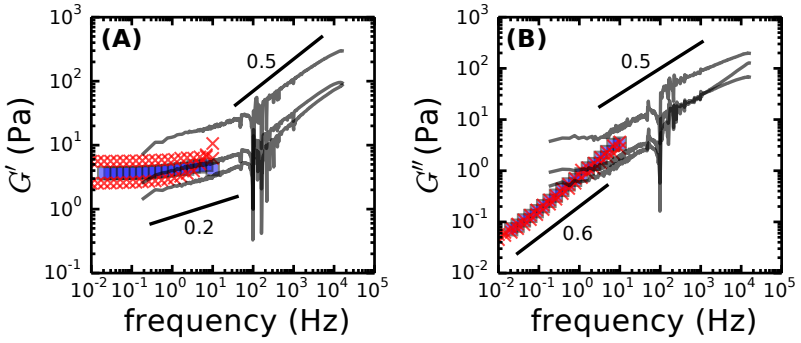

Figure 5.5: The low strain elastic (A) and viscous (B) mechanical properties of PAA measured by macrorheology (red and blue symbols) and optical tweezer microrheology (gray lines). Macrorheology were done on gels without beads (control, blue squares) and two gels with beads (red crosses). The solid black lines show the power law dependences seen at the varying frequency domains (see main text).

Overall, the microrheology experiments provide reliable measurements of the viscoelastic moduli of PAA, including the $f^{0.5}$ frequency dependence of G' and G'' at intermediate to high frequencies expected on the basis of the Rouse model [548,562,563]. Next, we aimed to investigate the local mechanical properties of fine fibrin gels.

5.3.2 Bead Surface Properties Affect Stiffness Measurements inside Fibrin Gels

Having validated our microrheology setup using Newtonian fluids and PAA gels, we investigated the effect of the bead surface properties on the micromechanical properties of fine fibrin networks. For this purpose, 1.5 μm polystyrene beads were either covalently coated with Pluronic to render them inert, or left uncoated so fibrin adhered to the bead surface. The average pore size of these networks decreased from 350 to 115 nm when the concentration was raised from 0.4 to 2 mg/ml, as estimated using $\xi \simeq 1/\sqrt{\rho}$ (see section 2.4.2 in Chapter 2). Thus, depending on the fibrin concentration, the beads were between 4 and 13 times larger compared to the average mesh size. As a first step, the mechanical properties of 1 mg/ml fine fibrin networks were determined using optical tweezer microrheology with the coated and uncoated beads and compared with macrorheology measurements on corresponding networks prepared without beads.

The bead surface properties play a major role in the determination of the

mechanical properties, as shown in Fig. 5.6A and B. The most striking observation is that the noncoated beads (red curves) report higher G' and G'' values compared to the beads coated with Pluronic (gray curves). The frequency dependence of G'' also differs between the two bead types: G'' reported by the noncoated beads show a weaker frequency dependence compared to the coated beads. Note that similar to the PAA gels, noise peaks originating from vibrations are present for G' and G'' curves at frequencies around $\sim$100 Hz. Compared to macrorheology data (blue squares), the uncoated beads report larger values for G' and G'', whereas the coated beads report smaller values for G' and on average comparable values for G''.

To determine the origin for the different micromechanics reported by coated and uncoated beads, we investigated the local fibrin structure. As shown in Fig. 5.6C, in the absence of a surface coating, the density of fibrin close to the beads is much higher than the fibrin density between beads. Apparently, beads accumulate fibrin and possibly act as nucleation centers. In the case of coated beads, the network microstructure as observed by confocal microscopy (Fig. 5.6D right) is qualitatively similar to the control network structure without beads (Fig. 5.6E). However, beads often coincide with regions of lower

Figure 5.6 *(facing page)*: The effect of bead surface properties on the mechanical properties of 1 mg/ml fine fibrin gels measured by optical tweezer microrheology (A,B), and on network structure (C-E). The gray and red curves in (A) and (B) denote the G' and G'' measured by beads that are covalently coated with Pluronic or uncoated, respectively. The blue squares denote corresponding macrorheology measurements on networks without beads. Each line represent the geometric average of an independent measurement (see also Table 5.2 in the SI for statistics). The dashed black lines in (A) and (B) are power laws with exponent 3/4. (C) Noncoated bead inside a fine fibrin network causes a locally enhanced fibrin density. (D) Coated beads do not seem to perturb the fibrin network. (E) 1 mg/ml fine fibrin network without beads (control). The radial intensity distribution for (F) noncoated beads (n=5) and (G) beads covalently coated with Pluronic (n=15). For (F) and (G) the intensity distributions are centered on the bead ($r = 0$) and the intensity is normalized by the average intensity I_{bkg}, 5 μm away from the bead's center. Red is the average intensity distribution, gray are single bead measurements, and the vertical dashed line indicates the location of the bead surface ($r_{bead} = 0.75$ μm). The insets are zoom-ins (log-log scale) of I/I_{bkg} in the range $r[r_{bead}, 4$ μm]. For (C) and (D), the left image are DIC images showing the bead positions, while the right panels are sum images of confocal fluorescence image stacks over 5 μm or 10 μm depth respectively. The control confocal image in (E) is a summation over 10 μm depth. Scale bar denotes 5 μm for all images.

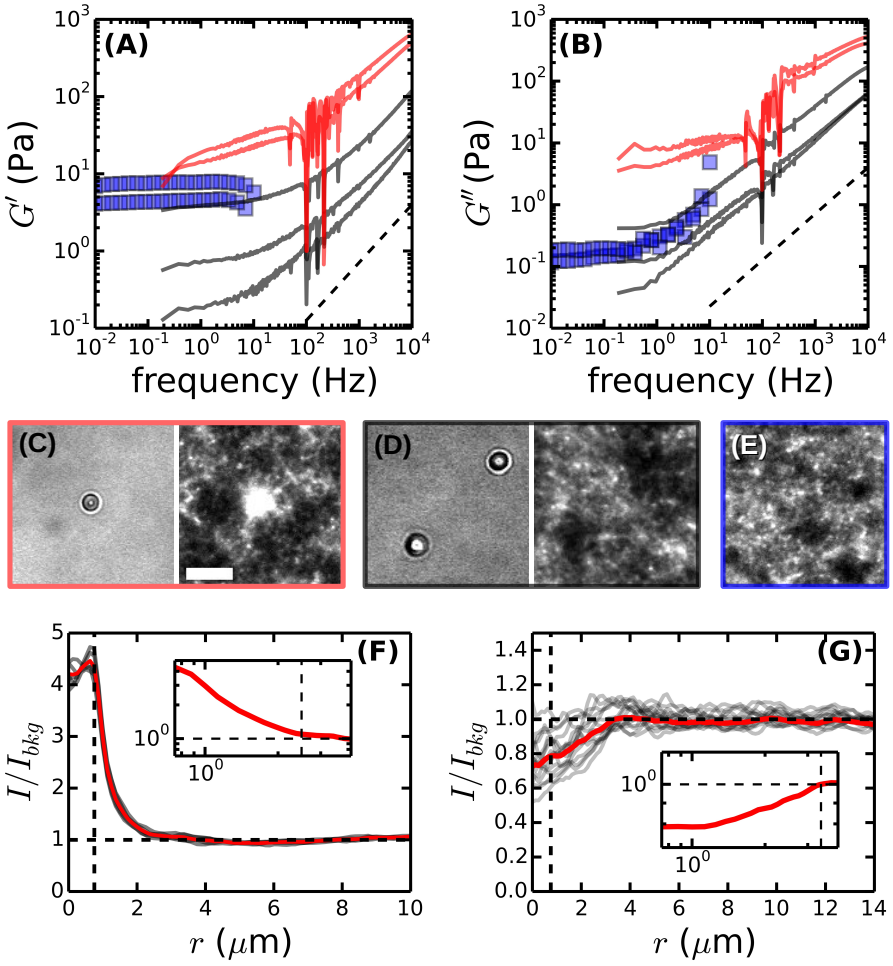
(A)
(B)
G' (Pa)
G'' (Pa)
frequency (Hz)
frequency (Hz)
(C)
(D)
(E)
(F)
(G)
I/I_{bkg}
I/I_{bkg}
r (μm)
r (μm)

fibrin density (Fig. 5.6D). This qualitative observation is consistent with prior measurements on networks of filamentous actin, where passivated beads were shown to settle in weaker parts of the gel and to be surrounded by a thin layer depleted of actin [518,522]. We quantified the density distribution of fibrin around the uncoated and coated beads by determining the average radial fluorescence intensity distribution, as shown in Fig. 5.6F and G respectively. The intensity was normalized by the background level, I_{bkg}, which was defined as the average intensity of the fibrin network in-between beads (>5 μm away from bead centers). Noncoated beads show a 4 times increase in normalized intensity close to their surface, which decays back to 1 over a range of about 2.5 μm (best seen in inset Fig. 5.6F). Thus, a fibrin layer of about 1.8 μm thick is accumulated on the bead surface. In contrast, in the coated beads case there is a depleted region, where the normalized intensity is about 80% near the bead's surface and decays to 100% over a range of 3.4 μm (best seen in inset Fig. 5.6G). The depletion layer is thus about 2.6 μm.

The observation of a depletion layer surrounding inert beads immersed in a semiflexible polymer network is in line with publications on microrheology of actin gels [521,522], where coated beads also showed a lower modulus [517–519] and higher frequency dependence [521,537] compared to sticky beads. It was proposed that the thickness of this depletion layer can be estimated by considering a bead in a composite system, as sketched in Fig. 5.7A [546]. Close to the bead, we assume a local incompressible medium with a local modulus G_{loc}, while further away from the bead we recover the bulk modulus G_{bulk}. In this simplified system, the modulus measured by the bead, G_{bead}, is [521,546,567]:

$$G_{bead}(\omega) = \frac{2G_{bulk}(\omega)[\kappa'' - 2\beta^5\kappa']}{4\beta^6\kappa'^2 - 9\beta^5\kappa\kappa' + 10\beta^3\kappa\kappa' - 9\beta\kappa' - 15\beta\kappa' + 2\kappa\kappa''} \qquad (5.14)$$

Here $\beta = a/b < 1$, $\kappa = G_{bulk}/G_{loc}$, $\kappa' = \kappa - 1$ and $\kappa'' = 3 + 2\kappa$. We used eq. 5.14 to estimate the depletion layer for coated beads, taking for G^*_{bulk} the modulus reported by macrorheology, and assuming that the local modulus G_{loc} in the depletion layer corresponds to the modulus expected for a fine fibrin network with a concentration equal to 90% of the bulk concentration, c_p. Based on the macrorheology data shown in Fig. 5.8B and D, we assume that $G'_{loc} = (0.9)^{11/5}G'_{bulk}$ and $G''_{loc} = (0.9)^{0.85}G''_{bulk}$, since $G' \sim c_p^{11/5}$ and $G'' \sim c_p^{0.85}$. Taking the moduli reported by microrheology at ~5 Hz as G_{bead} (see Fig. 5.8), we get values of ~3 μm for the depletion layer (see Fig. 5.7B). This estimation is in agreement with the estimation based on the fibrin fluorescence intensity profiles measured by confocal microscopy (Fig. 5.6G), though there is a large uncertainty. This can be attributed, in part, to sample-to-sample variations in G_{bulk}. In the future this variability may be circumvented by estimating G_{bulk} by two particle microrheology on the same sample [521,567].

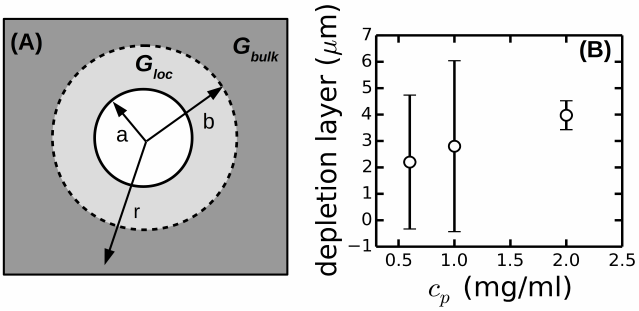

Figure 5.7: (A) Schematic of the local depletion layer around the Pluronic coated beads. The bead radius is a, the depletion layer is $b - a$ and r denotes the radial coordinate. In the depletion layer, we assume a local modulus G_{loc}, which is lower than the bulk modulus, while further away we recover the bulk modulus G_{bulk}. The bead measures a superposition of G_{loc} and G_{bulk} according to eq. 5.14. (B) The estimated depletion layer thickness for beads in fine fibrin networks as a function of fibrin concentration, estimated assuming the fibrin density in the depletion layer is 90% of the bulk density.

However, we note that there is also quite a large variation in the intensity distribution of the fibrin network near the beads, as evident in Fig. 5.6G. To get a more accurate estimate of the depletion layer of surrounding each bead, one should ideally correlate the micro-environment as visualized by confocal microscopy directly with the measured mechanical properties reported for that bead. Also, we note that we made the simplifying assumption that the local reduction in fibrin concentration near the bead surface is 10% for all fibrin concentrations. In any case, the estimated depletion layer is in the same order of magnitude as values reported for actin networks [521,568,569], which ranged between 0.8 and 2.5 μm, depending on bead size and average filament length. The depletion layer in fine fibrin networks is larger than reported for beads in semidilute solutions of λ-DNA ($\leq$0.6 μm) [567], which is reasonable, since DNA has a shorter persistence length ($\sim$50 nm [570,571]) than fine fibrin fibers ($\sim$150 nm, see Chapter 2).

The confocal microscopy results indicate that noncoated beads are confined by a layer of fibrin with an enhanced fibrin density compared to the bulk, whereas coated beads tend to probe regions that on average have a (locally) reduced fibrin concentration. Consequently, the elastic and viscous moduli measured by sticky beads are about a factor 5 to 6 higher compared to those reported by the inert beads (see also Fig. 5.8). This observation is again

consistent with prior measurements on actin networks, where the modulus reported by beads was correlated with the number of actin molecules bound on the particle surface [518]. Since the fibrin networks are formed in the presence of the beads, it is conceivable that the beads alter the network structure by acting as nucleation or crosslinking points. It would be interesting to test this hypothesis by imaging the networks with scanning electron microscopy and also by following fibrin polymerization with confocal microscopy in time in the presence of beads.

Both the coated and uncoated beads show systematic differences in G' and G'' compared to the macrorheology control measurements (blue squares in Fig. 5.6A and B). The noncoated beads overestimate both G' and G'', while the coated beads show a very good agreement with macrorheology for G'', but systematically report a lower G'. To facilitate a direct comparison, we compared the values of for G' and G'' obtained by macrorheology at a frequency of 5 Hz with corresponding values determined by microrheology in Fig. 5.8. For the optical tweezer data, we averaged over 5 data points in the frequency domain between 5 and 6 Hz to limit the contribution of noise.

In the case where the beads stick to the fibrin network, G' is about 3 times higher than the macrorheology control (Fig. 5.8B), though showing a similar concentration dependence. Both micro- and macrorheology reveal a power law increase of G' with concentration, with an exponent of 2.3 ± 0.3 in case of microrheology and 2.0 ± 0.1 in case of macrorheology. Both exponents are close to the expected exponent of $11/5$ indicated by the red dotted line (see Chapter 2 section 2.4.2). This correspondence is consistent with prior measurements on actin [516], where noncoated (sticky) beads also showed a similar concentration dependence of G' as the bulk modulus measured in that case by two particle microrheology. Interestingly, beads that stick to biopolymer networks that have a more open mesh work, like collagen, were found to *underestimate* the network stiffness [538], though still reporting the same concentration dependence as macrorheology experiments. Thus, the magnitude of the moduli reported by the probe beads is determined by a combination of surface chemistry and the ratio between bead size and mesh size. The concentration dependence of G'' reported by the noncoated beads was steeper for microrheology (with a power law exponent of 2.0 ± 0.2) compared to macrorheology (which showed an exponent of 0.85 ± 0.09), as shown in Fig. 5.8D.

In case where the beads are inert, G' is about 3 time lower than the macrorheology control (Fig. 5.8A), but showing a similar concentration dependence that is consistent with the expected $11/5$ power law (red dotted line). The values for G'' for the inert beads nicely agree with the corresponding values reported by macrorheology (Fig. 5.8C). Previous measurements in actin also showed an underestimation of the elastic modulus when beads were inert [517, 519]. This underestimation ranged between a factor 2 up to 10

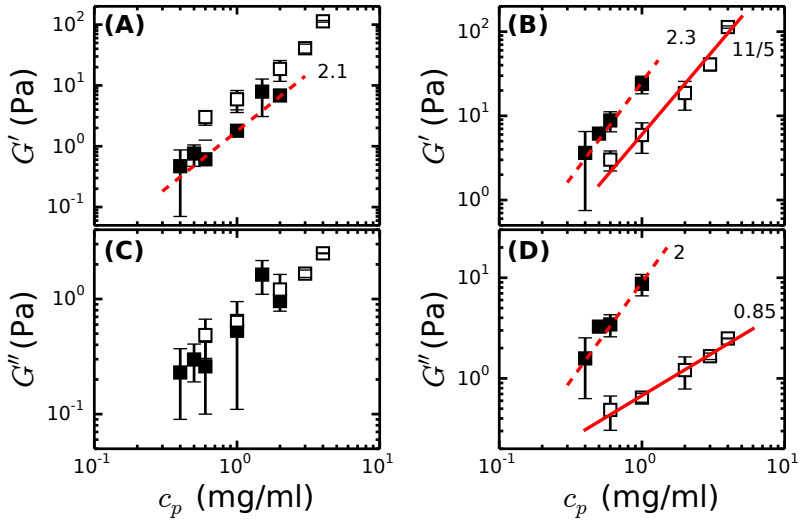

Figure 5.8: The effect of bead surface properties on the measured mechanical properties of fine fibrin gels measured with optical tweezer microrheology (closed squares, averaged between 5-6 Hz) and compared with macrorheology (open squares, at 5 Hz). (A) and (C) are for beads covalently coated with Pluronic, while (B) and (D) are for noncoated beads. The dotted red lines are power law fits with exponent 2.1±1.8, 2.3±0.3 and 2.0±0.2 for (A), (B) and (D) respectively. The solid line in (B) denotes the expected 11/5 power law dependence based on the thermal bundle model (see Chapter 2), while the solid line in (D) is a power law fit with exponent 0.85±0.09.

depending on actin concentration.

It has been suggested by Van Citters *et. al.* [572] that the stiffness dependence on frequency reported by one particle microrheology will not report the bulk modulus dependence if the beads are not (somewhat) linked to the network. Indeed, prior measurements in actin show that the typical $G'' \sim \omega^{3/4}$ dependence [427,521,573] (expected for semiflexible polymer networks [574–576]) is replaced for inert beads by a steeper, $\sim \omega^1$ dependence [521]. To check this behavior also occurs in the fibrin networks, we determined the dependence of G'' on frequency in the high frequency regime ($f > 500$ Hz), where G'' is expected to be sensitive to the bending and contour length fluctuations of the fibrin filaments.

As shown in Fig. 5.9, we find that G'' reported by inert beads (solid black

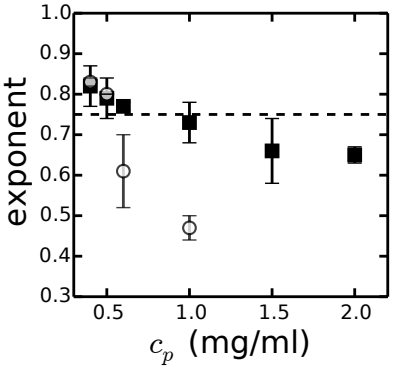

Figure 5.9: The power law exponent of G'' at high frequency (>500 Hz) for coated (black squares) and noncoated, i.e. sticky (gray open circles) beads in fine fibrin networks of varying concentration. The expected 3/4 dependence for semiflexible polymers is depicted in a dashed black line.

squares) follows a power law in frequency with an exponent that systematically decreases with fibrin concentration, from 0.85 at 0.4 mg/ml, down to 0.65 for 2 mg/ml. Sticky (noncoated) beads report an even steeper dependence of the frequency exponent of G'' on fibrin concentration, decreasing from about 0.85 at 0.4 mg/ml to about 0.5 at 1 mg/ml. For the same fibrin concentration, the power law exponent is higher in the case of inert beads (black symbols), and closer to the expected 3/4 dependence for semiflexible polymers than the sticky beads. It could be that the fibrin networks in the bead surrounding is prestressed at increasing fibrinogen concentration, especially when formed in the presence of sticky beads, thus lowering the frequency dependence of G'' [372, 575, 576]. In the limit of a highly prestressed network, we expect a 1/2 power law dependence of G'' on frequency [372], which corresponds to the smallest exponent we observe for sticky beads in 1 mg/ml fibrin networks.

To summarize, we find that both sticky and inert beads reproduce the correct concentration dependence of G', which is expected on the basis of macrorheology measurements and theoretical models of semiflexible polymer gels. The two bead types, however, report different values for the low frequency modulus compared to the macrorheology control measurements: Sticky beads overestimate both G' and G'', while inert beads underestimate G', but not G''. Overall, beads passivated with Pluronic capture the macroscopic modulus more faithfully than uncoated beads, in terms of magnitude as well as frequency dependence. The small discrepancy between the magnitude of G'

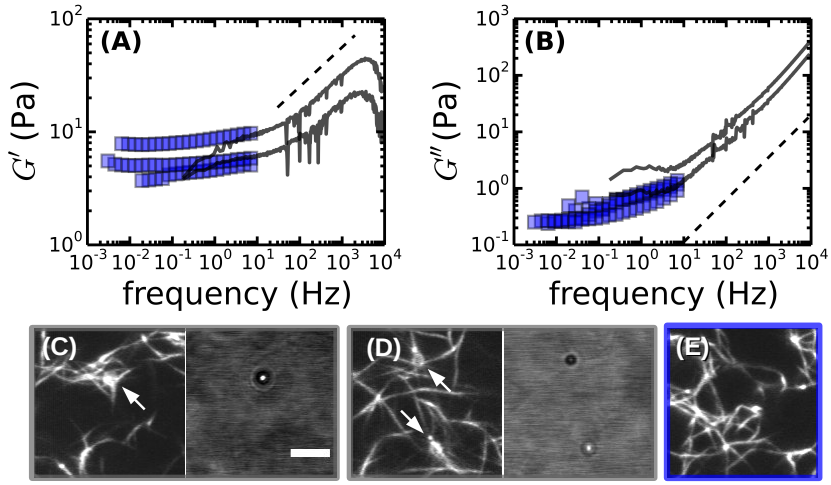

Figure 5.10: The elastic G' (A) and viscous G'' (B) moduli for 0.5 mg/ml coarse fibrin networks measured using macrorheology (blue squares) or optical tweezer microrheology (solid gray lines). For optical tweezer measurements, 1.5 μm polystyrene beads were used. The dashed black line in (B) denotes a power law with exponent 3/4, as expected for semiflexible polymer networks [574–576], while the dashed line in (A) denotes a power law with exponent 0.35. (C-E) Microscopy images of 1 mg/ml coarse fibrin gels with (C,D) and without (control, E) beads. The networks contain 1.5 μm polystyrene (C) or 1 μm silica (D) beads. For (C) and (D), the left images correspond to summations of confocal images recorded over a 5 μm depth, while right images are single plane differential interference contrast (DIC) images showing the beads. White arrows denote the positions of the beads. Scale bar denotes 5 μm for all images.

and G'' reported by micro- and macrorheology can be quantitatively explained by accounting for the presence of a thin layer depleted of fibrin surrounding the beads.

5.3.3 Sticky Beads Inside Fibrin Networks with Large Pores

We have shown that the surface properties of the probe beads inside fibrin networks with small pore size ($\xi \sim$200 nm) play an important role in the reported mechanical properties. In order to extend the microrheology measurements to fibrin networks prepared under more physiologically relevant conditions, we also investigated coarse fibrin networks. These networks form an open mesh

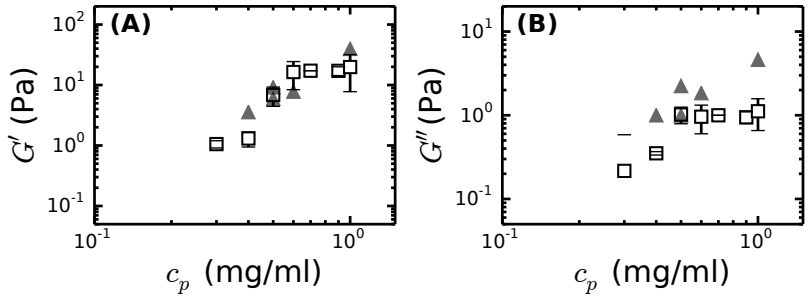

Figure 5.11: Comparison of the elastic (A) and viscous (B) shear moduli of coarse fibrin gels at a frequency of ∼5 Hz, as measured by macro- (open black squares) and microrheology (closed gray triangles).

work of ∼100 nm diameter fibers with an average pore size on the order of 10 μm at 0.5 mg/ml when prepared at 37°C and at pH 7.4 [66] (see also Fig. 2.1 in Chapter 2). Since the 1.5 μm passivated polystyrene beads will diffuse freely within the water-filled pores and will not be confined in these networks [523], we selected uncoated 1.5 μm polystyrene beads that adhered to the fibrin network, as shown in Fig. 5.10C.

G' as measured with macrorheology shows virtually no dependence on frequency for low frequencies, with an extremely weak power law dependence with exponent of 0.04, as shown in Fig. 5.10A (blue squares). In the microrheology measurements, G' also becomes nearly flat at low frequencies (<50 Hz, solid gray curves), while it increases at higher frequencies with a power law dependence on frequency with exponent 0.35 (dashed line in panel (A)). The viscous modulus, G'', shows a slow increase with frequency in the macrorheology case and overlaps with data from microrheology. At high frequencies (>50 Hz), G'' determined by microrheology follows a power law with exponent close to the expected 3/4 dependence for semiflexible polymers (dashed line in (B)) [574–576].

We note that untreated silica beads also spontaneously adhere to the fibrin network and can therefore also be used for microrheology, as shown in Fig. 5.10D.

Interestingly, we see from Fig. 5.10 that both the macroscopic G' and G'' are well approximated by microrheology measurements in the overlapping frequency range. To better quantify this, we again compare G' and G'' from micro- and macrorheology at a fixed frequency range (5−6 Hz) in Fig. 5.11. Even though statistics is low (with a total of 5 samples, see also Table 5.2 in SI), G' falls in the same range as reported by macrorheology, while G'' is a

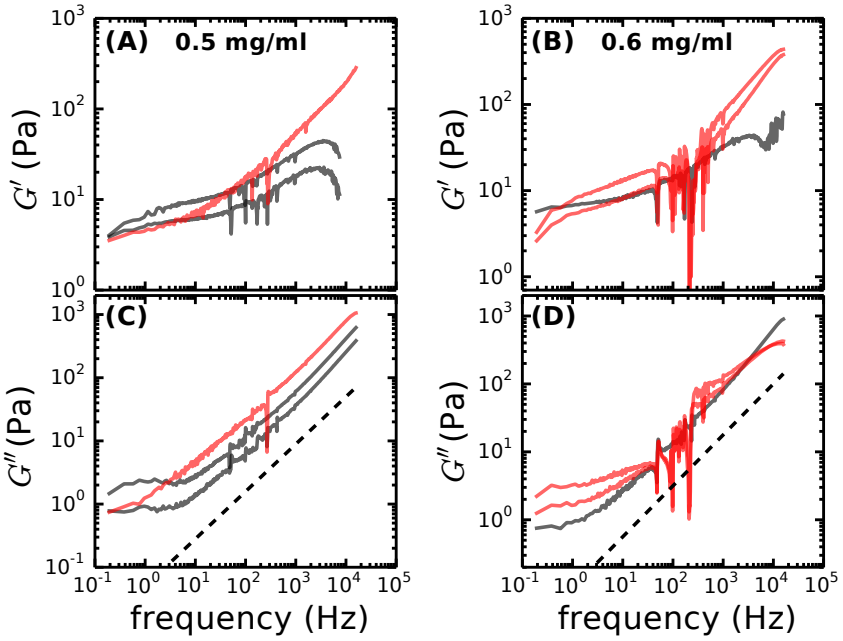

Figure 5.12: The low strain viscoelastic moduli of fine (red) and coarse (gray) fibrin networks, as measured by optical tweezer microrheology using sticky (noncoated) 1.5 μm polystyrene beads. Panels (A) and (C) depict G' and G'' for 0.5 mg/ml fibrin gels respectively, while (B) and (D) are for 0.6 mg/ml gels. The dashed line in (C) and (D) depict a 3/4 dependence predicted for semiflexible polymer networks [574–576].

bit overestimated. These results are surprising, since coarse fibrin networks are far from the incompressible continuum assumption that our data analysis assumes. Interestingly, a recent video particle tracking microrheology study of collagen networks, which have a similar pore size as fibrin, also reported agreement between micro- and macrorheometry [577], although another study reported an underestimation of the moduli by microrheology [538].

Next we compared the frequency dependence of the moduli for the two fibrin network limits of small mesh size ('fine clots', $\xi \sim$200 nm) and large mesh size ('coarse clots', $\xi \sim$10 μm), as shown in Fig. 5.12. The storage modulus, G', shows a steeper frequency dependence for the coarse clots compared to the fine clots, both at 0.5 mg/ml (Fig. 5.12A) and 0.6 mg/ml (Fig. 5.12B). Since the frequency range probed is intermediate between the low-frequency (plateau)

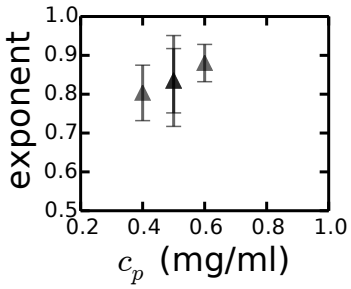

Figure 5.13: The high frequency (>500 Hz) power law dependence of G'' for coarse fibrin networks. Data points denote the average per individual prepared sample and error bars denote standard deviations of that particular sample.

regime and the high-frequency ($\omega^{3/4}$ scaling) regime, it is difficult to interpret this finding. At 0.5 mg/ml fibrin, the viscous modulus, G'', shows an identical frequency dependence for fine and coarse clots (Fig. 5.12C). In both cases, G'' scales approximately as a power law with exponent 3/4 (see dashed line). This scaling is consistent with the model of coarse clots that we presented in Chapter 2, where we showed that coarse fibrin fibers can be modeled as wormlike bundles of semiflexible protofibrils. At 0.6 mg/ml (Fig. 5.12D), G'' for the coarse clots again shows 3/4 power law scaling with frequency, but G'' for the fine clots shows a somewhat weaker frequency dependence. As discussed in section 5.3.2, we suspect that the deviation from a 3/4 scaling in case of fine clots is caused by the strong accumulation of fibrin on the noncoated bead's surface. Confocal imaging suggests that in case of the coarse clots, the sticky beads have a lesser tendency to recruit fibrin (compare Fig. 5.8C and Fig. 5.10C), which may explain why we observe 3/4 scaling for G''. A summary of the scaling exponents observed for the high-frequency scaling of G'' in coarse fibrin clots at three different concentrations is shown in Fig. 5.13. In each case, the exponents are close to, but somewhat larger, than the theoretical value of 3/4 expected in case of semiflexible polymers.

5.3.4 Calculation of Fibrin Fiber Persistence Length

So far, we have extensively investigated the effects of bead surface properties (section 5.3.2) and network pore size (section 5.3.3) on the apparent micromechanical properties of fibrin networks at low frequencies. In this section, we focus on the high frequency response. In particular, we will estimate a fundamental length scale of fibrin fibers, namely the persistence length l_p,

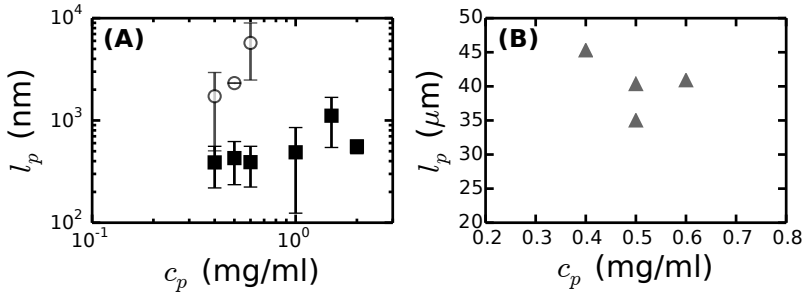

Figure 5.14: The persistence length for fine (A) and coarse (B) fibrin clots calculated from the high-frequency G measured by microrheology according to eq. 5.15, utilizing sticky (noncoated) polystyrene beads (gray circles and triangles in (A) and (B) respectively) or inert probe beads (coated with Pluronic, filled squares in (A)).

from the high frequency response of G''.

At high frequencies, the complex shear modulus is governed by the stress relaxation via bending fluctuations of the individual fibers within the network. For semiflexible polymers, we expect [574, 578]:

$$G^*(\omega) = \frac{1}{15}\rho\kappa l_p(-i2\gamma_L/\kappa)^{3/4}\omega^{3/4} - i\mu\omega \tag{5.15}$$

where $\kappa = l_p k_B T$ is the bending modulus of the fibers, $\gamma_L = 4\pi\mu/\ln(0.6\lambda/d)$ is the lateral drag coefficient and μ is the viscosity of the solvent (here $\mu = 0.001$ Pa·s); λ denotes the maximum relaxation length of the fiber, for which we take the mesh size. We estimate for the fiber diameter $d = 20$ nm for fine fibrin networks (as determined by electron microscopy, see Fig. 2.12 in Chapter 2) and $d = 120$ nm for coarse fibrin networks (as determined by turbidimetry [66, 297]). We base the l_p calculations only on microrheology measurements where G'' exhibits a power law dependence on frequency with an exponent close to 7.5±1.

The apparent persistence length for fine fibrin networks determined from microrheology data obtained with passivated beads does not change with fibrin concentration, as shown in Fig. 5.14A (closed black squares) and is on average 547±330 nm. It should be noted, however, that eq. 5.15 is valid for $\omega > \omega_1$, where $\omega_1 = \frac{\kappa}{L drag}\left(\frac{\pi}{L}\right)^4$ [578]. This limit holds for the most dilute networks ($<$ 1 mg/ml), where we estimate ω_1 to be about 300 Hz. However, for the more concentrated gels, ω_1 is expected to shift up to the kHz range ($\sim$ 5000 Hz for the 2 mg/ml case). If we only consider measurements within the range of the

assumption $\omega > \omega_1$, then the average l_p is lowered to 406±150 nm. In Chapter 2, we have shown that we can consider fine fibrin clots as networks of loose semiflexible bundles of on average two protofibrils. The persistence length of one protofibril is thus related to l_p by: $l_p^F = l_p^{pf} N_p$ where $N_p = 2$ [320] (see section 2.3 eq. 2.4). The apparent persistence length of one protofibril is thus 203±75 nm. This value is in line with previous reports based on light scattering (120−200 nm for human fibrinogen [353, 355]) and electron and atomic force microscopy (500 nm for fish fibrinogen [39, 354]). However, the apparent value obtained by microrheology is larger than the value that we derived for the same fine fibrin clots from macrorheology experiments (75 nm, see section 2.5 in Chapter 2). It should be noted that both estimates of the persistence length, from micro- and macrorheology, are model-dependent, and represent average numbers from measurements that ensemble averages over many fibers. Moreover, as discussed in section 5.3.2, the microrheology data are influenced by the presence of a depletion layer surrounding the beads.

The apparent persistence length for fine fibrin networks determined from microrheology data obtained with sticky beads is consistently larger than the values determined with passivated beads (Fig. 5.14A open gray circles). Furthermore, the persistence length shows an apparent increase with increasing fibrin concentration. A likely explanation for these two observations is the evident accumulation of fibrin on the bead surface (Fig. 5.6C and F), giving rise to a significant increase in local fibrin concentration. Due to this accumulation of fibrin, it seems unlikely that the sticky beads in fine fibrin networks reflect single fiber motion, even at high frequencies.

The apparent persistence length for coarse fibrin networks determined from microrheology data obtained with sticky beads is around 40 μm, as shown in Fig. 5.14B (triangles), taking into account that G'' is overestimated by a factor ∼3 [579]. This number for the persistence length is in the same range as reported in a previous study that also used optical tweezer microrheology (∼60 μm [66]). However, it is significantly smaller than values reported for similar coarse clot systems using video microrheology (∼40 cm [533]). In Chapter 2 we have shown that coarse fibrin fibers can be considered as tight bundles of N_p semiflexible protofibrils, for which the persistence length can be calculated as $l_p^F = l_p^{pf} N_p^2$. Given a bundle size N_p of about 65 measured for similar clots in earlier work [66], this relation suggests a persistence length of only ∼10 nm for an individual protofibril. This number seems unphysically low, given that it even lower than the persistence length reported for DNA (∼50 nm [570, 571]), which can be considered as a flexible polymer. A complementary way to interpret the rigidity measurement is to estimate the Young's modulus, assuming that the fibers can be modeled as a uniform rigid rod with radius 60 nm and persistence length 40 μm. This assumption gives a Young's modulus of 16 kPa, which is much lower than earlier reports for ligated fibrin fibers based

on micromanipulation (∼MPa [281–283]). Together with the observation that the coarse clot case is far from the continuum assumption made for the optical tweezer microrheology data analysis, we consider it likely that the microrheology measurements underestimate the persistence length for coarse clots.

5.4 Discussion

Both the elastic and viscous properties of the ECM have shown to play a vital role in the regulation of cell behavior [3, 4, 72, 499, 500]. Here we focus on the local mechanical properties of the ECM, which have been shown to influence cell migration [310] as well as cell division [501]. In particular, we aimed to measure both the low and high frequency response to get simultaneously information about the network and single fiber level.

We developed an optical tweezer setup in-house to investigate the local mechanical properties of biopolymer networks by passive one particle microrheology. The setup was validated using water and a 50% water-glycerol mixture, where we showed that the viscous properties were accurately captured above frequencies of 5 Hz. We showed that the mechanics of PAA hydrogels, which have a significant elastic component, can also be accurately measured with our setup.

In fibrin networks, non-passivated probe beads tend to accumulate fibrin on their surface, as shown in Fig. 5.6C for fine networks and in Fig. 5.10C and D for coarse networks. This observation is consistent with previous studies of microrheology in fibrin, showing that fibrin sticks to beads without any special treatment [523, 533]. Fibrin is thus very sticky, which is important for its purpose *in vivo* to serve as a plug during wound healing.

We showed that fibrin adhesion to the uncoated 1.5 μm polystyrene beads led to an overestimation of the elastic and viscous shear moduli (G' and G'') compared to the bulk rheological properties. In contrast, beads covalently coated with Pluronic (rendering them inert) reported smaller values for G' and on average comparable values for G'' as macrorheology. These observations are consistent with measurements of actin networks, where the shear modulus reported by (partially) inert beads was lower compared to the modulus reported by beads that stuck to the network [517–519]. Confocal microscopy revealed a depletion layer with a reduced fibrin density around the inert beads with a thickness of ∼2.6 μm. This depletion layer can account for the reported micromechanical modulus, using a model that assumes that the beads sense a superposition of the bulk modulus and a lower local modulus, as shown in eq. 5.14 and in Fig. 5.7A. However, the estimate from eq. 5.14 can be further optimized by measuring the bulk modulus for each sample individually, to remove sample-to-sample variation, for instance with two particle microrheology [521,567]. Also, the reduction in fibrin concentration in the depletion layer might not be the same for all fibrin concentrations, as assumed in Fig. 5.7B.

This assumption needs to be checked by confocal microscopy in the future.

We measured the thermal persistence length of the fibrin fibers from the high frequency response of G'' using eq. 5.15. This equation assumes that the high frequency response reports bending fluctuations of single filaments [574, 578]. We showed that the estimates for l_p are reasonable for inert beads, where the apparent persistence length of the fine fibrin fibers was 432 nm. Given that we can consider the fine fibrin fibers as bundles of 2 protofibrils (see Chapter 2), we estimate the persistence length of protofibrils to be 215 nm, which is in line with previous reports based on light scattering (120-200 nm for human fibrinogen [353, 355]) and electron and atomic force microscopy (500 nm for fish fibrinogen [39, 354]). However, for sticky beads, the apparent persistence length increased with increasing fibrin concentration. It is likely that in this case the beads do not reflect single fiber relaxation, given the accumulation of a dense fibrin layer around the beads and the localization of beads at fiber junctions.

Surprisingly, the modulus reported by sticky beads in coarse fibrin networks reported similar values for G' as reported by macrorheology, but overestimated G'' by about a factor 3 (see Fig. 5.11), though statistics for these measurements is low (total of 5 samples). Coarse fibrin networks have a pore size that is larger than the size of the beads (as shown in Fig. 5.10E). Thus, the situation is far from the elastic continuum assumption that we make to calculate G' and G'' from the thermal position fluctuations of the beads. Rather, the beads likely sample the fluctuations of the fiber that they are adhered to. The apparent persistence length of the fibers according to the microrheology measurements is on the order of 40μm, which is in line with previous optical tweezer microrheology results [66], but lower than video microrheology results ($\sim$40 cm [533]). The reported persistence length for coarse clots is likely an underestimate, given that it corresponds to an apparent Young's modulus of only 16 kPa assuming a cylindrical and uniform fiber, which is much lower than earlier reports for ligated fibrin fibers based on micromanipulation ($\sim$MPa [281–283]). In future it will be interesting to use our microrheology setup to perform similar active micromanipulation of the fibers by using the AOD's to move the trap. Alternatively, single fibrin fibers may be bent or stretched by AFM [281].

5.5 Conclusion

The local mechanical properties of the ECM were shown to be important parameters for cell behavior [310, 501]. In this chapter, we aimed to measure the elastic and viscous micromechanical properties of fibrin networks over a wide range of frequencies, to obtain simultaneous information about stress relaxation at both the network and single fiber level.

For this purpose, we developed an optical tweezer based setup to perform

high bandwidth microrheology on fibrous protein networks. The setup was validated using viscous fluids of known viscosity and PAA gels. Next, we showed that we can measure the low and high frequency response of fibrin networks. For this we used two different bead types: One set of beads that stick to the network (plain polystyrene beads) and one set of passivated beads that are inert (polystyrene beads covalently coated with Pluronic). Both bead types report the macroscopic concentration dependence for G', but the sticky beads overestimate G', while the inert beads underestimate G'. We can explain this over- and under estimation in terms of a change in local fibrin concentration at the bead's surface. At high frequencies for the inert beads, we observe clear evidence of entropic elasticity for G'', with a characteristic $\omega^{3/4}$ frequency dependence, which strongly supports the entropic network model presented in Chapter 2. We estimated the persistence length of protofibrils to be 203 $\pm$ 75 nm, which is in line with previous publications.

We can now apply optical tweezer microrheology to probe the influence of cells on their local tissue environment, for instance during cell-mediated stiffening [67,524,525,528]. The method could also be combined with intracellular microrheology to probe the response of the cell [539].

5.6 Acknowledgments

I would like to thank Dominique Thies-Weesie from the University of Utrecht with help for growing the 1.2 μm silica beads and size quantification; Bjorn Stuhrmann, Marko Kamp, Marco Seynen and Erik Claij for help with building and testing the optical tweezer setup, and the design and mechanical workshop at AMOLF for realizing the different mechanical components. I also like to thank Fred MacKintosh for helpful discussions and Andre Scholich for performing some of the experiments. This work is part of the research programme of the Foundation for Fundamental Research on Matter (FOM), which is financially supported by the Netherlands Organisation for Scientific Research (NWO). This work is further supported by NanoNextNL, a micro- and nanotechnology programme of the Dutch Government and 130 partners.

5.7 Supporting Information

Supplementary Figures and Tables

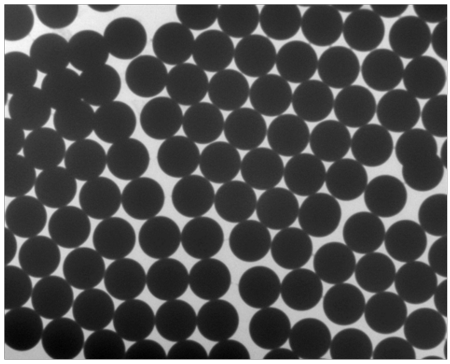

Figure 5.15: TEM image of the home-made silica microspheres. The bead diameter was 1.2 μm with 3.4% polydispersity. The imaging and analysis of the bead polydispersity is done by Dominique Thies-Weesie at the University Utrecht.

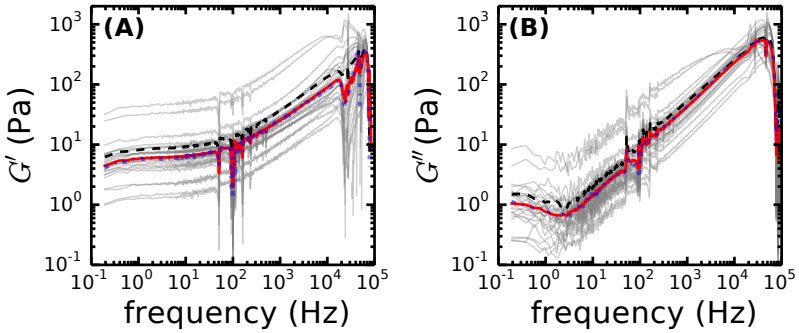

Figure 5.16: Optical tweezer microrheology in 2 mg/ml fibrin fibrin with coated polystyrene beads (n=15). (A) and (B) denote the elastic and viscous modulus G' and G'' respectively of individual bead measurements in gray. The dashed black lines denote the average over these measurements, while the red line is the geometric average. The average is sensitive to outliers with high modulus. The dotted blue line denotes the median, which is often close to the geometric average.

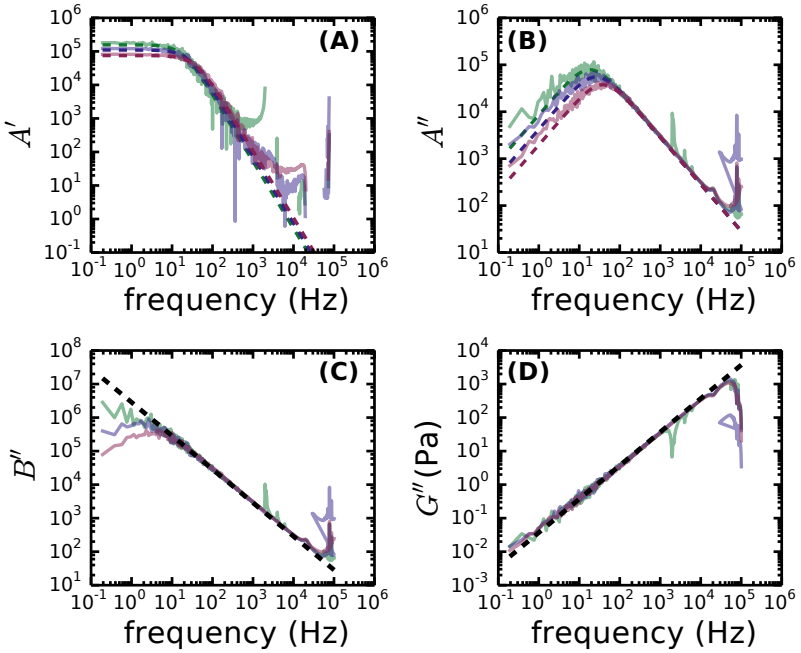

Figure 5.17: The response function of a 50% glycerol mixture with water. (A) The real part of the apparent response function. (B) The imaginary part of the apparent response function. The trap stiffness was varied from 6.39 $\cdot 10^{-6}$ (green), to 9.08$\cdot 10^{-5}$ (blue) and 1.33$\cdot 10^{-5}$ N/m (purple) by modifying the laser power.

z (μm)	n
10	11
15	11
20	5
25	2

Table 5.1: Statistics for the optical tweezer microrheology data with 1.2 μm silica beads in water, at varying sample depths.

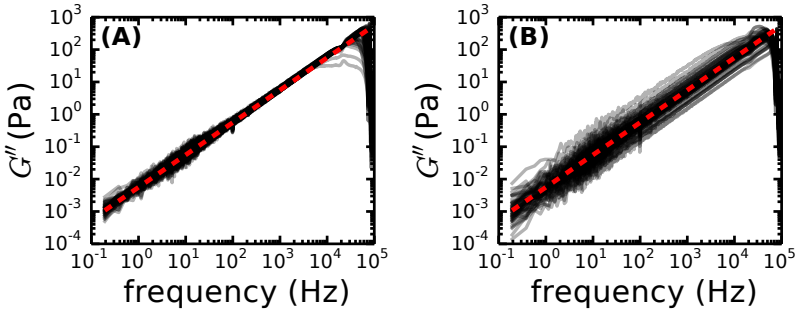

Figure 5.18: The viscous modulus of water a measured by 1.5 μm PS beads covalently coated with Pluronic. (A) The viscous modulus of water can be reproduced when taking the individual trap stiffness for each bead. (B) The measured viscous modulus gives a large spread in G'' when assuming one trapstiffness for all beads. In total 28 beads were measured. Red dotted lines are the theoretical predictions for water. Gray lines are the measurements.

c_p (mg/ml)	f , coated	f , noncoated	c , noncoated
0.4	2	3	1
0.5	3	1	2
0.6	2	2	1
1	2	2	1
1.5	3	-	-
2	3	-	-

Table 5.2: Statistics for the optical tweezer microrheology measurements in coarse ('c') and fine ('f') fibrin networks with 1.5 μm polystyrene beads, with a covalent Pluronic coating ('coated') or no coating ('noncoated'). The typical sample size was more than 10 beads per sample, except for the 0.4 mg/ml for the coated bead case. In this case, the typical sample size was 5 beads per sample. In the case of 1 mg/ml coarse clots, the beads were 1 μm silica instead of 1.5 μm polystyrene.

6. Architecture and Normal Stress Govern Collagen Network Mechanics

Collagen is the most abundant protein in the human body and its architecture is tailored to serve tissue-specific purposes. Recent computational studies predicted that collagen can be considered as an athermal polymer network, whose elastic properties are governed by the network geometry since the average coordination number is less than the critical connectivity needed for mechanical stability. It was proposed that the linear modulus is governed by fiber bending, while strain-stiffening occurs as a consequence of a transition to a stretching-dominated regime. In the limit of vanishing bending rigidity, this strain-controlled bend-to-stretch transition is a mechanical phase transition with a critical point. Here we show experimentally that reconstituted collagen networks show signatures of critical behavior in vitro. By systematically performing non-linear rheology measurements on collagen networks whose architecture is controlled through temperature and concentration, we show that the mechanical properties are controlled by the network architecture, consistent with the theoretical predictions. To characterize the network architecture, we combine confocal and electron microscopy with turbidity measurements. We show that the networks are stabilized by bending elasticity in the linear regime, and by a shear-induced normal stress in the nonlinear regime. In summary, we now have a quantitative theoretical framework to predict the mechanical properties of collagen networks as a function of architecture, which provides a powerful tool to design collagen networks with certain mechanical properties.

K.A. Jansen, A. J. Licup, A. Sharma, R. Rens, M. Sheinman, F.C. MacKintosh, G.H. Koenderink

6.1 Introduction

Collagen is the most important structural molecule in the mammalian body, providing mechanical strength to all connective tissues and making up about 30% of the total protein content [301, 580, 581]. The collagen family consists of 29 genetically distinct members, but the predominant member in most tissues is type I [582–584]. Collagen Type I monomers consist of a long (300 nm) and thin (1.5 nm) triple helix of three polypeptides, flanked by two non-helical telopeptides [584]. Cells secrete collagen molecules with protective propeptides, which are removed in the extracellular space by enzymatic cleavage [584]. This process triggers spontaneous formation of fibrils. The diameter and higher-order organization of the fibrils are controlled in a tissue-specific manner by supporting ECM components, such as minor fibrillar collagens like collagen V and small leucine rich proteoglycans [127]. The monomers within a collagen fibril form a densely interconnected rope-like structure with a precise axial stagger of 67 nm, referred to as the "D-period" [316, 580]. Reinforcement by permanent intermolecular crosslinks provides the fibrils with a high tensile strength [585–587].

The mechanical properties of collagen are intricately linked to tissue function: Abnormalities in collagen organization and mechanics due to mutations in genes encoding for collagen can cause severe diseases characterized by weak and fragile tissues [581, 588]. Excessive crosslinking of collagen creates abnormally stiff tissues, which also hamper normal tissue function [3, 587]. The mechanics of collagen is thus essential for normal tissue functioning.

In addition to being responsible for the structural integrity of tissues, collagen also contributes to the functional architecture of tissues by providing anchoring support to cells in the tissue. The structural as well as the mechanical properties of the collagen matrix are known to impact cell behavior. Matrix mechanics has been shown to influence cell spreading, migration, proliferation and cell fate decisions [41, 43–47] (see Chapter 1.3 section 1.3.1 for a more extensive overview). Also, abnormal changes in the collagen matrix *in vivo* have been shown to trigger tumor cell behavior and tumor-like behavior of non-tumorigenic cells [3–5].

In view of the crucial role of collagen mechanics in cell and tissue biology and function, there is a long history of research on its mechanical properties, dating back to at least 1904 [589]. But despite this long history, the physical basis of collagen mechanics remains poorly understood. Mechanical measurements on whole tissues have demonstrated intriguing material properties, including a pronounced strain-stiffening response to an applied mechanical load [301, 590–593]. This strain-stiffening response is thought to protect tissues from mechanical damage and to tailor their biological functions [594]. However, the hierarchical architecture and complex molecular composition of collagenous tissues have made it difficult to reveal the origin of this remarkable mechanical

behavior. *In situ* X-ray scattering studies on mechanically stretched tendons suggest that all hierarchical levels contribute to the macroscopic response [301]. Due to this complexity, increasing focus is on reconstituted model systems of purified collagen. Here one can control the molecular and structural complexity, facilitating a quantitative comparison of experiments with predictions from theoretical or computational models.

In vitro collagen gels are made by self-assembly, where one typically starts with an acidic aqueous solution of collagen monomers. When the pH is raised to physiological values, an homogeneous network of collagen fibrils is formed, which show a comparable 67 nm axial repeat in electron microscopy images and X-ray scattering as seen *in vivo* [303]. The diameter of the fibrils and the structure of the networks they form can be tuned by changing the solvent pH [307–310], salt conditions [308] or the polymerization temperature [90,305,306]. Using these control parameters, the network structure can be varied from a highly porous mesh work with a pore size of a few tenths of microns and thick fibers (order microns) to networks with thin collagen fibers ($\sim$100 nm) and small pore sizes on the order of 1 μm or less [90, 306, 307, 309, 310]. A number of experimental studies have shown that these purified collagen network stiffen when strained by shearing or stretching, in a similar manner as whole tissues [251, 253, 272, 279].

In the past few years, there has been tremendous progress in computational modeling of collagen mechanics. Due to collagen's complex hierarchical structure, it is difficult to model it while taking into account all hierarchical levels. The most detailed models, based on atomistic simulations, are limited to single collagen molecules and microfibrils [595–597] and require coarse-graining approaches to reach to the fibril level [588]. In contrast, models aimed to describe collagen at the network level usually treat the fibrils as simple polymers and ignore the internal molecular packing structure [279, 598, 599]. These models treat the fibrils either as (athermal) elastic beams, or as semiflexible polymers, depending on their bending rigidity κ. The bending rigidity is characterized by the polymer's thermal persistence length, $l_p = \kappa/k_BT$, which quantifies the distance over which angular correlations along the polymer decorrelate as a consequence of thermal fluctuations, where k_B is Boltzmann's constant and T is temperature [278]. There is strong evidence that collagen fibrils can be considered as essentially athermal, meaning that their persistence length is much larger than their contour length. The Young's modulus of a collagen fibril in the hydrated state is on the order of 0.1 GPa [251, 284–288]. With a typical diameter of 200 nm, this implies that l_p is on the order of a meter, while the typical fibril length is of the order of microns.

Computer simulations of athermal fibrous networks have shown that the elasticity of such networks critically depends on its local connectivity [279]. ECM networks such as interstitial collagen have an average connectivity be-

tween 3 and 4 [279,390,600], which implies a sub-marginal state: This connectivity is lower than the Maxwell criterion and the network is expected to be unstable. This criterion states that for a network of springs to be stable, the average connectivity (in 3D) should be at least 6 [601]. Collagen networks are nevertheless stable, due to the large bending rigidity of the filaments [279,280]. Several computational studies suggest that mechanically shearing an athermal fibrous networks will cause strain-stiffening by inducing a transition from a soft, bending-dominated regime at low strain to a stiffer, elastic stretching-dominated regime at high strain [277, 425]. However, a recent computational model of Licup and co-workers [279] suggests that collagen networks already start to stiffen well before the stretch-dominated regime sets in. It was proposed that normal stress builds up, which stabilizes the sub-marginal network as it strain-stiffens.

The recent computational model of Licup *et. al.* [279] makes several predictions for the rheology of collagen networks that can be tested experimentally. First, it predicts that the network stiffness in the small strain regime scales a power law in collagen concentration with an exponent of 2, assuming that the network architecture is constant. Experimentally, a wide range of exponents has been observed, often between 2 and 3 [253,272,395,602,603], though sometimes smaller exponents have been reported (between 1 and 2) [92,251,527,603]. The reason behind this variability is not well understood. Second, the model predicts that the initial strain-stiffening response is governed by normal stress buildup. In particular, the elasticity K' is predicted to increase with normal stress σ_N as: $K' \simeq G_0 + \chi|\sigma_N|$, where G_0 is the linear (low strain) modulus and χ the susceptibility. This prediction has not been tested yet in experiments. Third, the model predicts that collagen networks undergo a mechanical transition from a floppy, bend-dominated regime to a rigid, stretch-dominated regime, which is governed by an underlying critical point determined by the network architecture [604,605]. Also this prediction has not been tested yet in experiments.

In this chapter, we measure the rheological properties of reconstituted collagen networks as a function of network architecture. We vary the architecture by tuning collagen concentration over a wide range, and by varying the polymerization temperature. The fibril diameter, the network connectivity and pore size are characterized by light scattering, scanning electron microscopy and confocal reflectance microscopy. To interpret our findings, we compare the experimental results with predictions of the computational model of Licup *et. al.* [279], which treats the collagen networks as a disordered lattice of rigid (athermal) beams. We show that the rheology of collagen networks is in quantitative agreement with the model. First, the concentration dependence of the linear elastic modulus of the networks is consistent with the model by taking into account a subtle change in network architecture with changing collagen

concentration. Second, we are able to confirm the theoretical prediction that the initial strain-stiffening of collagen networks is governed by normal stress. Third, we are able to confirm the theoretical prediction that collagen networks exhibit critical behavior. We show that the entire strain-dependence of the elastic modulus can be described by an analytical expression based on a mechanical equation of state. Our findings provide a firm basis to tie together the different hierarchical levels of collagen structure into a unifying model. Moreover, our work provides a quantitative approach to relate collagen network structure to mechanics, which is essential to understand the influence of collagen network architecture on migration, spreading, and proliferation of healthy and tumorigenic cells [90, 310, 606].

6.2 Materials and Methods

6.2.1 Sample Preparation

To reconstitute collagen networks, we polymerized purified rattail collagen type I (high concentration rat tail collagen type I in 0.02 N acetic acid, BD Biosciences, Breda) under solution conditions compatible with *in vitro* cell culture. Cell culture medium (DMEM10x without phenol red), antibiotics (penicillin/streptomycin, pen/strep), sodium bicarbonate (7.5% sterile solution) and 4-(2-hydroxyethyl)-1-piperazineethanesulfonic acid (HEPES) were all obtained from Sigma and stored at 4°C, except for pen/strep, which was stored in aliquots at -20°C. Fetal bovine serum (FBS) was obtained from Gibco and stored in aliquots at -20°C. DMEM10x, antibiotics and FBS solutions were divided in aliquots in a sterile environment, which were used only for 1 day after thawing.

Collagen samples were obtained by mixing all components on ice. First, collagen solution was pipetted into a precooled 2 ml Eppendorf tube on ice. Due to the high viscosity of the collagen stock, we weighted the tube to determine the exact amount of collagen. The sample was then centrifuged at 4 °C to transport the collagen to the bottom of the tube. Next, the solution ingredients were added in the following sequence: DMEM10x, HEPES, antibiotics, FBS, sodium bicarbonate and sterile milliQ water. The final gel conditions are: DMEM 1x, 1% FBS, 50 mM HEPES, 1.5 mg/ml sodium bicarbonate and 0.1% pen/strep. The pH was adjusted to 7.3−7.4, by the addition of NaOH, with the help of a pH meter (Hanna Instruments, Germany) equipped with a micro-electrode. The time between setting the pH with NaOH and transporting the sample to a sample holder was always kept close to 10 min, in order to minimize potential variations due to premature polymerization on ice [607]. Bubbles were removed by centrifuging the samples before polymerization for 10 seconds at room temperature for samples of 2−4 mg/ml collagen, and for a few minutes at 4 °C for samples of $\geq$ 5 mg/ml.

The following sample holders were used: a cuvette (turbidity), a flow cham-

ber (light microscopy), a 5 ml Eppendorf tube (SEM) or a pre-cooled glass-bottom petridish (Mattek, light microscopy). In all cases, the sample holders were pre-cooled (on ice) and the collagen gels were polymerized in a humid atmosphere to prevent solvent evaporation. After the addition of sample, the sample holders were rapidly warmed to the desired temperature. The polymerization temperature was varied between $22-37\,^{\circ}$C to achieve different network architectures. The collagen concentration was varied between 0.2 mg/ml up to 6 mg/ml. For rheology, samples were polymerized *in situ* using a cone-plate geometry that was preheated to the desired temperature.

6.2.2 Rheology

Rheology tests were performed with a stress-controlled rheometer (Physica MCR 501, Anton Paar, Graz, Austria). We used a stainless steel cone-plate geometry with 40 mm diameter and $1\,^{\circ}$ cone angle, which was prewarmed to the desired temperature ($22-37\,^{\circ}$C) in the presence of water in the wells. We note that we preformed preliminary tests using a 40 mm cone-plate with $2\,^{\circ}$ cone angle of either polycarbonate or stainless steel, which gave similar results to the stiffening curves shown in this chapter (*not shown*). Neutralized cold collagen solution was added to the plate and the cone was lowered immediately. The sample was trimmed while the angular position of the cone was kept constant, a solvent trap was added to further prevent evaporation. The time between adding the sample, trimming the sample and adding the solvent trap was typically around 20 seconds. The collagen solution was not probed for 6 hours, to allow for unperturbed polymerization. Since collagen gels are known to polymerize rather slowly at low temperatures [304, 306, 608], we checked the polymerization time at 22°C (see turbidity section 6.2.3). For all collagen concentrations studied at 22°C, the network was fully formed after ∼200 minutes polymerization (Fig. 6.20 in SI).

Once the network was formed, we probed its linear viscoelastic moduli by performing oscillatory shear tests with a small (0.5%) strain amplitude and frequencies ranging from 10 to 0.05 Hz. Next, a prestress protocol was performed to determine the nonlinear mechanical properties. First, a creep test was performed by applying a constant shear stress, σ, for 30 seconds and measuring the resulting strain γ. The creep rate was defined as the slope of a linear fit over the last 20 seconds of the time-dependent γ. Then a small oscillatory stress, $\delta\sigma$, was superposed on top of the constant prestress, where $\delta\sigma$ was 10 times lower than σ, while monitoring the differential oscillatory strain, $\delta\gamma$. The frequency was set to 0.5 Hz. In total, 6 oscillations were performed per prestress value and the differential modulus $K' = \delta\sigma/\delta\gamma$ was determined as an average over the last 5 oscillations. The onset of strain-stiffening was defined as the local minimum of K'/σ (see Fig. 6.21 in the SI). The critical strain, γ_c, was obtained as the inflection point of the $\log(K')$ versus $\log(\gamma)$ curves in the strain-stiffening regime. Per shear stress decade, 11 prestress data points were

collected, equally spaced on a logarithmic scale. To characterize the nonlinear regime, we determined the maximal power law slope of the strain-stiffening curve (K' versus σ_0) from its first derivative. This slope is referred to as the stiffening exponent β.

For plotting the mean quantities, the average values $\pm$ the standard deviation are shown for three independently prepared samples, unless stated otherwise. In case of fits, the errors in the best-fit values are expressed as the standard error, unless stated otherwise.

6.2.3 Turbidity

Turbidity measurements were performed using a Cary300 UV-Vis spectrophotometer (Agilent Technologies, Amstelveen, Netherlands). Samples were polymerized inside disposable plastic cuvettes (UV-Cuvette micro, Plastibrand, Germany) for at least 6 hours and up to overnight at temperatures in the range of $22 - 37\,^{\circ}\mathrm{C}$. The blank for background correction was prepared in the same way as the collagen samples, but with collagen replaced by a corresponding volume of 0.02 N acetic acid. The optical density I_0 of both sample and blank were measured over a range of wavelengths λ of 350−900 nm. The turbidity τ follows from I_0 as:

$$\tau = \frac{I_0 \ln(10)}{L} \tag{6.1}$$

where L is the optical path length. If one assumes that there is no light absorbed, and that the collagen fibers can be modeled as randomly oriented, monodisperse rod-like particles with small radius and long length compared to the wavelength used, then the wavelength dependence of the turbidity can be rescaled to reveal the the mass-length ratio μ and the radius a of the fibers [295, 296]:

$$\tau\lambda^5 = A\mu(\lambda^2 - Ba^2) \tag{6.2}$$

A and B are constants and respectively equal to $(88/15)c_p\pi^3 n_s(dn/dc_p)^2/N_A$ and $(184/154)\ \pi^2 n_s^2$. Here c_p is the collagen concentration in g/ml, n_s is the solvent refractive index (which is 1.33), dn/dc_p is the specific refractive index increment (which is 0.186 cm^3/g for collagen [609]) and N_A is Avogadro's constant. The turbidity data were replotted according to eq. 6.2 and a linear fit was made between 890 nm and 650 nm. This regime was chosen to limit the chance of signal saturation of the spectrometer at low wavelengths and noise at high wavelengths. The slope and intercept were used to calculate the mass-length ratio, μ, and the radius, a. The number of monomers N_p in a cross-section was determined from μ based on the known quarter-staggered molecular packing arrangement of collagen molecules within the fibrils [302]:

$$N_p = \frac{4.6D \cdot \mu}{M} \tag{6.3}$$

where D is the axial periodicity (67.2 nm) and M is the molecular mass of a collagen monomer (290 kDa [610]).

In some cases, the solution turbidity was measured as a function of time during polymerization, in order to quantify the kinetics of fibril nucleation and growth. Here, the Cary300 instrument was preheated to the desired temperature using a Cary temperature controller (Agilent Technologies) and measurements were started directly after sample preparation. Every two minutes during polymerization, a wavelength scan was taken from 900 nm to 350 nm. We observed a typical sigmoidal dependence of the turbidity on polymerization time, with a lag phase in which the turbidity remains close to zero, a growth phase in which the turbidity rises, and a plateau phase in which the turbidity saturates to a constant level (see Fig. 6.20 in SI). The lag time, t_τ, that characterizes the duration of the lag phase, was determined from turbidity measurements at $\lambda = 600$ nm by normalizing I_0 by the maximum scattered intensity reached in the plateau phase, I_{max}, and fitting the time dependence to the following functional form [611]:

$$I_0/I_{max} = a - b \cdot ln(t + c) \tag{6.4}$$

where t is time, and a,b and c are fitting constants. I_0/I_{max} was fitted over the range 0.25 to 0.75. The fit was extrapolated to the time point where $I_0/I_{max} = 0$, which was defined as the lag time t_τ.

6.2.4 Imaging

Confocal reflectance images of collagen gels polymerized at different collagen concentrations and different polymerization temperatures were collected using an inverted Eclipse Ti microscope (Nikon) with an 488 Ar laser (Melles Griot, Albuquerque, NM) for illumination. We obtained z-stacks by recording confocal slices over a total distance of 20 μm for the 100x (N.A. 1.49) objective with 0.2 μm z-spacing and 40 μm with step size 0.2 μm for the 40x (N.A. 1.30) objective, starting at least 10 μm away from the coverslip surface. For display purposes, the confocal stacks were summed to give an impression of the 3D network structure and the typical mesh size.

For scanning electron microscopy (SEM), 4 mg/ml collagen gels (50-100 μl) were polymerized overnight inside 5 ml Eppendorf tubes at different temperatures ($22 - 37\,^\circ$C, water bath) in humid conditions. Humid conditions were obtained by adding a small wet tissue inside the Eppendorf tubes. Samples were prepared for SEM using a protocol adapted from the group of John Weisel [600, 612]. After polymerization, samples were washed three times with sodium cacodylate buffer (50 mM cacodylate, 150 mM NaCl, pH 7.4) for 30−60

min each, at their polymerization temperature. Samples were fixed with 2.5% glutaraldehyde in the same buffer for at least 2 hours. Next, samples were washed three times with sodium cacodylate buffer (room temperature) and dehydrated with an increasing percentage of ethanol in milliQ water (30%, 50%, 70%, 80%, 90%, 95%, and finally 3 times 100%v/v). After complete dehydration, 50% hexamethyldisilazane (HMDS) in ethanol was added (twice), left for 30 min, and then removed by pipetting under the hood and afterwards replaced by 100% HMDS. The HMDS was removed after 30 min and the samples were left to dry overnight in the hood. The next day, the dry samples were transported to a stub with carbon tape and sputter coated using a K575X sputter coater (Quorum Technologies, Gouda, The Netherlands). A layer of 15.4 nm of Au/Pd was sputtered using a current of 80 mA. The SEM samples were visualized using a STEM setup (Verios 460, FEI Company, Eindhoven, the Netherlands) using 50 pA, 5 kV and 4 mm working distance, in immersion mode. The average connectivity of the networks was determined by subdividing the SEM images taken at a magnification of 20,000 up to 50,000 magnification (depending on polymerization temperature) into 5x5 squares. In each other square, we manually determined the number of fibers at each junction in focus. We analyzed more than 100 junctions per sample. In total, we analyzed 4 samples for $T = 26°C$, 3 for $T = 30°C$, 2 for $T = 34°C$ and 3 for $T = 37°C$. Due to the inhomogeneous nature of the $T = 22°C$ collagen gels, we could not determine an average connectivity for these samples.

6.3 Computational Model of Collagen Network Rheology

Since previous studies have convincingly shown that collagen I networks behave as networks of rigid rods for which thermal fluctuations are negligible [279], we compare our data to computational models that treat the fibers as athermal, elastic beams. Simulations have shown that the elastic properties of an athermal fibrous network are primarily determined by the local connectivity [280]. Collagen networks are inherently sub-marginal: the number of fibers meeting at each junction is less than the isostatic limit needed to ensure a stable network if the filaments were springs. As shown by Maxwell [601], spring networks require a local coordination number, or connectivity, z of at least $z_{crit} = 2d$, where d is the dimensionality, for mechanical stability. At the isostatic (or marginal) point, corresponding to $z = 6$ for a 3D network, the number of degrees of freedom is just balanced by the number of constraints so that the system is marginally stable to small deformations. Upon increasing the connectivity from $z < z_{crit}$ through the z_{crit} point, spring networks undergo a mechanical phase transition from a floppy to a rigid phase. Collagen networks have a typical average connectivity between 3 (local branching) and 4 (binary crosslinking), placing them well below both 2D and 3D isostatic

thresholds [279, 390]. Such sub-isostatic networks can, nevertheless, exhibit a finite elasticity as a result of other mechanical constraints. One such constraint is that the fibers have a finite bending rigidity [280, 613, 614]. An externally applied strain can also stabilize fiber as well as spring networks [615].

Two classes of models have been used to analyze the mechanical properties of submarginal fibrous networks. The first class of models, referred to as Mikado models, represents the fiber network as a collection of rigid rods that are randomly deposited in a 2D box until the desired connectivity is obtained [613, 614]. The second class of models represents the network by a 2D or 3D disordered lattice-based structure [280]. Lattice models have the advantage that they are more computationally tractable, making it easier to simulate large networks. Moreover, lattice models are versatile, since the network architecture and connectivity can be easily tuned. In this chapter, we will therefore compare our experimental data primarily to a computational model of (mostly 2D) disordered lattices. The model makes several quantitative predictions that we will test in this chapter via experiments on collagen networks.

We will focus specifically on a recent computational model that was developed by Albert Licup, Abhinav Sharma, Robbie Rens, Misha Sheinman and Fred MacKintosh at the VU University (Amsterdam, the Netherlands). All simulation data shown in this chapter (Fig. 6.2, Fig. 6.12, Fig. 6.14A, Fig. 6.18B, Fig. 6.19B and Table 6.1) were kindly provided by these authors. The details of the model are described in detail elsewhere [279,604,605], but will be briefly summarized here. Networks are modeled as 2D triangular lattices. The size of the networks is WxW, where W is the linear dimension while the lattice spacing is l_c and $W = 50l_c$. In 2D, local 4-fold connectivity is enforced by randomly selecting two of the three fibers at each vertex and forming a binary cross-link between them. The remaining fiber crosses this vertex as a phantom that does not interact with the other two fibers. After this phantomization procedure, the average connectivity is further reduced to a value characteristic of collagen networks (3.2) by randomly removing segments (random bond dilution) with a probability $q = 1 - p$, where p is the probability of an existing bond. This procedure reduces the average fiber length to $L = l_c/q$. Thus, the networks are, by construction, sub-isostatic and floppy in the absence of bending interactions.

Each filament is assigned a stretching modulus, μ_s, and a bending modulus, κ. These two parameters define a dimensionless measure of the relative bend-stretch stiffness:

$$\widetilde{\kappa} = \kappa/\mu_s l_c^2 \tag{6.5}$$

For fibers behaving as homogeneous elastic beams with a cylindrical cross-section, $\mu_s = \pi a^2 E$, and $\kappa = \frac{1}{4}\pi a^4 E$ [616]. Here, a is the fibril radius and E is the Young's modulus. Thus, $\widetilde{\kappa} = \frac{1}{4}\frac{a^2}{l_c^2}$. Note that $\widetilde{\kappa}$ is determined purely by

the geometrical parameters a and l_c, while being independent of the material properties of the fibers.

The networks are subjected to a simple shear strain γ and allowed to relax by minimization of the total elastic energy per unit volume, H, which is calculated using a discrete form of the extensible wormlike chain Hamiltonian [279,605]. The stress follows from the minimum energy H as: $\sigma = dH/d\gamma$, while the differential elastic shear modulus follows as: $K = d^2H/d\gamma^2$. Stress and stiffness are measured in units of μ/l_c^{d-1}, where $d = 2$ is the dimensionality.

6.4 Results

6.4.1 Impact of Polymerization Conditions on Collagen Elastic Properties

The aim of this chapter is to relate the rheological properties of reconstituted collagen networks to the underlying network architecture. Since collagen networks are formed by a self-assembly process driven by noncovalent interactions, the final architecture is highly sensitive to the solution conditions (i.e. pH and ionic conditions), protein concentration and temperature. Here, we employ two control parameters to tune network architecture and mechanics: We vary the collagen concentration over a wide range (0.2−6 mg/ml at 37°C, 1−5 mg/ml at 22°C and 2−5 mg/ml at 30°C), and we vary the polymerization temperature (from 22°C to 37°C) for a fixed collagen concentration of 4 mg/ml. The pH and ionic conditions are chosen to be close to physiological conditions, which are compatible with cell culture (DMEM at pH 7.3−7.4, supplemented with 50 mM HEPES, 1.5 mg/ml sodium bicarbonate and 1% serum).

We first tested the dependence of collagen network elasticity on protein concentration by performing shear rheology measurements on networks polymerized at 37°C. We employed a differential prestress protocol, whereby a constant prestress, σ, was applied to the sample with a small superposed oscillatory stress to probe the differential stiffness at this prestress value, $K'(\sigma)$. For each sample, the prestress was increased until network rupture occurred. As shown in Fig. 6.1A, the networks strongly strain-stiffen at all concentrations, until rupturing at strains of around 50% (see also Fig. 6.33 in supplementary information (SI)). At low strains, the networks exhibit a linear response characterized by a constant elastic shear modulus, denoted as G_0. However, after an onset strain γ_0 (red symbols in Fig 6.1A), the stiffness markedly increases with increasing strain. In a few cases, the nonlinear regime showed an initial strain-softening, which was followed by strain-stiffening, similar to earlier findings with large amplitude oscillatory shear [252]. An example of this behavior is shown in Fig. 6.22 in the SI. We speculate that these samples may be prestressed, causing them to have a higher low-strain modulus than the majority of samples, which do not show this initial stiffening. Since this

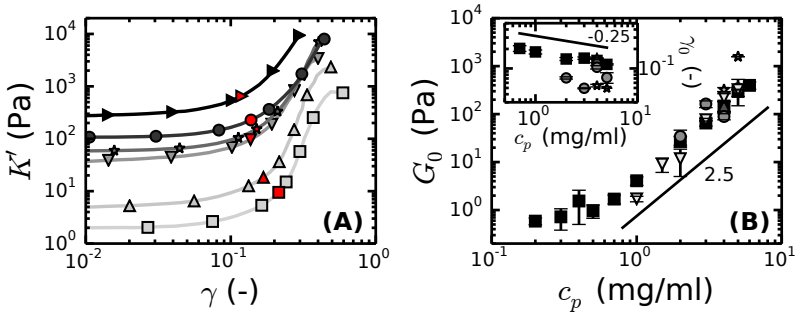

Figure 6.1: Rheological properties of collagen networks measured for different polymerization conditions. (A) Strain-dependence of the differential elastic modulus measured at 37°C and at collagen concentrations of 0.7 (squares), 1 (triangles up), 2 (triangles down), 3 (stars), 4 (circles) and 5 mg/ml (triangles right), in increasing shades of gray. The onset of strain-stiffening is depicted by red symbols. (B) Concentration dependence of the low strain (linear) plateau modulus, G_0, at 22°C (triangles down), 26°C (stars) , 30°C (circles), 34°C (triangle up) and 37°C (squares) in increasing shades of gray. (*inset*) Concentration dependence of the strain at the onset of strain-stiffening, γ_0, as depicted by the red points in panel (A), at 26°C (stars) , 30°C (circles), 34°C (triangle up) and 37°C (squares) in increasing shades of gray. The 37°C data show a weak power law dependence on c_p with an exponent of -0.25±0.03. In (A), the symbols show every 5th data point, while the lines show the full dataset.

non-monotonic nonlinear behavior was rare, these samples were excluded from further analysis.

With increasing collagen concentration, the stiffening curves do not change in overall shape, although they shift up to larger moduli. This is in qualitative agreement with simulations results for fibrous networks with an average coordination of 3.2 shown in Fig. 6.2A. Here, the unit-less bending rigidity $\widetilde{\kappa}$ is progressively increased from 10^{-6} to 10^{-3}, which is equivalent to an increase in concentration by a factor 1000, since $\widetilde{\kappa}$ is proportional to collagen concentration. Similar to our experimental findings, increasing $\widetilde{\kappa}$ causes the linear modulus to shift up, while the stiffening curves do not change their overall shape.

Experimentally, we find that the linear elastic modulus G_0 of the networks increases with collagen concentration, c_p, as a power law with an exponent of 2.5 (with fitting error ± 0.05) as shown in Fig. 6.1B (black squares). However,

this dependence only holds for c_p>0.6 mg/ml. Below 0.6 mg/ml, G_0 shows a weaker, close to linear, dependence on concentration. Coincidently, at these low concentrations, the collagen networks are very inhomogeneous, as seen in confocal reflectance microscopy (CRM) (Fig. 6.23 in SI). At the lowest concentration tested, namely 0.2 mg/ml, the network is barely connected, and the fibrils exhibit thermal fluctuations indicative of the presence of dangling ends (*not shown*). It should be noted that at an even lower concentration of 0.1 mg/ml, there is no network formed at all. Based on these observations, we hypothesize that the fibrils in networks formed at low concentrations (<0.6 mg/ml) are not fully connected and thus do not all contribute to the network stiffness. We therefore exclude these low density gels from the analysis in the rest of this chapter. At concentrations above 0.6 mg/ml, the network do look homogeneous and well connected. The power law exponent 2.5 is comparable to values found in several earlier studies [253, 272, 395, 602, 603]. But we note that this exponent is higher than the exponent of 2 predicted by simulations of fibrous networks when we assume that the geometry of the network in terms of z (or L/l_c) is concentration independent. Thus, the concentration dependence of G_0 we observe suggests that the architecture of the networks changes with collagen concentration.

Next, we tested the dependence of collagen network rheology on network architecture by varying the polymerization temperature, prompted by earlier work demonstrating a strong effect of this parameter on network structure [305, 602]. When we polymerize collagen networks at 22°C, we found a somewhat stronger increase of G_0 with collagen concentration (power law exponent 3±0.1) than at 37°C, as shown in Fig 6.1B (light gray triangles down). This is consistent with earlier findings [602]. The magnitude of the modulus depends non-monotonically on polymerization temperature (see Fig. 6.1B and 6.29A in SI): at a fixed collagen concentration, the stiffest gel is formed at 26°C, while the softest one is formed at 30°C. This finding is consistent with an earlier study that demonstrated a stiffness maximum at 27°C [602]. However, another study reported a monotonic increase of stiffness with increasing polymerization temperature between 4°C and 37°C [305]. These contradictory findings may be due to slight differences in salt conditions, which are known to affect the stiffness dependence on temperature [617]. It should be anyhow noted that the variations in network stiffness with temperature are rather small, remaining within a factor 3 (Fig. 6.29A in SI).

The onset strain for strain-stiffening, γ_0 (red symbols in Fig. 6.1A) decreases with collagen concentration according to a weak power law with an exponent of -0.25 for networks formed at 37°C (Fig. 6.1B *inset*, black squares). This dependence is consistent with earlier reports [251, 272], where the onset strain also decreased with increasing collagen concentration and varied by about a factor 2 within a similar concentration range. Note, however, that

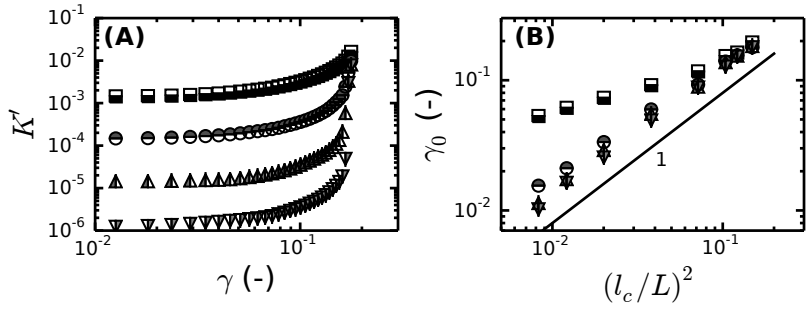

Figure 6.2: Simulation results for a 2D network showing the elastic properties of athermal fibrous networks subjected to a shear deformation. (A) Strain-stiffening response of networks with varying dimensionless bending rigidity, $\widetilde{\kappa}$, and $L/l_c = 3.1$ ($z = 3.2$). (B) The onset strain for strain-stiffening depends significantly on network architecture l_c/L. For both (A) and (B), bending rigidities were varied between 10^{-6} (triangles down), 10^{-5} (triangles up), 10^{-4} (circles), and 10^{-3} (squares).

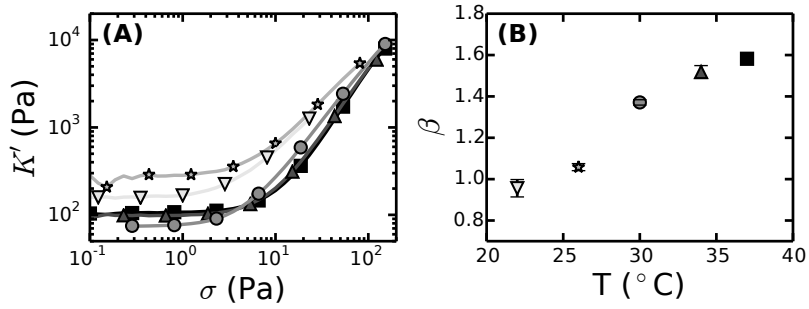

Figure 6.3: Stress-stiffening behavior of collagen networks measured for different polymerization conditions. (A) The differential elastic modulus K' for 22°C (triangles down), 26°C (stars), 30°C (circles), 34° (triangle up) and 37°C (squares) in increasing shades of gray. (B) The stiffening exponent, β, defined as the maximum power law slope of the stress-stiffening curves in the nonlinear regime, measured for 4 mg/ml collagen as a function of polymerization temperature.

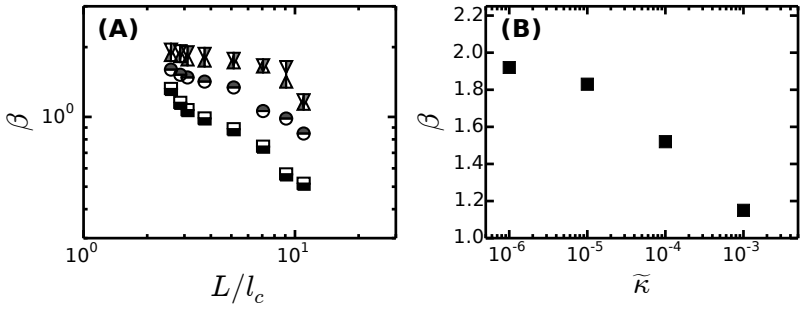

Figure 6.4: Stiffening exponent β for 2D simulated networks shows a dependence on network architecture and the dimensionless bending rigidity $\widetilde{\kappa}$. (A) The stiffening exponent β with varying dimensionless bending rigidity, $\widetilde{\kappa}$. Bending rigidities were varied between 10^{-6} (triangles down), 10^{-5} (triangles up), 10^{-4} (circles), and 10^{-3} (squares). (B) The stiffening exponent β for strain-stiffening depends on $\widetilde{\kappa}$ at fixed network architecture. Data are shown for $L/l_c = 3.1$.

different definitions for the onset strain were used, so the absolute magnitudes of γ_0 cannot be directly compared. Consistent with the concentration dependence of G_0, the weak concentration dependence of γ_0 also suggests that the network geometry changes somewhat with collagen concentration. Simulations for fibrous networks assuming a concentration-independent architecture namely predict that γ_0 should be insensitive to concentration, as shown in Fig. 6.2B (where $\widetilde{\kappa} \sim c_p$ and l_c/L is a measure for architecture). Instead, γ_0 is sensitive to changing architecture. When the architecture of the triangular lattices is varied by changing l_c/L, the simulations reveal a linear increase of γ_0 with increasing $(l_c/L)^2$ for small $\widetilde{\kappa}$ (10^{-6} up to 10^{-4}) and a somewhat weaker increase of γ_0 with increasing $(l_c/L)^2$ for larger $\widetilde{\kappa}$ (10^{-3}), as shown in Fig. 6.2B. We note that we expect $\widetilde{\kappa} \sim 10^{-4}$ to be relevant for collagen networks [279] (see also Fig. 6.15 in section 6.4.4). As summarized in Table 6.1 in the SI, γ_0 is predicted to go down when the average connectivity goes up from 3 to 3.87, i.e. with a decreasing degree of branching. Thus, the concentration dependence of γ_0 we observe experimentally indicates that the collagen networks polymerized at 37°C become less branched with increasing collagen concentration. When we vary the polymerization temperature between 22 and 37°C at a fixed collagen concentration of 4 mg/ml, we find a slight decrease of γ_0 with decreasing temperature (see Fig. 6.29B in SI). In view of the simulation results for networks with varying l_c/L (or equivalently, z), this finding suggests that networks formed at lower temperatures are less branched.

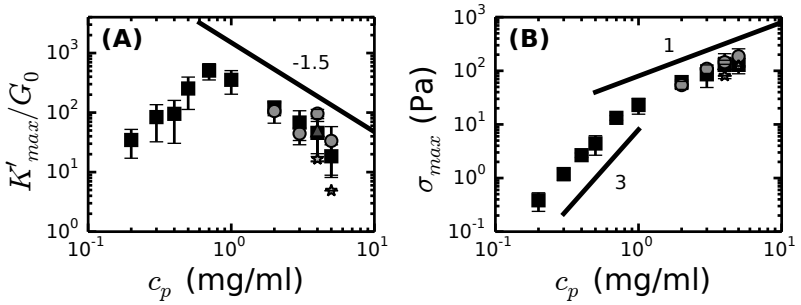

Figure 6.5: The maximum extent of strain-stiffening, K_{max}/G_0, until apparent network rupture, together with the corresponding maximum shear stress, σ_{max}, for collagen gels polymerized at 26°C (stars), 30°C (circles), 34° (triangle up) and 37°C (squares) in increasing shades of gray. (A) Concentration dependence of the maximal extent of stiffening, showing a maximum at 0.7 mg/ml and a power law decrease with concentration above 0.7 mg/ml with a slope close to -1.5 (as indicated by the solid line). (B) The maximum stress increases as c_p^3 below 0.7 mg/ml and linearly in c_p above 0.7 mg/ml. The corresponding maximum strain levels are depicted in Fig. 6.33 in SI.

The extent of strain-stiffening that is reached before the network ultimately breaks is dependent on the polymerization temperature. Networks polymerized at temperatures between 30°C and 37°C stiffen about 100-fold before breakage (Fig. 6.1A). In contrast, networks formed at 22°C or 26°C stiffen only about 3-10 times their original stiffness before rupture and they rupture at a smaller shear stress (Fig. 6.1A). To characterize the stiffening response, we determine the power-law slope of the $K'(\sigma)$ response at high stress, which we denote as β. As shown in Fig. 6.3B, β increases monotonically with increasing polymerization temperature, from a value close to 1 at 22°C to 1.6 at 37°C. Note that the value of β measured at 22°C may not be fully representative of the elastic limit since these networks exhibit creep (see section 6.4.2). As shown in Fig. 6.31 in the SI, β exhibits a weak dependence on collagen concentration. For networks formed at 37°C, β increases from ∼1.4 at 0.7 mg/ml to 1.6 at 4 mg/ml. Consistent with the concentration dependence observed for G_0 and γ_0, these results suggest that the network geometry changes with collagen concentration. Simulations of networks with constant L/l_c (or equivalently z) and varying $\widetilde{\kappa}$ namely predict a weak *decrease* of β for increasing $\widetilde{\kappa}$ (or equivalently, c_p) (Fig. 6.4B). However, β also heavily depends on varying architecture (i.e. z or L/l_c), as shown in (Fig. 6.4A), where $\widetilde{\kappa}$ is

kept constant. Thus, the model predicts that the stiffening exponent is mainly dictated by geometry and is also dependent on c_p. We also note that the simulations predict $\beta \sim 1.2 - 1.5$ for $\widetilde{\kappa} \sim 10^{-4}$ and $z = 3.2$, which is in line with the stiffening exponent reported for the higher temperature data (Fig. 6.3B). We conclude that the architecture of the collagen networks must change with concentration as well as with polymerization temperature.

We further quantify the extent of strain-stiffening by plotting the ratio of the modulus at the breakage point, K_{max}, over the linear modulus, G_0. In the absence of architecture changes with varying c_p, we expect from simulations that all stiffening curves measured at different collagen concentrations should go to the same affine, stretch-dominated limit, whereas the low strain modulus should scale with $\widetilde{\kappa}$. This means that we expect for experiments that this maximum stiffness K_{max} (which should be close to the stiffness in the stretch-dominated limit) is dependent on protein content, and thus c_p. From simulations, we also expect the linear modulus to scale as $G_0 \sim c_p^2$ in the absence of changes in architecture. Thus, the ratio K_{max}/G_0 should scale as $\sim c_p^{-1}$ in the absence of architecture changes. However, we have seen that the linear modulus shows a larger concentration dependence of $c_p^{2.5}$. Thus, we expect that the extent of stiffening scales as $c_p^{-1.5}$. As shown in Fig. 6.5A, we indeed observe that K_{max}/G_0 measured at 37°C decreases as a power law in concentration with an exponent close to -1.5 (best-fit value -1.7±1.3), but only above 0.7 mg/ml. At 0.7 mg/ml, K_{max}/G_0 exhibits a maximum. The breakage stress likewise shows a concentration dependence with two regimes (Fig. 6.5B). Below 0.7 mg/ml, the breakage stress increases as a power law with exponent close to 3, while above 0.7 mg/ml, it increases nearly linearly with concentration (fit gives 1.2 ± 0.5). This linear dependence is expected when the network failure is due to failure of the stretched fibers. The presence of two regimes for K_{max}/G_0 and for σ_{max} again indicates that the networks are inhomogeneous below 0.7 mg/ml. The network is likely not fully connected at low concentrations, i.e. there are dangling ends that do not contribute to the network response.

6.4.2 Impact of Polymerization Conditions on Collagen Viscoelastic Properties

Given that collagen networks are expected to behave as viscoelastic solids [72, 413, 500], we also tested whether variations in collagen concentration or polymerization temperature have an impact on the ratio of the elastic and viscous shear moduli. We quantified this via the loss tangent, which is defined as the ratio between the viscous and elastic shear modulus, $\tan(\delta) = G''/G'$. As shown in Fig. 6.6, $\tan(\delta)$ changes little with concentration and with temperature, varying between 0.1 and 0.2. Thus, the collagen networks behave as elastic solids when probed at a frequency of 0.5 Hz. Frequency-dependent

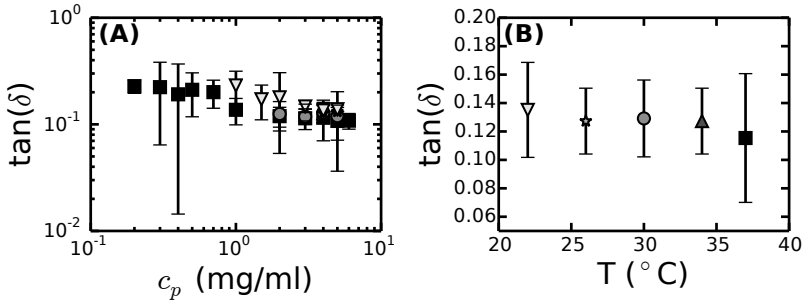

Figure 6.6: Viscoelastic behavior of collagen networks in the linear regime for different polymerization conditions. (A) Concentration dependence of the loss tangent, tan(δ), at 22°C (triangles down), 26°C (stars) , 30°C (circles), 34° (triangle up) and 37°C (squares) in increasing shades of gray. (B) Temperature dependence of the loss tangent for networks of 4 mg/ml collagen (same color coding as in panel A). The loss tangent is in all cases smaller than about 0.2, indicating predominantly elastic behavior ($G' \gg G''$). In both (A) and (B), the loss tangent was determined at 0.5 Hz.

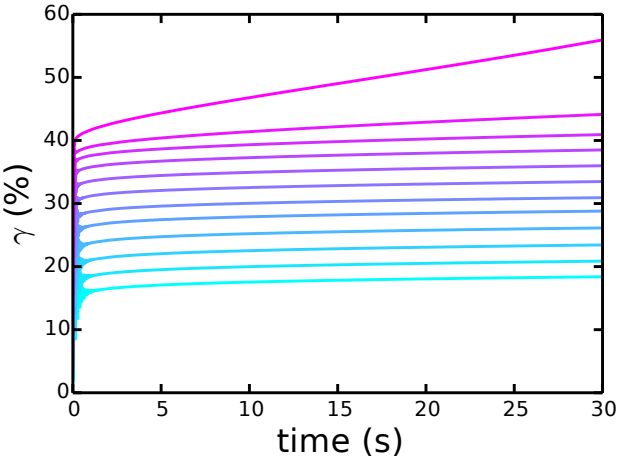

Figure 6.7: Creep response of a 4 mg/ml collagen polymerized at 37°C at increasing constant shear stress levels: from light blue to pink (bottom to top) the shear stress is 18.7, 23.1, 28.5, 35.1, 43.3, 53.4, 65.8, 81.1, 100, 123, 152 and 187 Pa respectively. The last stress level was just before apparent sample breakage and determined to be σ_{max} for this particular sample.

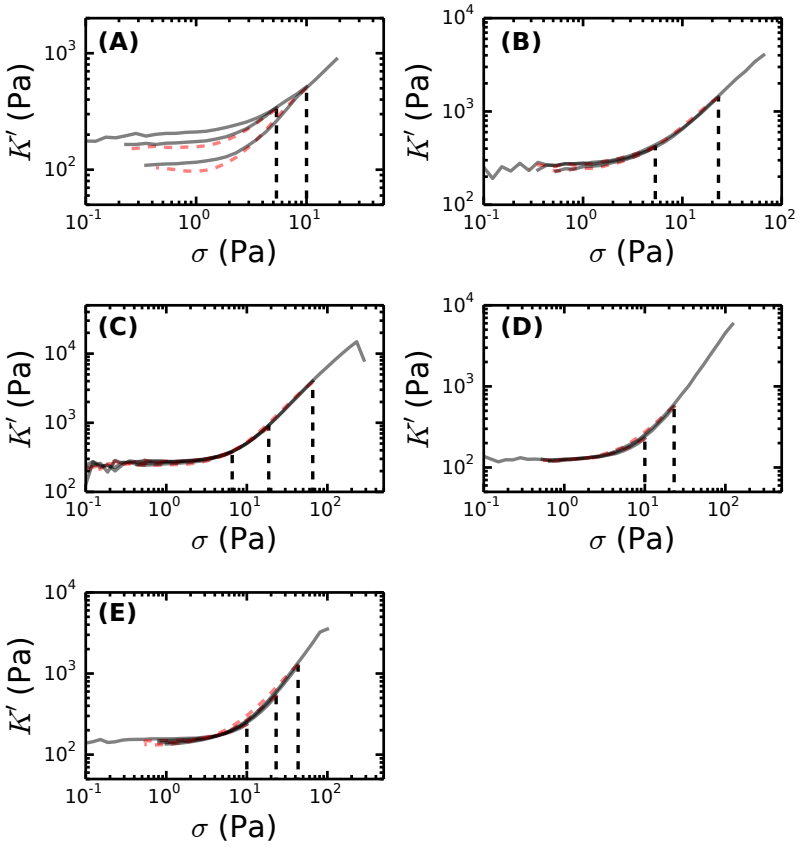

Figure 6.8: Inelastic behavior of 4 mg/ml collagen gels formed at different polymerization temperatures. The shear stress was increased up to a certain level (vertical dashed lines) and then decreased back down to the linear regime. This procedure was repeated, with increasing maximum stress level. Gray lines are increasing stress, while red dotted lines are decreasing stress. The polymerization temperature was 22°C (A), 26°C (B), 30°C (C), 34°C (D) and 37°C (E). Inelastic behavior is observed only for networks formed at 22°C.

oscillatory measurements show that the samples remain solid-like down to frequencies of at least 0.05 Hz (see Fig. 6.25, Fig. 6.26 and Fig. 6.27 in SI).

To test whether viscous dissipation becomes important at longer time scales, we also measured the creep response of collagen networks by applying a constant shear stress and measuring the time-dependent strain. As shown in Fig. 6.7, the samples show a quick rise of the strain upon application of stress, characteristic of an elastic solid, followed by a gradual increase in the strain, characteristic of a viscous fluid. To quantify this dissipative response, we determined the creep rate as the slope of the strain versus time curves (in units of %/s) as a function of strain (taken at $t = 30$ s). As shown in Fig. 6.28C in the SI, the creep rate is independent of the polymerization temperature at small strains of 1%. However, at strains above ∼10%, samples prepared at 22°C exhibit substantially more creep than samples polymerized at higher temperatures (Fig. 6.28A in the SI). This temperature dependence is more obvious when we directly compare the strain dependence of the creep rate measured at different polymerization temperatures while keeping the collagen concentration fixed at 4 mg/ml, as shown in Fig. 6.28B in the SI. The same curves are shifted for clarity in Fig. 6.28D in the SI. At strains below ∼3−5% the creep curves all overlap. Above ∼5%, the 22°C sample continues to creep at the same rate. For temperatures between 26°C and 37°C, the creep rate first rises with strain, then plateaus, and finally increases sharply just before breakage (Fig. 6.28D).

To test whether network creep influences the determination of K' [345], we checked whether the strain-stiffening behavior of the collagen networks was reversible. We first ramped the prestress up in a stepwise manner, and then ramped it back down to the linear regime, as shown Fig. 6.8. For samples polymerized at temperatures of 26°C and above the strain-stiffening curves showed hardly any hysteresis and the network stiffness returned to its original value (Fig 6.8(B-E)). In contrast, gels polymerized at 22°C showed a pronounced hysteresis between the upward and downward curves and significant softening (Fig. 6.8A). This hysteresis prevented a quantitative comparison of the data obtained at 22°C to the simulations, which consider perfectly elastic networks with permanent crosslinks.

6.4.3 Impact of Polymerization Conditions on Network Architecture

The rheology data (in particular G_0, γ_0 and β) suggest that the architecture of the collagen networks changes with polymerization temperature as well as collagen concentration. However, this is a somewhat indirect conclusion, since it is based on a comparison of the data with simulation results for disordered lattice-like networks. To directly test how the network structure changes

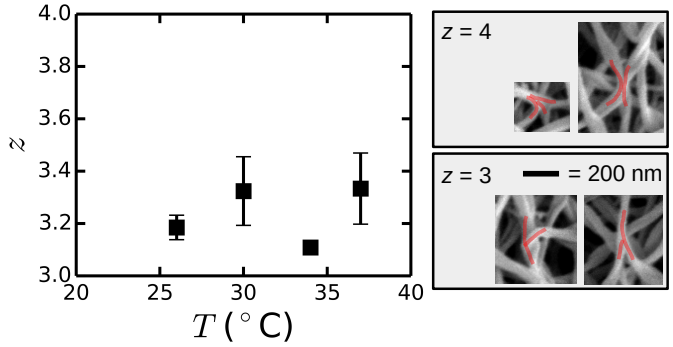

Figure 6.9: The average coordination number for 4 mg/ml collagen gels as a function of polymerization temperature, determined by counting the number of fibrils crossing each junction with SEM. Two examples for $z = 4$ and $z = 3$ junctions each ($T = 37°$C) are shown on the right, where the junctions are indicated in red. Scale bar denotes 200 nm for all images.

with assembly conditions, we visualized collagen networks formed at different temperatures directly using Confocal Reflectance Microscopy (CRM), as well as scanning electron microscopy (SEM) (see Fig. 6.10). CRM is convenient to characterize the network homogeneity and porosity on length scales of $\sim 10 - 100$ μm under hydrated conditions without sample labeling, but it does not provide enough spatial resolution to determine fiber diameter and connectivity. In contrast, SEM provides high resolution images that give insight into the network connectivity and fiber diameter, but it requires intensive sample preparation and dehydrated conditions. Previous studies on collagen have shown that SEM shows qualitatively the same trend as seen with optical microscopy techniques (i.e. a decrease in mesh size in confocal microscopy accompanies a decrease in diameter in SEM) [90,602,618]. We expect that the fiber diameter as seen with SEM is an underestimate, however, due to loss of water [619].

CRM reveals that the collagen networks are rather homogeneous and dense at 34°C and 37 °C, while at lower temperatures, the network become increasingly inhomogeneous. In the most extreme case, at room temperature (22°C), we observe fan-shaped bundles of collagen fibrils. Similar structures have been seen before in other studies for collagen at low polymerization temperatures (4−27 °C) [305,306,577,606,620]. With CRM, not all fibers are detected [621]. In particular, fibers that are orientated (close to) parallel to the imaging axis will not be visible. Furthermore, fibers that are thin compared to the imaging

wavelength will be missed using this technique [608]. It is therefore difficult to identify how the fan-shaped structures are connected to form a 3D network. Using SEM however, it is possible to see that the 'fans' are connected by a bundle of collagen fibrils (Fig. 6.10). The fans are composed of bundles of thinner fibrils, which splay out on one end. We speculate that these fan-shaped bundles may arise as a consequence of kinetic arrest when the growing fibrils meet another fibril and adhere [577]. These fan-shaped bundles disappear when the polymerization temperature is raised to 26°C or 30 °C. Consistent with CRM, the SEM images show that the microstructure at these higher temperatures is rather homogeneous, though some bundling is still visible. This bundling is further reduced at 34°C and 37°C, where the networks look homogeneous both in SEM and CRM images. From the SEM images, we can estimate the average connectivity z of the networks by counting the number of fibrils/bundles crossing each junction. We did not attempt this analysis for networks formed at 22°C, in view of the inhomogeneous network structures. As shown in Fig. 6.9, z is around 3.1 for temperatures of 26°C and 34°C, and is around 3.3 at temperatures of 30°C and 37°C. This implies that the network junctions are mainly provided by branches (see images on the right in Fig. 6.9). However, we do observe also examples of junctions made of two adjoining fibers with $z = 4$ (see images on the right in Fig. 6.9). We note that these values for the average connectivity are in excellent agreement with an earlier study of collagen [390] and fibrin networks [600].

The CRM images clearly reveal a decreasing pore size with increasing polymerization temperature, which is accompanied by a decrease in bundling, as seen by SEM. To quantify the degree of bundling in the hydrated state, we measured the turbidity of collagen polymerized at different temperatures. In case the collagen networks can be considered as mesh works of rod-like particles, where the rods are long compared to their diameter and to the wavelength of the incoming light, rescaling the turbidity according to eq. 6.2 should give a straight line, from which the mass-length ratio, μ, and fiber radius, a, can be readily extracted. Fig. 6.11A shows that this rescaling indeed holds for collagen networks polymerized at temperatures between 26−37°C. However, at 22°C this rescaling does not result in a straight line. This is probably due

Figure 6.10 ***(facing page)*****: Network architecture of 4 mg/ml collagen networks polymerized at different temperatures (22−37°C), as indicated by the (rotated) columns (in units of °C).** ***(row 1)*** **Confocal reflection images, showing at 22°C an open network of 'fan-shaped' fibril bundles, while with increasing temperature the networks look increasingly homogeneous and dense.** ***(row 2–4)*** **Scanning Electron Microscopy (SEM) images at increasing magnification. Scale bar denotes 20 μm for rows 1 and 2, 2 μm for row 3, and 200 nm for row 4.**

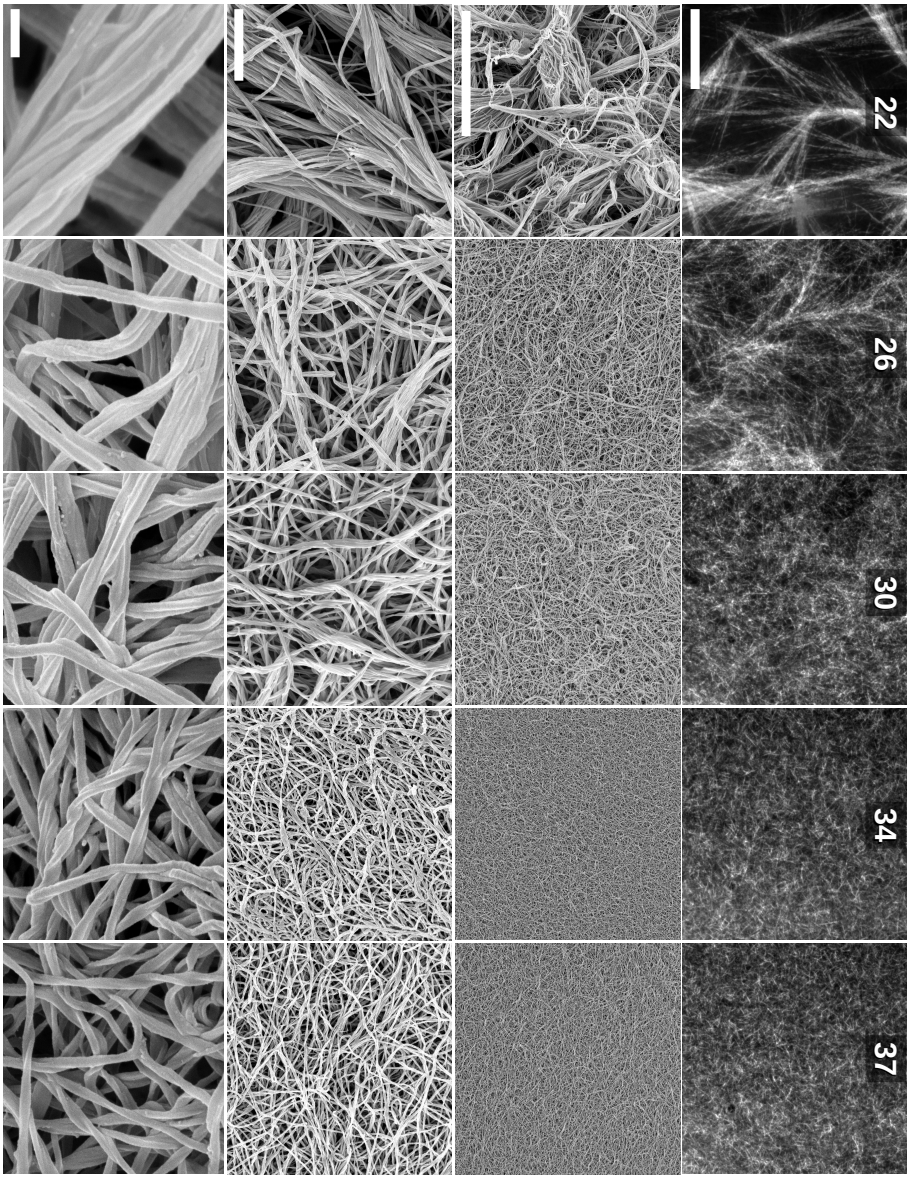
22
26
30
34
37

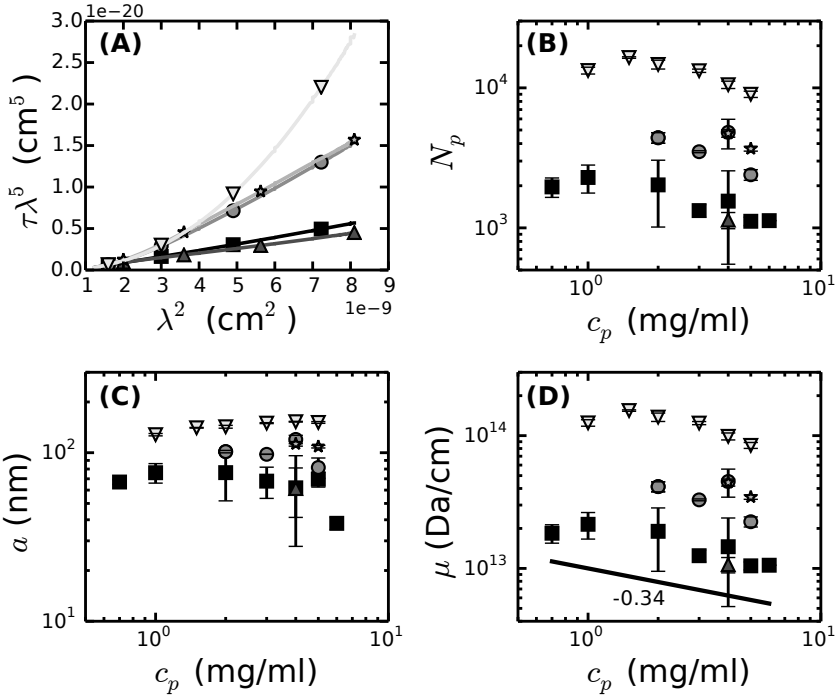

Figure 6.11: Light scattering measurements of the fibril diameter and mass-length ratio for collagen networks polymerized under different conditions. (A) Turbidity, τ, as a function of wavelength, λ, of 4 mg/ml collagen networks, rescaled according to eq. 6.2. The curves are straight for polymerization temperatures between 26°C and 37°C, whereas they deviate from the model for the more inhomogeneous networks formed at 22°C. (B-D) The number of monomers in a fibril cross-section, N_p, the radius of a collagen fibril, a, and its mass-per-length ratio μ, calculated from eq. 6.2 and 6.3. In all panels, the polymerization temperature was 22 (light gray triangles down), 26 (gray stars), 30 (gray circles), 34 (dark gray triangles up) or 37°C (black squares). In panel(A), data points were taken every 2 nm wavelength, and the symbols are for clarification only. In panel (D), the solid line represents a power law fit with exponent -0.34 ± 0.49 to the 37°C dataset (shifted for clarity).

to the large inhomogeneity in fiber structure and non-random arrangements of the fibers in these networks. Thus, the numbers extracted from scattering data for the 22°C networks are indicative only. As shown in Fig. 6.11, the mass-length ratio (panel D), the number of monomers in a cross-section (panel B), N_p, and radius a (panel C) of the collagen fibrils all depend on polymerization temperature as well as collagen concentration. At fixed concentration, the fibers become thinner and are of smaller mass with increasing temperature, which is consistent with the imaging data shown in Fig. 6.10. Previous studies also report an increase in mesh size with decreasing polymerization temperature [90, 305].

6.4.4 Collagen Mechanics Shows Signatures of Critical Behavior

In section 6.4.1 of this Chapter, we have shown that collagen networks stiffen when subjected to an increasing shear strain. Simulations of sub-marginal networks with a similar connectivity ($z = 3.2$) as the collagen networks predict that the strain-stiffening is accompanied by a continuous transition from a bending dominated elastic regime to a stretching dominated elastic regime at a critical strain γ_c [605], as shown in Fig. 6.12A. Below γ_c, the network elasticity is dominated by bending modes. For a rope-like network, for which the dimensionless fiber rigidity $\widetilde{\kappa} = 0$, the network is floppy and there is no linear regime below a strain threshold γ_c (red dashed line). In the other extreme limit of $\widetilde{\kappa} \to \infty$, the network already has a high modulus in the linear regime, because deformation is dominated by affine fiber stretching (full red line). In this case only little stiffening occurs above γ_c, which reflects shear-induced fiber alignment along the shear direction. For networks with a finite $\widetilde{\kappa}$, the rope limit is approached as $\widetilde{\kappa}$ decreases. However, even below the critical point of the rope-like networks, these networks are mechanically stable. The linear modulus G_0 increases linearly with increasing $\widetilde{\kappa}$ (see inset), clearly demonstrating that G_0 is determined by fiber bending. Irrespective of $\widetilde{\kappa}$, above γ_c, all curves converge onto the affine limit, where the elasticity is proportional to the enthalpic stretch modulus of the fibers. Since the simulation data for K are in units of $\rho\mu$, and since $\widetilde{\kappa} \sim \rho$, linear scaling of G_0 with $\widetilde{\kappa}$ implies that $G_0 \sim \rho^2 \sim c_p^2$, where ρ is the total length per volume. Indeed, a nearly quadratic power law dependence has been seen before for collagen gels [253, 272, 395, 602, 603], although stronger and weaker dependencies have also been reported [92, 251, 527, 603].

If strain-stiffening involves a continuous transition from a bend-dominated to a rigid stretch-dominated state at γ_c, we expect that the stress-stiffening curves can be collapsed unto one master curve via critical scaling [280, 605]:

$$K \sim |\Delta\gamma|^f \mathcal{G}_{\pm}\left(\frac{\widetilde{\kappa}}{|\Delta\gamma|^{\phi}}\right) \tag{6.6}$$

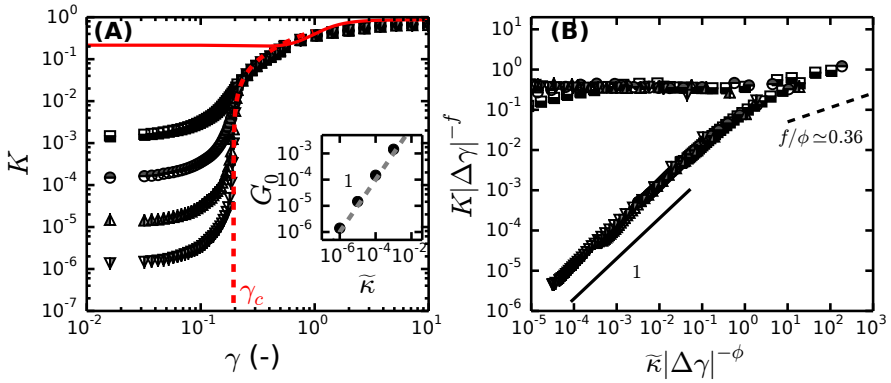

Figure 6.12: Simulation data showing critical scaling of the elastic modulus of athermal fibrous networks of varying $\widetilde{\kappa}$ and fixed architecture of $L/l_c = 3.1$ (corresponding to $z = 3.2$) with strain. (A) Dimensionless differential elastic modulus K for fibrous networks with $\widetilde{\kappa} = 0$ (dotted red line), 10^{-6} (triangles down), 10^{-5} (triangles up), 10^{-4} (circles), 10^{-3} (squares) and $\sim \infty$ (red solid line). *(inset)* The linear modulus, G_0, shows a linear dependence on $\widetilde{\kappa}$ (dashed line), where $G_0 \simeq \widetilde{\kappa}$. (B) The data from panel (A) collapsed according to eq. 6.6 using scaling exponents $f = 0.75$ and $\phi = 2.1$. The lines show power law scaling with exponents of 1 for the lower critical branch, and f/ϕ for the upper branch.

Here, $\Delta\gamma = \gamma - \gamma_c$ denotes the proximity to the critical point and $\mathcal{G}_\pm$ is a scaling function to capture the asymptotic behavior of $K(\gamma)$ in the limits $\gamma \to 0$ and $\gamma \to \infty$. $\mathcal{G}_\pm$ has a negative branch that corresponds to networks below the critical point ($\Delta\gamma < 0$) and a positive branch that corresponds to networks above the critical point ($\Delta\gamma > 0$). Simulations of networks with varying z indicate that the critical exponents f and ϕ are set by the architecture (i.e. L/l_c or equivalently z) of the network (see Table 6.1 in SI). As shown in Fig. 6.12B, the simulation data for $K(\gamma)$ in Fig. 6.12A with varying $\widetilde{\kappa}$ can indeed be collapsed onto one mastercurve according to eq. 6.6, using $f = 0.75$ and $\phi = 2.1$. Note that we determined the critical point, γ_c, as the inflection point of the $\log(K)$ versus $\log(\gamma)$ curves in the strain-stiffening regime. In the limit where $\gamma \to 0$, we observe the expected linear dependence of G_0 on $\widetilde{\kappa}$ (solid line in Fig. 6.12B). This regime corresponds to the negative branch of $\mathcal{G}_\pm$, for ($\Delta\gamma < 0$). When γ approaches γ_c, the scaling shows a power law with exponent that is proportional to f/ϕ (dashed line in Fig. 6.12B). Since K must be finite at $\Delta\gamma = 0$, we expect $K \sim \kappa^{f/\mu}\mu^{1-f/\phi}$. When γ increases above γ_c, all rescaled prestress curves converge to a plateau value that is independent of

$\widetilde{\kappa}$. We note that this critical scaling, though obtained for an athermal system, is analogous to the critical scaling of the magnetization in the presence of an applied field for a ferromagnet at varying temperatures [622].

In experiments, we can test whether our collagen systems also show a continuous transition from a stretch-dominated to a bend-dominated regime at γ_c, by using a slightly modified expression for the critical scaling [605]:

$$K' \sim c_p |\Delta\gamma|^f \mathcal{G}_{\pm}\left(\frac{c_p}{|\Delta\gamma|^{\phi}}\right) \tag{6.7}$$

As shown in Fig. 6.13A, the prestress data measured at 37°C and at varying collagen concentrations (0.7−5 mg/ml) nicely collapse to one universal curve when we use scaling exponents of $f = 0.8$ and $\phi = 2.2$. For networks polymerized at 30°C (2−5 mg/ml), we obtain data collapse with comparable exponents, $f = 0.8$ and $\phi = 2.1$. In simulations, these exponents are consistent with $\langle z \rangle = 3.3$ (Table 6.1 in SI). This z-value is consistent with our determined average $\langle z \rangle$ for both 37°C and 30°C (Fig. 6.9). Moreover, this z-value is close to a previously reported value of 3.4 [390] and interestingly, it is also close to reported values for fibrin networks [600]. Thus, our data show that the nonlinear elastic response of collagen networks can be understood as a mechanical transition from a soft, bending-dominated state, to a rigid, stretching-dominated state. In the limit where $\widetilde{\kappa} = 0$, this is a mechanical phase transition with a critical point γ_c.

We will now more closely examine the concentration dependence of the critical scaling obtained at 37°C and 30°C. In the linear elastic regime, where $\gamma \ll \gamma_c$, we expect from eq. 6.7 a concentration dependence of K' according to:

$$\frac{K'}{c_p} \sim c_p \gamma_c^{(f-\phi)} \tag{6.8}$$

If we assume that γ_c only varies due to architecture changes, then we can write:

$$\frac{K'}{c_p} \sim c_p^{1+\alpha} \tag{6.9}$$

Experimentally we find $K'/c_p \sim c_p^{1.25}$ and $K'/c_p \sim c_p^{1.1}$ for the lower branch of the critical scaling for 37°C and 30°C respectively (see solid lines in Fig. 6.13A and B). The bottom insets of Fig. 6.13A and B show that this scaling is consistent with the measured concentration dependence of G_0. Note that the scaling is also close to the scaling of G_0 with c_p shown earlier (Fig. 6.1B), where we found $G_0 \sim c_p^{2.5\pm0.05}$ for 37°C and $G_0 \sim c_p^{1.9\pm0.49}$ for 30°C.

Experimentally, we also observed a weak concentration dependence for the critical strain:

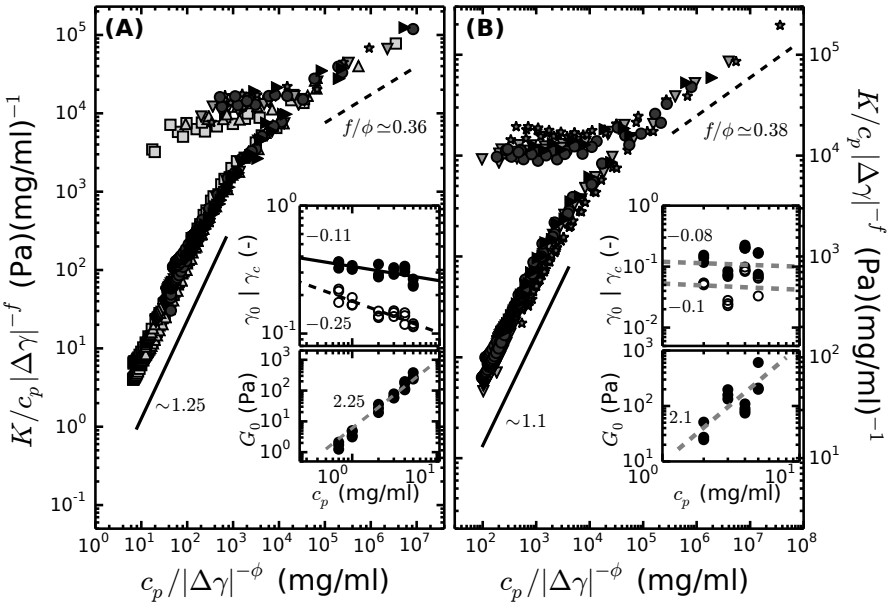

Figure 6.13: Critical rescaling for collagen networks polymerized at 37°C (A) and 30°C (B) according to eq. 6.7. The lines show power law scalings with exponents close to 1 for the lower critical branch (1.25 and 1.1) and f/ϕ for the upper branch. (*bottom insets*) The linear modulus G_0 (solid symbols) is consistent with the concentration scaling observed in the lower critical branch, where $\gamma \to 0$ and $\gamma < \gamma_c$ (dashed lines). (*top insets*) Open and closed symbols correspond to γ_0 and γ_c respectively. In panel (A) the lines are best power law fits with exponents -0.11 ± 0.03 and -0.25 ± 0.03 for γ_c and γ_0 respectively. In panel (B), the expected concentration dependences are shown in the insets, based on the critical rescalings. In panel (A), the expected dependence for G_0 is shown in the inset (2.25). The critical exponents are (A) $f = 0.8$ and $\phi = 2.2$, (B) $f = 0.8$ and $\phi = 2.1$. Increasing concentration is indicated in increasing shades of gray (0.7−5 mg/ml for (A) and 2−5 mg/ml for (B)).

$$\gamma_c \sim c_p^{-\epsilon} \tag{6.10}$$

where $\epsilon \sim 0.1$ at 37°C as well as 30°C. This concentration dependence suggests that the network architecture changes with concentration, since simulations of networks with constant architecture predict a concentration-independent γ_c (see Fig. 6.12A). By combining eq. 6.8 and eq. 6.9, we find that the exponents f, ϕ, α and ϵ should be internally consistent:

$$\gamma_c \sim c_p^{\alpha/(f-\phi)} \tag{6.11}$$

Based on our data, $\epsilon = \alpha/(\phi - f) \simeq 0.2$ for 37°C and $\epsilon \simeq 0.1$ for 30°C, which is indeed nicely consistent with the observed dependence of γ_c on c_p as shown in the insets in Fig. 6.13A and B.

For the upper critical branch corresponding to the limit of $\gamma \to \gamma_c$, we expect that $K'/c_p|\Delta\gamma|^{-f}$ should increase as a power law in $c_p/|\Delta\gamma|^{-\phi}$ with a power law exponent of f/ϕ (dashed lines in Fig. 6.13). Experimentally, we find $f/\phi \simeq 0.36$ for 37°C and $f/\phi \simeq 0.38$ for 30°C. In the limit where γ is much larger than γ_c, simulations predict that all rescaled prestress curves should converge to the some constant level (see Fig. 6.12B). We do observe an approximate convergence of data obtained at different concentrations at both 37°C and 30°C. Interestingly, this plateau value has the same order of magnitude for both temperatures (i.e. $K'/c_p|\Delta\gamma|^{-f} \sim 10^4$). This is expected, since in this high strain regime, the affine elastic stretching limit, architecture no longer plays a role since the fibers in the network become more aligned with shear direction in the affine limit.

On the basis of the successful critical scaling presented in Fig. 6.13, the internal consistency of the scaling exponents, and the agreement of the exponent with predictions of simulations of sub-marginal fibrous networks, we can conclude that the nonlinear elasticity of collagen gels polymerized at 37°C and 30°C is well-explained by a strain-induced transition from a soft to a rigid state. However, we find clear evidence that the network architecture changes with concentration, c_p: Both G_0 and γ_0 show a dependence on collagen concentration that deviates from the dependencies expected in case of scale-invariant networks. This is especially obvious for γ_c, which decreases with increasing concentration, whereas it is expected to be constant in case of scale-invariant networks. The onset strain for strain-stiffening likewise shows a power law dependence on collagen concentration, as shown in the top insets of Fig. 6.13A and B:

$$\gamma_0 \sim c_p^{-\alpha}, \tag{6.12}$$

where $\alpha = 0.25$ at 37°C and 0.1 at 30°C. If changes in architecture provide the only source of the concentration dependence for γ_0 and γ_c, than we can

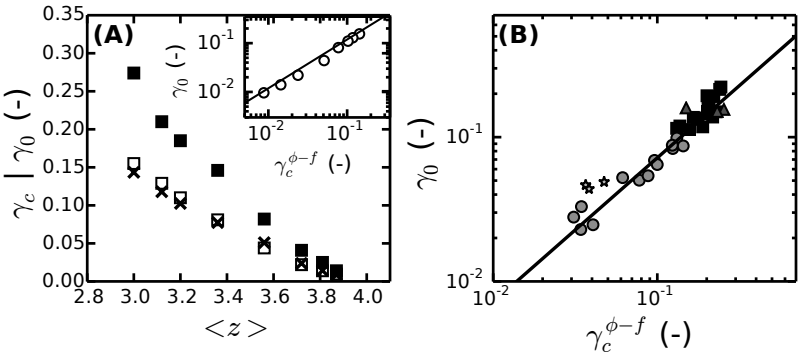

Figure 6.14: Internal consistency of the critical exponents. (A) Simulation data for the dependence of γ_0 (open symbols) and γ_c (closed symbols) on the average network connectivity, $\langle z \rangle$, for athermal fibrous networks. Data for γ_0 are consistent with estimates from eq. 6.14 (crosses), which assumes that γ_0 and γ_c are interrelated via the critical scaling exponents f and ϕ. (*inset*) Consistent with eq. 6.14, γ_0 increases linearly with $\gamma_c^{\phi-f}$ (full line). For each data point in panel (A), the individual f and ϕ values were used as summarized in Table 6.1 in SI. (B) Experimental data for γ_0 and γ_c likewise show a linear dependence according to eq. 6.14. Data are shown for 0.7−5 mg/ml for 37°C (squares), 4−5 mg/ml for 26°C (stars), 1−5 mg/ml for 30°C (circles) and 4 mg/ml for 34°C (triangle up) in increasing shades of gray. For the 30 and 37°C datasets, we used the exponents from the critical rescaling (Fig. 6.13, $f = 0.8$ and $\phi = 2.1$ for 30°C and $f = 0.8$ and $\phi = 2.2$ for 37°C). For the 34°C and 26°C data sets, we assumed $f = 0.75$ and $\phi = 2.1$, based on simulation data for an average connectivity $\langle z \rangle \simeq 3.2$ (Table 6.1 in SI) as measured under these conditions (Fig. 6.9). The full line denotes the expected linear scaling.

write the following [623]:

$$\frac{\log \gamma_0}{\log \gamma_c} \sim \frac{-\alpha \log c_p}{\frac{\alpha}{f-\phi} \log c_p} \sim \phi - f \tag{6.13}$$

Thus if changes in architecture are the only source of the concentration dependence for γ_0 and γ_c, these two quantities should be related by:

$$\gamma_0 \sim \gamma_c^{(\phi - f)} \tag{6.14}$$

We checked this relation both for simulations and experiments in Fig. 6.14. As shown in panel A, the simulations demonstrate that γ_0 indeed scales linearly with $\gamma_c^{(\phi-f)}$ (see *inset*), and that γ_0 calculated from γ_c (crosses) agree with values of γ_0 directly measured from the simulated stiffening curves (open squares). To test eq. 6.14 for the experimental data, we used the critical exponents as determined in Fig. 6.13 for the 30°C and 37°C data sets, and expected values of f and ϕ for the 26°C and 34°C data sets as predicted (Table 6.1 in SI) for networks having the same connectivity as measured in SEM images (Fig. 6.9). We find that also in case of the experiments, γ_0 increases linearly with $\gamma_c^{(\phi-f)}$, and the data measured for temperatures between 26−37°C collapse onto a single curve with exponent 1 (Fig. 6.14B). This strongly indicates that changes in architecture provide the main source of the concentration dependence of γ_0 and γ_c.

The turbidity measurements indeed corroborate the conclusion that the architecture of the collagen networks changes with concentration. These data show that the fibril mass-length ratio, and consequently N_p, weakly decreases as a power law with increasing concentration for collagen networks formed at the 37°C (Fig. 6.11B and D). Intriguingly, this power law exponent is close to the concentration exponent of $\gamma_0(c_p)$ (Fig. 6.13A *top inset*). This correspondence suggests that μ and network architecture may be related. One possible way to explain this, is that fibers with a higher mass-length ratio are less likely to branch, thereby increasing z, while fibers with lower mass-length ratio branch more frequently. However, this effect is apparently small, since the experimental stiffening curves still show a good collapse onto a mastercurve, using a single set of critical exponents (albeit on a log-log scale). It will be interesting to test this hypothesis in the future by determining the connectivity as a function of collagen concentration.

In view of the evidence for critical behavior, we can write down an equation of state for fiber networks under shear deformation [605] in analogy to ferromagnetism [622]. By numerical inversion of this equation of state, an approximate scaling function $\mathcal{G}_{\pm}$ can be computed that holds over the entire strain range:

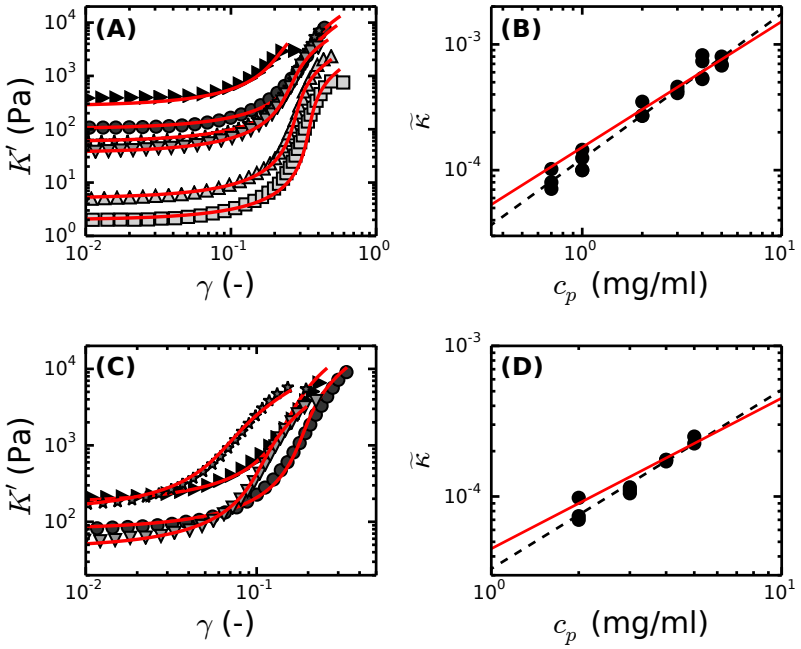

Figure 6.15: Quantitative comparison of the measured strain-stiffening behavior of collagen networks polymerized at different collagen concentrations with scaling theory for fibrous networks undergoing a mechanical transition from bend-dominated to stretch-dominated elasticity, measured at (A,B) 37°C, and (C,D) 30°C. In panels (A,C) experimental data (symbols) are compared with fits (red lines) to the scaling prediction in eq. 6.15, using $\widetilde{\kappa}$ as the only fitting parameter. The collagen concentration was 0.7 (squares), 1 (triangles up), 2 (triangles down), 3 (stars), 4 (circles) and 5 mg/ml (triangles right), in increasing shades of gray. In panels (B,D) the best-fit values for $\widetilde{\kappa}$ are shown as a function of collagen concentration. The red lines denote the expected linear scaling, while the dashed black lines denote a power law fit with exponents of 1.15±0.09 in (B) and 1.19±0.02 in (D).

$$\frac{\widetilde{\kappa}}{|\Delta\gamma|^{\phi}} \sim \frac{K}{|\Delta\gamma|^{f}}\left(\pm 1 + \frac{K^{1/f}}{|\Delta\gamma|}\right)^{\phi-f} \tag{6.15}$$

Using eq. 6.15, we can fit the experimental K' versus γ data, using $\widetilde{\kappa}$ as the sole fitting parameter. For this, we need to convert the dimensionless modulus, K, from simulations to physical units by $K' = \mu\rho K$, where K is a function of z, $\widetilde{\kappa}$ and γ. A change in architecture gives an extra c_p^{α} dependence in the low strain regime. If we assume we can write $K' = \mu\rho F(z)K(\widetilde{\kappa},\gamma)$, where $F(z)$ contains the architecture dependence, then $K' = A_T c_p^{1+\epsilon} K$, where A_T is a constant per polymerization temperature containing the Young's modulus of a fiber among other geometric factors. Using this K' relation in eq. 6.15, and $\alpha = 0.25$ for 37°C and 0.1 for 30°C, we can fit our experimental curves. As shown in Fig. 6.15A and C, eq. 6.15 (red lines) indeed accurately captures the entire stiffening curves of 37°C and 30°C collagen gels for all concentrations tested.

As a consistency check, we show that $\widetilde{\kappa}$ extracted from the fits indeed scales approximately linearly with collagen concentration as expected from simulations in Fig. 6.15B and D. For the 37°C dataset, $\widetilde{\kappa}$ increases from $\sim 8{\cdot}10^{-5}$ to $\sim 7{\cdot}10^{-4}$ as c_p increases from 0.7 to 5 mg/ml. For the 30° data, $\widetilde{\kappa}$ is slightly lower at the same collagen concentration, increasing from $\sim 8{\cdot}10^{-5}$ to $\sim 2{\cdot}10^{-4}$ as c_p increases from 2 to 5 mg/ml. These values for $\widetilde{\kappa}$ are consistent with earlier estimations of $\widetilde{\kappa} \leq 10^{-3}$, based on measurements on rat tail collagen I gels polymerized under different buffer conditions (pH 9.5 instead of pH 7.3) [279].

In this section, we have shown for the first time that collagen shows signatures of critical behavior, as shown in Fig. 6.13, and that collagen mechanics can be described by eq. 6.15 (Fig. 6.15). Also, the concentration dependences of the linear modulus, the onset of stiffening and the critical strain are related via their critical exponents f and ϕ (Fig. 6.14), which are governed by architecture changes.

6.4.5 Quantitative Prediction of Collagen Network Stiffness

In this section, we will make a quantitative comparison between simulations and experiment. For this, we first need to estimate the total amount of fiber length per unit volume, ρ, in the 3D FCC lattice. The total fiber length in an FCC lattice is $L_{total} = 6N^3 l_c$, where N^3 is the total number of vertices and l_c is the spacing between vertices. The factor 6 originates from the fact that every lattice site is the intersection of 6 fibers. The total volume of the lattice is given by $V = v_0 N^3$, where v_0 is the volume of a unit cell. To identify v_0, we enclose every vertex by a sphere of radius $r_0 = l_c/2$, such that we have a close packing of spheres. Each sphere then encloses a total fiber length of $6l$. Thus, the fiber length per volume within one sphere is $6 \times 2R_0/V_{sphere} = 9/(\pi R_0^2)$,

where the sphere volume is $4\pi R_0^3/3$. The maximum length of fiber per volume (i.e. before random dilution) in the full packing is smaller than this by a factor ϕ_{max}, where $\phi_{max} = \pi/\sqrt{18}$ is the volume fraction of the FCC lattice. Thus, $\rho_{max} = 3/\sqrt{2}R_0^{-2}$. Since the lattice spacing $l_c = 2R_0$, $\rho_{max} = 12/\sqrt{2}l_c^{-2}$. This expression provides an overestimate of the density of an actual network, since the FCC lattice is highly ordered. Also, we did not allow for bond dilution yet. To obtain an average connectivity $\langle z \rangle \simeq 3.4$ that is comparable to the typical connectivity of a collagen network, typically 20% of fiber segments are removed in the simulations. Even then, the simulated networks are likely still denser than actual networks [624]. Thus, henceforth, we will assume that the actual fiber length per volume is about 50% of the maximum length per volume in the FCC lattice, so $\rho = 4l_c^{-2}$. The polymer volume fraction is proportional to ρ according to: $\phi_{vol} = \pi a^2 \rho = 4\pi a^2 l_c^{-2}$.

To allow a quantitative comparison between simulations and experiment, we next need to map the dimensionless bending rigidity from the simulations onto actual network parameters. The filaments have a stretching modulus, μ_s, and bending modulus, κ. Assuming that the collagen fibrils behave as tight bundles with a cylindrical cross-section, $\mu_s = \pi a^2 E$, and $\kappa = \frac{1}{4}\pi a^4 E$ [616]. Here, a is the fibril radius and E is the Young's modulus. Combining these expressions, we obtain $\widetilde{\kappa} = \frac{1}{4}a^2/l_c^2$. Note that $\widetilde{\kappa}$ is determined purely by the network geometry, and is independent of the material properties of collagen. We can rewrite this expression for $\widetilde{\kappa} = 1/16\pi\phi_{vol}$, where ϕ_{vol} is the fiber volume fraction. Micromechanical measurements on bovine collagen fibrils and tendons under hydrated conditions indicate values of E between 0.03 and 0.6 GPa [251,284–288], though larger values were found in one study of human collagen fibrils (∼3 GPa [625]).

The simulations show that at low stress, the elastic energy of the network is governed by soft bending modes. Thus, the linear elastic modulus is proportional to the fiber bending rigidity:

$$G_0 = F(z)\mu_s/l^2\widetilde{\kappa} = F(z)\frac{1}{4}\phi_{vol}E\widetilde{\kappa} = F(z)\frac{1}{64\pi}\phi_{vol}^2 E \qquad (6.16)$$

The prefactor F depends on the coordination number z. If z is independent of concentration, as assumed in the simulations, then this model predicts a quadratic increase of G_0 with protein concentration. Indeed an approximate quadratic dependence has been observed in several [602,603], but not all [251, 602,603], experimental studies of collagen. We can thus directly estimate G_0 based on the Young's modulus of a collagen fiber and the fiber volume fraction, if we assume that the factor $F(z)$ is close to unity. The fiber volume fraction we can estimate using the turbidity results (Fig. 6.11), where the total length per volume is $c_p N_A/\mu$, where N_A is Avogadro's number. For a 1 mg/ml collagen gel polymerized at 37°C, where we have shown that $\alpha = 0.25$ (see section 6.4.4 and Fig. 6.13A), $\mu = 2.1 \cdot 10^{13}$Da/cm (Fig. 6.11D) and taking $E \simeq 0.1$

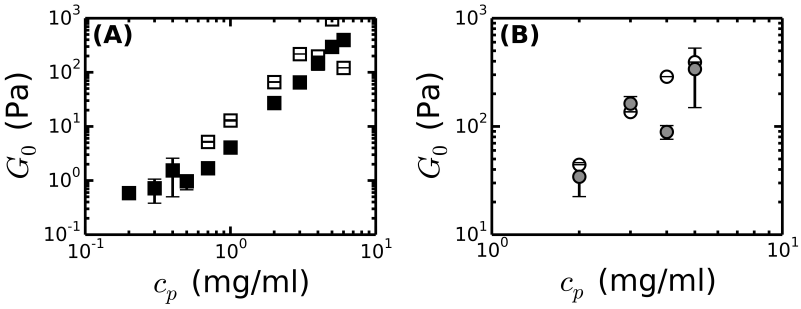

Figure 6.16: Concentration dependence of the low strain (linear) plateau modulus calculated according to eq. 6.16 (using $F(z) = 1$) (open symbols) compared with measured G_0 values (closed symbols) at a polymerization temperature of 37°C (A) or 30°C (B).

GPa [251, 284–288], we obtain $G_0 \simeq 13$ Pa. This value is indeed reasonably close to the measured value of 5 Pa measured by rheology.

In Fig. 6.16, we checked the concentration dependence of G_0 estimated following the above reasoning. The estimated G_0 values indeed show a similar concentration dependence as the experimental data, both for networks gelled at 37°C (panel A) and at 30°C. However, the calculated values are systematically somewhat larger than the measured values, except in the 30°C case (panel B). Potentially, the Young's modulus of the reconstituted collagen fibrils is lower than the literature values, which were mostly measured for fibrils extracted from tissue. Note that the elastic moduli are several orders of magnitude lower than the affine limit, where G_0 is dominated by the mechanical resistance of the fibers to axial stretch. For an isotropic network of rods, the elasticity in the affine limit is $G_0 = (1/15)\rho\mu_s$ [613]. At 1 mg/mL collagen concentration, μ_s is ~ 1800 nN (taking $a = 80$ nm and $E = 0.1$ GPa), so G_0 is 34 kPa, which grossly overestimates the measured stiffness. All in all, these considerations strongly suggest that the low strain elastic modulus is governed by fiber bending and can be predicted based on geometrical arguments. We also note that we find a somewhat stronger concentration dependence for the linear modulus with a power law of 2.25 for 37°C and 2.1 for 30°C, in contrast to what this model predicts (power law of 2). These findings suggest that the average coordination number $\langle z \rangle$ of collagen networks does depend on concentration, at least under the self-assembly conditions used here. This can be accounted for by assuming that the factor $F(z)$ can be expressed by a factor c_p^α. With this assumption, the linear modulus is also in quantitative agreement with the 37°C data set (see Fig. 6.32 in SI).

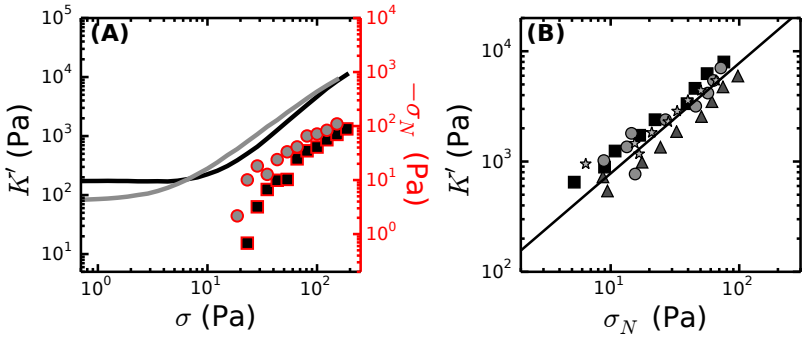

Figure 6.17: (A) Shear deformation causes a build-up of negative normal stress in the nonlinear elastic regime. Lines are experimental data for K' (left axis) for 4 mg/ml collagen networks polymerized at 37°C (black) or 30°C (gray). Red outlined symbols denote the corresponding (negative) normal stress (σ_N, right y-axis) for 37°C (black squares) or 30°C (gray circles). (B) The stiffness of collagen networks in the nonlinear elastic regime linearly increases with the normal stress, σ_N. Data are shown for 4 mg/ml collagen gels, polymerized at different temperatures. The symbols denote 22°C (triangles down), 26°C (stars), 30°C (circles), 34°C (triangles up) and 37°C (squares). The line shows the expected linear relation.

6.4.6 Normal Force Tunes Network Stiffness

We have presented the nonlinear elasticity of collagen gels polymerized at different temperatures in section 6.4.1. In section 6.4.4 we showed that the nonlinear elasticity of collagen networks is consistent with multiple predictions made by computational studies of sub-marginal fibrous networks. In particular, collagen networks exhibit mechanical critical behavior, which explains the concentration dependence of the linear elastic modulus, the strain at the onset of stiffening, the critical strain γ_c, and the full strain-dependence of K'.

In this section we will check another prediction of the athermal network model. When a fibrous network is sheared between two plates with a fixed gap, it will develop a negative (contractile) normal stress [255,454,626]. Recent simulation data of athermal fibrous networks using the same model as described in this Chapter showed that K grows in direct proportion to the normal stress, σ_N [279, 604]:

$$K' \simeq G_0 + \chi|\sigma_N| \tag{6.17}$$

Here χ is a constant that will be referred to as the susceptibility. Based on

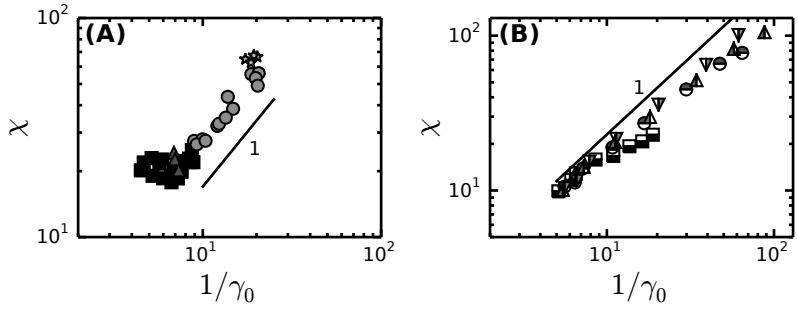

Figure 6.18: The susceptibility of collagen networks exhibits a linear dependence on the inverse of the onset strain for strain-stiffening, $1/\gamma_0$, in experiments as well as simulations. (A) Measured susceptibility as a function of onset strain, which was varied by varying the polymerization temperature and collagen concentration (see Fig. 6.1B). Data are shown for 0.7−5 mg/ml collagen gels polymerized at 37°C (squares), 4 mg/ml gels at 34°C (triangles up), 1−5 mg/ml gels at 30°C (circles) and 4−5 mg/ml networks at 26°C (stars), in decreasing shades of gray. (B) Simulation data for the susceptibility as a function of the onset strain, which was varied through L/l_c (see Fig. 6.14A). Simulations were performed for $\widetilde{\kappa}$ values of 10^{-6} (triangles down), 10^{-5} (triangles up), 10^{-4} (circles), and 10^{-3} (squares). The solid lines indicate the expected linear scaling.

this observation, it was hypothesized that normal stresses can stabilize submarginal collagen networks at strains below γ_c. However, this hypothesis was not tested experimentally until now. To test it, we measured the normal stress for collagen gels polymerized at different temperatures and collagen concentrations. As shown in Fig. 6.17A, we indeed observe a negative normal stress upon shearing, as expected for biopolymer networks [255,454,626]. We can observe a negative normal stress in all gels having collagen concentrations above ∼1 mg/ml, except in the 22°C case, where the data are too noisy and the strain-stiffening regime is rather small (*not shown*). We always observe an offset for the normal force F_n in the linear regime, which is likely dominated by the surface tension of the sample at the outer edge of the cone-plate. Since this effect is not related to the collagen network itself, and since we expect F_n to be close to zero when there is no shear stress applied [626], we subtracted the offset from the normal stress data.

Based on eq. 6.17, we expect to find a linear dependence of K' on σ_N. We checked this for varying collagen temperatures and collagen concentrations (Fig. 6.17B). Indeed, we find a linear dependence of K' on σ_N, from which we

can in principle determine χ by linear fitting. However, since it was difficult to measure σ_N reliably for the lower collagen concentrations (i.e. $c_p < 2$ mg/ml), we employed an alternative way to determine χ.

Simulations previously showed that at the onset of stiffening, the shear stress and the normal stress are equal in magnitude [255, 604, 626]. Thus, eq. 6.17 can be rewritten as $K'/\sigma_0 \simeq \chi$, where σ_0 is the onset stress. We used this relation to determine χ for all collagen experiments. The resulting susceptibility data are depicted in Fig. 6.18A and compared with simulations in panel B. In both cases, we find that the susceptibility increases linearly with $1/\gamma_0$, meaning that it depends on network architecture. We next checked whether K' follows the prediction made in eq. 6.17. For this we focused on collagen gels with $c_p \geqslant 2$, where F_n could be measured over more than half a decade of σ. As shown in Fig. 6.19, eq. 6.17 provides a reasonable prediction of K', especially in terms of slope, for all collagen concentrations tested, both at 37°C (panel A) and at 30° (panel C). This observation suggests that normal force indeed governs the nonlinear elasticity of collagen gels. The consistent underestimation of K' by a factor of about 2 could be due to a residual offset in F_n. However, for the simulation data, K' at high stresses is underestimated by the theoretical prediction as well. Indeed, eq. 6.17 is no longer expected to hold when σ approaches the critical stress σ_c.

6.5 Discussion and Conclusion

Collagen is the most important structural and mechanical component of the ECM [301]. For this reason, collagen has been a popular model system for in vitro studies of cell in a 3D ECM environment in the context of mechanobiology, and normal and tumor cell migration [90, 271, 606, 627, 628]. There has been quite a large number of publications reporting on the linear and nonlinear rheological properties of collagen [92, 251–253, 272, 279, 395, 413, 527, 602, 603], with some attempts to quantitatively relate the rheology to the underlying network structure [251,252,272,413,602]. However, a consensus about the physical basis of the nonlinear mechanics of collagen networks has been lacking.

Here we have shown for the first time that the mechanics of collagen gels is governed by a mechanical transition from a floppy, bend-dominated elastic regime to a rigid, stretch-dominated elastic regime. This is a consequence of the gels being sub-marginal, with an average connectivity of ~ 3.4, which is below the isostatic limit of $z = 6$ in 3D. The development of rigidity is characterized by a strain-controlled continuous phase transition with signatures of criticality. The critical exponents f and ϕ are set by the network architecture, in particular the average connectivity $\langle z \rangle$. We showed that the strain-stiffening behavior of collagen networks is well described across the entire accessible strain range by an approximate scaling function (eq. 6.15) derived in analogy to ferromagnetism [605,622], as shown in Fig. 6.15. Also, the concentration dependencies

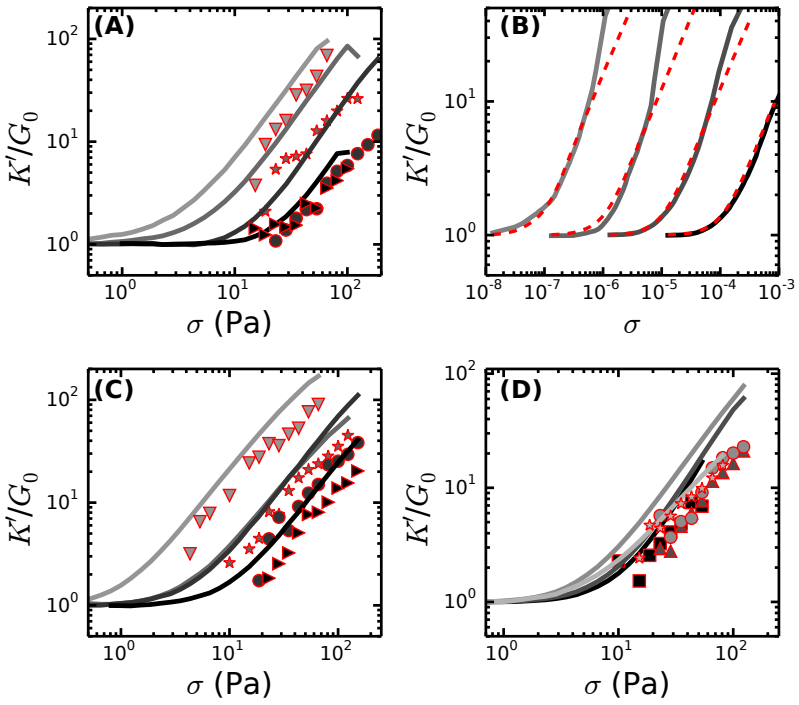

Figure 6.19: Experiments and simulations demonstrate that the strain-stiffening response of collagen gels is governed by normal stress. (A,C,D) Measured K' (lines) for collagen gels polymerized at different concentrations and at fixed temperatures of 37°C (A) or 30°C (C), and for gels polymerized at different temperatures ranging between 26°C and 37°C and at a fixed concentration of 4 mg/ml (D), compared with predictions made using eq. 6.17 (red-outlined symbols), using measurements of the normal stress and the susceptibility (see Fig. 6.18) as input. In (A) and (B) the collagen concentration was 2 (triangles down), 3 (stars), 4 (circles) and 5 mg/ml (triangles right), in increasing shades of gray. In (D), the symbols denote collagen polymerized at 26°C (stars), 30°C (circles), 34°C (triangles up) and 37°C (squares) in increasing shades of gray. (B) Corresponding simulation data for athermal fibrous networks of varying normalized bending stiffness, $\widetilde{\kappa}$ and fixed $L/l_c = 3.1$, where the gray lines are the rescaled K'/G_0 data and the red dotted lines are the predictions of eq. 6.17. In increasing shades of gray, $\widetilde{\kappa}$ is 10^{-6}, 10^{-5}, 10^{-4} and 10^{-3}.

of the linear modulus, the onset of stiffening, and the critical strain are interrelated via the critical exponents f and ϕ (Fig. 6.14). Experimentally, we could vary these exponents by inducing architecture changes by varying the collagen concentration and the polymerization temperature over a wide range. Between 22°C and 37°C, the collagen architecture could be changed from a very open and heterogeneous mesh work of thick collagen fibril bundles to a homogeneous dense network of collagen fibrils with small pore size.

Earlier computational studies had suggested that strain-stiffening of athermal fiber networks originates from a transition from bending-dominated elasticity at low strain to a stretch-dominated elasticity regime at high strain [425]. However, here we showed that the networks already stiffen substantially even well before the strain-controlled transition to the stretch-dominated state. Thus, the strain-stiffening that sets in at γ_0 is actually not caused by a bend-to-stretch transition. The simulations suggest that stiffening in the bend-dominated stiffening regime is induced by a build-up of normal stress. When a fibrous networks is sheared between two plates with a fixed gap, the networks develop a negative normal stress [255, 626]. Based on simulation data, it was hypothesized that this normal stress can stabilize sub-marginal collagen network for strains below γ_c. Here we could support this hypothesis by our experimental data showing that K' grows in direct proportion to the normal stress σ_N.

Now that we have a complete quantitative understanding of the nonlinear elastic properties of collagen, we can predict the elastic stiffening of a given collagen network based its connectivity and the fiber volume fraction. This gives us a powerful tool to predict the elastic mechanical properties of more physiologically relevant collagen systems, where the mass-length ratio of the fibers is regulated by accessory ECM molecules such as the minor fibrillary collagens type V or III [251].

We found that collagen gels exhibit significantly more viscous dissipation than the fibrin networks presented in Chapter 2. The loss tangent for collagen is typically around 0.1, whereas it is ~ 0.01 for fibrin [66,297]. The microscopic basis for this viscous behavior is still unknown. It may originate at the level of fiber-fiber contacts, or at the level of the fibers themselves. It has been proposed in prior studies of single collagen fibril mechanics that viscous dissipation may be mediated by sliding between monomers [287,629]. We discovered a significant dependence of the inelastic behavior on polymerization temperature. Collagen gels polymerized at 22°C were clearly inelastic, whereas collagen gels polymerized at temperatures of 26°C were more elastic. This observation is consistent with a picture where sliding between or within fibrils contributes to viscous dissipation, since increasing temperatures should strengthen the hydrophobic interactions that hold collagen monomers together [630, 631]. Several recent studies showed that viscous dissipation of cell substrates can have

a major influence on cell behavior [69, 70, 500]. It was suggested that viscous dissipation is especially significant at the slow time scales relevant for cells ($\sim$ min) [72]. In terms of experiments on cellular mechanosensing, the viscous and inelastic properties of collagen networks should be considered for cell tests inside 3D collagen gels.

6.6 Acknowledgments

I like to thank Albert Licup, Abhinav Sharma, Robbie Rens, Misha Sheinman and Fred MacKintosh for the modeling and sharing the data for this chapter, and for fruitful discussions. This work is part of the research programme of the Foundation for Fundamental Research on Matter (FOM), which is financially supported by the Netherlands Organisation for Scientific Research (NWO). This work is further supported by NanoNextNL, a micro and nanotechnology programme of the Dutch Government and 130 partners.

6.7 Supplementary Information

Supplementary Figures and Tables

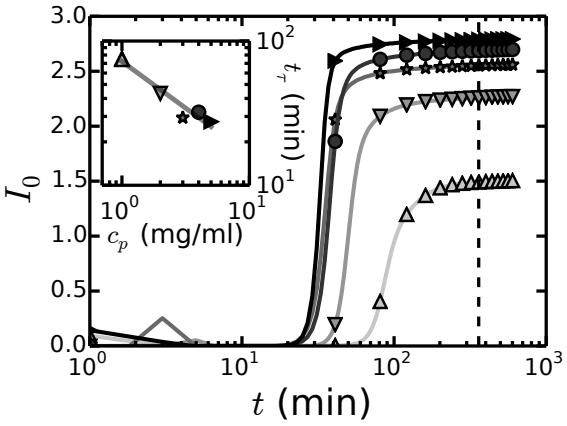

Figure 6.20: Time dependence of the scattered light intensity measured at a wavelength of 600 nm for polymerizing collagen gels at room temperature, at varying collagen concentrations. Concentrations are 1 (triangles up), 2 (triangles down), 3 (stars), 4 (circles) and 5 mg/ml (triangles right), in increasing shades of gray. Every 2 minutes, a data point was collected. The vertical dotted line indicates the time when rheology measurements were always started. The curves exhibit a typical sigmoidal shape with a characteristic lag time before the turbidity starts to increase. The lag time decreases with concentration, whereas the final turbidity reached in the plateau phase increases with concentration. *(inset)* Concentration dependence of the lag time, t_τ. The gray line denotes a power law fit with exponent -0.65±0.08.

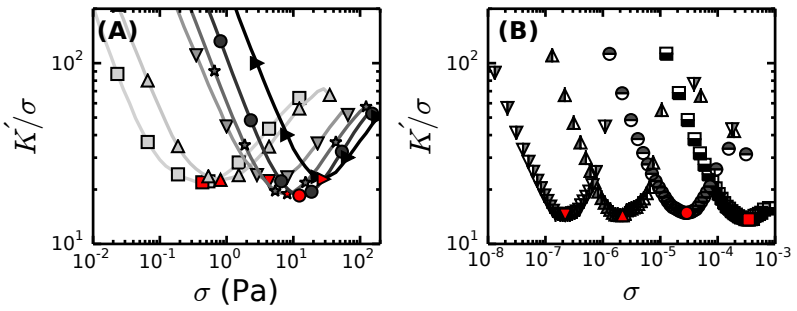

Figure 6.21: Definition of the onset strain, γ_0, of stiffening as the minimum of K'/σ. (A) Experimental data for collagen gels polymerized at 37°C and at varying collagen concentrations. Concentrations are 0.7 (squares), 1 (triangles up), 2 (triangles down), 3 (stars), 4 (circles) and 5 mg/ml (triangles right), in increasing shades of gray. (B) Simulation data for fixed $L/l_c = 3.1$ and varying dimensionless bending rigidities $\widetilde{\kappa}$: 10^{-6} (triangles down), 10^{-5} (triangles up), 10^{-4} (circles), and 10^{-3} (squares). Red symbols in (A) and (B) are taken as the onset of stiffening.

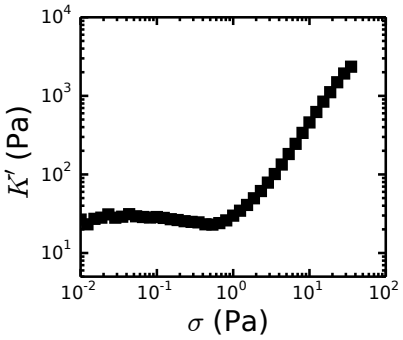

Figure 6.22: Example curve for the nonlinear elastic response of a 1 mg/ml collagen gel that initially shows softening before it starts to stiffen as the stress is further increased. This non-monotonic type of behavior was only seen for 1, 2 and 3 mg/ml gels and at 37°C. Since this behavior was rare, these gels were excluded from further analysis.

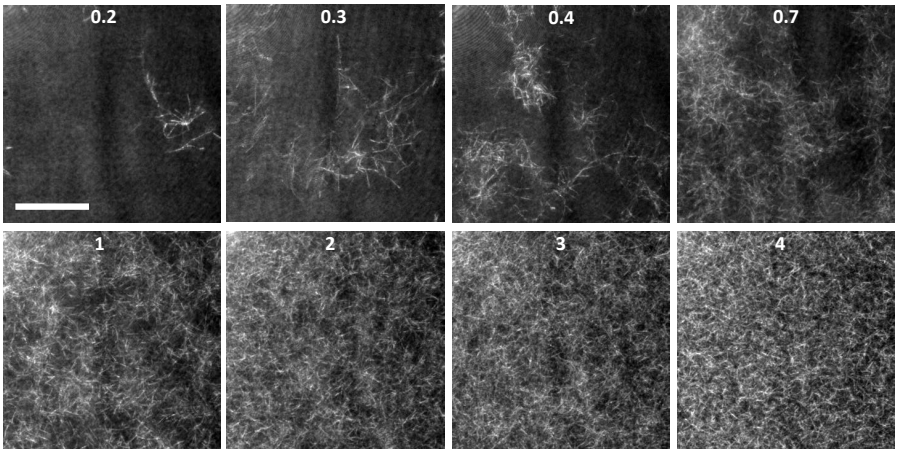

Figure 6.23: Confocal reflection images of collagen networks formed at different collagen concentrations and a fixed polymerization temperature of 37°C. Concentration is indicated in the images in mg/ml. Scale bar denotes 20 μm for all images. All images are summations over a distance of 20 μm in z, starting ~10 μm above the surface and using a z-spacing of 0.2 μm.

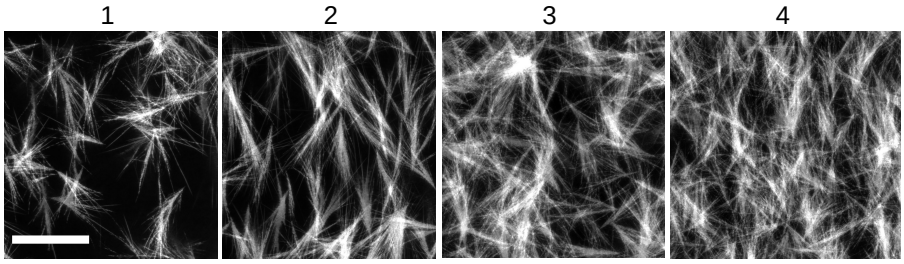

Figure 6.24: Confocal reflection images of collagen networks formed at different collagen concentrations and a fixed polymerization temperature of 22°C. Concentration is indicated in the images in mg/ml. Scale bar denotes 50 μm for all images. All images are summations over a distance of 40 μm in z, starting at least 10 μm away from the surface and using a z-spacing of 0.2 μm.

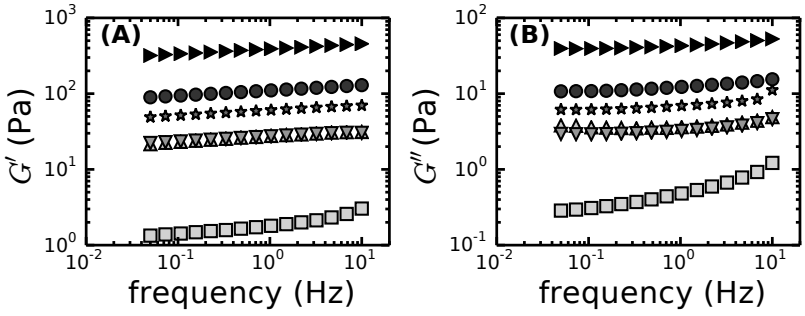

Figure 6.25: Frequency dependence of the viscoelastic shear moduli of collagen gels polymerized at 37° at different collagen concentrations. (A) Example curves of the elastic shear modulus, G', and (B) the corresponding viscous shear modulus, G''. Symbols denote collagen concentration: 0.7 (squares), 1 (triangles up), 2 (triangles down), 3 (stars), 4 (circles) and 5 mg/ml (triangles right), in increasing shades of gray

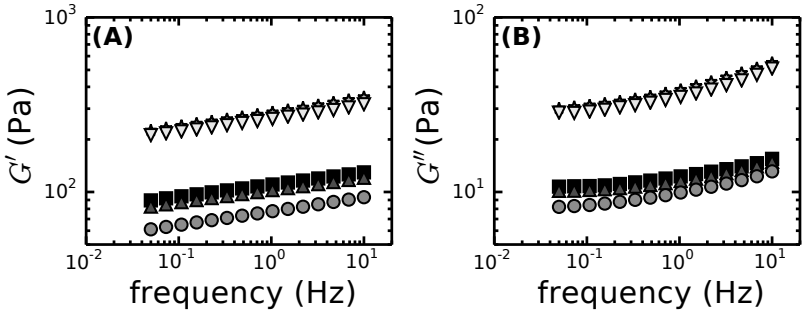

Figure 6.26: Frequency dependence of the viscoelastic shear moduli of collagen gels polymerized at 4 mg/ml and at different polymerization temperatures. (A) Example curves of the elastic shear modulus, G', and (B) the corresponding viscous shear modulus, G''. Symbols denote collagen polymerized at 26°C (stars), 30°C (circles), 34°C (triangles up) and 37°C (squares) in increasing shades of gray.

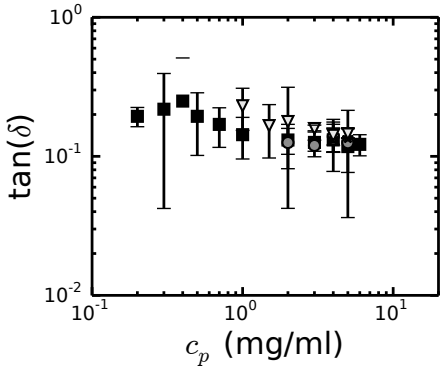

Figure 6.27: The loss tangent determined at 0.05 Hz at different collagen concentrations for networks polymerized at 22°C (triangles down), 26°C (stars), 30°C (circles), 34°C (triangles up) and 37°C (squares) in increasing shades of gray.

f	ϕ	z	γ_0 (-)	γ_c (-)
0.7	2.2	3	0.155	0.274
0.73	2.1	3.12	0.129	0.21
0.75	2.1	3.2	0.11	0.185
0.77	2.1	3.36	0.081	0.146
0.81	2	3.56	0.044	0.082
0.83	2	3.72	0.022	0.0409
0.85	2	3.81	0.014	0.025
0.89	2	3.87	0.0096	0.014

Table 6.1: Simulation results for the critical scaling exponents, f and ϕ, and the onset strain for strain-stiffening, γ_0, and critical strain, γ_c, determined for disordered 2D triangular lattices of varying average coordination number, z. Data were kindly provided by Albert Licup, Abhinav Sharma, Robbie Rens, Misha Sheinman and Fred MacKintosh at the VU University Amsterdam.

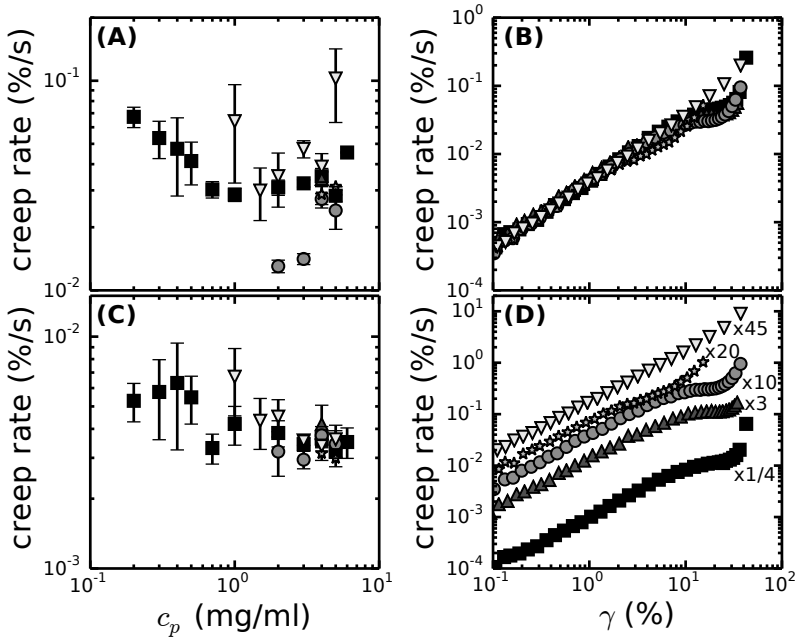

Figure 6.28: Creep behavior of collagen gels formed at different collagen concentrations and polymerization temperatures. (A and C) Creep rate evaluated at a strain of 12% (A) or 1% (C) for different collagen concentrations and temperatures. (B) The full creep behavior for 4 mg/ml collagen networks at varying strain levels. The creep curves overlap at low strains, but they deviate at high strains. (D) Same creep curves as in panel (B), but now shifted to better compare the shapes. For all panels, symbols denote 22°C (triangles down), 26°C (stars), 30°C (circles), 34°C (triangles up) and 37°C (squares) in increasing shades of gray.

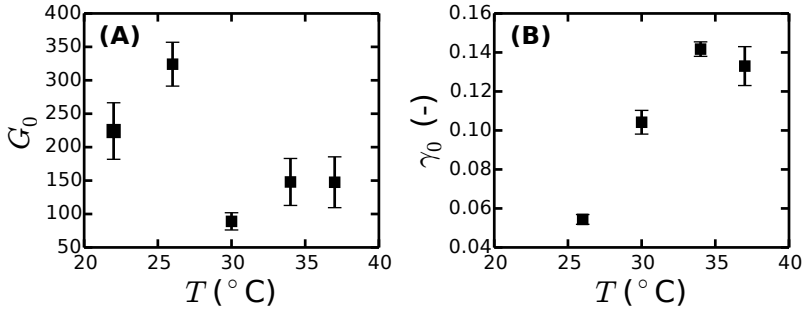

Figure 6.29: Linear elastic behavior of 4 mg/ml collagen gels as a function of polymerization temperature. (A) Linear (low strain) modulus, G_0, and (B) onset strain for strain-stiffening, γ_0.

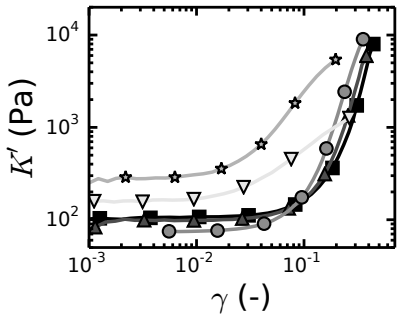

Figure 6.30: Stiffening behavior of 4 mg/ml collagen gels polymerized at different temperatures. Increasing gray-scale indicates increasing polymerization temperature. Symbols denote 22°C (triangles down), 26°C (stars), 30°C (circles), 34°C (triangles up) and 37°C (squares). The symbols show every 5th data point, while the lines represent the full data sets.

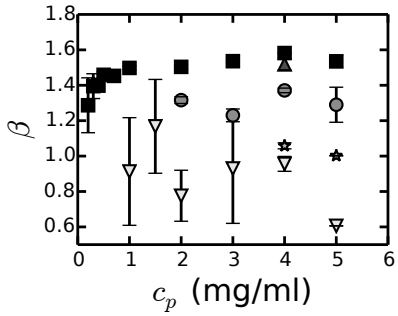

Figure 6.31: The stiffening exponent, β, in the high strain regime for 4 mg/ml collagen gels polymerized at varying temperatures. Increasing gray-scale indicates increasing polymerization temperature. Symbols denote 22°C (triangles down), 26°C (stars), 30°C (circles), 34°C (triangles up) and 37°C (squares).

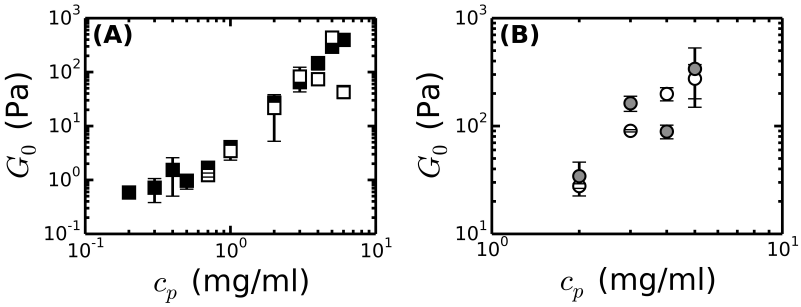

Figure 6.32: Concentration dependence of the low strain (linear) plateau modulus calculated using eq. 6.16 (open symbols), using $F(z) = c_p^{\alpha}$, compared with measured G_0 values (closed symbols) at a polymerization temperature of 37°C ($\alpha = 0.25$) (A) or 30°C ($\alpha = 0.1$) (B).

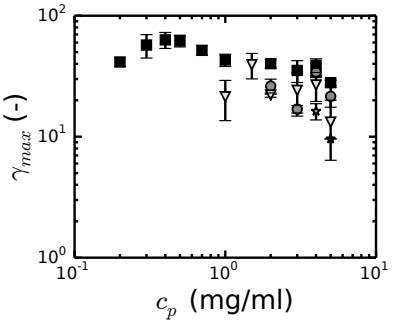

Figure 6.33: Concentration dependence of the maximal strain, γ_{max}, reached before apparent network breakage, measured for collagen gels polymerized at different polymerization temperatures. Symbols denote 22°C (triangles down), 26°C (stars), 30°C (circles), 34°C (triangles up) and 37°C (squares) in increasing shades of gray.

7. Cells in Collagen Type I gels

Collagen is a widely used extracellular matrix (ECM) material to study cell physiology in a tissue-mimetic, three dimensional environment. The mechanical properties of collagen are known to influence cell behavior, while, in turn, cells can restructure the matrix and change its mechanical properties by the exertion of traction forces and enzymatic degradation. In this chapter, we study the contribution of cellular traction and network remodeling on the mechanical properties of collagen networks. For this purpose, we employ 3T3 mouse fibroblasts inside collagen networks reconstituted from collagen I extracted from rat tail. Surprisingly, we find no difference in the mechanical properties of collagen networks with and without cells. By using time-lapse microscopy, we can explain this observation in terms of limited cell spreading. Obvious candidate mechanisms to increase cell spreading (changing cell density, serum concentration, collagen concentration and dimensionality) did not improve cell spreading. Using quantitative polymerase chain reaction assays, we verified that the fibroblasts in principle did express collagen binding integrins. Apparently, the cells are unable to form sufficiently mature adhesions to the collagen matrix to allow them to exert significant traction forces. Therefore we recommend to use a different cell line for future experiments, which is more contractile than the 3T3 cell line used here.

Karin A. Jansen, Hendy Kristyanto, Gijsje H. Koenderink

7.1 Introduction

Collagen is the most abundant and structurally important component of the extracellular matrix [301]. The predominant type of collagen in all connective tissues, except cartilage, is collagen type I. Collagen I forms networks of stiff fibrils whose stiffness and tensile strength is essential for healthy tissue functioning [3,587]. Moreover, the collagen network provides important mechanical cues to cells, which regulate a multitude of cell functions including motility, proliferation, and differentiation, as discussed in detail in Chapter 1. Abnormal increases in stiffness of the collagen matrix have been shown to trigger tumor cell behavior and tumor-like behavior of non-tumorigenic cells [3–5]. In turn, cells also actively change the structural and mechanical properties of the collagen matrix by matrix synthesis and enzymatic degradation as well as by exerting traction forces [244, 632].

This bidirectional mechanochemical interplay between cells and their extracellular matrix has been widely studied using reconstituted collagen gels as a minimal tissue system. Bell and co-workers [238, 633] pioneered the use of cell-seeded collagen gels for so-called contraction assays, demonstrating that cellular contractile forces could macroscopically compact collagen gels *in vitro*. Since then, fibroblast-populated collagen gels have served as a model system to study cell-matrix interactions during physiological processes like wound healing [243–245,634–637]. Cell-seeded collagen matrices are also widely studied for their potential use in tissue engineering applications [638,639], and are increasingly popular as model systems to study the effect of the three-dimensional (3D) fibrous collagen matrix on cellular mechanotransduction and cell migration [90, 271, 606, 627, 628].

Since cells are known to remodel and tense collagen gels, many of the reported studies of cell-seeded collagen gels focused specifically on the question whether the cells change the mechanical properties of the gel, which would cause a mechanical feedback loop for mechanosensing. The mechanical properties of cell-seeded collagen gels have been measured using uniaxial tensile tests [393, 627, 640–643], shear rheology [395], and microrheology [403]. Several studies showed an increase in collagen stiffness with increasing cell density [394,395] (see Table 7.1), which was attributed to a combination of cellular contractility and (permanent) ECM remodeling. Evans and coworkers [394] described the low strain modulus based on an 'inclusion model', where cells create small dense inclusions whereas the bulk of the network is uninfluenced. Some studies reported a decrease in gel stiffness upon the inclusion of cells, which was attributed to digestion of the collagen matrix by cell-secreted metalloproteases [393,395]. It is unclear which mechanism dominates under which conditions. Moreover, most of these studies have focused on the low strain modulus and ignored possible changes to the nonlinear elastic modulus. Elsewhere in this thesis (see Chapter 3), we showed that cells can stiffen fibrin gels,

as a consequence of the highly non-linear elastic response of these gels. Like fibrin, collagen networks also strongly stiffen when subjected to a mechanical stress [251–253, 272]. We confirmed this nonlinear behavior for *in vitro* polymerized collagen in Chapter 6, and in addition we demonstrated that this nonlinearity can be quantitatively understood based on the network architecture and the normal stress. Since we now have a quantitative model to link macroscopic observables, such as stiffness and onset strain for strain-stiffening, to the underlying network architecture, it should in principle be possible to elucidate the degree of remodeling (change in architecture) and degree of traction force generation (change in normal force) by investigating the nonlinear elastic response of cell-seeded versus acellular gels.

Motivated by these findings, we here aimed to test whether cells can stiffen collagen networks, in analogy to the cell-seeded fibrin networks presented in Chapter 3. We directly measured the contribution of cellular traction to collagen network mechanics by comparing the nonlinear mechanical properties of cell-seeded gels with acelular gels. We use macrorheology to measure the mechanical properties, and optical and confocal microscopy to study cell spreading and network structure. Unexpectedly, cell spreading was low, both inside and on top of thick collagen gels. We investigated the possible origin of the lack of cell spreading by varying serum concentration, cell density, collagen concentration, and the source of collagen. However, these parameters did not improve cell spreading. Next, we quantified the integrin expression profiles for cells on top of 2D collagen gels and inside the 3D gels by a quantitative polymerase chain reaction (qPCR) assay. Even though collagen-binding integrins were expressed, we conclude that the 3T3 fibroblast cell line that we used is not ideal to study changes in mechanical properties due to cell traction forces. This is supported by a pilot measurement with a different fibroblast line (human CCL-224), which gave better cell spreading.

Table 7.1: Overview of articles reporting mechanics of cell-seeded collagen gels, where 'Rheology' stands for macrorheology, 'Tensile' for tensile tests, 'Microrheology' for magnetic tweezer microrheology and CFM for cell force monitor (a form of tensile test that monitors force over time, and optimized for cell culture).

Ref.	Collagen source	Cell type and density	[Mechanical probe] Main observations
[395]	Rat tail[1] (BD Biosciences)	CHO cells [2], 7,000-18,000 cells/μl	[Rheology] At 0.42 mg/ml collagen, G_0' increases with cell density, whereas at 1.8 mg/ml, G_0' decreases with cell density. Nonlinear properties were not tested.
[644]	Rat tail[1] (BD Biosciences)	Corneal fibroblasts, 100-500 cells/μl	[Ball indentation][3] The Young's modulus increased over several days of culture. At 1 day of culture, cell-seeded gels were stiffer than acellular gels, except at 3.5 mg/ml collagen.
[394]	Bovine skin[4] (Organogenesis)	NHDFs[5], 50-250 cells/μl	[Tensile] Increasing Young's modulus with increasing cell density.
[403]	Bovine skin [4] (Vitrogen 100)	LL-24[6], 25-100 cells/μl	[Microrheology] On day 1 of culture, the gel stiffness decreased with cell density (2 mg/ml collagen). On day 2 and up, the stiffness increased with cell density.
[64]	Collagen Type I [1] (Integra Life Sciences), 5 mg/ml	Dermal rabbit fibroblasts	[CFM] Force per cell increases with time and saturates after 6 hours, independent of stiffness of its environment.

continued on next page

[1] acid-soluble and has intact telopeptides
[2] CHO, Chinese hamster ovary
[3] A sphere of 4 mm diameter was placed on top of a suspended (thin) cell-seeded collagen gel and the deformation was measured. [645]
[4] pepsin-treated and lacking the telopetides
[5] Neonatal human dermal fibroblasts
[6] human lung fibroblasts

Ref.	Collagen source	Cell type and density	[Mechanical probe] Main observations
[393, 640]	Rat tail[7] (Upstate Biotechnology)	Chicken embryonic fibroblasts, 100-1,000 cells/μl	[Tensile] The collagen gels become stiffer over the time scale of days, partly due to cell-matrix remodeling (already apparent after 2 hours). In the absence of serum, cells still spread, but there was no increase in force. Antibody blocking of integrin β1 did not completely inhibit contractile force generation.
[646]	Rat tail[7] (First Link Ltd.)	Human dermal fibroblasts, 1,000 cells/μl	[Tensile] Buildup of contractile force with time. Cells adapted their contractile force to changes in external tension to keep the total matrix tension at a constant level of $\sim$ 40-60 dynes/million fibroblasts.
[627, 647]	Rat tail[7] (First Link Ltd.)	Human foreskin fibroblasts, 1000 cells/μl	[Tensile] There is less contractile force generation when the external strain on the collagen matrix is increased (5, 10, 15% strain). In the absence of serum, cell spreading and force generation was inhibited, but the cells remained viable.
[648]	Rat tail[7] (Upstate Biotechnology Inc.)	Chicken embryo fibroblasts, 6,000-100,000 cells/μl	[Tensile] After 3 days of culture, experiments were started. Gel stiffness increased with increasing cell density due to cellular contraction and ECM remodeling.
[641]	Rat tail[7](First Link Ltd.), plasticaly compressed	MG-63 [8] (600-100k cells/μl post-compression)	[Tensile] Due to collagen degradation, the rupture force decreases with cell density after 10 days of culture.

continued on next page

[7]acid-soluble and has intact telopeptides
[8]Human osteosarcoma

Ref.	Collagen source	Cell type and density	[Mechanical probe] Main observations
[649]	Rat tail[9] (Collaborative Biomedical Products), 1.5 mg/ml	Adult dermal fibroblasts, HOS and KHOS-240, 100-1000 cells/μl	[CFM] In the control case, force increased rapidly within 5 hours. With an antibody to integrin $\beta 1$, force generation was lower and slower. Force generation was related to $\alpha 2\beta 1$ integrin levels.

7.2 Materials and Methods

7.2.1 Cell culture and Cell labeling

3T3 mouse fibroblasts (a gift from Dominique Donato, Leiden Institute of Physics, University of Leiden, the Netherlands) were cultured to near-confluency in Dulbecco's Modified Eagle Medium (DMEM) supplemented with 10% fetal bovine serum (FBS, Gibco), 20 mM 4-(2-hydroxyethyl)-1-piperazineethanesulfonic acid (HEPES) buffer (Sigma-Aldrich, Zwijndrecht, NL) and 0.1% antibiotics (10 μg/ml pen/strep, Sigma-Aldrich). Human CCL-224 fibroblasts (a gift from Prof. J. Boonstra, Biology Department, Utrecht Universiteit, NL) were cultured to near-confluency in the same medium, but supplemented with 1% L-Glutamine (Gibco). Unless stated otherwise, 3T3 cells were used in experiments. Both cell cultures were incubated at 37 °C in a 5% CO_2 humidified incubator. Cells were harvested by trypsinization with a 0.1% EDTA/0.25% trypsin solution and were pelleted by centrifugation. The pellets were resuspended in DMEM. The cell density was determined with a counting chamber (Hemacytometer, Optik Labor, Lancing, UK). The cell suspension was aliquotted and the volume of the aliquots was adjusted to obtain a cell density that was 10x the cell density in the final experiment. The aliquots were protected from light and used within one hour. To visualize cells by confocal fluorescence microscopy, the plasma membrane of cells in culture was labeled with CellTracker^{TM} Green CMFDA (Invitrogen). Cells were labeled at about 50% confluency by incubation for 1 hour with 1.25 μM in DMEM, and subsequently washed for 30 min with DMEM to remove unbound dye. The next day, the labeled cells were trypsinized and used for experiments.

7.2.2 Collagen Gel Preparation and Cell Seeding

We used rat tail collagen Type I (BD Biosciences, Breda) in all experiments, except in a few cases (explicitly states), where we used bovine dermal collagen type I (Nutragen, Advanced Biomatrix, San Diego, CA). Aliquots of the

[9] acid-soluble and has intact telopeptides

collagen stock solution, DMEM, DMEM10x (Sigma-Aldrich), HEPES 1M solution, antibiotics, FBS, 1M NaOH and sterilized milliQ water were stored on ice for at most 1 day, to prevent bacteria growth. Collagen type I was pipetted into a precooled 2 ml Eppendorf tube and weighed to determine the pipetted amount. We followed this procedure because the high viscosity of the collagen stock solution creates problems with accurate pipetting. We then added in the following order: DMEM1x, DMEM10x, HEPES, antibiotics, FBS and sterile milliQ water. The pH was set with NaOH, using a pH meter (Hanna Instruments, Germany) with a micro-electrode. In the case of cell-seeded collagen gels, cells suspended in DMEM 1xwere added last (after setting the pH). The final buffer composition was 1x DMEM, 1% FBS, 20mM HEPES and 0.1% antibiotics, unless stated otherwise. The time between setting the pH with NaOH and transporting the sample to a sample holder (the rheometer bottom plate or a glass-bottom petridish) was kept around 10 min to minimize possible variations due to premature polymerization on ice [607].

All collagen gels were polymerized at 37 °C in a humidified atmosphere to prevent solvent evaporation.

We performed a few experiments with cells cultured on top of collagen gels (2D situation). In this case, collagen gels were prepolymerized overnight at 37 °C in a humid atmosphere. The cell suspension was added on top of the collagen gel, in 1x DMEM, 1% FBS, 20mM HEPES and 0.1% antibiotics, and the cells were left to spread overnight.

7.2.3 Microscopy

To visualize the effect of the cells on the structure of the collagen networks, we imaged collagen gels with and without cells using an inverted Eclipse Ti microscope (Nikon). Confocal reflectance images of the collagen fibers were obtained using a 488 Ar laser (Melles Griot, Albuquerque, NM) for illumination, using a 40x (N.A. 1.30) oil immersion objective. Cells labelled with CellTracker^{TM} Green CMFDA (Invitrogen) were imaged in a separate channel using the same laser to excite a fluorescent signal. Three-dimensional image stacks to determine the time course of cell spreading inside 1 and 2 mg/ml collagen gels were obtained by scanning through the z-direction with a step size $\delta z = 0.5$ μm over a 40 μm total depth.

To quantify the degree of cell spreading, cell-seeded collagen gels were polymerized in a humid atmosphere at a 37 °C room, protected from light and imaged after overnight spreading. Images were taken using a Nikon inverted microscope in phase contrast, equipped with a 10x air objective, additional 1.5x magnification, and an EM-CCD camera (Roper Coolsnap, Photometrics, Tucson, US) with an exposure time of 200 ms. The cell spreading ratio was determined by counting the number of spread cells, round cells, and dead cells based on the cell morphology. The results are shows as normalized counts (normalized by the total number of cells). Where error bars are shown, a min-

imum of 3 measurements were averaged and the standard deviation is shown. In these cases, at least 80 cells were counted per gel.

To follow the kinetics of cell spreading, the Nikon inverted microscope was equipped with a humidified incubation chamber in combination with an objective heater to maintain a constant temperature of 37 °C (TokaiHit, Shizuoka-ken, Japan), in a similar geometry as presented in Chapter 3 (Fig. 3.1A). The cells were imaged in bright field using a 10x air objective at a rate of 1 frame/5 min or 1 frame/min. The exposure time was fixed at 200 ms. Cell viability was maintained by blocking infrared and UV light with a bandpass filter and by controlling light exposure with a light shutter synchronized with image frame grabbing. Typically, at least 10 cells were tracked per sample.

7.2.4 Rheology

Rheology tests were performed with a stress-controlled rheometer (Physica MCR 501, Anton Paar, Graz, Austria) equipped with a 40 mm steel cone and bottom plate. The cone angle was 1 °. The plates were prewarmed to 37 °C. Collagen solution (∼300 μl) was pipetted onto the bottom plate and the cone was immediately lowered. The sample was trimmed and a solvent trap was added while keeping the cone stationary. Collagen polymerization was followed continuously by applying a small amplitude (0.5%) oscillatory strain at a constant frequency of 0.5 Hz to probe the development of the elastic modulus, *G'*, and viscous modulus, *G"*, during a period of 6 hours. The linear viscoelastic moduli of the fully formed gels were determined by small amplitude (0.5%) oscillatory shear tests at a range of frequencies between 10 and 0.05 Hz. To probe the nonlinear response of the gels, we performed differential measurements using a prestress protocol. A stepwise increasing steady prestress σ was applied, and a small oscillatory stress with an amplitude of 0.1σ was superposed. The differential elastic, *K'*, and viscous, *K"*, moduli were determined from the oscillatory differential strain response. The onset of stiffening, σ_0, was defined as the point where $K' = 1.1K'_0$, where K'_0 is the linear low strain modulus.

7.2.5 qPCR

To quantify integrin expression, qPCR (quantitative real time polymerase chain reaction) analysis was used following published procedures [435]. Cells were allowed to spread overnight, either on top of collagen gels or seeded within collagen gels, at a cell density of $1000/\mu$l. Cell-seeded collagen gels were incubated for about 5 minutes on ice with TRIsure (Bioline) to isolate the RNA and vortexed until the gels were fully dissolved. The samples were stored at −80 °C until further use. RNA was precipitated in 2-propanol for 1 hour at room temperature. 500 ng of RNA was DNaseI treated and used as a template to generate cDNA following the manufacturer's instructions (Quantitect-Qiagen, Venlo, the Netherlands) with a mixture of oligo dT and random primers at

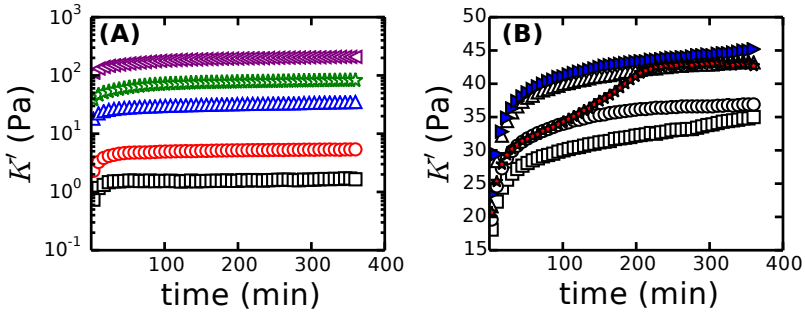

Figure 7.1: Time course of polymerization of cell-seeded and acellular collagen gels monitored by small amplitude oscillatory shear rheology. (A) Examples of the time course of the linear elastic modulus, *G'*, of cell-free collagen type I gels at collagen concentrations ranging from 0.5 to 4 mg/ml (bottom black squares to top purple left triangles). (B) Examples of polymerization curves of two individually prepared cell-seeded gels (containing 500 cells/μl and 2 mg/ml collagen; solid symbols) compared with polymerization curves of three individually prepared acellular gels (open symbols, 2 mg/ml collagen).

42°C during 30 min. The resulting cDNA (10 μl) was diluted 20-fold and served as a template in real-time quantitative PCR assays (SYBR Green PCR Master Mix (ABI)). Quantification and normalization procedures are described in detail elsewhere [436]. Briefly, a B-element primer was used to normalize the detected integrin expression, which gives an estimate of the total mRNA expression, and was developed by Jo Vandesompele (Universiteit Gent, Belgium). Primers were designed for the PCR product to be intron spanning using NCBI's Primer Blast [437]. qPCR was performed for integrin β3, β1, α1, α2, α10 and α11.

A two tailed student t-test was performed on the relative expression levels for the different integrin subunits. $p < 0.05$ was considered significant.

7.3 Results

7.3.1 Rheology of Acellular and Cell-seeded Collagen Gels

In Chapter 3, we showed that cells can stiffen fibrin gels by generating an internal contractile stress that exceeds the critical stress for strain-stiffening. Our goal for this Chapter is to investigate whether a similar stiffening mechanism exists for collagen. Previous studies mostly show an increase in collagen stiffness with increasing cell density [394,395] (see also Table 7.1), which has been

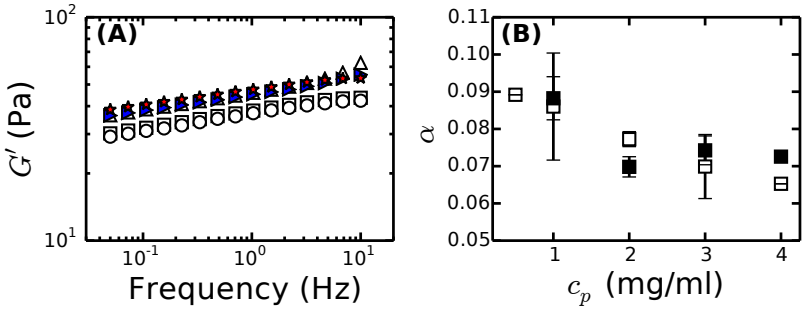

Figure 7.2: Frequency dependence of the linear elastic modulus, *G'*, for acellular (open black symbols) and cell-seeded (red and blue filled symbols) collagen gels. (A) Example curves of the frequency dependence of *G'* for 2 mg/ml collagen gels. (B) The frequency exponent for acellular (open symbols) and cell-seeded (filled symbols) collagen gels plotted as a function of collagen concentration. Cell-seeded gels contained 500 cells/μl.

attributed to a combination of cellular contractility and (permanent) matrix remodeling. In some cases, collagen decreased in stiffness, which was attributed to collagen digestion [395]. We aimed to directly measure the contribution of cellular traction and matrix remodeling on collagen network mechanics by comparing the linear and nonlinear mechanical properties of cell-seeded gels with acellular gels.

First, we investigated the polymerization kinetics of collagen in the absence and presence of cells. We measured the development of the linear viscoelastic moduli by small amplitude oscillatory shear measurements with a cone-plate rheometer. In the absence of cells, there is an immediate and rapid increase of *G'* (Fig. 7.1A). We note that the rheology experiment is started about two minutes after placing the sample on the preheated rheometer plate. The fast kinetics we observe here are consistent with prior observations for rat tail collagen I [90]. When the collagen concentration is raised from 0.5 to 4 mg/ml, the kinetics remain unchanged but the final elastic modulus increases strongly, from 1.7 Pa at 0.5 mg/ml to 200 Pa at 4 mg/ml, similar to what has been shown in Chapter 6.

When cells were included during polymerization, we observed two types of polymerization curves (Fig. 7.1B): one category showed a monotonic increase of *G'* that resembled the behavior of acellular gels (blue squares), whereas the second category exhibited a biphasic increase (red stars) for *G'* (but *not* for *G"*).

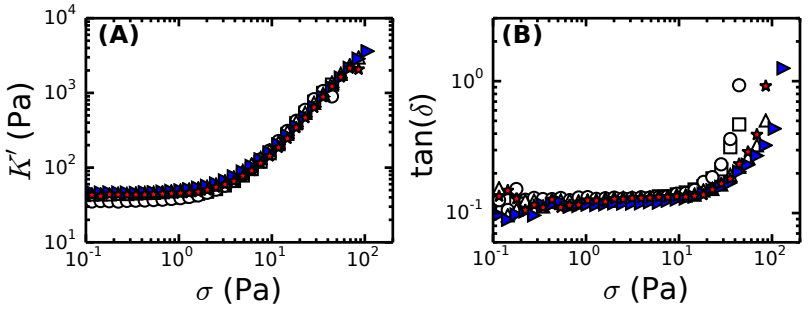

Figure 7.3: Differential measurements of the nonlinear viscoelastic response of cell-seeded collagen gels (500 cells/μl, color filled symbols) and acellular 2 mg/ml collagen gels (black open symbols). (A) Example curves for the differential elastic modulus *K'* against prestress σ. (B) Example curves for the differential loss tangent, K''/K', against prestress σ.

To probe the viscoelastic properties of the fully formed gels (considered complete after 6 hours), we performed small amplitude oscillatory shear measurements over a range of frequencies (Fig. 7.2). We observed identical behavior for the cell-seeded and the acellular gels (Fig. 7.4): the elastic modulus was only weakly dependent on frequency and much larger than the viscous modulus, indicating solid-like behavior. Furthermore, the moduli were independent of the presence of cells. For both the cell-seeded and the acellular gels, *G'* increased with collagen concentration according to an approximate power law with an exponent of around 2.5. Similar dependences have been reported in prior studies of acellular collagen gels, with reported exponents varying between 2 and 3 [253, 272, 395, 602, 603]. However, a weaker dependence on collagen concentration has also been observed [92, 251, 527, 603]. The linear modulus for cell-seeded gels was indistinguishable from that of the acellular gels for all collagen concentrations tested (Fig. 7.4A). This finding is in contrast to earlier studies, where the addition of cells was reported to cause either an increase [394] or a decrease [403] in stiffness [395]. To our knowledge, there is only one earlier study that reports no change in network stiffness [647], although this study was performed in the absence of serum.

The nonlinear elastic mechanical properties likewise showed no change upon the addition of cells, as shown in Fig. 7.3. The elastic differential modulus, K', increased with increasing shear stress (σ), after an onset stress (panel A). The modulus increased until apparent sample breakage. Close to sample breakage, the loss tangent K''/K' also sharply increased (panel B). The maximal stiffness before apparent network failure, K_{max}, increased with increasing

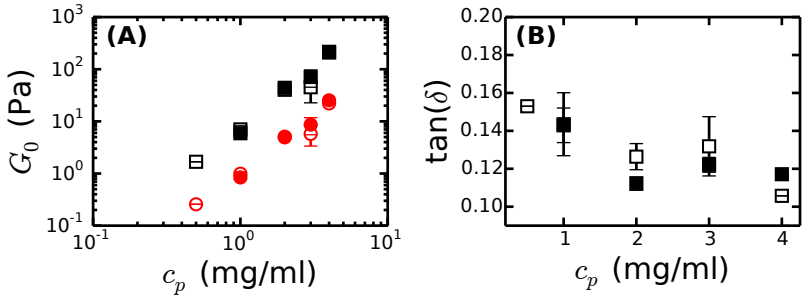

Figure 7.4: Plateau moduli G_0 (A) and loss tangent (B) of cell-seeded (closed symbols) and acellular (open symbols) collagen gels as a function of collagen concentration. (A) The plateau moduli were taken as the linear elastic moduli measured at 0.5 Hz. Black squares depict *G'*, while red circles denote *G"*. (B) Corresponding loss tangents.

collagen concentration (Fig. 7.5 panel A), but was indistinguishable from the control case without cells (panel B). The stress just before the onset of stiffening also increased with collagen concentration, and was also independent of the presence of cells. If the network architecture would be much affected by the presence of cells, one would expect a change in the onset of stiffening, as discussed in detail in Chapter 6. Also the stiffening exponent β is unaffected by the presence of cells (panel D). Altogether these observations suggest that cells do not generate enough traction forces to change the network structure and mechanical properties, nor do they significantly remodel the network by enzymatic degradation.

7.3.2 Cell Morphology and Spreading

To understand why the cells do not influence the viscoelastic properties of the collagen networks, we studied the cell morphology, survival, and the spatial distribution of cells inside the gels. To this end, fibroblast-populated collagen gels were imaged in phase contrast and in bright field. In the most dilute gels (0.5 mg/ml collagen), the cells were mainly found near the bottom glass surface, indicating that they sediment under gravity during polymerization of these soft gels. In the higher-density collagen gels, the cells were more evenly distributed, indicating that they are trapped in the network (Fig. 7.6C). Time-lapse imaging of cells during spreading showed that both at low (0.5 mg/ml) and high collagen densities (3 mg/ml), a large fraction of cells exhibited blebbing behavior. This behavior has been seen before for suspended cells [650]. A fraction of these transient blebbing cells did eventually successfully

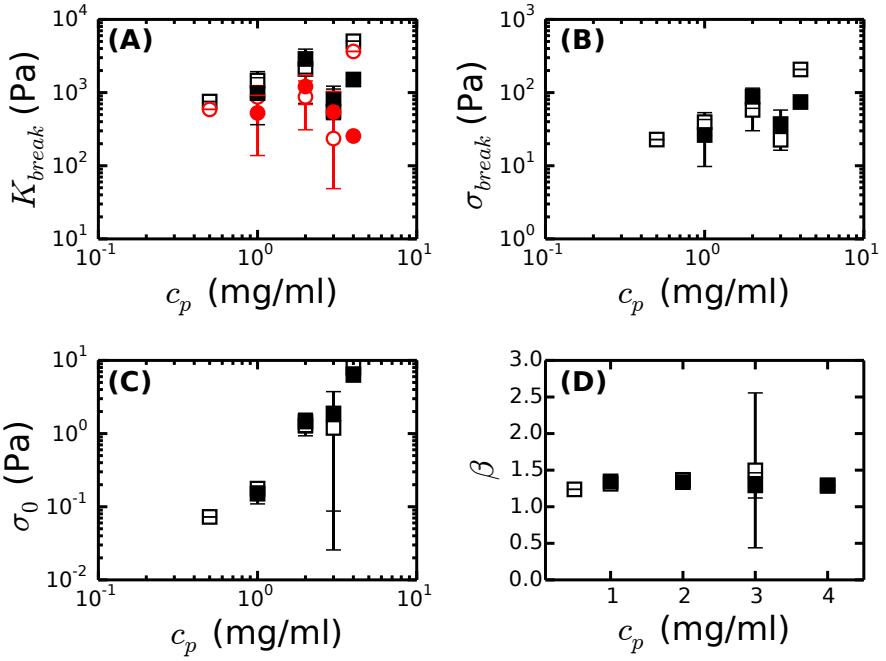

Figure 7.5: Parameters characterizing the nonlinear elastic properties of cell-seeded collagen gels (solid symbols) and acellular collagen gels (open symbols) plotted as a function of collagen concentration. (A) Maximum differential elastic and viscous moduli reached just before sample breakage. Solid symbols represent *K'*, while open symbols represent *K"*. (B) Maximum stress reached before sample breakage, σ_{break}. (C) The stress at the onset of strain-stiffening. (D) Stiffening exponent, β, defined as the power law exponent characterizing stiffening in the nonlinear elastic regime. In all cases, the cell-seeded gels contained 500 cells/μl.

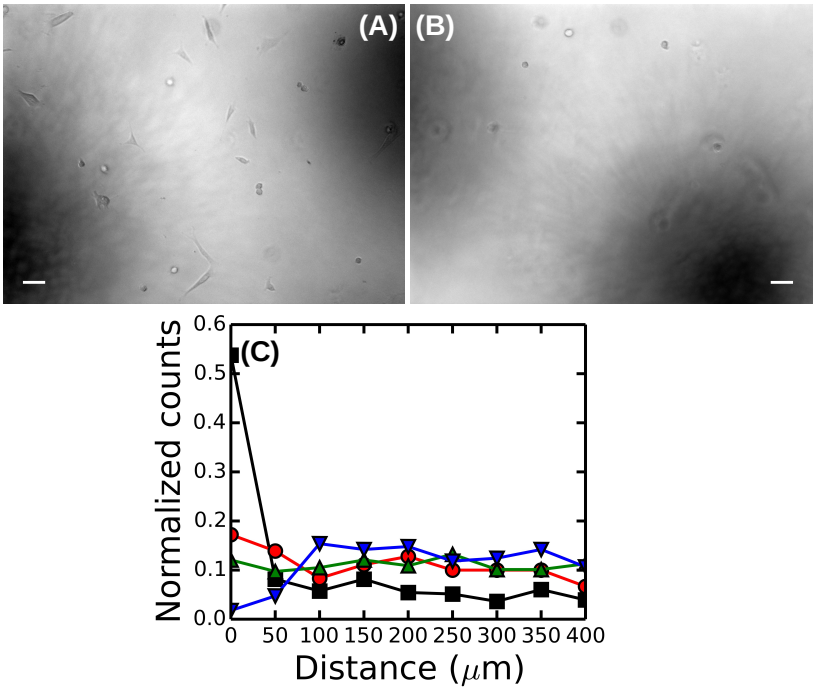

Figure 7.6: Cell distribution as a function of height inside collagen gels. (A) Typical image of cells in a 0.5 mg/ml collagen gel taken at a height of 0 μm from the bottom coverslip surface. (B) Typical image of cells in a 0.5 mg/ml collagen gel taken at a height of 200 μm. Scale bars denote 50 μm. (C) Cell distribution as a function of height, where a height of zero corresponds to the bottom coverslip surface, for 0.5 mg/ml (black squares), 1 mg/ml (red circles), 2 mg/ml (green triangles up) and 3 mg/ml (blue triangles down) collagen. Every data point is an average over 10 images, where only cells that were well in focus were counted.

spread (Fig. 7.7). The time point where cells first started to spread varied greatly, from almost immediately after the start of collagen polymerization to about 5 hours later. Most of the cells remained round, indicating that they did not spread well (Fig. 7.9A).

The cells that did spread exhibited highly dynamic membrane extensions, which were observed both for high and low collagen concentrations (Fig. 7.7B and C). Time-lapse imaging showed that new extensions were formed every 20-30 minutes and retracted at similar time scales. We observed polar cell shapes and random ('star') shaped morphologies, resembling previous observations of fibroblasts in type I collagen gels [393, 403, 410, 651, 652]. Highly dynamic extensions are indicative of low force generation, since focal adhesions need time to mature to permit transmission of high traction forces (see section 1.6.1 in Chapter 1).

To verify whether the cells attached to the collagen networks, we performed confocal imaging of cell-seeded gels, using fluorescence imaging to visualize the cells, which were labeled with CellTracker^{TM} Green CMFDA, and reflectance imaging to visualize the collagen fibers. We observed that the round cells did attach to the surrounding collagen network, although they did not extend protrusions into the collagen networks (Fig. 7.8A). In some cases, we observed density modulations in the collagen network surrounding the cells, with densifications and empty pockets near the cell surface (Fig. 7.8B). These remodeled regions extended out to distances ranging up to 3 times the cell diameter, leaving the rest of the network unaltered. For well-spread cells with membrane protrusions, extensive recruitment of collagen was seen near the cell body and the cellular extensions (Fig. 7.8C). Similar local condensation of collagen fibrils has been reported before [394, 410, 653, 654], where collagen fibers aligned along the direction of the cellular traction forces. The notion of local collagen densification around the cells has been used to model the low strain mechanics of cell-seeded collagen gels [394]. The empty pockets near round cells are reminiscent of prior observations of collagen matrix degradation by cell-secreted proteases [395].

We tested various possible scenarios that might explain the limited extent of cell spreading. First, cell spreading could be hampered due to the small mesh size of the collagen gels. To investigate this possibility, we varied the collagen concentration between 0.5 and 3 mg/ml, corresponding to a three-fold decrease of the pore size from $\sim$10 down to $\sim$3 μm^2 [90, 92, 194]. The largest pore size is thus about half the cell size, which is about 20μm^2, which should be large enough to allow for cell spreading and migration [90]. However, the spreading ratio did not change with collagen concentration (see Fig. 7.9A). It is thus unlikely that effective cell spreading is restricted by the collagen mesh work. The second scenario that we tested is that the serum concentration in the cell culture medium was insufficient to promote cell spreading, in view

Figure 7.7: Time-lapse image sequences of cells spreading inside collagen gels. (A) Example of a cell in a 0.5 mg/ml collagen gel that stays spherical over the entire 6 hour time scale that was investigated and exhibits transient blebbing. (B) Example of a cell that spreads inside a 3 mg/ml collagen gel. During the first hour, the cell shows blebbing behavior. (C) Example of a spreading cell in a 0.5 mg/ml collagen gel. Blebbing was apparent in the first few hours, similar to the example shown in panel B. Scale bars denote 50 μm. The cell density was 500-1000 cells/μl for all cases.

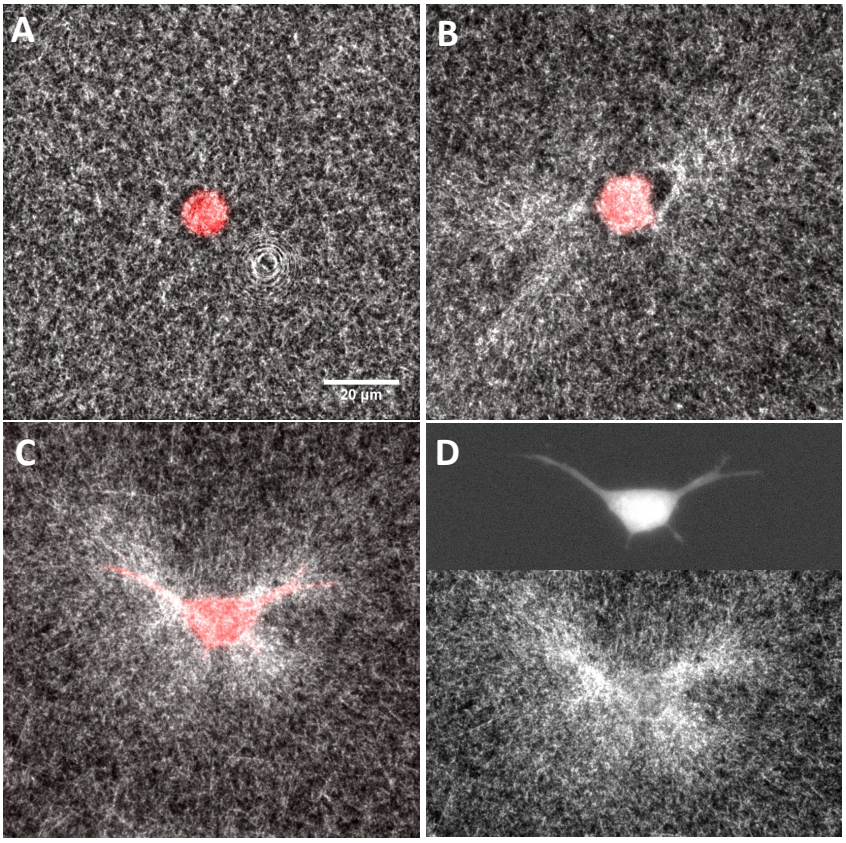

Figure 7.8: Confocal images of cells fluorescently labeled with CellTracker™ Green CMFDA (shown in red red) inside 2 mg/ml collagen gels (reflectance channel, shown in white). (A) Merged image of a cell which, despite having a round morphology, shows attachments to the collagen network. (B) Merged image of another round cell, where the surrounding network shows signs of remodeling. (C) Merged image of a well-spread cell, with extensive collagen recruitment around the cellular protrusions. (D) Same image as (C), but now fluorescence channel (top) and reflectance channel (bottom) are split. All images are summations of images acquired over a total depth of 40 μm. The cell density was 1000 cells/μl. Scale bars denote 20 μm.

of reports showing effects of serum concentration on cell-induced contraction of collagen gels [647, 652, 655, 656]. However, we observed no change in cell

spreading over a serum concentration range of 1 to 4% (Fig. 7.9C). The third scenario that we tested is that cell spreading could depend on cell density. We observed a decrease in cell spreading and a concomitant increase in cell death with increasing cell density (Fig. 7.9B), possibly due to depletion of nutrients. Finally, we tested whether cells spread better on top of collagen gels instead of inside the gels. Cells were seeded on top of thick collagen gels and incubated overnight at a range of cell densities (Fig. 7.9D). We observed an even smaller fraction of spread cells than inside the gels. The fraction of spread cells was also low compared to prior observations for cells cultured on top of 2D glass coated with fibrillar collagen I [657]. Moreover, the latter study reported an increase in cell spreading with increasing cell density, opposite to the trend we observe here for cells inside collagen gels.

A few other studies also reported a mixture of spread and round cells, both inside and on top of collagen gels [606, 658]. However, we cannot make a quantitative comparison to those data, since the spreading ratio was not quantified. It is known that fibroblasts spread better in anchored collagen gels in which contractile tension can build up, than in free-floating collagen gels [632, 643, 659, 660]. This is not likely to be the limiting factor in the rheology and imaging experiments, since the gels are adhered to the cone and plate and glass surfaces, respectively. Moreover, even in a freely floating gel where there is no build-up of tension, the cells should still show spreading, albeit less compared to a gel with fixed boundaries [660].

Figure 7.9 ***(facing page)*****: Fibroblast spreading ratios measured under different experimental conditions. Top panels: Cells were classified as spread when they exhibited extensions, round (and non-spread) if they retained a spherical shape and did not make protrusions, or dead, when the cell showed fragmentation and was not spread. (A) Normalized counts of morphologies observed in collagen gels under standard culture conditions, plotted as a function of collagen concentration. Each data point corresponds to a measurement on one gel with a cell density of 500 cells/μl, where about 100 cells were counted. (B) Cell spreading ratios in gels of a fixed collagen concentration (2 mg/ml), plotted as a function of cell density. The error bars represent standard deviations over 3 independent measurements, except for the data point at 500 cells/μl, which shows one measurement. (C) Cell spreading ratios for cells cultured inside 2 mg/ml collagen gels at a fixed cell density of 1000 cells/μl, plotted as a function of serum concentration. One measurement was done per data point. (D) Cell spreading ratios for cells spreading on top of thick collagen gels (1 mg/ml). One measurement was done per data point. Inset in (D): Example image of spread and round cells on top of thick collagen gels. Scale bars of all the images denote 50 μm.**

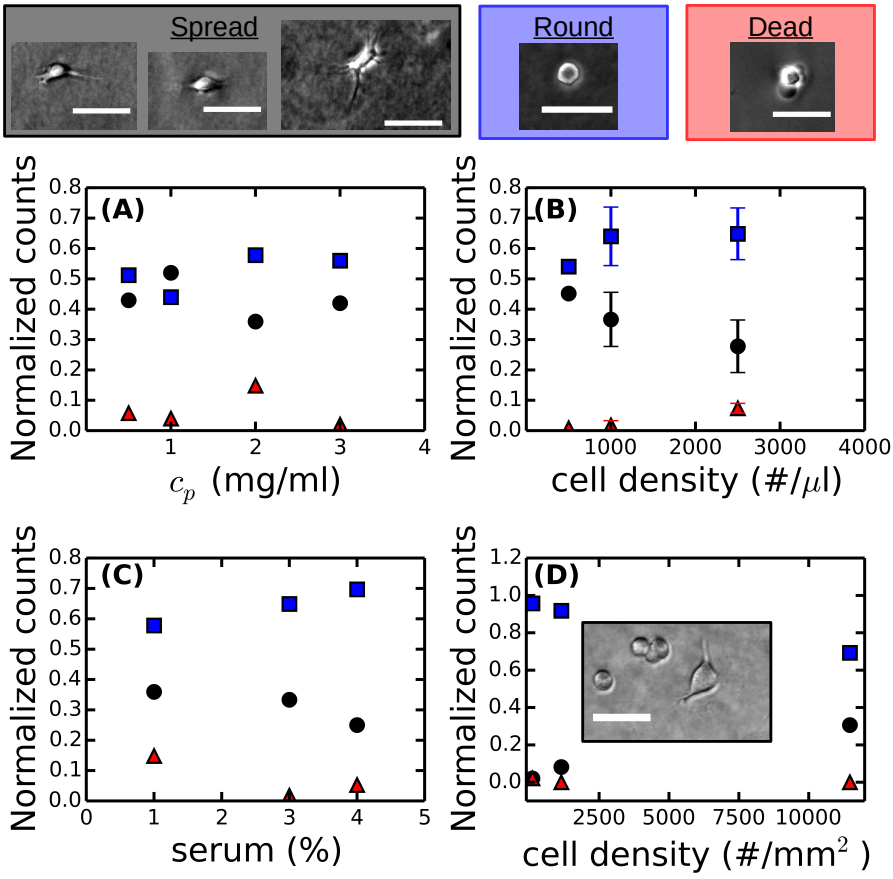
Spread
Round
Dead
(A)
Normalized counts
c_p (mg/ml)
(B)
cell density (#/μl)
(C)
serum (%)
(D)
cell density (#/mm^2)

7.3.3 Integrin Expression

In an attempt to further resolve the question why the cells do not spread well in the collagen gels, we determined the expression levels of integrins that are known to bind collagen using qPCR (see Fig. 7.10). We compared integrin expression levels for cells cultured either on top of thick collagen gels or inside collagen gels, using the same samples that were used for quantification of spreading ratios (data shown in Fig. 7.9B and Fig. 7.9D). Known collagen-binding integrins are mostly heterodimers of $\beta 1$ integrins with $\alpha 1$, $\alpha 2$, $\alpha 10$, or $\alpha 11$ [24, 661–663]. These integrins differ in binding strength and are associated with different cell behaviors [662, 664] (see Table 7.2). Integrin $\alpha v\beta 3$ can indirectly bind to collagen via fibronectin (which is present in serum) or fibrin [665] and can directly bind to RGD sequences in the triple helical domain of collagen [666]. Different collagen-binding integrins play distinct roles in regulating cell behavior. For instance, $\alpha 1\beta 1$ is related to cell proliferation inside collagen gels, $\alpha 2\beta 1$ is related to cellular contraction and matrix remodeling [664], and $\alpha v\beta 3$ is related to cell migration inside collagen gels as well as contraction [666].

We found that the integrins $\alpha 1$ and $\alpha 10$ are only sporadically expressed by cells cultured on top of collagen gels (2D case) or inside of collagen gels (3D case), as shown in Fig. 7.10A. This result is not surprising, since integrin $\alpha 10$ is expressed by chondrocytes and highly specialized fibroblasts [667, 668] *in vivo* and mostly in collagen type II expressing tissues. The integrins $\alpha 11$ and $\beta 1$ are expressed in all three cases that we investigated, i.e. cells on top of a 2 mg/ml collagen gel, and cells inside 1 mg/ml or 2 mg/ml collagen gels. For integrin αv, the expression was elevated in the 3D case compared to the 2D case ($p<0.05$, 1 mg/ml). Interestingly, however, the dimerization partner, integrin $\beta 3$, did not follow the same trend (panel B) ($p>0.05$). Instead, $\beta 3$ increased when the collagen density was increased from 1 mg/ml to 2 mg/ml in the 3D case ($p<0.05$). This could mean that αv dimerizes with a different integrin partner in our system, or that there is enough $\beta 1$ present in the cytosol as dimerizing partner until more ligands (i.e. collagen) are presented to the cell membrane. The integrin $\alpha 2$ is expressed, though not for all the samples tested and there was no significant difference between 2D and 3D for this integrin subunit. The $\beta 1$ subunit was expressed in all the samples tested (panel B). Without the $\beta 1$ subunit, cell spreading, migration and ECM compaction is reduced [669] and loss of $\beta 1$ is embryonic lethal in mice [8]. Interestingly, the expression of $\beta 1$ decreases with dimensionality (i.e. going from 2D to 3D), following the opposite trend to $\beta 3$. These data suggest that the 3T3 cells do express receptors for collagen, and the most likely candidate is the integrin $\alpha v\beta 3$, since its two subunits increase in expression upon increasing the ligand (i.e. collagen) density. This integrin is related to cell contraction. Together with the confocal imaging of collagen networks in the neighborhood of spread cells

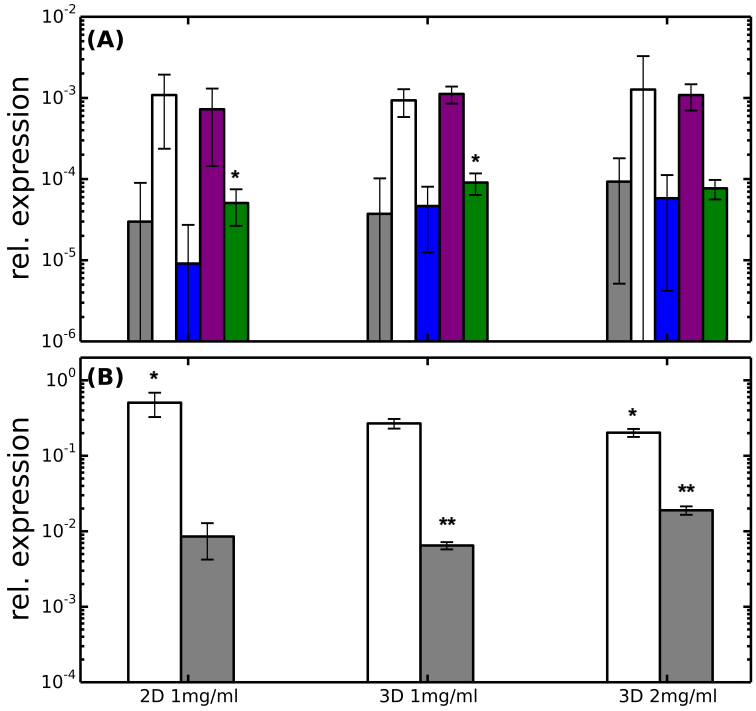

Figure 7.10: Relative integrin expression levels for the α integrin subunits (A) and the β integrin subunits (B) measured by qPCR in 3 different conditions. (A) Five different α integrin subunits were checked. From left to right: α1 (gray), α2 (white), α10 (blue), α11 (purple) and αv (green). (B) Two different β integrin subunits were checked. From left to right: β1 (white) and β3 (gray). The cell density was 1000 cells/μl. Stars indicate statistically significant differences between the two indicated conditions ($p<0.05$).

(Fig. 7.8), we can conclude that the 3T3 cells are in principle able to attach to the collagen matrix. However, time-lapse movies of cells spreading using bright field microscopy show thin and highly dynamic protrusions (Fig. 7.7). We therefore hypothesize that these cells do not form mature focal adhesions, which result in a lack of large traction forces. This would explain why our microscopy images show little evidence of cell-induced network contraction, and the rheology data show no change in network stiffness.

Given that studies reported in the literature use different sources of col-

lagen, we decided to compare cell spreading in gels prepared from either rat tail collagen or bovine dermal collagen, the two main sources of collagen that have been used. Confocal reflection imaging of these networks prepared at the same concentration shows that bovine dermal collagen forms a network with larger pores than rat tail collagen (Fig. 7.11) [90, 606]. Thus, one might anticipate better cell spreading since the pores are less confining and the fibers are thicker and allow for larger focal adhesions to form. Surprisingly, the cell spreading ratio in gels prepared from bovine dermal collagen was even smaller than in gels prepared from rat tail collagen, as shown in Fig. 7.12. Perhaps the biochemical cues offered by the gels made of bovine dermal collagen are less favorable than for gels made of rat tail collagen. One important difference is that the bovine dermal collagen is pepsin-treated and therefore lacks the telopeptides, in contrast to rat tail collagen.

We conclude that the 3T3 fibroblast cells, even though they have been widely used in other studies [643, 651, 660, 670, 671], may not be ideal for studying the effect of cellular traction forces on collagen mechanics. This idea is supported by a recent study, showing that 3T3 fibroblasts exert only small traction forces on a surrounding collagen matrix as judged from limited matrix remodeling over time [671]. Also, it has been suggested that the 3T3 cell line can lose their ability to contract collagen gels [528]. Indeed, a reduced ability to contract collagen gels have been reported for some established cell lines [672]. To test the hypothesis that the 3T3 cell line might not be ideal, we did a pilot experiment using a different fibroblast cell line (CCL224, Fig. 7.12), which we selected because these cells showed excellent cell spreading inside 3D fibrin networks (see Chapter 3). With this cell line the spreading ratio inside 3D collagen networks improved from about 0.4 to about 0.7.

7.4 Conclusion and Outlook

Our original aim was to understand the effect of cell-generated traction forces on the nonlinear mechanical properties of cell-seeded collagen gels. However, we discovered in our rheology assay that there was no difference in the mechanics of cell-seeded and acellular collagen gels, even though several earlier studies showed otherwise (see Table 7.1).

Imaging of the gels by optical microscopy revealed that a large fraction of the fibroblasts did adhere to the collagen gels, but they stayed round and did not exert substantial traction. Cell spreading was not improved when we tested several parameters known to affect cell spreading (serum concentration, collagen density, and cell density). qPCR analysis confirmed that the fibroblasts do express known collagen-binding integrins. This result was consistent with confocal imaging, which revealed that the cells developed cellular extensions that attached to collagen fibers. Time-lapse imaging revealed that the cells showed transient blebbing behavior in the first hour or so, before thin and dy-

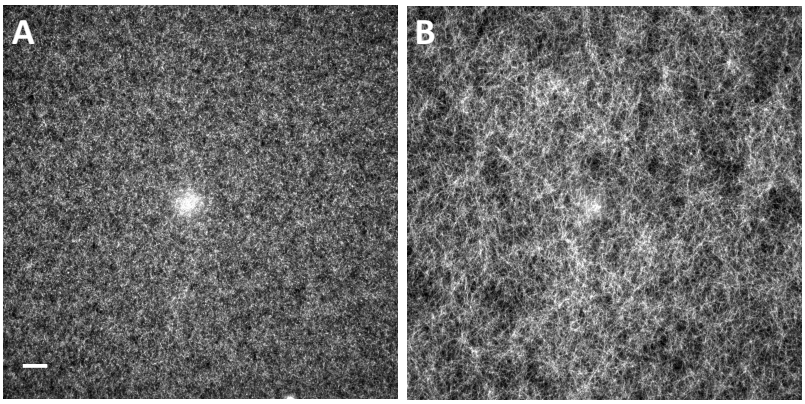

Figure 7.11: Confocal reflection images of 2 mg/ml collagen type I gels prepared from different collagen sources. (A) Rat tail collagen. (B) Bovine dermal collagen. Scale bars denote 20 μm. Images are summations of images acquired over a total depth of 40 μm in z

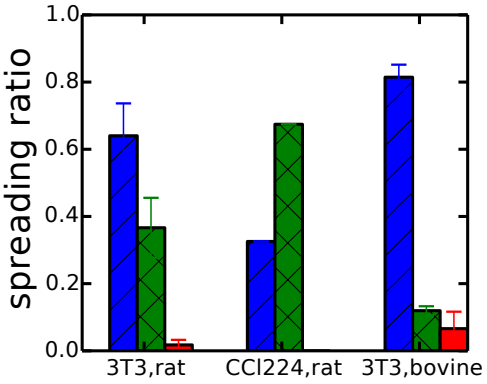

Figure 7.12: Cell spreading ratio for 3T3 ('3T3') and CCL224 ('CCL224') fibroblasts, which were cultured inside 2 mg/ml rat tail collagen ('rat') or bovine dermal collagen ('bovine') networks. Blue bars denote a spherical cell morphology, green bars are spread morphologies and red are dead cells. The cell density was 1000 cell/μl. For the 3T3 cell line, we have 2 samples per condition, while we have 1 for the CCL224 case.

namic extensions were seen. We hypothesize that, due to the highly dynamic nature of these extensions, there is insufficient focal adhesion maturation to support large traction force generation.

We conclude that the fibroblasts here are not an ideal candidate cell line to test how cellular traction forces influence collagen mechanics. Cells that are known to show substantial force generation and spreading inside collagen would be better candidates, for instance human corneal fibroblasts [673] or myofibroblasts [674].

7.5 Acknowledgments

I would like to thank Oscar Stassen and Elly Hol for performing the qPCR experiments, Dominique Donato and Thomas Schmidt for the 3T3 cell-line, Hendy Kristyanto for starting this project, our technician Marjolein Vinkenoog for testing the Celltracker dye and Prof. J. Boonstra for his gift of the CCL224 cell-line. Furthermore, I would like to thank everyone from the MechanobiologyNL FOM program for helpful discussions, in particular Hayri E. Balcioglu for discussion about the 3T3 cell line. This work is part of the research programme of the Foundation for Fundamental Research on Matter (FOM), which is financially supported by the Netherlands Organisation for Scientific Research (NWO). This work is further supported by NanoNextNL, a micro and nanotechnology programme of the Dutch Government and 130 partners.

Table 7.2: Collagen type I integrins: Summary of their binding strength and function.

Ref.	Integrin	Relative Binding strength [10]	Function
[649, 663, 664, 675, 676]	$\alpha1\beta1$	Binds more weakly compared to $\alpha2\beta1$	Stimulates proliferation and decreased collagen production.
[663, 664, 675, 676]	$\alpha2\beta1$	High binding strength	Stimulates cell contraction and matrix remodeling.
[675]	$\alpha10\beta1$	Similar binding strength as $\alpha1\beta1$	Important for cartilage development.
[664, 677]	$\alpha11\beta1$	*unknown*[11] [12]	Stimulates cell contraction and collagen remodeling (similar to $\alpha2\beta1$).
[664, 666]	$\alpha v\beta3$	*unknown*[11]	Stimulates cell contraction and cell migration.

[10] Predicted from cell spreading experiments on top of 2D substrated coated with collagen fibrils.

[11] To our knowledge not quantified or compared with other collagen binding integrins.

[12] $\alpha11$ was identified as a collagen I receptor based on binding of the $\alpha10$I domain, using solid phase binding assays.

8. English Summary

The cells inside our body do not sit alone. Each cell is surrounded by neighboring cells and a mesh work termed the extracellular matrix (ECM). The ECM provides chemical information in terms of ligands and growth factors, mechanical information in terms of elastic stiffness and viscous dissipation, and structural information in terms of dimensionality, mesh size, and local nanotopography. The cell actively senses the mechanical cues in a process referred to as *mechanosensing* and responds to them in a process referred to as *mechanoresponse*, as discussed in detail in Chapter 1.

Mechanobiology is a growing interdisciplinary field involving biologists, chemists, engineers, and physicists. Until now, cellular mechanosensing has mostly been studied using synthetic gels like polyacrylamide, which have much simpler mechanical and chemical properties than biological tissues. Synthetic gels are characterized by one stiffness value over a wide range of strain levels, and they tend to be mainly elastic. In contrast, ECM networks stiffen when subjected to a mechanical deformation (*strain-stiffening*) as a consequence of their fibrous and hierarchical structure. The physical origin of this strain-stiffening response and the consequences for cell-matrix interactions are not clear. The central goal of this thesis was to elucidate the origin of the mechanical properties of two important ECM networks: fibrin (Chapter 2-5) and collagen (Chapter 6 and 7). Both of these ECM networks are widely used as model systems for studying cell-matrix interactions in three dimensions *in vitro*. We use shear rheology to measure the viscoelastic properties of networks reconstituted from purified fibrinogen and collagen, and compare our data with theoretical models for semiflexible polymers. In addition, we embedded cells in the ECM networks and tested whether the cells are able to change the structural and mechanical properties of the matrices.

Fibrin is a temporary ECM network that forms at sites of vascular injury to stop the bleeding. Cells use this matrix to migrate to the injury site and rebuild the lost tissue. The fibrin network thus needs to be able to withstand substantial forces, both from blood flow and cellular traction forces. In Chapter 2, we showed that the strain-stiffening response of fibrin is directly related to the hierarchical architecture of the fibrin fibers. Fibrin fibers are built up of semiflexible protofibrils, which are coupled together by covalent crosslinking mediated by the enzyme FXIII. We discovered that the mechanical properties of fibrin networks polymerized under conditions that suppress protofibril bundling agree well with predictions of an entropic network model, where stretching out of fiber undulations gives rise to stiffening. By varying

the number of protofibrils inside a fibrin fiber, and by varying how tightly these protofibrils are coupled together, we showed that the stiffness of fibrin networks is well described by a model that treats the fibers as semiflexible polymer bundles with a rigidity that is controlled by the protofibril number and the degree of intrafiber crosslinking.

An important consequence of the strain-stiffening response of fibrin gels is that cells can actively stiffen the gels, as shown in Chapter 3. The cells generate traction forces using their actomyosin cytoskeleton, which drives the fibrin network into a stiffened state. The low-strain modulus of cell-seeded fibrin gels is a function of cell density, while the nonlinear mechanical properties remain unaltered. This work has important implications for studying cell-matrix interactions in a three dimensional ECM environment, since cellular traction can create a (local) stiffer environment that can act as a positive feedback loop for cellular mechanosensing.

The entropic network model presented in Chapter 2 describes fibrin mechanics accurately, except at very high strain levels. One central assumption of the model is a constant stretch modulus of the protofibrils. However, it was previously shown by micromanipulation studies that fibrin fibers are elastomeric and stiffen when stretched. Various mechanisms for this nonlinear force-extension behavior have been proposed, including forced unfolding of fibrin monomers. However, direct evidence for any of these mechanisms is still lacking. To investigate whether forced monomer unfolding contributes to the elastomeric and nonlinear mechanics of fibrin networks, we performed *in situ* small-angle X-ray scattering (SAXS) measurements on uniaxially stretched fibrin networks to probe changes in molecular packing structure. By comparing our results with SAXS spectra calculated from molecular dynamics simulations of protofibril stretching, we showed that network stretching indeed causes unfolding of the γ-nodule of the fibrin molecules starting at a strain level of 30%. Moreover, the alpha-helical coiled coils are transformed into beta-sheet structures, explaining the extensibility as well as stiffening of fibrin fibers upon stretching. Altogether, our results show that fibrinogen unfolding plays a dominant role in fibrin network extension at high strain levels.

Most work on ECM mechanics has focused on the network mechanics on a global length scale, as probed by macroscopic shear rheology or tensile tests. However, cells embedded in an open fibrous ECM network probe its mechanical properties at a scale comparable to their own size, i.e. on the micron scale. To gain insight into the local mechanical properties of ECM networks, we have developed an optical tweezer setup to track the thermal displacement fluctuations of micron-sized probe beads embedded in an ECM network as a probe of the local shear modulus, as described in Chapter 5. By using a quadrant photodiode for position detection, we could probe the shear modulus over a broad frequency range from 1 Hz to 20 kHz. From the high frequency response,

which originates from the fluctuations of the fibrin fibers, we could infer that fibrin fibers behave as thermally undulating, semiflexible polymers, consistent with the entropic network model presented in Chapter 2. At low frequencies, we could measure the local network modulus, which we found to be in the same range as measured with macrorheology (within a factor 3). However, the magnitude of the local modulus depended on the probe surface properties, which we could relate to changes in the local network microstructure around the probe particles.

In Chapter 6 we switch our attention to collagen ECM networks. Collagen type I is the most abundant protein in the mammalian body and is widely used as an ECM model system for studying cell-matrix interactions *in vitro*. Despite its widespread use, the mechanics of collagen remains poorly understood. In Chapter 6, we measured the nonlinear elastic properties of collagen networks and showed that these are in quantitative agreement with an athermal network model, where stiffening occurs as a consequence of the submarginal connectivity of these networks. The average number of fibers coming together at each network junction is between 3 and 4, which is less than the Maxwell criterion for isostaticity of 3D spring networks, which requires a critical connectivity of 6 for network stability. At low strain, collagen networks are stabilized by the bending rigidity of the fibers. With increasing strain, a negative normal stress builds up, which causes network stiffening. When the strain reaches values on the order of 30%, the network undergoes a transition to stretch-dominated elasticity. We show that the strain-stiffening response of collagen networks shows signatures of an underlying mechanical phase transition. By varying collagen architecture through the protein concentration and polymerization temperature, we showed that the local architecture, in terms of the connectivity, governs the linear modulus and the strain-stiffening response. We can now use the athermal network model to predict the stiffness of collagen networks with more complex compositions and to study cell-collagen interactions.

In Chapter 7 we set out to test whether cellular traction forces could actively stiffen collagen networks in a similar manner as for the fibrin gels studied in Chapter 3. However, we could not observe any measurable difference in the mechanical properties of cell-seeded gels and unseeded gels. By using microscopy, we could track the absence of cell-induced matrix stiffening down to limited cell spreading inside the networks. We investigated several factors known to influence cell spreading, but to no affect. We conclude that, while in principle the cell line we used (3T3 fibroblasts) does express integrins that bind collagen I, this cell line is not ideal for studying the effect of cellular traction forces on collagen mechanical properties.

In summary, in this thesis we showed the physical basis for the remarkable strain-stiffening behavior of two major components of the ECM, namely fibrin and collagen. A major new insight is that the molecular packing structure of

the fibers plays an important role in controlling the network mechanics. Even though collagen and fibrin fibers have similar diameters and build networks with a comparable architecture, fibrin networks exhibit entropic elasticity and elastomeric properties with rupture strains of up to 200%, whereas collagen networks behave as athermal fibrous networks that break at strains of only 40%. We attribute this remarkable difference to the difference in packing structure of the two systems: collagen fibers are rigid, tightly packed bundles of thousands of collagen molecules across, whereas fibrin fibers are flexible, open bundles containing only on the order of 100 fibrin molecules across. Also, the presence of molecular domains that can undergo forced unfolding plays a major role in the mechanics of fibrin networks.

The work in this thesis can provide new insights into the origin of mechanical deficiencies in human diseases related to mutations in collagen and fibrinogen. Also, the mechanical models presented in this work can in future be utilized to design either bio-based or synthetic materials of a desired stiffness, for instance for tissue engineering purposes. Finally, the difference in mechanical behavior of fibrin and collagen networks likely has consequences for cellular mechanobiology.

9. Nederlandse Samenvatting

Cellen in ons lichaam zitten niet alleen. Iedere cel is omgeven door andere cellen en een fiber netwerk genaamd de extracellulaire matrix (ECM). Dit netwerk geeft structuur en stijfheid aan het weefsel, zodat weefsels interne en externe krachten kunnen weerstaan. Cellen oefenen continu kracht uit op hun omgeving ('tractiekrachten') om er informatie over in te winnen. Mensen doen iets vergelijkbaars: We oefenen krachten uit met onze handen om te voelen hoe stijf iets is. Dat de omgeving stijf of zacht is heeft belangrijke consequenties. Een mooi voorbeeld hiervan is dat de mechanische eigenschappen alleen al kunnen bepalen in welke cel een stamcel differentieert. Hoe een cel reageert op de mechanische eigenschappen van zijn ECM omgeving wordt *mechanosensing* genoemd. Dit process wordt in detail besproken in hoofdstuk 1.

Het veld *mechanobiology* is een groeiend interdisciplinair gebied waar zowel biologen, chemici, ingenieurs en natuurkundigen aan meewerken. Tot nu toe wordt cellulaire mechanosensing vooral onderzocht met synthetische polymeer substraten, zoals polyacrylamide. Deze substraten hebben eenvoudige mechanische en chemische eigenschappen vergeleken met de ECM: Ze worden beschreven door een enkele stijfheid die niet afhangt van de kracht die erop uitgeoefend wordt. De ECM is echter heel complex: Het wordt namelijk stijver met toenemende deformatie (genaamd '*strain-stiffening*'). Dit komt deels door de hierarchische fiber structuur. Het doel in dit proefschrift, getiteld 'Extracellulaire Matrix Mechanica en de Consequenties voor Cellulaire Mechanosensing', was om te onderzoeken waar deze bijzondere mechanische eigenschappen van twee belangrijke ECM networken vandaan komen: fibrine (hoofdstuk 2−5) en collageen (hoofdstuk 6 en 7). Deze twee netwerken worden vaak gebruikt als model systemen om cel-matrix interacties te bestuderen, zowel in 2D als 3D. We gebruiken macroscopische deformatie (macrorheology) om de elastische en visceuze mechanische eigenschappen te meten van de twee netwerken en vergelijken dit met theoretische modellen voor semiflexibele polymeer netwerken. We kijken ook naar het effect van cellen op de structurele en mechanische eigenschappen van deze twee netwerken.

In hoofdstuk 2 bestuderen we de mechanische eigenschappen van fibrine. Fibrine is een tijdelijk netwerk dat vormt wanneer we ons verwonden en is de eerste stap naar de vorming van een korst. Cellen gebruiken dit netwerk om naar de wond te migreren en om het verloren weefsel te herstellen. Fibrine moet voor zijn taak dus substantiele krachten kunnen weerstaan, namelijk de deformaties door de bloedstroom en deformaties door cellulaire tractiekrachten. De fibrine fibers zijn opgebouwd uit semiflexibele protofibrillen, die met elkaar

verbonden zijn door permanente bindingen (gemaakt door het enzyme FXIII). Door de polymerizatie condities te variëren hebben we netwerken gecrieëerd bestaande uit hele dunne protofiberbundels. We laten zien dat de mechanische eigenschappen van deze netwerken goed beschreven worden door een entropisch netwerk model. Dit model voorspelt dat het 'strain-stiffening' gedrag komt door het uitrekken van de thermische fluctuaties in de fibers. We hebben ontdekt dat de mechanische eigenschappen van fibrine netwerken goed beschreven kunnen worden door een bundel model dat stelt dat de stijfheid van het *netwerk* afhangt van hoeveel protofibrillen een fibrine *fiber* heeft en hoe sterk deze protofibrillen verbonden zijn aan elkaar.

Een belangrijke consequentie van het 'strain-stiffening' gedrag van fibrine netwerken is dat cellen actief de stijfheid van hun omgeving kunnen aanpassen. Dit wordt in detail gebestudeerd in hoofdstuk 3. Wanneer cellen in een fibrine netwerk zitten, wordt het fibrine netwerk stijver door de tractiekrachten van de cellen op het netwerk. De stijfheid van zo'n netwerk bij kleine deformaties is afhankelijk van de celldichtheid, terwijl de stijfheid bij grote deformaties niet verandert vergeleken met netwerken zonder cellen. Cellen kunnen dus hun omgeving stijver maken door de krachten die ze uitoefenen, wat als weer terug gekoppeld kan worden naar mechanosensing van de cel. Met andere woorden, cellen reageren niet op de stijfheid van het netwerk die het zou hebben zonder cellen, maar op de (stijvere) modulus die het netwerk heeft door de interne tractiekrachten.

Het entropisch model dat gepresenteerd is in hoofdstuk 2 beschrijft de mechanica van fibrine netwerk goed, behalve bij grote deformaties. Een belangrijke aanname in dit model is dat de protofibrillen in de fibrine fibers een constante modulus hebben, net zoals een veer een constante veerconstante heeft die niet verandert met de uitgeoefende kracht. Echter, experimenten op individuele fibrine fibers hebben aangetoond dat deze fibers stijver worden wanneer ze worden uitgerekt. Er zijn meerdere verklaringen voor dit fenomeen, waaronder het ontvouwen van fibrine monomeren in de fibers. Echter, geen enkele van deze verklaringen zijn tot nu toe direct gelinkt aan experimenten. In hoofdstuk 4 rekken we fibrine netwerken uit en kijken we naar de moleculaire lengteschalen in de fibrine fibers met small-angle X-ray scattering (SAXS). Deze SAXS spectra vergelijken we met gesimuleerde spectra van uitgerekte protofibrillen, gebruikmakend van molecular dynamics simulaties. We laten zien dat ontvouwing van de γ-nodule van fibrine moleculen plaatsvind bij een uitrekking van 30%. Dit gaat gepaard met veranderingen in de structuur van de monomeren in de fiber, waarbij de alpha-helical content in de monomeren omlaag gaat en deze worden omgezet in (stijvere) beta-sheets. Dit zorgt ervoor dat fibrine fibers erg uitrekbaar zijn en het verklaart ook waarom ze stijver worden. Dit werk laat zien dat ontvouwing van fibrine moleculen een belangrijke rol speelt voor de uitrekbaarheid van fibrine netwerken bij hoge mechanische

deformaties.

Het meeste werk dat zich richt op het bestuderen van de mechanische eigenschappen van de ECM maken gebruik van macroscopische meettechnieken, zoals extensie testen en macrorheologie. Echter, een cel in een 3D netwerk ziet niet het hele netwerk, maar juist de fibers in hun directe omgeving. Met andere woorden, cellen meten de mechanische eigenschappen om de micron schaal, in plaats van de millimeter of centimeter schaal. Om meer inzicht te krijgen in de mechanische eigenschappen op deze kleinere lengteschaal, maken we gebruik van een optisch pincet ('optical tweezer') in hoofdstuk 5, waarbij we de thermische fluctuaties van kleine deeltjes bestuderen in fibrine netwerken. Deze thermische fluctuaties geven informatie over de lokale mechanische eigenschappen over een breed frequentie bereik (1 Hz tot 20 kHz), waardoor we zowel informatie winnen over de stijfheid van het netwerk (lage frequenties) en van individuele fibrine fibers (hoge frequencties). We laten zien dat fibrine fibers zich gedragen als semiflexibele polymeren, dat consistent is met het model gepresenteerd in hoofdstuk 2. De stijfheid gemeten bij lage frequenties komt in de buurt van wat we meten met macrorheology, echter de absolute waarde is afhankelijk van de oppervlakte chemie van de deeltjes.

In hoofdstuk 6 bestuderen we collageen netwerken, en in het bijzonder collageen type I. Collageen type I is een proteine die het meeste voorkomt in ons lichaam en daarom vaak gebruikt wordt als model systeem voor experimenten met cellen. Ondanks dat dit ECM veel gebruikt wordt, is de oorsprong van hun mechanische eigenschappen niet goed bekend. Wij bestuderen de origine van het strain-stiffening van collageen netwerken in hoofdstuk 6, waarbij de metingen van macrorheologie goed beschreven worden door een athermisch netwerk model. De netwerken die gevormd worden laten een connectiviteit zien van tussen de 3 en 4, terwijl voor een netwerk van mechanische veren een connectiveit van 6 nodig is om stabiel te zijn. Collageen netwerken zijn desondanks stabiel bij lage krachten, vanwege de hoge modulus van de fibers bij buiging. Dus de weerstand die fibers bieden om buiging te weerstaan, zorgt ervoor dat het netwerk stabiel is. Bij hogere deformaties wordt negatieve normaal krachten opgebouwd die het netwerk stijver maken. Bij een deformatie van ongeveer 30% is de elasticiteit van het netwerk niet meer gedomineerd door de buiging van de fibers, maar door het rekken van de fibers. We laten zien dat het strain-stiffening gedrag van collageen wijst naar een mechanisch, kritische transitie. Door de polymerizatie condities aan te passen, laten we zien dat het strain-stiffening gedrag van collageen, en de stijfheid daarvan bij lage krachten, afhankelijk is van de lokale architectuur (connectiviteit). Het athermisch netwerk model kan nu gebruikt worden om collageen netwerken te creeëren met bepaalde stijfheden voor cel-matrix experimenten.

In hoofdstuk 7 hadden we als doel gesteld om te kijken naar het effect van tractiekrachten van cellen op de mechanische eigenschappen van collageen, in

analogie van hoofdstuk 3. Echter, we zagen geen enkel verschil tussen de mechanische eigenschappen van netwerken met en zonder cellen. Gebruikmakend van microscopie laten we zien dat de afwezigheid van een effect kwam door de gelimiteerde celspreiding in deze netwerken. We bestudeerden meerdere factoren die invloed zouden moeten hebben op celspreiding, maar zonder success. We concluderen dat, ook al heeft de cellijn die we gebruiken in principe de juiste integrines (of 'handen') om te kunnen binden aan collageen, de cellijn niet ideaal is voor het bestuderen van cellulaire tractiekrachten op collageen mechanica.

In dit proefschrift hebben we de oorsprong van het strain-stiffening gedrag van twee belangrijke ECM netwerken onderzocht, namelijk die van fibrine en collageen. Een belangrijke nieuwe observatie is dat de moleculaire structuur van de *fibers* erg belangrijk is voor de mechanische eigenschappen van het *netwerk*. Ook al hebben fibrine en collageen fibers in principe een vergelijkbare diameter en netwerk structuur, de oorsprong van hun mechanische eigenschappen zijn heel anders: Fibrine netwerken hebben een elasticiteit dat voorkomt door thermische fluctuaties en de fibers zijn erg uitrekbaar (tot $\sim$200%), terwijl collageen netwerken zich gedragen als athermische fiber netwerken, en breken bij ongeveer 40% uitrekking. Deze verschillen komen door het verschil in interne pakkingstructuur: Collageen fibers zijn heel stijf en bevatten ongeveer 1000 monomeren in een fiber doorsnede, terwijl fibrine fibers veel flexibeler zijn en ongeveer 100 monomeren hebben in een fiber doorsnede. Ook spelen ontvouwingsdomeinen in de monomeren een belangrijke rol in de mechanica van fibrine netwerken bij grote deformaties.

Het werk van dit proefschrift geeft inzicht in de oorsprong van mechanische mankementen in ziektes gerelateerd aan genetische mutaties in collageen en fibrine. Ook geven de mechanische modellen gepresenteerd in dit werk een mooie basis voor het ontwerpen van meer complexe biologische of synthetische polymeren met bepaalde gewensde stijfheid, bijvoorbeeld voor tissue engineering. Ook heeft het verschil in de mechanische eigenschappen tussen fibrine en collageen wellicht consequenties voor cellular mechanosensing.

10. Bibliography

[1] A. J. Engler, S. Sen, H. L. Sweeney, and D. E. Discher, "Matrix elasticity directs stem cell lineage specification," *Cell*, vol. 126, pp. 677–689, 2006.

[2] A. W. Orr, B. P. Helmke, B. R. Blackman, and M. A. Schwartz, "Mechanisms of mechanotransduction," *Developmental Cell*, vol. 10, pp. 11–20, 2006.

[3] P. Lu, V. M. Weaver, and Z. Werb, "The extracellular matrix: A dynamic niche in cancer progression," *J. Cell Biol.*, vol. 196, no. 4, pp. 395–406, 2012.

[4] D. E. Jaalouk and J. Lammerding, "Mechanotransduction gone awry," *Nature Reviews Molecular Cell Biology*, vol. 10, pp. 63–73, 2009.

[5] K. R. Levental, H. M. Yu, L. Kass, J. N. Lakins, M. Egeblad, J. T. Erler, S. F. T. Fong, K. Csiszar, A. Giaccia, W. Weninger, M. Yamauchi, D. L. Gasser, and V. M. Weaver, "Matrix crosslinking forces tumor progression by enhancing integrin signaling," *Cell*, vol. 139, no. 5, pp. 891–906, 2009.

[6] O. Campás, T. Mammoto, S. Hasso, R. A. Sperling, D. O'Connell, A. G. Bischof, R. Maas, D. A. Weitz, L. Mahadevan, and D. E. Ingber, "Quantifying cell-generated mechanical forces within living embryonic tissues," *Nature Methods*, vol. 11, no. 2, pp. 183–189, 2014.

[7] T. Brunet, A. Bouclet, P. Ahmadi, D. Mitrossilis, B. Driquez, A.-C. Brunet, L. Henry, F. Serman, G. Béalle, C. Ménager, F. Dumas-Bouchiat, D. Givord, C. Yanicostas, D. Le-Roy, N. M. Dempsey, A. Plessis, and E. Farge, "Evolutionary conservation of early mesoderm specification by mechanotransduction in bilateria," *Nature Communications*, vol. 4, p. 2821, 2013.

[8] R. O. Hynes, "Integrins: bidirectional, allosteric signaling machines," *Cell*, vol. 110, no. 6, pp. 673–687, 2002.

[9] S. W. Moore, P. Roca-Cusachs, and M. P. Sheetz, "Stretchy proteins on stretchy substrates: The important elements of integrin-mediated rigidity sensing," *Developmental Cell*, vol. 19, pp. 194–207, 2010.

[10] A. M. Pasapera, I. C. Schneider, E. Rericha, D. D. Schlaepfer, and C. M. Waterman, "Myosin II activity regulates vinculin recruitment to focal adhesions through FAK-mediated paxillin phosphorylation," *J. Cell Biol.*, vol. 188, no. 6, pp. 877–890, 2010.

[11] G. Diez, V. Auernheimer, B. Fabry, and W. H. Goldmann, "Head/tail interaction of vinculin influences cell mechanical behavior," *Biochem. Biophys. Res. Commun.*, vol. 406, no. 1, pp. 85–88, 2011.

[12] A. Carisey, R. Tsang, A. M. Greiner, N. Nijenhuis, N. Heath, A. Nazgiewicz, R. Kemkemer, B. Derby, J. Spatz, and C. Ballestrem,

"Vinculin regulates the recruitment and release of core focal adhesion proteins in a force-dependent manner," *Current Biology*, vol. 23, pp. 271–281, 2013.

[13] A. del Rio, R. Perez-Jimenez, R. Liu, P. Roca-Cusachs, J. M. Fernandez, and M. P. Sheetz, "Stretching single talin rod molecules activates vinculin binding," *Science*, vol. 323, pp. 638–641, 2009.

[14] Y. Sawada, M. Tamada, B. J. Dubin-Thaler, O. Cherniavskaya, R. Sakai, S. Tanaka, and M. P. Sheetz, "Force sensing by extension of the src family kinase substrate, p130cas," *Cell*, vol. 127, no. 5, pp. 1015–1026, 2006.

[15] H. van Hoorn, D. M. Donato, H. E. Balcioglu, E. H. Danen, and T. Schmidt, "p130cas is a mechanosensor that modulates force exertion," *Proceedings of the National Academy of Sciences, U.S.A.*, in review.

[16] E. A. Novikova and C. Storm, "Contractile fibers and catch-bond clusters: a biological force sensor?," *Biophys. J.*, vol. 105, no. 6, pp. 1336–1345, 2013.

[17] A. Elosegui-Artola, E. Bazellières, M. D. Allen, I. Andreu, R. Oria, R. Sunyer, J. J. Gomm, J. F. Marshall, J. L. Jones, X. Trepat, and P. Roca-Cusachs, "Rigidity sensing and adaptation through regulation of integrin types," *Nature Materials*, vol. 13, no. 6, pp. 631–637, 2014.

[18] D.-H. Kim, A. B. Chambliss, and D. Wirtz, "The multi-faceted role of the actin cap in cellular mechanosensation and mechanotransduction," *Soft Matter*, vol. 9, pp. 5516–5523, 2013.

[19] K. Burridge and E. S. Wittchen, "The tension mounts: Stress fibers as force-generating mechanotransducers," *J. Cell Biol.*, vol. 200, no. 1, pp. 9–19, 2013.

[20] K. Hayakawa, H. Tatsumi, and M. Sokabe, "Mechano-sensing by actin filaments and focal adhesion proteins," *Communicative & Integrative Biology*, vol. 5, no. 6, pp. 572–577, 2012.

[21] T. Kobayashi and M. Sokabe, "Sensing substrate rigidity by mechanosensitive ion channels with stress fibers and focal adhesions," *Current Opinion in Cell Biology*, vol. 22, pp. 669–676, 2010.

[22] S. Huveneers and J. de Rooij, "Mechanosensitive systems at the cadherin-F-actin interface," *JCS*, vol. 126, pp. 1–11, 2013.

[23] A. K. Barry, N. Wang, and D. E. Leckband, "Local VE-cadherin mechanotransduction triggers long-ranged remodeling of endothelial monolayers," *Journal of Cell Science*, vol. 128, pp. 1341–1351, 2015.

[24] J. D. Humphries, A. Byron, and M. J. Humphries, "Integrin ligands at a glance," *Journal of Cell Science*, vol. 119, pp. 3901–3903, 2006.

[25] P. D. Yurchenco, "Basement membranes: Cell scaffoldings and signaling platforms," *Cold Spring Harb Perspect Biol*, vol. 3, p. a004911, 2011.

[26] C. Frantz, K. M. Stewart, and V. M. Weaver, "The extracellular matrix at a glance," *Journal of Cell Science*, vol. 123, pp. 4195–4200, 2010.

[27] A. Wang, C. de la Motte, M. Lauer, and V. Hascall, "Hyaluronan matrices in pathobiological processes," *FEBS Journal*, vol. 278, pp. 1412–1418, 2011.

[28] J. E. Murphy-Ullrich and E. H. Sage, "Revisiting the matricellular concept," *Matric Biology*, vol. 37, pp. 1–14, 2014.

[29] G. L. Lin, D. M. Cohen, R. A. Desai, M. T. Breckenridge, L. Gao, M. J. Humphries, and C. S. Chen, "Activation of beta 1 but not beta 3 integrin increases cell traction forces," *FEBS Letters*, vol. 587, no. 6, pp. 763–9, 2013.

[30] O. Chaudhuri, S. T. Koshy, C. Branco da Cunha, J.-W. Shin, C. S. Verbeke, K. H. Allison, and D. J. Mooney, "Extracellular matrix stiffness and composition jointly regulate the induction of malignant phenotypes in mammary epithelium," *Nat Mater*, vol. 13, no. 10, pp. 970–978, 2014.

[31] C. E. Barcus, P. J. Keely, K. W. Eliceiri, and L. A. Schuler, "Stiff collagen matrices increase tumorigenic prolactin signaling in breast cancer cells," *Journal of Biological Chemistry*, vol. 288, no. 18, pp. 12722–12732, 2013.

[32] C. Gaggioli, S. Hooper, C. Hidalgo-Carcedo, R. Grosse, J. F. Marshall, K. Harrington, and E. Sahai, "Fibroblast-led collective invasion of carcinoma cells with differing roles for RhoGTPases in leading and following cells," *Nat Cell Biol*, vol. 9, no. 12, pp. 1392–1400, 2007.

[33] M. J. Paszek, N. Zahir, K. R. Johnson, J. N. Lakins, G. I. Rozenberg, A. Gefen, C. A. Reinhart-King, S. S. Margulies, M. Dembo, D. Boettiger, D. A. Hammer, and V. M. Weaver, "Tensional homeostasis and the malignant phenotype," *Cancer Cell*, vol. 8, pp. 241–254, 2005.

[34] F. Zampieri, M. Coen, and G. Gabbiani, "The prehistory of the cytoskeleton concept," *Cytoskeleton*, vol. 71, pp. 464–471, 2014.

[35] R. H. Pritchard, Y. Y. S. Huang, and E. M. Terentjev, "Mechanics of biological networks: from the cell cytoskeleton to connective tissue," *Soft Matter*, vol. 10, pp. 1864–1884, 2014.

[36] D. E. Ingber, "Tensegrity-based mechanosensing from macro to micro," *Progress in Biophysics and Molecular Biology*, vol. 97, pp. 163–179, 2008.

[37] P. A. Janmey, U. Euteneuer, P. Traub, and M. Schliwa, "Viscoelastic properties of vimentin compared with other filamentous biopolymer networks," *JCB*, vol. 113, no. 1, pp. 155–160, 1991.

[38] H. B. Michael Schopferer and, B. Hochstein, S. Sharma, N. Mücke, H. Herrmann, and N. Willenbacher, "Desmin and vimentin intermediate filament networks: Their viscoelastic properties investigated by mechanical rheometry," *J. Mol. Biol.*, vol. 388, pp. 133–143, 2009.

[39] C. Storm, J. J. Pastore, F. MacKintosh, T. Lubensky, and P. A. Janmey, "Nonlinear elasticity in biological gels," *Nature*, vol. 435, pp. 191–194, 2005.

[40] T. Yeung, P. C. Georges, L. A. Flanagan, B. Marg, M. Ortiz, M. Funaki, N. Zahir, W. Ming, V. Waver, and P. A. Janmey, "Effects of substrate stiffness on cell morphology, cytoskeletal structure, and adhesion," *Cell Motility and the Cytoskeleton*, vol. 60, pp. 24–34, 2005.

[41] M. Ghibaudo, A. Saez, L. Trichet, A. Xayaphoummine, J. Browaeys, P. Silberzan, A. Buguin, and B. Ladoux, "Traction forces and rigidity sensing regulate cell functions," *Soft Matter*, vol. 4, pp. 1836–1843, 2008.

[42] J. H. Wen, L. G. Vincent, A. Fuhrmann, Y. S. Choi, K. C. Hribar, H. Taylor-Weiner, S. Chen, and A. J. Engler, "Interplay of matrix stiffness and protein tethering in stem cell differentiation," *Nature Materials*, vol. 13, pp. 979–987, 2014.

[43] P. A. DiMilla, K. Barbee, and D. A. Lauffenburger, "Mathematical model for the effects of adhesion and mechanics on cell migration speed," *Biophys. J.*, vol. 60, pp. 15–37, 1991.

[44] A. Huttenlocher, M. H. Ginsberg, and A. F. Horwitz, "Modulation of cell migration by integrin-mediated cytoskeletal linkages and ligand-binding affinity," *J. Cell Biol.*, vol. 134, pp. 1551–1562, 1996.

[45] N. Wang, J. D. Tytell, and D. E. Ingber, "Mechanotransduction at a distance: mechanically coupling the extracellular matrix with the nucleus," *Nature Reviews Molecular Cell Biology*, vol. 10, pp. 75–82, 2009.

[46] C. A. Reinhart-King, M. Dembo, and D. A. Hammer, "Cell-cell mechanical communication through compliant substrates," *Biophys. J.*, vol. 95, pp. 6044–6051, 2008.

[47] Q.-Y. Zhang, Y.-Y. Zhang, J. Zie, C.-X. Li, W.-Y. Chen, B.-L. Liu, X. an Wu, S.-N. Li, B. Huo, L.-H. Jiang, and H.-C. Zhao, "Stiff substrates enhance cultured neuronal network activity," *Scientific Reports*, vol. 4, p. 6215, 2013.

[48] J. K. Mouw, Y. Yui, L. Damiano, R. O. Bainer, J. N. Lakins, I. Acerbi, G. Ou, A. C. Wijekoon, K. R. Levental, P. M. Gilbert, Y.-Y. Chen, and V. M. Weaver, "Tissue mechanics modulate microRNA-dependent PTEN expression to regulate malignant progression," *Nat. Med.*, vol. 20, no. 4, pp. 360–367, 2014.

[49] C. Yang, M. W. Tibbitt, L. Basta, and K. S. Anseth, "Mechanical memory and dosing influence stem cell fate," *Nature Materials*, vol. 13, pp. 645–652, 2014.

[50] B. Trappmann, J. E. Gautrot, J. T. Connelly, D. G. T. Strange, Y. Li, M. L. Oyen, M. A. C. Stuart, H. Boehm, B. Li, V. Vogel, J. P. Spatz, F. M.Watt, and W. T. S. Huck, "Extracellular-matrix tethering regulates stem-cell fate," *Nature Materials*, vol. 11, pp. 642–649, 2012.

[51] A. K. Yip, K. Iwasaki, C. Ursekar, H. Machiyama, M. Saxena, H. Chen, I. Harada, K.-H. Chiam, and Y. Sawada, "Cellular response to substrate rigidity is governed by either stress or strain," *Biophys. J.*, vol. 104, pp. 19–29, 2013.

[52] J. M. Maloney, E. B. Walton, C. M. Bruce, and K. J. V. Vliet, "Influence of inite thickness and stiffness on cellular adhesion-induced deformation of compliant substrata," *PRE*, vol. 78, p. 041923, 2008.

[53] A. Buxboim, K. Rajagopal, A. E. Brown, and D. E. Discher, "How deeply cells feel: methods for thin gels," *J. Phys. Condens Matter*, vol. 22, no. 19, p. 194116, 2010.

[54] W. S. Leong, C. Y. Tay, H. Yu, A. Li, S. C. Wu, D.-H. Duc, C. T. Lim, and L. P. Tan, "Thickness sensing of hMSCs on collagen gel directs

stem cell fate," *Biochemical and Biophysical Research Communications*, vol. 401, pp. 287–292, 2010.

[55] J. P. Winer, S. Oake, and P. A. Janmey, "Non-linear elasticity of extracellular matrices enables contractile cells to communicate local position and orientation," *PLoS ONE*, vol. 4, no. 7, p. e6382, 2009.

[56] X. Ma, M. E. Schickel, M. D. Stevenson, A. L. Sarang-Sieminski, K. J. Gooch, S. N. Ghadiali, and R. T. Hart, "Fibers in the extracellular matrix enable long-range stress transmission between cells," *Biophys. J.*, vol. 104, pp. 1410–1418, 2013.

[57] M. S. Rudnicki, H. A. Cirka, M. Aghvami, E. A. Sander, Q. Wen, and K. L. Billiar, "Nonlinear strain stiffening is not sufficient to explain how far cells can feel on fibrous protein gels," *Biophys. J.*, vol. 105, pp. 11–20, 2013.

[58] H. Wang, A. Abhilash, C. S. Chen, R. G. Wells, and V. B. Shenoy, "Long-range force transmission in fibrous matrices enabled by tension-driven alignment of fibers," *Biophys. J.*, vol. 107, pp. 2592–2603, 2014.

[59] R. De, A. Zemel, and S. A. Safran, "Do cells sense stress or strain? measurement of cellular orientation can provide a clue," *Biophys. J.*, vol. 94, no. 5, pp. L29–L31, 2008.

[60] A. Saez, A. Buguin, P. Silberzan, and B. Ladoux, "Is the mechanical activity of epithelial cells controlled by deformations or forces?," *Biophys. J.*, vol. 89, no. 6, pp. L52–L54, 2005.

[61] L. Trichet, J. L. Digabel, R. J. Hawkins, S. R. K. Vedula, M. Gupta, C. Ribrault, P. Hersen, R. Voituriez, and B. Ladoux, "Evidence of a large-scale mechanosensing mechanism for cellular adaptation to substrate stiffness," *PNAS*, vol. 109, no. 18, pp. 6933–6938, 2012.

[62] A. Zemel, F. Rehfeldt, A. E. X. Brown, D. E. Discher, and S. A. Safran, "Optimal matrix rigidity for stress fiber polarization in stem cells," *Nat. Phys*, vol. 6, no. 6, pp. 468–473, 2010.

[63] S. He, Y. Su, B. Ji, and H. Gao, "Some basic questions on mechanosensing in cell-substrate interaction," *Journal of the Mechanics and Physics of SOlids*, vol. 70, pp. 116–135, 2014.

[64] T. Freyman, I. Yannas, R. Yokoo, and L. Gibson, "Fibroblast contractile force is independent of the stiffness which resists the contraction," *Experimental Cell Research*, vol. 272, pp. 153–162, 2002.

[65] Q. Wen and P. A. Janmey, "Effects of non-linearity on cell-ECM interactions," *Experimental Cell Research*, vol. 319, pp. 2481–2489, 2013.

[66] I. Piechocka, R. Bacabac, M. Potters, F. Mackintosh, and G. Koenderink, "Structural hierarchy governs fibrin gel mechanics," *Biophys. J.*, vol. 98, no. 10, pp. 2281–2289, 2010.

[67] K. A. Jansen, R. G. Bacabac, I. K. Piechocka, and G. H. Koenderink, "Cells actively stiffen fibrin networks by generating contractile stress," *Biophys. J.*, vol. 105, no. 10, pp. 2240–2251, 2013.

[68] F. Grinnell, "Fibroblast biology in three-dimensional collagen matrices," *TRENDS in Cell Biology*, vol. 13, no. 5, pp. 264–269, 2003.

[69] A. R. Cameron, J. E. Frith, and J. J. Cooper-White, "The influence of substrate creep on mesenchymal stem cell behaviour and phenotype," *Biomaterials*, vol. 32, pp. 5979–5993, 2010.

[70] C. Müller, A. Müller, and T. Pompe, "Dissipative interactions in cell-matrix adhesion," *Soft Matter*, vol. 9, p. 6207, 2013.

[71] O. Chaudhuri, L. Gu, M. Darnell, D. Klumpers, S. A. Bencherif, J. C. Weaver, N. Huebsch, and D. J. Mooney, "Substrate stress relaxation regulates cell spreading," *Nature Communications*, vol. 6, p. 6364, 2015.

[72] H. Mohammadi, P. D. Arora, C. A. Simmons, P. A. Janmey, and C. A. McCullock, "Inelastic behaviour of collagen networks in cell-matrix interactions and mechanosensation," *J. R. Roc. Interface*, vol. 12, p. 20141074, 2014.

[73] V. Ottania, D. Martinia, M. Franchia, and M. R. A. Ruggeria, "Hierarchical structures in fibrillar collagens," *Micron*, vol. 33, pp. 587–596, 2002.

[74] Z. Yang, I. Mochalkin, and R. F. Doolittle, "A model of fibrin formation based on crystal structures of fibrinogen and fibrin fragments complexed with synthetic peptides," *PNAS*, vol. 97, no. 26, pp. 14156–14161, 2000.

[75] E. Klotzsch, M. L. Smith, K. E. Kubow, S. Muntwyler, W. C. Little, F. Beyeler, D. Gourdon, B. J. Nelson, and V. Vogel, "Fibronectin forms the most extensible biological fibers displaying switchable force-exposed cryptic binding sites," *PNAS*, vol. 106, no. 43, pp. 18267–18272, 2009.

[76] M. Nikkhah, F. Edalat, S. Manoucheri, and A. Khademhosseini, "Engineering microscale topographies to control the cell-substrate interface," *Biomaterials*, vol. 33, pp. 5230–5246, 2012.

[77] D.-H. Kim, P. P. Provenzano, C. L. Smith, and A. Levchenko, "Matrix nanotopography as a regulator of cell function," *J. Cell Biol.*, vol. 197, no. 3, pp. 351–360, 2012.

[78] I. A. Janson and A. J. Putnam, "Extracellular matrix elasticity and topography: Material-based cues that affect cell function via conserved mechanisms," *J Biomed Mater Res Part A*, vol. 103A, pp. 1246–1258, 2015.

[79] J. Sun, Y. Ding, N. J. Lin, J. Zhou, H. Ro, C. L. Soles, M. T. Cicerone, and S. Lin-Gibson, "Exploring cellular contact guidance using gradient nanogratings," *Biomacromolecules*, vol. 11, no. 11, pp. 3067–3072, 2010.

[80] V. Brunetti, G. Maiorano, L. Rizzello, B. Sorce, S. Sabella, R. Cingolani, and P. P. Pompa, "Neurons sense nanoscale roughness with nanometer sensitivity," *PNAS*, vol. 107, no. 14, pp. 6264–6269, 2010.

[81] W. Chen, Y. Sun, and J. Fu, "Microfabricated nanotopological surfaces for study of adhesion-dependent cell mechanosensitivity," *Small*, vol. 9, no. 1, pp. 81–89, 2013.

[82] L. E. McNamara, T. Sjöström, K. Seunarine, R. D. Meek, B. Su, and M. J. Dalby, "Investigation of the limits of nanoscale filopodial interactions," *Journal of Tissue Engineering*, vol. 5, p. 2041731414536177, 2014.

[83] M. Arnold, E. A. Cavalcanti-Adam, R. Glass, J. Blümmel, W. Eck, M. Kantlehner, H. Kessler, and J. P. Spatz, "Activation of integrin function by nanopatterned adhesive interfaces," *ChemPhysChem*, vol. 5, no. 3, pp. 383–388, 2004.

[84] E. A. Cavalcanti-Adam, T. Volberg, A. Micoulet, H. Kessler, B. Geiger, and J. P. Spatz, "Cell spreading and focal adhesion dynamics are regulated by spacing of integrin ligands," *Biophys. J.*, vol. 92, pp. 2964–2974, 2007.

[85] M. J. Dalby, N. Gadegaard, R. Tare, A. Andar, M. O. Riehle, P. Herzyk, C. D. W. Wilkinson, and R. O. C. Oreffo, "The control of human mesenchymal cell differentiation using nanoscale symmetry and disorder," *Nature Materials*, vol. 6, pp. 997–1003, 2007.

[86] A. Ballo, H. Agheli, J. Lausmaa, P. Thomsen, and S. Petronis, "Nanostructured model implants for in vivo studies: influence of well-defined nanotopography on de novo bone formation on titanium implants," *International Journal of Nanomedicine*, vol. 6, pp. 3415–3428, 2011.

[87] M. H. Zaman, L. M. Trapani, A. L. Sieminski, D. MacKellar, H. Gong, R. D. Kamm, A. Wells, D. A. Lauffenburger, and P. Matsudaira, "Migration of tumor cells in 3d matrices is governed by matrix stiffness along with cell-matrix adhesion and proteolysis," *PNAS*, vol. 103, no. 29, pp. 10889–10894, 2006.

[88] T. A. Ulrich, A. Jain, K. Tanner, J. L. MacKay, and S. Kumar, "Probing cellular mechanobiology in three-dimensional culture with collagen-agarose matrices," *Biomaterials*, vol. 31, pp. 1875–1884, 2010.

[89] N. Huebsch, P. R. Arany, A. S. Mao, D. Shvartsman, O. A. Ali, S. A. Bencherif, J. Rivera-Feliciano, and D. J. Mooney, "Harnessing traction-mediated manipulation of the cell/matrix interface to control stem-cell fate," *Nature Materials*, vol. 9, pp. 518–526, 2010.

[90] K. Wolf, M. te Lindert, M. Krause, S. Alexander, J. te Riet, A. L. Willis, R. M. Hoffman, C. G. Figdor, S. J. Weiss, and P. Friedl, "Physical limits of cell migration: Control by ECM space and nuclear deformation and tuning by proteolysis and traction force," *Journal of Cell Biology*, vol. 201, no. 7, pp. 1069–1084, 2013.

[91] Y. li Yang, S. Motte, and L. J. Kaufman, "Pore size variable type I collagen gels and their interaction with glioma cells," *Biomaterials*, vol. 31, pp. 5678–5688, 2010.

[92] M. Miron-Mendoza, J. Seemann, and F. Grinnell, "The differential regulation of cell motile activity through matrix stiffness and porosity in three dimentional collagen matrices," *Biomaterials*, vol. 31, pp. 6425–6435, 2010.

[93] A. Pathak and S. Kumar, "Independent regulation of tumor cell migration by matrix stiffness and confinement," *PNAS*, vol. 109, no. 26, pp. 10334–10339, 2012.

[94] S. R. Peyton, Z. I. Kalcioglu, J. C. Cohen, A. P. Runkle, K. J. V. Vliet, D. A. Lauffenburger, and L. G. Griffith, "Marrow-derived stem cell motility in 3D synthetic scaffold is governed by geometry along with adhesivity and stiffness," *Biotechnology and Bioengineering*, vol. 108, no. 5, pp. 1181–1193, 2011.

[95] J. Lee, A. A. Abdeen, D. Zhang, and K. A. Kilian, "Directing stem cell fate on hydrogel substrates by controlling cell geometry, matrix mechanics and adhesion ligand composition," *Biomaterials*, vol. 34, pp. 8140–8148, 2013.

[96] N. R. Lang, K. Skodzek, S. Hurst, A. Mainka, J. Steinwachs, J. Schneider, K. E. Aifantis, and B. Fabry, "Biphasic response of cell invasion to matrix stiffness in three-dimensional biopolymer networks," *Acta Materialia*, vol. 13, pp. 61–67, 2015.

[97] K. A. Kyburz and K. S. Anseth, "Three-dimensional hMSC motility within peptide-functionalized PEG-based hydrogel of varying adhesivity and crosslinking density," *Acta Biomater.*, vol. 9, no. 5, pp. 6381–6392, 2013.

[98] H. Wang, L. Cai, A. Paul, A. Enejder, and S. C. Heilshorn, "Hybrid elastin-like polypeptide-polyethylene gluco (ELP-PEG) hydrogels with improved transparency and independent control of matrix mechanics and cell ligand density," *Biomacromolecules*, vol. 15, pp. 3421–3428, 2014.

[99] K. E. Kubow, S. K. Conrad, and A. R. Horwitz, "Matrix microarchitecture and myosin II determine adhesion in 3D matrices," *Current Biology*, vol. 23, pp. 1607–1619, 2013.

[100] W. J. Polacheck, A. E. German, A. Mammoto, D. E. Ingber, and R. D. Kamm, "Mechanotransduction of fluid stresses governs 3D cell migration," *PNAS*, vol. 111, no. 7, pp. 2447–2452, 2014.

[101] A. D. Doyle, F. W. Wang, K. Matsumoto, and K. M. Yamada, "One-dimensional topography underlies three-dimensional fibrillar cell migration," *J. Cell Biol.*, vol. 184, no. 4, pp. 481–490, 2009.

[102] O. Tolde, D. Rösel, R. Janoštiak, P. V. Ý, and J. Braábek, "Dynamics and morphology of focal adhesions in complex 3D environment," *Folia Biologica (Praha)*, vol. 58, no. 5, pp. 177–184, 2012.

[103] F. Rehfeldt, A. E. Brown, M. Raab, S. Cai, A. L. Zajac, A. Zemel, and D. E. Discher, "Hyaluronic acid matrices show matrix stiffness in 2D and 3D dictates cytoskeletal order and myosin-II phosphorylation within stem cells," *Integrative Biology*, vol. 4, pp. 422–430, 2012.

[104] K. M. Hakkinen, J. S. Harunaga, A. D. Doyle, and K. M. Yamada, "Direct comparisons of the morphology, migration, cell adhesions, and actin cytoskeleton of fibroblasts in four different three-dimensional extracellular matrices," *Tissue Engineering: Part A*, vol. 17, pp. 713–724, 2011.

[105] K. A. Beningo, M. Dembo, and Y. li Wang, "Responses of fibroblasts to anchorage of dorsal ecm receptors," *PNAS*, vol. 101, no. 52, pp. 18024–18029, 2004.

[106] R. I. Litvinov, V. Barsegov, A. J. Schissler, A. R. Fisher, J. S. Bennett, J. W. Weisel, and H. Shuman, "Dissociation of bimolecular αIIbβ3-fibrinogen complex under a constant tensile force," *Biophys. J.*, vol. 100, pp. 165–173, 2011.

[107] F. Kong, A. J. Garcia, A. P. Mould, M. J. Humphries, and C. Zhu, "Demonstration of catch bonds between an integrin and its ligand," *Journal of Cell Biology*, vol. 185, no. 7, pp. 1275–1284, 2009.

[108] J. C. Friedland, M. H. Lee, and D. Boettiger, "Mechanically activated integrin switch controls $\alpha_5\beta_1$ function," *Science*, vol. 323, pp. 642–644, 2009.

[109] S. Hertig and V. Vogel, "Catch bonds," *Current Biology*, vol. 22, no. 19, pp. R823–R825, 2012.

[110] E. Altrock, C. A. Muth, G. Klein, J. P. Spatz, and C. Lee-Thedieck, "The significance of integrin ligand nanopatterning on lipid raft clustering in hematopoietic stem cells," *Biomaterials*, vol. 33, no. 11, pp. 3107–3118, 2012.

[111] J. E. Frith, R. J. Mills, and J. J. Cooper-White, "Lateral spacing of adhesion peptides influences human mesenchymal stem cell behaviour," *Journal of Cell Science*, vol. 125, pp. 317–327, 2011.

[112] L. Y. Koo, D. J. Irvine, A. M. Mayes, D. A. Lauffenburger, and L. G. Griffith, "Co-regulation of cell adhesion by nanoscale RGD organization and mechanical stimulus," *Journal of cell science*, vol. 115, no. 7, pp. 1423–1433, 2002.

[113] S. P. Massia and J. A. Hubbell, "An RGD spacing of 440 nm is sufficient for integrin αvβ3-mediated fibroblast spreading and 140 nm for focal contact and stress fiber formation," *The Journal of cell biology*, vol. 114, no. 5, pp. 1089–1100, 1991.

[114] E. A. Cavalcanti-Adam, T. Volberg, A. Micoulet, H. Kessler, B. Geiger, and J. P. Spatz, "Cell spreading and focal adhesion dynamics are regulated by spacing of integrin ligands," *Biophysical journal*, vol. 92, no. 8, pp. 2964–2974, 2007.

[115] G. Le Saux, A. Magenau, K. Gunaratnam, K. A. Kilian, T. Böcking, J. J. Gooding, and K. Gaus, "Spacing of integrin ligands influences signal transduction in endothelial cells," *Biophysical journal*, vol. 101, no. 4, pp. 764–773, 2011.

[116] J. Huang, S. V. Grater, F. Corbellini, S. Rinck, E. Bock, R. Kemkemer, H. Kessler, J. Ding, and J. P. Spatz, "Impact of order and disorder in rgd nanopatterns on cell adhesion," *Nano letters*, vol. 9, no. 3, pp. 1111–1116, 2009.

[117] Y. Liu, R. Medda, Z. Liu, K. Galior, K. Yehl, J. P. Spatz, E. A. Cavalcanti-Adam, and K. Salaita, "Nanoparticle tension probes pat-

terned at the nanoscale: Impact of integrin clustering on force transmission," *Nano Letters*, vol. 14, no. 10, pp. 5539–5546, 2014.

[118] H. B. Schiller, M.-R. Hermann, J. Polleux, T. Vignaud, S. Zanivan, C. C. Friedel, Z. Sun, A. Raducanu, K.-E. Gottschalk, M. Théry, M. Mann, and R. Fässler, "β1- and αv-class integrins cooperate to regulate myosin II during rigidity sensing of fibronectin-based microenvironments," *Nat Cell Biol*, vol. 15, no. 6, pp. 625–636, 2013.

[119] H. E. Balcioglu, H. van Hoorn, D. M. Donato, T. Schmidt, and E. H. J. Danen, "The integrin expression profile modulates orientation and dynamics of force transmission at cell-matrix adhesions," *Journal of Cell Science*, vol. 128, pp. 1316–1326, 2015.

[120] P. Roca-Cusachs, N. C. Gauthier, A. del Rio, and M. P. Sheetz, "Clustering of α5β1 integrins determines adhesion strength whereas αvβ3 and talin enable mechanotransduction," *PNAS*, vol. 106, no. 38, pp. 16245–16250, 2009.

[121] A. Fuhrmann, J. Li, S. Chien, and A. J. Engler, "Cation type specific cell remodeling regulates attachment strength," *PLoS ONE*, vol. 9, no. 7, p. e102424, 2014.

[122] D. P. White, P. T. Caswell, and J. C. Norman, "αvβ3 and α5β1 integrin recycling pathways dictate downstream Rho kinase signaling to regulate persistent cell migration," *The Journal of Cell Biology*, vol. 177, no. 3, pp. 515–525, 2007.

[123] E. H. J. Danen, P. Sonneveld, C. Brakebusch, R. Fassler, and A. Sonnenberg, "The fibronectin-binding integrins α5β1 and αvβ3 differentially modulate RhoA-GTP loading, organization of cell matrix adhesions, and fibronectin fibrillogenesis," *Journal of Cell Biology*, vol. 159, no. 6, pp. 1071–1086, 2002.

[124] H. Miao, S. Li, Y.-L. Hu, S. Yuan, Y. Zhao, B. P. C. Chen, W. Puzon-McLaughlin, T. Tarui, J. Y.-J. Shyy, Y. Takada, S. Usami, and S. Chien, "Differential regulation of Rho GTPases by β1 and β3 integrins: the role of an extracellular domain of integrin in intracellular signaling," *Journal of Cell Science*, vol. 115, no. 10, pp. 2199–2206, 2002.

[125] H. L. Goe, T. Gritsko, B. Pursell, C. Chang, L. D. Shultz, D. L. Greiner, J. H. Norum, R. Toftgard, L. M. Shaw, and A. M. Mercurio, "Regulated splicing of the α6 integrin cytoplasmic domain determines the fate of breast cancer stem cells," *Cell Reports*, vol. 7, pp. 747–761, 2014.

[126] Y. Mao and J. E. Schwarzbauer, "Fibronectin fibrillogenesis, a cell-mediated matrix assembly process," *Matrix Biology*, vol. 24, no. 6, pp. 389–99, 2005.

[127] K. E. Kadler, A. Hill, and E. G. Canty-Laird, "Collagen fibrillogenesis: fibronectin, integrins, and minor collagens as organizers and nucleators," *Curr Opin Cell Biol*, vol. 20, no. 5, pp. 495–501, 2008.

[128] N. E. Ramirez, Z. Zhang, A. Madamanchi, K. L. Boyd, L. D. O'Rear, A. Nashabi, Z. Li, W. D. Dupont, A. Zijlstra, and M. M. Zutter, "The

$\alpha_2\beta_1$ integrin is a metastasis suppressor in mouse models and human cancer," *J. Clin. Invest.*, vol. 2011, pp. 226–237, 2011.

[129] K. Moran-Jones, A. Ledger, and M. J. Naylor, "β1 integrin deletion enhances progression of prostate cancer in the TRAMP mouse model," *Scientific Reports*, vol. 2, p. 526, 2012.

[130] J. G. Parvani, A. J. Galliher-Beckley, B. J. Schiemann, and W. P. Schiemann, "Targeted inactivation of β1 integrin induces β3 integrin switching that drives breast cancer metastasis by TGF-β," *Molecular Biology of the Cell*, vol. 24, no. 21, pp. 3449–3459, 2013.

[131] H. H. Truong, J. Xiong, V. P. S. Ghotra, E. Nirmala, L. Haazen, S. E. Le Devedec, H. E. Balcioglu, S. He, B. E. Snaar-Jagalska, E. Vreugdenhil, J. H. N. Meerman, B. van de Water, and E. H. J. Danen, "beta1 integrin inhibition elicits a prometastatic switch through the TGFbeta-mir-200-ZEB network in E-cadherin-positive triple-negative breast cancer," *Sci. Signal.*, vol. 7, no. 312, p. ra15, 2014.

[132] J. S. Munger and D. Sheppard, "Cross talk among TGF-β signaling pathways, integrins, and the extracellular matrix," *Cold Spring Harb Perspect Biol*, vol. 3, p. a005017, 2011.

[133] X. Tong and F. Yang, "Engineering interpenetrating network hydrogels as biomimetic cell niche with independently tunable biochemical and mechanical properties," *Biomaterials*, vol. 35, no. 6, pp. 1807–1815, 2014.

[134] S. Khetan, M. Guvendiren, W. R. Legant, D. M. Cohen, C. S. Chen, and J. A. Burdick, "Degradation-mediated cellular traction directs stem cell fate in covalently crosslinked three-dimensional hydrogels," *Nature Materials*, vol. 12, no. 5, pp. 458–465, 2013.

[135] C. Grashoff, B. D. Hoffman, M. D. Brenner, R. Zhou, M. Parsons, M. T. Yang, M. A. McLean, S. G. Sligar, C. S. Chen, T. Ha, and M. A. Schwartz, "Measuring mechanical tension across vinculin reveals regulation of focal adhesion dynamics," *Nature*, vol. 466, pp. 263–267, 2010.

[136] K. E. Kubow and A. R. Horwitz, "Reducing background fluorescence reveals adhesions in 3D matrices," *Nat Cell Biol.*, vol. 13, no. 1, pp. 3–7, 2011.

[137] C.-L. Chiu, J. S. Aguilar, C. Y. Tsai, G. Wu, E. Gratton, and M. A. Digman, "Nanoimaging of focal adhesion dynamics in 3D," *PLoS ONE*, vol. 9, no. 6, p. e99896, 2014.

[138] S. I. Fraley, Y. Feng, R. Krishnamurthy, D.-H. Kim, A. Celedon, G. D. Longmore, and D. Wirtz, "A distinctive role for focal adhesion proteins in three-dimensional cell motility," *Nat. Cell Biol.*, vol. 12, no. 6, pp. 598–604, 2010.

[139] P. A. Janmey, R. G. Wells, R. K. Assoian, and C. A. McCulloch, "From tissue mechanics to transcription factors," *Differentiation*, vol. 86, no. 3, pp. 112–120, 2013.

[140] R. Janoštiak, J. Brábek, V. Auernheimer, Z. Tatárová, L. A. Lautscham, T. Dey, J. Gemperle, R. Merkel, W. H. Goldmann, B. Fabry, *et al.*,

"Cas directly interacts with vinculin to control mechanosensing and focal adhesion dynamics," *Cellular and Molecular Life Sciences*, vol. 71, no. 4, pp. 727–744, 2014.

[141] C. Lu, F. Wu, W. Qiu, and R. Liu, "P130cas substrate domain is intrinsically disordered as characterized by single-molecule force measurements," *Biophysical chemistry*, vol. 180, pp. 37–43, 2013.

[142] K. Hotta, S. Ranganathan, R. Liu, F. Wu, H. Machiyama, R. Gao, H. Hirata, N. Soni, T. Ohe, C. W. Hogue, *et al.*, "Biophysical properties of intrinsically disordered p130Cas substrate domain - implication in mechanosensing," *PLoS computational biology*, vol. 10, no. 4, p. e1003532, 2014.

[143] L. M. Meenderink, L. M. Ryzhova, D. M. Donato, D. F. Gochberg, I. Kaverina, and S. K. Hanks, "P130Cas Src-binding and substrate domains have distinct roles in sustaining focal adhesion disassembly and promoting cell migration," *PLoS ONE*, vol. 5, no. 10, p. e13412, 2010.

[144] R. Janoštiak, A. C. Pataki, J. Brábek, and D. Rösel, "Mechanosensors in integrin signaling: The emerging role of p130cas," *European journal of cell biology*, vol. 93, 2014.

[145] M. Smith, L. Hoffman, and M. Beckerle, "Lim proteins in actin cytoskeleton mechanoresponse," *TRENDS in Cell Biology*, vol. 24, no. 10, pp. 575–583, 2014.

[146] J. Fradelizi, V. Noireaux, J. Plastino, B. Menichi, D. Louvard, C. Sykes, R. M. Golsteyn, and E. Friederich, "ActA and human zyxin harbour Arp2/3-independent actin-polymerization activity," *Nature cell biology*, vol. 3, no. 8, pp. 699–707, 2001.

[147] B. E. Drees, K. M. Andrews, and M. C. Beckerle, "Molecular dissection of zyxin function reveals its involvement in cell motility," *The Journal of cell biology*, vol. 147, no. 7, pp. 1549–1560, 1999.

[148] M. A. Smith, E. Blankman, M. L. Gardel, L. Luettjohann, C. M. Waterman, and M. C. Beckerle, "A zyxin-mediated mechanism for actin stress fiber maintenance and repair," *Developmental cell*, vol. 19, no. 3, pp. 365–376, 2010.

[149] J. Colombelli, A. Besser, H. Kress, E. G. Reynaud, P. Girard, E. Caussinus, U. Haselmann, J. V. Small, U. S. Schwarz, and E. H. Stelzer, "Mechanosensing in actin stress fibers revealed by a close correlation between force and protein localization," *Journal of cell science*, vol. 122, no. 10, pp. 1665–1679, 2009.

[150] N. O. Deakin and C. E. Turner, "Paxillin inhibits HDAC6 to regulate microtubule acetylation, Golgi structure, and polarized migration," *JCB*, vol. 206, no. 3, pp. 395–413, 2014.

[151] A. B. Jaffe and A. Hall, "Rho GTPases: biochemistry and biology," *Annu. Rev. Cell Dev. Biol.*, vol. 21, pp. 247–269, 2005.

[152] M. Gregor, S. Osmanagic-Myers, G. Burgstaller, M. Wolfram, I. Fischer, G. Walko, G. P. Resch, A. Jörgl, H. Herrmann, and G. Wiche, "Mecha-

nosensing through focal adhesion-anchored intermediate filaments," *The FASEB Journal*, vol. 28, pp. 715–729, 2014.

[153] K. Chen, W. Zhang, J. Chen, S. Li, and G. Guo, "Rho-associated protein kinase modulates neurite extension by regulating microtubule remodeling and vinculin distribution," *Neural Regen Res.*, vol. 8, no. 32, pp. 3027–3035, 2013.

[154] P. P. Provenzano, D. R. Inman, K. W. Eliceiri, S. M. Trier, and P. J. Keely, "Contact guidance mediated three-dimensional cell migration is regulated by Rho/ROCK-dependent matrix reorganization," *Biophys. J.*, vol. 95, pp. 5374–5384, 2008.

[155] A. J. Putnam, J. J. Cunningham, B. B. Pillemer, and D. J. Mooney, "External mechanical strain regulates membrane targeting of rho gtpases by controlling microtubule assembly," *American Journal of Physiology-Cell Physiology*, vol. 284, no. 3, pp. C627–C639, 2003.

[156] K. G. Birukov, "Small GTPases in mechanosensitive regulation of endothelial barrier," *Microvascular research*, vol. 77, no. 1, pp. 46–52, 2009.

[157] C. B. Khatiwala, S. R. Peyton, M. Metzke, and A. J. Putnam, "The regulation of osteogenesis by ECM rigidity in MC3T3-E1 cells requires MAPK activation," *Journal of cellular physiology*, vol. 211, no. 3, pp. 661–672, 2007.

[158] K. Hamamura, G. Swarnkar, N. Tanjung, E. Cho, J. Li, S. Na, and H. Yokota, "RhoA-mediated signaling in mechanotransduction of osteoblasts," *Connective tissue research*, vol. 53, no. 5, pp. 398–406, 2012.

[159] A. W. Holle, X. Tang, D. Vijayraghavan, L. G. Vincent, A. Fuhrmann, Y. S. Choi, J. C. Álamo, and A. J. Engler, "In situ mechanotransduction via vinculin regulates stem cell differentiation," *Stem Cells*, vol. 31, no. 11, pp. 2467–2477, 2013.

[160] P. Gaspar and N. Tapon, "Sensing the local environment: actin architecture and Hippo signalling," *Current opinion in cell biology*, vol. 31, pp. 74–83, 2014.

[161] B. C. Low, C. Q. Pan, G. Shivashankar, A. Bershadsky, M. Sudol, and M. Sheetz, "YAP/TAZ as mechanosensors and mechanotransducers in regulating organ size and tumor growth," *FEBS Letters*, vol. 588, pp. 2663–2670, 2014.

[162] S. Dupont, L. Morsut, M. Aragona, E. Enzo, S. Giulitti, M. Cordenonsi, F. Zanconato, J. Le Digabel, M. Forcato, S. Bicciato, *et al.*, "Role of YAP/TAZ in mechanotransduction," *Nature*, vol. 474, no. 7350, pp. 179–183, 2011.

[163] K.-I. Wada, K. Itoga, T. Okano, S. Yonemura, and H. Sasaki, "Hippo pathway regulation by cell morphology and stress fibers," *Development*, vol. 138, no. 18, pp. 3907–3914, 2011.

[164] M. Aragona, T. Panciera, A. Manfrin, S. Giulitti, F. Michielin, N. Elvassore, S. Dupont, and S. Piccolo, "A mechanical checkpoint controls multicellular growth through YAP/TAZ regulation by actin-processing factors," *Cell*, vol. 154, no. 5, pp. 1047–1059, 2013.

[165] V. A. Codelia, G. Sun, and K. D. Irvine, "Regulation of YAP by mechanical strain through Jnk and Hippo signaling," *Current Biology*, vol. 24, pp. 2012–2017, 2014.

[166] F. Calvo, N. Ege, A. Grande-Garcia, S. Hooper, R. P. Jenkins, S. I. Chaudhry, K. Harrington, P. Williamson, E. Moeendarbary, G. Charras, *et al.*, "Mechanotransduction and YAP-dependent matrix remodelling is required for the generation and maintenance of cancer-associated fibroblasts," *Nature cell biology*, vol. 15, no. 6, pp. 637–646, 2013.

[167] B. Zhao, L. Li, L. Wang, C.-Y. Wang, J. Yu, and K.-L. Guan, "Cell detachment activates the Hippo pathway via cytoskeleton reorganization to induce anoikis," *Genes & development*, vol. 26, no. 1, pp. 54–68, 2012.

[168] A. Reginensi, R. P. Scott, A. Gregorieff, M. Bagherie-Lachidan, C. Chung, D.-S. Lim, T. Pawson, J. Wrana, and H. McNeill, "Yap-and Cdc42-dependent nephrogenesis and morphogenesis during mouse kidney development," *PLoS genetics*, vol. 9, no. 3, p. e1003380, 2013.

[169] D.-Z. Wang, P. S. Chang, Z. Wang, L. Sutherland, J. A. Richardson, E. Small, P. A. Krieg, and E. N. Olson, "Activation of cardiac gene expression by myocardin, a transcriptional cofactor for serum response factor," *Cell*, vol. 105, no. 7, pp. 851–862, 2001.

[170] F. Miralles, G. Posern, A.-I. Zaromytidou, and R. Treisman, "Actin dynamics control SRF activity by regulation of its coactivator MAL," *Cell*, vol. 113, no. 3, pp. 329–342, 2003.

[171] M. W. Chan, F. Chaudary, W. Lee, J. W. Copeland, and C. A. McCulloch, "Force-induced myofibroblast differentiation through collagen receptors is dependent on mammalian diaphanous (mDia)," *Journal of Biological Chemistry*, vol. 285, no. 12, pp. 9273–9281, 2010.

[172] F. Huber, A. Boire, M. P. López, and G. H. Koenderink, "Cytoskeletal crosstalk: when three different personalities team up," *Current Opinion in Cell Biology*, vol. 32, pp. 39–47, 2014.

[173] J. S. Kim, C.-H. Lee, B. Y. Su, and P. A. Coulombe, "Mathematical modeling of the impact of actin and keratin filaments on keratinocyte cell spreading," *Biophys. J.*, vol. 103, pp. 1828–1838, 2012.

[174] M. E. Murray, M. G. Mendez, and P. A. Janmey, "Substrate stiffness regulates solubility of cellular vimentin," *MBoC*, vol. 25, pp. 87–94, 2014.

[175] J. Solon, I. Levental, K. Sengupta, P. C. Georges, and P. A. Janmey, "Fibroblast adaptation and stiffness matching to soft elastic substrates," *Biophys. J.*, vol. 93, pp. 4453–4461, 2007.

[176] U. S. Schwarz and M. L. Gardel, "United we stand - integrating the actin cytoskeleton and cell-matrix adhesions in cellular mechanotransduction," *Journal of Cell Science*, vol. 125, pp. 3051–3060, 2012.

[177] C. Ciobanasu, B. Faivre, and C. L. Clainche, "Actomyosin-dependent formation of the mechanosensitive talin-vinculin complex reinforces actin anchoring," *Nature Communications*, vol. 5, p. 3095, 2014.

[178] M. Ochsner, M. Textor, V. Vogel, and M. L. Smith, "Dimensionality controls cytoskeleton assembly and metabolism of fibroblast cells in resonse to rigidity and shape," *PLoS ONE*, vol. 5, no. 3, p. e9445, 2010.

[179] F. C. Ho, W. Zhang, Y. Y. Li, and B. P. Chan, "Mechanoresponsive, omni-directional and local matrix-degrading actin protrusions in human mesenchymal stem cells microencapsulated in a 3D collagen matrix," *Biomaterials*, vol. 53, pp. 392–405, 2015.

[180] S. Rhee, H. Jiang, C.-H. Ho, and F. Grinnell, "Microtubule function in fibroblast spreading is modulated according to the tension state of cell-matrix interactions," *PNAS*, vol. 104, no. 13, pp. 5425–5430, 2007.

[181] S. Stehbens and T. Wittmann, "Targeting and transport: How microtubules control focal adhesion dynamics," *Journal of Cell Science*, vol. 198, no. 4, pp. 481–489, 2012.

[182] A. F. Palazzo and G. G. Gundersen, "Microtubule-actin cross-talk at focal adhesions," *Sci. STKE*, vol. 2002, no. 139, p. pe31, 2002.

[183] E. J. Ezratty, M. A. Partridge, and G. G. Gundersen, "Microtubule-induced focal adhesion disassembly is mediated by dynamin and focal adhesion kinase," *Nature Cell Biology*, vol. 7, no. 6, pp. 581–590, 2005.

[184] A. Efimov, N. Schiefermeier, I. Grigoriev, R. Ohi, M. C. Brown, C. E. Turner, J. V. Small, and I. Kaverina, "Paxillin-dependent stimulation of microtubule catastrophes at focal adhesion sites," *J. Cell Sci.*, vol. 121, pp. 196–204, 2008.

[185] X. Wu, A. Kodama, and E. Fuchs, "ACF7 regulates cytoskeletal-focal adhesion dynamics and migration and has ATPase activity," *Cell*, vol. 135, no. 1, pp. 137–148, 2008.

[186] M. P. López, F. Huber, I. Grigoriev, M. O. Steinmetz, A. Akhmanova, G. H. Koenderink, and M. Dogterom, "Actin-microtubule coordiation at growing microtubule ends," *Nature Communications*, vol. 5, p. 4778, 2014.

[187] A. Rape, W.-H. Guo, and Y. li Wang, "Microtubule depolymerization induces traction force increase through two distinct pathways," *Journal of Cell Science*, vol. 124, pp. 4233–4240, 2011.

[188] B. A. Danowski, "Fibroblast contractility and actin organization are stimulated by microtubule inhibitors," *Journal of Cell Science*, vol. 93, pp. 255–266, 1989.

[189] M. S. Kolodney and E. L. Elson, "Contraction due to microtubule disruption is associated with increased phosphorylation of myosin regulatory light chain," *PNAS*, vol. 92, pp. 10252–10256, 1995.

[190] A. Kim and W. M. Petroll, "Microtubule regulation of corneal fibroblast morphology and mechanical activity in 3-D culture," *Experimental eye research*, vol. 85, no. 4, pp. 546–556, 2007.

[191] D. H. J. Ng, J. D. Humphries, A. Byron, A. lique Millon-Frémillon, and M. J. Humphries, "Microtubule-dependent modulation of adhesion complex composition," *PLoS ONE*, vol. 9, no. 12, p. e115213, 2014.

[192] C. M. Kraning-Rush, S. P. Carey, J. P. Califano, B. N. Smith, and C. A. Reinhart-King, "The role of the cytoskeleton in cellular force generation in 2D and 3D environments," *Phys Biol.*, vol. 8, no. 1, p. 015009, 2011.

[193] J. N. Heck, S. M. Ponik, M. G. Garcia-Mendoza, C. A. Pehlke, D. R. Inman, K. W. Eliceiri, and P. J. Keely, "Microtubules regulate GEF-H1 in response to extracellular matrix stiffness," *MBoC*, vol. 23, pp. 2583–2592, 2012.

[194] N. R. Lang, S. Münster, C. Metzner, P. Krauss, S. Schürmann, J. Lange, K. E. Aifantis, O. Friedrich, and B. Fabry, "Estimating the 3D pore size distribution of biopolymer networks from directionally biased data," *Biophys. J.*, vol. 105, pp. 1967–1975, 2013.

[195] K. A. Myers, K. T. Applegate, G. Danuser, R. S. Fischer, and C. M. Waterman, "Distinct ECM mechanosensing pathways regulate microtubule dynamics to control endothelial cell branching morphogenesis," *J. Cell Biol.*, vol. 192, no. 2, pp. 321–334, 2011.

[196] A. Minin and M. Moldaver, "Intermediate vimentin filaments and their role in intracellular organelle distribution," *Biochemistry*, vol. 73, no. 13, pp. 1453–1466, 2008.

[197] J. Ivaska, H.-M. Pallari, J. Nevo, and J. E. Eriksson, "Novel functions of vimentin in cell adhesion, migration, and signaling," *Experimental Cell Research*, vol. 313, pp. 2050–2062, 2007.

[198] S. H. Shabbir, M. M. Cleland, R. D. Goldman, and M. Mrksich, "Geometric control of vimentin intermediate filaments," *Biomaterials*, vol. 35, pp. 1359–1366, 2014.

[199] G. Wiche and L. Winter, "Plectin isoforms as organizers of intermediate filament cytoarchitecture," *BioArchitecture*, vol. 1, no. 1, pp. 14–20, 2011.

[200] M. Ketema, M. Kreft, P. Secades, H. Janssen, and A. Sonnenberg, "Nesprin-3 connects plectin and vimentin to the nuclear envelope of sertoli cells but is not required for sertoli cell function in spermatogenesis," *MBoC*, vol. 24, pp. 2454–2466, 2013.

[201] D. Tsuruta and J. C. Jones, "The vimentin cytoskeleton regulates focal contact size and adhesion of endothelial cells subjected to shear stress," *Journal of Cell Science*, vol. 116, pp. 4977–4984, 2003.

[202] G. Burgstaller, M. Gregor, L. Winter, and G. Wiche, "Keeping the vimentin network under control: Cell-matrix adhesion-associated plectin 1f affects cell shape and polarity of fibroblasts," *Molecular Biology of the Cell*, vol. 21, pp. 3362–3375, 2010.

[203] R. Bhattacharya, A. M. Gonzalez, P. J. DeBiase, H. E. Trejo, R. D. Goldman, F. W. Flitney, and J. C. R. Jones, "Recruitment of vimentin to the cell surface by $\beta 3$ integrin and plectin mediates adhesion strength," *Journal of Cell Science*, vol. 122, no. 9, pp. 1390–1400, 2009.

[204] B. Eckes, D. Dogic, E. Colucci-Guyon, N. Wang, A. Maniotis, D. Ingber, A. Merckling, F. Langa, M. Aumailley, A. Delouvée, V. Koteliansky, C. Babinet, and T. Krieg, "Impaired mechanical stability, migration and

contractile capacity in vimentin-deficient fibroblasts," *Journal of Cell Science*, vol. 111, pp. 1897–1907, 1998.

[205] M. Mendez, D. Restle, and P. Janmey, "Vimentin enhances cell elastic behavior and protects against compressive stress," *Biophys. J.*, vol. 107, pp. 314–323, 2014.

[206] E. L. Baker and M. H. Zaman, "The biomechanical integrin," *Journal of Biomechanics*, vol. 43, pp. 38–44, 2010.

[207] A. K. Harris, P. Wild, and D. Stopak, "Silicone rubber substrata: A new wrinkle in the study of cell locomotion," *Science*, vol. 208, no. 11, pp. 177–179, 1980.

[208] K. A. Beningo and Y.-L. Wang, "Flexible substrata for the detection of cellular traction forces," *TRENDS in Cell Biology*, vol. 12, no. 2, pp. 79–84, 2002.

[209] K. Burton, J. H. Park, and D. L. Taylor, "Keratocytes generate traction forces in two phases," *Molecular Biology of the Cell*, vol. 10, pp. 3745–3769, 1999.

[210] K. Burton and D. L. Taylor, "Traction forces of cytokinesis measured with optically modified elastic substrata," *Nature*, vol. 385, pp. 450–454, 1997.

[211] J. Lee, M. Leonard, T. Oliver, A. Ishihara, and K. Jacobson, "Traction forces generated by locomoting keratocytes," *Journal of Cell Biology*, vol. 127, no. 6, pp. 1957–1964, 1994.

[212] T. Oliver, K. Jacobson, and M. Dembo, "Design and use of substrata to measure traction forces exerted by cultured cells," *Methods in Enzymology*, vol. 298, pp. 497–521, 1998.

[213] R. J. Pelham and Y.-L. Wang, "Cell locomotion and focal adhesions are regulated by substrate flexibility," *PNAS*, vol. 94, pp. 13661–13665, 1997.

[214] R. W. Style, R. Boltyanskiy, G. K. German, C. Hyland, C. W. Macminn, A. F. Mertz, L. A. Wilen, Y. Xu, and E. R. Dufresne, "Traction force microscopy in physics and biology," *Soft Matter*, vol. 10, p. 4047, 2014.

[215] Z. Yang, J.-S. Lin, J. Chen, and J. H.-C. Wang, "Determining substrate displacement and cell traction fields - a new approach," *Journal of Theoretical Biology*, vol. 242, pp. 607–616, 2006.

[216] S. S. Ng, C. Li, and V. Chan, "Experimental and numerical determination of cellular traction force on polymeric hydrogels," *Interface Focus*, vol. 1, pp. 777–791, 2011.

[217] R. Meili, B. Alonso-Latorre, J. C. del Álamo, R. A. Firtel, and J. C. Lasheras, "Myosin II is essential for the spatiotemporal organization of traction forces during cell motility," *Molecular Biology of the Cell*, vol. 21, pp. 405–417, 2010.

[218] J. C. del Álamo, R. Meili, B. Alonso-Latorre, J. Rodríguez-Rodríguez, A. Aliseda, R. A. Firtel, and J. C. Lasheras, "Spatio-temporal analysis of eukaryotic cell motility by improved force cytometry," *PNAS*, vol. 104, no. 33, pp. 13343–13348, 2007.

[219] B. Sabass, M. L. Gardel, C. M. Waterman, and U. S. Schwarz, "High resolution traction force microscopy based on experimental and computational advances," *Biophys. J.*, vol. 94, pp. 207–220, 2008.

[220] J. Toyjanova, E. Bar-Kochba, C. López-Fagundo, J. Reichner, D. Hoffman-Kim, and C. Franck, "High resoltuion, large deformation 3D traction force microscopy," *PLoS ONE*, vol. 9, no. 4, p. e90976, 2014.

[221] W. R. Legant, C. K. Choi, J. S. Miller, L. Shao, L. Gao, E. Betzig, and C. S. Chen, "Multidimensional traction force microscopy revals out-of-plane rotational moments about focal adhesions," *PNAS*, vol. 110, no. 3, pp. 881–886, 2013.

[222] J. C. del Álamo, R. Meili, B. Álvarex-González, B. Alonso-Latorre, E. Bastounis, R. Firtel, and J. C. Lasheras, "Three-dimensional quantification of cellular traction forces and mechanosensing of thin substrata by fourier traction force microscopy," *PLoS ONE*, vol. 8, no. 9, p. e69850, 2013.

[223] C.-W. Kuo, J.-Y. Shiu, F.-C. Chien, S.-M. Tsai, D.-Y. Chueh, and P. Chen, "Polymeric nanopillar arrays for cell traction force measurements," *Electrophoresis*, vol. 31, pp. 3152–3158, 2010.

[224] M. T. Yang, N. J. Sniadecki, and C. S. Chen, "Geometric considerations of micro- to nanoscale elastomeric post arrays to study cellular traction forces," *Advanced Materials*, vol. 19, pp. 3119–3123, 2007.

[225] I. Schoen, W. Hu, E. Klotzsch, and V. Vogel, "Probing cellular traction forces by micropillar arrays: Contribution of substrate warping to pillar deflection," *Nano Letters*, vol. 10, no. 5, pp. 1823–1830, 2010.

[226] A. Saez, M. Ghibaudo, A. Buguin, P. Silberzan, and B. Ladoux, "Rigidity-driven growth and migration of epithelial cells on microstructured anisotropic substrates," *PNAS*, vol. 104, no. 20, pp. 8281–8286, 2007.

[227] J. L. Tan, J. Tien, D. M. Pirone, D. S. Gray, K. Bhadriraju, and C. S. Chen, "Cells lying on a bed of microneedles: An approach to isolate mechanical force," *PNAS*, vol. 100, no. 4, pp. 1484–1489, 2003.

[228] A. Crow, K. D. Webster, E. Hohlfeld, W. P. Ng, P. Geissler, and D. A. Fletcher, "Contractile equilibration of single cells to step changes in extracellular stiffness," *Biophys. J.*, vol. 102, no. 3, pp. 443–451, 2012.

[229] K. D. Webster, A. Crow, and D. A. Fletcher, "An AFM-based stiffness clamp for dynamic control of rigidity," *PLoS ONE*, vol. 6, no. 3, p. e17807, 2011.

[230] P. Fernández, P. A. Pullarkat, and A. Ott, "A master relation defines the nonlinear viscoelasticity of single fibroblasts," *Biophys. J.*, vol. 90, pp. 3796–3805, 2006.

[231] D. Mitrossilis, J. Fouchard, D. Pereira, F. Postic, A. Richert, M. Saint-Jean, and A. Asnacios, "Real-time single-cell response to stiffness," *PNAS*, vol. 107, no. 38, pp. 16518–16523, 2010.

[232] J. W. Weisel, H. Shumand, and R. I. Litvinov, "Protein-protein unbinding induced by force: single-molecule studies," *Current Opinion in Structural Biology*, vol. 13, pp. 227–235, 2003.

[233] K. C. Patterson, R. Yang, B. Zeng, B. Song, S. Wang, N. Xi, and M. D. Basson, "Measurement of cationic and intracellular modulation of integrin binding affinity by AFM-based nanorobot," *Biophys. J.*, vol. 105, no. 1, pp. 40–47, 2013.

[234] A. Taubenberger, D. A. Cisneros, J. Friedrichs, P.-H. Puech, D. J. Muller, and C. M. Franz, "Revealing early steps of $\alpha 2\beta 1$ integrin-mediated adhesion to collagen type I by using single-cell force spectroscopy," *Molecular Biology of the Cell*, vol. 18, pp. 1634–1644, 2007.

[235] H. Jeon, E. Kim, and C. P. Grigoropoulos, "Measurement of contractile forces generated by individual fibroblasts on self-standing fiber scaffolds," *Biomedical Microdevices*, vol. 13, pp. 107–115, 2011.

[236] T. Freyman, I. Yannas, Y.-S. Pek, R. Yokoo, and L. Gibson, "Micromechanics of fibroblast contraction of a collagen-gag matrix," *Experimental Cell Research*, vol. 269, pp. 140–153, 2001.

[237] B. A. Harley, T. M. Freyman, M. Q. Wong, and L. J. Gibson, "A new technique for calculating individual dermal fibroblast contractile forces generated within collagen-GAG scaffolds," *Biophys. J.*, vol. 93, pp. 2911–2922, 2007.

[238] E. Bell, B. Ivarsson, and C. Merrill, "Production of a tissue-like structure by contraction of collagen lattices by human fibroblasts of different proliferative potential in vitro," *Proc. Natl. Acad. Sci. USA*, vol. 76, no. 3, pp. 1274–1278, 1979.

[239] I. Cohen, J. M. Gerrard, and J. G. White, "Ultrastructure of clots during isometric contraction," *Journal of Cell Biology*, vol. 93, pp. 775–787, 1982.

[240] S. L. Rowe, S. Lee, and J. P. Stegemann, "Influence of thrombin concentration on the mechanical and morphological properties of cell-seeded fibrin hydrogels," *Acta Biomaterialia*, vol. 3, no. 1, pp. 59–67, 2007.

[241] E. Kniazeva and A. J. Putnam, "Endothelial cell traction and ECM density influence both capillary morphogenesis and maintenance in 3-D," *Am. J. Physiol. Cell Physiol.*, vol. 297, pp. C179–187, 2009.

[242] C. M. Kraning-Rush, S. P. Carey, J. P. Califano, B. N. Smith, and C. A. Reinhart-King, "The role of the cytoskeleton in cellular force generation in 2D and 3D environments," *Physical Biology*, vol. 8, no. 1, p. 0150099 (9pp), 2011.

[243] G. A. Monteiro, A. V. Fernandes, H. G. Sundararaghavan, and D. I. Shreiber, "Positively and negatively modulating cell adhesion to type I collagen via peptide grafting," *Tissue Engineering: Part A*, vol. 17, no. 13-14, pp. 1663–1673, 2011.

[244] F. Grinnell, C.-H. Ho, Y.-C. Lin, and G. Skuta, "Differences in the regulation of fibroblast contraction of floating versus stressed collagen ma-

trices," *Journal of Biological Chemistry*, vol. 274, no. 2, pp. 918–923, 1999.

[245] M. Abe, C.-H. Ho, K. E. Kamm, and F. Grinnell, "Different molecular motors mediate platelet-derived growth factor and lysophosphatidic acid-stimulated floating collagen matrix contraction," *Journal of Biological Chemistry*, vol. 278, no. 48, pp. 47707–47712, 2003.

[246] M. Lopez-Garcia, D. Beebe, and W. Crone, "Mechanical interactions of mouse mammary gland cells with collagen in a three-dimensional construct," *Annals of Biomedical Engineering*, vol. 38, no. 8, pp. 2485–2498, 2010.

[247] T. M. Koch, S. Münster, N. Bonakdar, J. P. Butler, and B. Fabry, "3D traction forces in cancer cell invasion," *PLoS ONE*, vol. 7, no. 3, p. e33476, 2012.

[248] S. Vanni, B. C. Lagerholm, C. Otey, D. L. Taylor, and F. Lanni, "Internet-based image analysis quantifies contractile behavior of individual fibroblasts inside model tissue," *Biophys. J.*, vol. 84, pp. 2715–2727, 2003.

[249] M. S. Hall, R. Long, X. Feng, Y. Huang, C.-Y. Hui, and M. Wu, "Toward single cell traction microscopy within 3D collagen matrices," *Experimental Cell Research*, vol. 319, pp. 2396–2408, 2013.

[250] N. Gjorevski and C. M. Nelson, "Mapping of mechanical strains and stresses around quiescent engineered three-dimensional epithelial tissues," *Biophys. J.*, vol. 103, pp. 152–162, 2012.

[251] I. K. Piechocka, A. S. van Oosten, R. G. Breuls, and G. H. Koenderink, "Rheology of heterotypic collagen networks," *Biomacromolecules*, vol. 12, pp. 2797–2805, 2011.

[252] N. A. Kurniawan, L. H. Wong, and R. Rajagopalan, "Early stiffening and softening of collagen: Interplay of deformation mechanisms in biopolymer networks," *Biomacromolecules*, vol. 13, pp. 691–698, 2012.

[253] S. Motte and L. J. Kaufman, "Strain stiffening in collagen I networks," *Biopolymers*, vol. 99, no. 1, pp. 35–46, 2012.

[254] C. A. Jones, M. Cibula, J. Feng, E. A. Kmacik, D. H. McIntyre, H. Levine, and B. Sun, "Micromechanics of cellularized biopolymer networks," *PNAS*, pp. E5117–E5112, 2015.

[255] E. Conti and F. C. MacKintosh, "Cross-linked networks of stiff filaments exhibit negative normal stress," *PRL*, vol. 102, p. 088102, 2009.

[256] I. Thievessen, N. Fakhri, J. Steinwachs, V. Kraus, R. S. McIsaac, L. Gao, B.-C. Chen, M. A. Baird, M. W. Davidson, E. Betzig, R. Oldenbourg, C. M. Waterman, and B. Fabry, "Vinculin is required for cell polarization, migration, and extracellular matrix remodeling in 3D collagen," *The FASEB Journal*, vol. 29, pp. 1–13, 2015.

[257] W. R. Legant, J. S. Miller, B. L. Blakely, D. M. Cohen, G. M. Genin, and C. S. Chen, "Measurement of mechanical traction exerted by cells in three-dimensional matrices," *Nature Methods*, vol. 7, no. 12, pp. 969–971, 2010.

[258] J. S. Miller, C. J. Shen, W. R. Legant, J. D. Baranski, B. L. Blakely, and C. S. Chen, "Bioactive hydrogels made from step-growth derived PEG-peptide macromers," *Biomaterials*, vol. 13, pp. 3736–3743, 2010.

[259] P. Roy, W. Petroll, H. Cavanagh, C. Chuong, and J. Jester, "An *in Vitro* Force Measurement Assay to Study the Early Mechanical Interaction between Corneal Fibroblasts and Collagen Matrix," *Experimental Cell Research*, vol. 232, pp. 106–117, 1997.

[260] R. J. Polackwich, D. Koch, R. Arevalo, A. M. Miermont, K. J. Jee, J. Lazar, J. Urbach, S. C. Mueller, and R. G. McAllister, "A novel 3d fibril force assay implicates Src in tumor cell force generation in collagen networks," *PLoS ONE*, vol. 8, no. 3, p. e58138, 2013.

[261] J. D. Humphries, P. Wang, C. Streuli, B. Geiger, M. J. Humphries, and C. Ballestrem, "Vinculin controls focal adhesion formation by direct interactions with talin and actin," *Journal of Cell Biology*, vol. 179, no. 5, pp. 1043–1057, 2007.

[262] M. Morimatsu, A. H. Mekhdjian, A. S. Adhikari, and A. R. Dunn, "Molecular tension sensors report forces generated by single integrin molecules in living cells," *Nanoletters*, vol. 13, pp. 3985–3989, 2013.

[263] C. H. Lee, A. Singla, and Y. Lee, "Biomedical applications of collagen," *International Journal of Pharmaceutics*, vol. 2001, pp. 1–22, 2001.

[264] E. S. Place, N. D. Evans, and M. M. Stevens, "Complexity in biomaterials for tissue engineering," *Nature Materials*, vol. 8, pp. 457–470, 2009.

[265] R. Uibo, I. Laidmäe, E. S. Sawyer, L. A. Flanagan, P. C. Georges, J. P. Winer, and P. A. Janmey, "Soft materials to treat central nervous system injuries: Evaluation of the suitability of non-mammalian fibrin gels," *Biochimica et Biophysica Acta*, vol. 2009, pp. 924–930, 2009.

[266] T. A. Ahmed, E. V. Dare, and M. Hincke, "Fibrin: A versatile scaffold for tissue engineering applications," *Tissue Engineering: Part B*, vol. 14, no. 2, pp. 199–215, 2008.

[267] W. D. Spotnitz, "Fibrin sealant: The only approved hemostat, sealant, and adhesive - a laboratory and clinical perspective," *ISRN Surgery*, vol. 2014, p. 28, 2014.

[268] S. Ravindran, M. Kotecha, C.-C. Huang, A. Ye, P. Pothirajan, Z. Yin, R. Magin, and A. George, "Biological and MRI characterization of biomimentic ECM scaffolds for cartilage tissue regeneration," *Biomaterials*, vol. 71, pp. 58–70, 2015.

[269] O. Singh, S. S. Gupta, M. Soni, S. Moses, S. Shukla, and R. K. Mathur, "Collagen dressing versus conventional dressings in burn and chronic wounds: A retrospective study," *J. Cutan. Aesthet. Surg.*, vol. 2011, pp. 12–16, 2011.

[270] J. V. Shah and P. A. Janmey, "Strain hardening of fibrin gels and plasma clots," *Rheol. Acta*, vol. 36, pp. 262–268, 1997.

[271] J. A. Pedersen and M. A. Swartz, "Mechanobiology in the third dimension," *Annals of Biomedical Engineering*, vol. 33, no. 11, pp. 1469–1490, 2005.

[272] D. Vader, A. Kabla, D. Weitz, and L. Mahadevan, "Strain-induced alignment in collagen gels," *PLoS ONE*, vol. 4, no. 6, p. e5902, 2009.

[273] M. Guthold, W. Liu, E. Sparks, L. Jawerth, L. Peng, M. Falvo, R. Superfine, R. Hantgan, and S. Lord, "A comparison of the mechanical and structural properties of fibrin fibers with other protein fibers," *Cell Biochem Biophys*, vol. 49, pp. 165–181, 2007.

[274] M. Gardel, J. Shin, F. MacKintosh, L. Mahadevan, P. Matsudaira, and D. Weitz, "Scaling of F-actin network rheology to probe single filament elasticity and dynamics," *PRL*, vol. 93, p. 188102, 2004.

[275] M. Gardel, F. Nakamura, J. Hartwig, J. Crocker, T. Stossel, and D. Weitz, "Prestressed F-actin networks cross-linked by hinged filamins replicate mechanical properties of cells," *PNAS*, vol. 103, no. 6, pp. 1762–1767, 2006.

[276] Y.-C. Lin, N. Y. Yao, C. P. Broedersz, H. Herrmann, F. C. MacKintosh, and D. A. Weitz, "Origins of elasticity in intermediate filament networks," *PRL*, vol. 104, p. 058101(4), 2010.

[277] G. Žagar, P. R. Onck, and E. van der Giessen, "Two fundamental mechanisms govern the stiffening of cross-linked networks," *Biophys. J.*, vol. 108, pp. 1470–1479, 2015.

[278] C. Broedersz and F. MacKintosh, "Modeling semiflexible polymer networks," *Reviews of Modern Physics*, vol. 86, pp. 995–1036, 2014.

[279] A. J. Licup, S. Münster, A. Sharma, M. Sheinman, L. M. Jawerth, B. Fabry, D. A. Weitz, and F. C. MacKintosh, "Stress controls the mechanics of collagen networks," *PNAS*, vol. 112, no. 31, pp. 9573–9578, 2015.

[280] C. P. Broedersz, X. Mao, T. C. Lubensky, and F. C. MacKintosh, "Criticality and isostaticity in fibre networks," *Nature Physics*, vol. 7, pp. 983–988, 2011.

[281] J.-P. Collet, H. Shuman, R. E. Ledger, S. Lee, and J. W. Weisel, "The elasticity of an individual fibrin fiber in a clot," *PNAS*, vol. 102, pp. 9133–9137, 2005.

[282] J. R. Houser, N. E. Hudson, L. Ping, E. T. O. III, R. Superfine, S. T. Lord, and M. R. Falvo, "Evidence that αC region is origin of low modulus, high extensibility, and strain stiffening in fibrin fibers," *Biophys. J.*, vol. 99, pp. 3038–3047, 2010.

[283] C. C. Helms, R. A. S. Ariëns, S. U. de Willige, K. F. Standeven, and M. Guthold, "α-α cross-links increase fibrin fiber elasticity and stiffness," *Biophys. J.*, vol. 102, pp. 168–175, 2012.

[284] N. Sasaki and S. Odajima, "Elongation mechanism of collagen fibrils and force-strain relations of tendon at each level of structural hierarchy," *J. Biomechanics*, vol. 29, no. 9, pp. 1131–1136, 1996.

[285] J. A. van der Rijt, K. O. van der Werf, M. L. Bennink, P. J. Dijkstra, and J. Feijen, "Micromechanical testing of individual collagen fibrils," *Macromol. Biosci.*, vol. 6, pp. 697–702, 2006.

[286] S. Gevorkian, A. Allahverdyan, D. Gevorgyan, and C.-K. Hu, "Glassy state of native collagen fibril?," *EPL*, vol. 95, no. 2, p. 23001, 2011.

[287] L. Yang, K. van der Werf, P. Dijkstra, J. Feijen, and M. Bennink, "Micromechanical analysis of native and cross-linked collagen type I fibrils supports the existence of microfibrils," *Journal of the Mechanical Behavior of Biomedical Materials*, vol. 6, pp. 148–158, 2012.

[288] J. S. Graham, A. N. Vomund, C. L. Phillips, and M. Grandbois, "Structural changes in human type I collagen fibrils investigated by force spectroscopy," *Experimental Cell Research*, vol. 2004, pp. 335–342, 2004.

[289] J. W. Weisel, "The electron microscope band pattern of human fibrin: Various stains, lateral order, and carbohydrate localization," *J. Ultrastruct. Mol. Struct. Res.*, vol. 96, pp. 176–188, 1986.

[290] I. S. Yermolenko, V. K. Lishko, T. P. Ugarova, and S. N. Magonov, "High-resolution visualization of fibrinogen molecules and fibrin fibers with atomic force microscopy," *Biomacromolecules*, vol. 12, pp. 370–379, 2011.

[291] J. W. Weisel, C. Nagaswami, and L. Makowski, "Twisting of fibrin fibers limits their radial growth," *PNAS*, vol. 84, pp. 8991–8995, 1987.

[292] M. D. Bale and J. D. Ferry, "Strain enhancement of elastic modulus in fine fibrin clots," *Thrombosis Research*, vol. 52, no. 6, pp. 565–572, 1988.

[293] E. A. Ryan, L. F. Mockros, J. W. Weisel, and L. Lorand, "Structural originas of fibrin clot rheology," *Biophys. J.*, vol. 77, pp. 2813–2826, 1999.

[294] J. W. Weisel and R. I. Litvinov, "Mechanisms of fibrin polymerization and clinical implications," *Blood*, vol. 121, no. 10, pp. 1712–1719, 2013.

[295] C. Yeromonahos, B. Polack, and F. Caton, "Nanostructure of the fibrin clot," *Biophys. J.*, vol. 99, pp. 2018–2027, 2010.

[296] M. E. Carr and J. Hermans, "Size and density of fibrin fibers from turbidity," *Macromolecules*, vol. 11, no. 1, pp. 46–50, 1978.

[297] I. K. Piechocka, *Biopolymers: from structural hierarchy to nonlinear rheology*. PhD thesis, Vrije Universiteit Amsterdam, 2011.

[298] J. Torbet, J.-M. Freyssinet, and G. Hudry-Clergeon, "Oriented fibrin gels formed by polymerization in strong magnetic fields," *Nature*, vol. 289, pp. 91–93, 1981.

[299] A. Zhmurov, A. E. Brown, R. I. Litvinov, R. I. Dima, J. W. Weisel, and V. Barsegov, "Mechanism of fibrin(ogen) forced unfolding," *Structure*, vol. 19, pp. 1615–1624, 2011.

[300] Y.-L. Sun, Z.-P. Luo, A. Fertala, and K.-N. An, "Direct quantification of the flexibility of type I collagen monomer," *BBRC*, vol. 295, pp. 382–386, 2002.

[301] P. Fratzl, ed., *Collagen Structure and Mechanics*. Springer Science+Business Media, 2008.

[302] M. de Wild, W. Pomp, and G. H. Koenderink, "Thermal memory in self-assembled collagen fibril networks," *Biophys. J.*, vol. 105, pp. 200–210, 2013.

[303] M. Fang, E. L. Goldstein, A. S. Turner, C. M. Les, B. G. Orr, G. J. Fisher, K. B. Welch, E. D. Rothman, and M. M. B. Holl, "Type I collagen D-spacing in fibril bundles of dermis, tendon, and bone: Bridging between nano- and micro-level tissue hierarchy," *ACS NANO*, vol. 6, no. 11, pp. 9503–9514, 2012.

[304] G. Wood and M. Keech, "The formation of fibrils from collagen solutions. 1. the effect of experimental conditions: Kinetec and electron-microscope studies," *Biochemical Journal*, vol. 75, pp. 588–589, 1960.

[305] C. B. Raub, V. Suresh, T. Krasieva, J. Lyubovitsky, J. D. Mih, A. J. Putnam, B. J. Tromberg, and S. C. George, "Noninvasive assessment of collagen gel microstructure and mechanics using multiphoton microscopy," *Biophys. J.*, vol. 92, pp. 2212–2222, 2007.

[306] Y.-J. Hwang and J. G. Lyubovitsky, "Collagen hydrogel characterization: multi-scale and multi-modality approach," *Analytical Methods*, vol. 3, pp. 529–536, 2011.

[307] B. A. Roeder, K. Kokini, J. E. Sturgis, J. P. Robinson, and S. L. Voytik-Harbin, "Tensile mechanical properties of three-dimensional type I collagen extracellular matrices with varied microstructure," *Transactions of the ASME*, vol. 124, pp. 214–222, 2002.

[308] F. Jiang, H. Hörber, J. Howard, and D. J. Müller, "Assembly of collagen into microribbons: effects of pH and electrolytes," *Journal of Structural Biology*, vol. 148, pp. 268–278, 2004.

[309] C. B. Raub, J. Unruh, V. Suresh, T. Krasieva, T. Lindmo, E. Gratton, B. J. Tromberg, and S. C. George, "Image correlation spectroscopy of multiphoton images correlates with collagen mechanical properties," *Biophys. J.*, vol. 94, pp. 2361–2373, 2008.

[310] J. Sapudom, S. Rubner, S. Martin, T. Kurth, S. Riedel, C. T. Mierke, and T. Pompe, "The phenotype of cancer cell invasion controlled by fibril diameter and pore size of 3D collagen networks," *Biomacromolecules*, vol. 52, pp. 367–375, 2015.

[311] D. J. Hulmes, T. J. Wess, D. J. Prockop, and P. Fratzl, "Radial packing, order, and disorder in collagen fibrils," *Biophys. J.*, vol. 68, pp. 1661–1670, 1995.

[312] Y. Yang, M. Bai, W. S. Klug, A. J. Levine, and M. T. Valentine, "Microrheology of highly crosslinked microtubule networks is dominated by force-induced crosslinker unbinding," *Soft Matter*, vol. 9, no. 2, pp. 383–393, 2013.

[313] M. M. A. E. Claessens, M. Bathe, E. Frey, and A. R. Bausch, "Actin-binding proteins sensitively mediate F-actin bundle stiffness," *Nature Materials*, vol. 5, pp. 748–753, 2006.

[314] T. Sanchez, D. Welch, D. Nicastro, and Z. Dogic, "Cilia-like beating of active microtubule bundles," *Science*, vol. 333, pp. 456–459, 2011.

[315] J.-F. Nolting, W. Möbius, and S. Köster, "Mechanics of individual keratin bundles in living cells," *Biophys. J.*, vol. 107, pp. 2693–2699, 2014.

[316] J. P. Orgel, T. C. Irving, A. Miller, and T. J.Wess, "Microfibrillar structure of type I collagen *in situ*," *PNAS*, vol. 103, pp. 9001–9005, 2006.

[317] G. M. Grason and R. F. Bruinsma, "Chirality and equilibrium biopolymer bundles," *PRL*, vol. 99, p. 098101, 2007.

[318] C. Heussinger and G. M. Grason, "Theory of crosslinked bundles of helical filaments: Intrinsic torques in self-limiting biopolymer assemblies," *J. Chem. Phys.*, vol. 135, p. 035104, 2011.

[319] I. R. Bruss and G. M. Grason, "Non-euclidean geometry of twisted filament bundle packing," *PNAS*, vol. 109, pp. 10781–10786, 2012.

[320] C. Heussinger, M. Bathe, and E. Frey, "Statistical mechanics of semiflexible bundles of wormlike polymer chains," *PRL*, vol. 99, p. 048101, 2007.

[321] A. Kis, G. Csányl, J.-P. Salvetat, T.-N. Lee, E. Couteau, A. Kulik, W. Benoit, J. Brugger, and L. Forró, "Reinforcement of single-walled carbon nanotube bundles by intertube bridging," *Nature Materials*, vol. 3, pp. 153–157, 2004.

[322] L. M. Ericson, H. Fan, H. Peng, V. A. Davis, W. Zhou, J. Sulpizio, Y. Wang, R. Booker, J. Vavro, C. Guthy, A. N. G. Parra-Vasquez, M. J. Kim, S. Ramesh, R. K. Saini, C. Kittrell, G. Lavin, H. Schmidt, W. W. Adams, W. E. Billups, M. Pasquali, W.-F. Hwang, R. H. Hauge, J. E. Fischer, and R. E. Smalley, "Macroscopic, neat, single-walled carbon nanotube fibers," *Science*, vol. 305, pp. 1447–1450, 2012.

[323] P. H. J. Kouwer, M. Koepf, V. A. A. L. Sage, M. Jaspers, A. M. van Buul, Z. H. Eksteen-Akeroyd, T. Woltinge, E. Schwartz, H. J. Kitto, R. Hoogenboom, S. J. Picken, R. J. M. Nolte, E. Mendes, and A. E. Rowan, "Responsive biomimetic networks from polyisocyanopeptide hydrogels," *Nature*, vol. 493, pp. 651–655, 2013.

[324] M. Jaspers, M. Dennison, M. F. Mabesoone, F. C. MacKintosh, A. E. Rowan, and P. H. Kouwer, "Ultra-responsive soft matter from strain-stiffening hydrogels," *Nature Communications*, vol. 5, p. 5808, 2014.

[325] M. Bathe, C. Heussinger, M. M. Claessens, A. R. Bausch, and E. Frey, "Cytoskeletal bundle mechanics," *Biophys. J.*, vol. 94, pp. 2955–2964, 2008.

[326] C. Heussinger, F. Schüller, and E. Frey, "Statics and dynamics of the wormlike bundle model," *PRE*, vol. 81, p. 021904, 2010.

[327] C. Heussinger, "Cooperative crosslink (un)binding in slowly driven bundles of semiflexible filaments," *Phys. Rev. E. Stat. Nonlin. Soft Matter Phys.*, vol. 83, p. 050902, 2011.

[328] R. L. C. Vink and C. Heussinger, "Cross-linked biopolymer bundles: Cross-link reversibility leads to cooperative binding/unbinding phenomena," *J. Chem. Phys.*, vol. 136, no. 3, p. 035102, 2012.

[329] J. M. Kollman, L. Pandi, M. R. Sawaya, M. Riley, and R. F. Doolittle, "Crystal structure of human fibrinogen," *Biochemistry*, vol. 48, pp. 3877–3886, 2009.

[330] A. L. C. L. Corte, H. Philippou, and R. A. Ariëns, "Role of fibrin structure in thrombosis and vascular disease," *Advances in Protein Chemistry and Structural Biology*, vol. 83, pp. 75–127, 2011.

[331] G. Tsurupa, I. Pechik, R. I. Litvinov, R. R. Hantgan, N. Tjandra, J. W. Weisel, and L. Medved, "On the mechanism of αC polymer formation in fibrin," *Biochemistry*, vol. 51, pp. 2526–2538, 2012.

[332] N. Kurniawan, J. Grimbergen, J. Koopman, and G. Koenderink, "Factor XIII stiffens fibrin clots by causing fiber compaction," *J Thromb Haemost*, vol. 12, pp. 1687–1696, 2014.

[333] W. Liu, L. M. Jawerth, E. A. Sparks, M. R. Falvo, R. R. Hantgan, R. Superfine, S. T. Lord, and M. Guthold, "Fibrin fibers have extraordinary extensibility and elasticity," *Science*, vol. 313, p. 634, 2006.

[334] W. Liu, C. Carlisle, E. Sparks, and M. Guthold, "The mechanical properties of single fibrin fibers," *Journal of Thrombosis and Haemostasis*, vol. 8, pp. 1030–1036, 2010.

[335] A. Zhmurov, O. Kononova, R. I. Litvinov, R. I. Dima, V. Barsegov, and J. W. Weisel, "Mechanical transition from α-helical coiled coils to β-sheets in fibrin(ogen)," *J. Am. Chem. Soc.*, vol. 134, pp. 20396–20402, 2012.

[336] R. I. Litvinov, D. A. Faizullin, Y. F. Zuev, and J. W. Weisel, "The α-helix to β-sheet transition in stretched and compressed hydrated fibrin clots," *Biophys. J.*, vol. 103, pp. 1020–1027, 2012.

[337] M. R. Falvo, D. Millard, E. T. O. III, R. Superfine, and S. T. Lord, "Length of tandem repeats in fibrin's αC region correlates with fiber extensibility," *J. Thromb. Haemost.*, vol. 6, no. 11, pp. 1991–1993, 2008.

[338] M. F. Muller, H. Ris, and J. D. Ferry, "Electron microscopy of fine fibrin clots and fine and coarse fibrin films," *J. Mol. Biol*, vol. 174, no. 2, pp. 369–384, 1984.

[339] P. A. Janmey, "Rheology of fibrin clots. VI. stress relaxation, creep, and differential dynamic modulus of fine clots in large shearing deformations," *Journal of Rheology*, vol. 27, no. 2, pp. 135–153, 1983.

[340] J. D. Ferry and P. R. Morrison, "Preparation and properties of serum and plasma proetins. VIII. the conversion of humand fibrinogen to fibrin under various conditions," *J. Am. Chem. Soc.*, vol. 69, no. 2, pp. 388–400, 1946.

[341] K. F. Standeven, A. M. Carter, P. J. Grant, J. W. Weisel, I. Chernysh, L. Masova, S. T. Lord, and R. A. S. Ariëns, "Functional analysis of fibrin γ-chain cross-linking by activated factor XIII: determination of a cross-linking pattern that maximizes clot stiffness," *Hemostasis, Thrombosis, and Vascular Biology*, vol. 110, no. 3, pp. 902–907, 2007.

[342] K. Freund, K. Doshi, S. Gaul, D. Claremon, D. Remy, J. Baldwin, S. Pitzenberger, and A. Stern, "Transglutainase inhibition by 2-[(2-oxopropyl)thio]imidazolium derivatives: mechanism of factor XIIIa inactivation," *Biochemistry*, vol. 33, no. 33, pp. 10109–10119, 1994.

[343] E. Hethershaw, A. C. L. Corte, C. Duval, M. Ali, P. Grant, R. Ariëns, and H. Philippou, "The effect of blood coagulation factor XIII on fibrin clot structure and fibrinolysis," *Journal of Thrombosis and Haemostasis*, vol. 12, pp. 197–205, 2014.

[344] L. Huang and S. T. Lord, "The isolation of fibrinogen monomer dramatically influences fibrin polymerization," *Thrombosis Research*, vol. 131, pp. e258–e263, 2013.

[345] C. P. Broedersz, K. E. Kasza, L. M. Jawerth, S. Münster, D. A. Weitz, and F. C. MacKintosh, "Measurement of nonlinear rheology of cross-linked biopolymer gels," *Soft Matter*, vol. 6, pp. 4120–4127, 2010.

[346] F. Caton, "personal communication,"

[347] M. D. Spirito, G. Arcòvito, M. Papi, M. Rocco, and F. Ferri, "Small- and wide-angle elastic light scattering study of fibrin structure," *J. Appl. Cryst.*, vol. 36, pp. 636–641, 2003.

[348] F. MacKintosh, J. Käs, and P. Janmey, "Elasticity of semiflexible biopolymer networks," *PRL*, vol. 75, no. 24, pp. 4425–4428, 1995.

[349] M. Gardel, J. Shin, F. MacKintosh, L. Mahadevan, P. Matsudaira, and D. Weitz, "Elastic behavior of cross-linked and bundled actin networks," *Science*, vol. 304, pp. 1301–1305, 2004.

[350] C. E. Hall and H. S. Slayter, "The fibrinogen molecule: Its size, shape, and mode of polymerization," *J. Biophysic. and Biochem. Cytol.*, vol. 5, no. 1, pp. 11–16, 1958.

[351] A. Protopopova, N. Barinov, E. Zavyalova, A. Kopylov, V. Sergienko, and D. Klinov, "Visualization of fibrinogen αC regions and their arrangement during fibrin network formation by high-resolution AFM," *J. Thromb. Haemost.*, vol. 13, no. 4, pp. 570–579, 2015.

[352] G. Nelb, C. Gerth, and J. Ferry, "Rheology of fibrin clots. III. Shear creep and creep recovery of fine ligated and coarse unligated clots," *Biophysical Chemistry*, vol. 5, pp. 377–387, 1976.

[353] S. Bernocco, F. Ferri, A. Profumo, C. Cuniberti, and M. Rocco, "Polymerication of rod-like macromolecular monomers studied by stopped-flow, multiangle light scattering: Set-up, data processing, and application to fibrin formation," *Biophys. J.*, vol. 79, pp. 561–583, 2010.

[354] Q. Wen, A. Basu, J. P. Winer, A. Yodh, and P. A. Janmey, "Local and global deformations in a strain-stiffening fibrin gel," *New Journal of Physics*, vol. 9, p. 428, 2007.

[355] M. Rocco, M. Molteni, M. Ponassi, G. Giachi, M. Frediani, A. Koutsioubas, A. Profumo, D. Trevarin, B. Cardinali, P. Vachette, F. Ferri, and J. Pérez, "A comprehensive mechanism of fibrin network formation

involving early branching and delaysed single- to double-strand transition from coupled time-resolved X-ray/light-scattering detection," *JACS*, vol. 136, pp. 5376–5384, 2014.

[356] H. Kojima, A. Ishijima, and T. Yanagida, "Direct measurement of stiffness of single actin filaments with and without tropomyosin by in vitro nanomanipulation," *PNAS*, vol. 91, pp. 12962–12966, 1994.

[357] R. Tharmann, M. Claessens, and A. Bausch, "Viscoelasticity of isotropically cross-linked actin networks," *PRL*, vol. 98, p. 088103, 2007.

[358] O. V. Gorkun, Y. I. Veklich, L. V. Medved, A. H. Henschen, and J. W. Weisel, "Role of the αC domains of fibrin in clot formation," *Biochemistry*, vol. 33, pp. 6986–6997, 1994.

[359] J. W. Weisel and L. Medved, "The structure and function of the αC domains of fibrinogen," *Ann. N. Y. Acad. Sci.*, vol. 936, pp. 312–327, 2001.

[360] E. A. Ryan, L. F. Mockros, A. M. Stern, and L. Lorand, "Influence of a natural and a synthetic inhibitor of factor XIIIa on fibrin clot rheology," *Biophys. J.*, vol. 77, pp. 2827–2836, 1999.

[361] R. A. Ariëns, T.-S. Lai, J. W. Weisel, C. S. Greenberg, and P. J. Grant, "Role of factor XIII in fibrin clot formation and effects of genetic polymorphisms," *Blood*, vol. 100, pp. 743–754, 2002.

[362] L. Mockros, W. Roberts, and L. Lorand, "Viscoelastic properties of ligation-inhibited fibrin clots," *Biophysical Chemistry*, vol. 2, pp. 164–169, 1974.

[363] C. Gerth, W. W. Roberts, and J. D. Ferry, "Rheology of fibrin clots. II. linear viscoelastic behavior in shear creep," *Biophysical Chemistry*, vol. 2, pp. 208–217, 1974.

[364] M. Guthold, W. Liu, B. Stephens, S. Lord, R. Hantgan, D. Erie, R. T. Jr., and R. Superfine, "Visualization and mechanical manipulations of individual fibrin fibers suggest that fiber cross section has fractal dimension 1.3," *Biophys. J.*, vol. 87, pp. 4226–4236, 2004.

[365] R. D. Averett, B. Menn, E. H. Lee, C. C. Helms, T. Barker, and M. Guthold, "A modular fibrinogen model that captures the stress-strain behavior of fibrin fibers," *Biophys. J.*, vol. 103, pp. 1537–1544, 2012.

[366] P. K. Purohit, R. I. Litvinov, A. E. Brown, D. E. Discher, and J. W. Weisel, "Protein unfolding accounts for the unusual mechanical behavior of fibrin networks," *Acta Biomaterialia*, vol. 7, pp. 2374–2383, 2011.

[367] F. MacKintosh and C. Schmidt, "Active cellular materials," *Current Opinion Cell Biology*, vol. 22, pp. 29–35, 2010.

[368] F. MacKintosh and C. Schmidt, *Mechanics of motor proteins and the cytoskeleton*. Sinauer Sunderland MA, 2001.

[369] N. Wang, K. Naruse, D. Stamenović, J. J. Fredberg, S. M. Mijailovick, I. M. Tolić-Nørrelykke, T. Polte, R. Mannix, and D. E. Ingber, "Mechanical behavior in living cells consistent with the tensegrity model," *PNAS*, vol. 98, pp. 7765–7770, 2001.

[370] F. Gallet, D. Arcizet, P. Bohec, and A. Richert, "Power spectrum of out-of-equilibrium forces in living cels: amplitude and frequency dependence," *Soft Matter*, vol. 5, pp. 2947–2953, 2009.

[371] P. Kollmannsberger, C. T. Mierke, and B. Fabry, "Nonlinear viscoelasticity of adherent cells is controlled by cytoskeletal tension," *Soft Matter*, vol. 7, pp. 3127–3132, 2011.

[372] D. Mizuno, C. Tardin, C. Schmidth, and F. MacKintosh, "Nonequilibrium mechanics of active cytoskeletal networks," *Science*, vol. 315, pp. 370–373, 2007.

[373] G. H. Koenderink, Z. Dogic, F. Nakamura, P. M. Bendix, F. C. MacKintosh, J. H. Hartwig, T. P. Stossel, and D. A. Weitz, "An active biopolymer network controlled by molecular motors," *PNAS*, vol. 106, no. 36, pp. 15192–15197, 2009.

[374] B. Geiger, J. P. Spatz, and A. D. Bershadsky, "Environmental sensing through focal adhesions," *Nature Reviews*, vol. 10, pp. 21–33, 2009.

[375] I. Bischofs and U. Schwarz, "Cell organization in soft media due to active mechanosensing," *PNAS*, vol. 100, no. 16, pp. 9274–9279, 2003.

[376] A. Zemel, R. De, and S. A. Safran, "Mechanical consequences of cellular force generation," *Current Opinion in Solid State and Materials Science*, vol. 15, pp. 169–176, 2011.

[377] N. Wang, I. M. Tolić-Norrelykke, J. Chen, S. M. Mijailovich, J. P. Butler, J. J. Fredberg, and D. Stamenovic, "Cell prestress. I. stiffness and prestress are closely associated in adherent contractile cells," *Am. J. Physiol. Cell. Physiol.*, vol. 282, pp. C606–C616, 2002.

[378] M. Dembo and Y.-L. Wang, "Stresses at the cell-to-substrate interface during locomotion of fibroblasts," *Biophys. J.*, vol. 76, pp. 2307–2316, 1999.

[379] N. Q. Balaban, U. S. Schwarz, D. Riveline, P. Goichberg, G. Tzur, I. Sabanay, D. Mahalu, S. Safran, A. Bershadsky, L. Addadi, and B. Geiger, "Force and focal adhesion assembly: a close relationship studied using elastic micropatterned substrates," *Nature Cell Biology*, vol. 3, pp. 466–472, 2001.

[380] R. McBeath, D. M. Pirone, C. M. Nelson, K. Bhadriraju, and C. S. Chen, "Cell shape, cytoskeletal tension, and rhoA regulate stem cell lineage commitment," *Developmental Cell*, vol. 6, pp. 483–495, 2004.

[381] E. A. Klein, L. Yin, D. Kothapalli, P. Castagnino, F. J. Byfield, T. Xu, I. Levental, E. Hawthorne, P. A. Janmey, and R. K. Assoian, "Cell-cycle control by physiological matrix elasticity and in vivo tissue stiffening," *Current Biology*, vol. 19, pp. 1511–1518, 2009.

[382] M. A. Wozniak and C. S. Chen, "Mechanotransduction in development: a growing role for contractility," *Nature Reviews Molecular Cell Biology*, vol. 10, pp. 34–43, 2009.

[383] D. Butcher, T. Alliston, and V. Weaver, "A tense situation: forcing tumour progression," *Nat. Rev. Cancer*, vol. 9, pp. 108–122, 2009.

[384] A. Harris, D. Stopak, and P. Wild, "Fibroblast traction as a mechanism for collagen morphogenesis," *Nature*, vol. 290, pp. 249–251, 1981.

[385] P. Fernandez and A. R. Bausch, "The compaction of gels by cells: a case of collective mechanical activity," *Integrative Biology*, vol. 1, pp. 252–259, 2009.

[386] I. B. Bischofs, F. Klein, D. Lehnert, M. Bastmeyer, and U. S. Schwarz, "Filamentous network mechanics and active contractility determine cell and tissue shape," *Biophys. J.*, vol. 95, pp. 3488–3496, 2008.

[387] S. E. Mutsaers, J. E. Bishop, G. McGrouther, and G. J. Laurent, "Mechanisms of tissue repair: from wound healing to fibrosis," *Int. J. Biochem. Cell Biol.*, vol. 29, no. 1, pp. 5–17, 1997.

[388] L. Urech, A. G. Bittermann, J. A. Hubbell, and H. Hall, "Mechanical properties, proteolytic degradability and biological modifications affect angiogenic process extension into native and modified fibrin matrices in vitro," *Biomaterials*, vol. 26, pp. 1369–1379, 2005.

[389] A. E. X. Brown, R. I. Litvinov, D. E. Discher, P. K. Purohit, and J. W. Weisel, "Multiscale mechanics of fibrin polymer: Gel stretching with protein unfolding and loss of water," *Science*, vol. 325, pp. 741–744, 2009.

[390] S. B. Lindström, D. A. Vader, A. Kulachenko, and D. A. Weitz, "Biopolymer network geometries: Characterization, regeneration, and elastic properties," *PRE*, vol. 82, p. 051905, 2010.

[391] O. Budtz-Olsen, *Clot retraction*. Charles C. Thomas, Springfield, Illinois, 1951.

[392] S. Niewiarowski, E. Regoeczi, and J. Mustard, "Adhesion of fibroblasts to polymerizing fibrin and retraction of fibrin induced by fibroblasts," *Proc. Soc. Exp. Biol. Med.*, vol. 140, pp. 199–204, 1972.

[393] T. Wakatsuki, M. S. Kolodney, G. I. Zahalak, and E. L. Elson, "Cell mechanics studied by a reconstituted model tissue," *Biophys. J.*, vol. 79, pp. 2353–2368, 2000.

[394] M. C. Evans and V. H. Barocas, "The modulus of fibroblast-populated collagen gels is not determined by final collagen and cell concentration: Experiments and an inclusion-based model," *Journal of Biomechanical Engineering*, vol. 131, pp. 101014–1–7, 2009.

[395] A. Iordan, A. Duperray, A. Gérard, A. Grechine, and C. Verdier, "Breakdown of cell-collagen networks through collagen remodeling," *Biorheology*, vol. 47, pp. 277–295, 2010.

[396] G. Gurtner, S. Werner, and Y. Barrandon, "Wound repair and regeneration," *Nature*, vol. 453, pp. 314–321, 2008.

[397] A. Falanga, M. Marchetti, and D. Balducci, "Clotting mechanisms and cancer: implications in thrombus formation and tumor progression," *Clin. Adv. Hematol. Oncol.*, vol. 1, pp. 673–678, 2003.

[398] A. Falanga, M. Marchetti, and D. Balducci, "In vitro fibroplasia: matrix contraction, cell growth, and collagen production of fibroblasts cultured in fibrin gels," *Exp. Cell Res.*, vol. 223, pp. 127–134, 1996.

[399] Y. Huang, R. Dennis, L. Larkin, and K. Baar, "Rapid formation of functional muscle in vitro using fibrin gels," *J. Appl. Physiol.*, vol. 98, pp. 706–713, 2005.

[400] P. Janmey, J. Winer, and J. Weisel, "Fibrin gels and their clinical and bioengineering applications," *J. R. Soc. Interface*, vol. 6, pp. 1–10, 2009.

[401] D. Mizuno, R. Bacabac, C. Tardin, D. Head, and C. Schmidt, "High-resolution probing of cellular force transmission," *PRL*, vol. 102, p. 168102, 2009.

[402] R. Redden and E. Doolin, "Collagen crosslinking and cell density have distinct effects on fibroblast-mediated contraction of collagen gels," *Skin Res. Technol.*, vol. 9, pp. 290–293, 2003.

[403] L. Y. Leung, D. Tian, C. P. Brangwynne, D. A. Weitz, and D. J. Tschumperlin, "A new microrheometric approach reveals individual and cooperative roles for TGF-β1 and IL-1β in fibroblast-mediated stiffening of collagen gels," *The FASEB Journal*, vol. 21, pp. 2064–2073, 2007.

[404] J. S. Weinbaum, J. Qi, and R. T. Tranquillo, "Monitoring collagen transcription by vascular smooth muscle cells in fibrin-based tissue constructs," *Tissue Engineering: Part C*, vol. 16, no. 3, pp. 459–467, 2010.

[405] J. Ross and R. Tranquillo, "ECM gene expression correlates with in vitro tissue growth and development in fibrin gel remodeling by neonatal smooth muscle cells," *Matrix Biology*, vol. 22, pp. 477–490, 2003.

[406] W. M. Petroll and L. Ma, "Direct, dynamic assessment of cell-matrix interactions inside fibrillar collagen lattices," *Cell Motility and the Cytoskeleton*, vol. 55, pp. 254–264, 2003.

[407] E. Cukierman, R. Pankov, D. R. Stevens, and K. M. Yamada, "Taking cell-matrix adhesions to the third dimension," *Science*, vol. 294, pp. 1708–1712, 2001.

[408] T. Tuan and F. Grinnell, "Fibronectin and fibrinolysis are not required for fibrin gel contraction by human skin fibroblasts," *J. Cell Physiol.*, vol. 140, pp. 577–583, 1989.

[409] A. Hartmann, P. Boukamp, and P. Friedl, "Confocal reflection imaging of 3D fibrin polymers," *Blood cells, Molecules, and Diseases*, vol. 36, pp. 191–193, 2006.

[410] M. Yamato, E. Acachi, K. Yamamoto, and T. Hayashil, "Condensation of collagen fibrils to the direct vicinity of fibroblasts as a cause of gel contraction," *Journal of Biochemistry*, vol. 117, no. 5, pp. 940–946, 1995.

[411] R. A. Campbell, K. A. Overmyer, C. H. Selzman, B. C. Sheridan, and A. S. Wolberg, "Contributions of extravascular and intravascular cells to fibrin network formation, structure, and stability," *Blood*, vol. 114, no. 23, pp. 4886–4896, 2009.

[412] J. Gailit, C. Clarke, D. Newman, M. Tonnesen, M. Mosesson, and R. Clark, "Human fibroblasts bind directly to fibrinogen at RGD sites through integrin αvβ3," *Exp. Cell Res.*, vol. 232, pp. 118–126, 1997.

[413] S. Münster, L. M. Jawerth, B. A. Leslie, J. I. Weitz, B. Fabry, and D. A. Weitz, "Strain history dependence of the nonlinear stress response of fibrin and collagen networks," *PNAS*, vol. 110, no. 30, pp. 12197–12202, 2013.

[414] S. Akiyama and K. Yamada, "The interaction of plasma fibronectin with fibroblastic cells in suspension," *J. Biol. Chem.*, vol. 260, pp. 4492–4500, 1985.

[415] M. Eastwood, V. Mudera, D. McGrouther, and R. Brown, "Effect of precise mechanical loading on fibroblast populated collagen lattices: Morphological changes," *Cell Motility and the Cytoskeleton*, vol. 40, pp. 13–21, 1998.

[416] A. Straight, A. Cheung, J. Limouze, I. Chen, N. Westwood, J. Sellers, and T. Mitchison, "Dissecting temporal and spatial control of cytokinesis with a myosin II inhibitor," *Science*, vol. 299, pp. 1743–1747, 2003.

[417] C. Jen and L. McIntire, "The structural properties and contractile force of a clot," *Cell Motil.*, vol. 2, pp. 445–455, 1982.

[418] J. Zhou, H. Y. Kim, J. H.-C. Wang, and L. A. Davidson, "Macroscopic stiffening of embryonic tissues via microtubules, rhoGEF and the assembly of contractile bundles of actomyosin," *Development*, vol. 137, pp. 2785–2794, 2010.

[419] P. Chen and V. Shenoy, "Strain stiffening induced by molecular motors in active crosslinked biopolymer networks," *Soft Matter*, vol. 7, pp. 355–358, 2011.

[420] W. A. Lam, O. Chaudhuri, A. Crow, K. D. Webster, T.-D. Li, A. Kita, J. Huang, and D. A. Fletcher, "Mechanics and contraction dynamics of single platelets and implications for clot stiffening," *Nature Materials*, vol. 10, pp. 61–66, 2011.

[421] F. MacKintosh and A. Levine, "Nonequilibrium mechanics and dynamics of motor-activated gels," *PRL*, vol. 100, p. 018104, 2008.

[422] K. Lee, H. Kong, R. Larson, and D. Mooney, "Hydrogel formation via cell crosslinking," *Adv. Mater.*, vol. 15, pp. 1828–1832, 2003.

[423] R. Bloom, J. George, A. Celedon, S. Sun, and D. Wirtz, "Mapping local matrix remodeling induced by a migrating tumor cell using three-dimensional multiple-particle tracking," *Biophys. J.*, vol. 95, pp. 4077–4088, 2008.

[424] W. Petroll, L. Ma, L. Ly, and M. Vishwanath, "Analysis of the pattern of subcellular force generation by corneal fibroblasts after Rho activation," *Eye Contact Lens*, vol. 34, pp. 65–70, 2008.

[425] P. Onck, T. Koeman, T. van Dillen, and E. van der Giessen, "Alternative explanation of stiffening in cross-linked semiflexible networks," *PRL*, vol. 95, p. 178102, 2005.

[426] A. E. Brown, R. I. Litvinov, D. E. Discher, and J. W. Weisel, "Forced unfolding of coiled-coils in fibrinogen by single-molecule AFM," *Biophys. J.*, vol. 92, no. 5, pp. L39–L41, 2007.

[427] G. Koenderink, M. Atakhorrami, F. MacKintosh, and C. Schmidt, "High-frequency stress relaxation in semiflexible polymer solutions and networks," *PRL*, vol. 96, p. 138307, 2006.

[428] K. Beningo and Y. Wang, "Flexible substrata for the detection fo cellular traction forces," *Trends Cell Biol.*, vol. 12, pp. 79–84, 2002.

[429] Y. Shokef and S. A. Safran, "Scaling laws for the response of nonlinear elastic media with implications for cell mechanics," *PRL*, vol. 108, p. 178103, 2012.

[430] U. Schwarz and S. Safran, "Elastic interactions of cells," *PRL*, vol. 88, p. 048102, 2002.

[431] I. Bischofs and U. Schwarz, "Effect of Poisson ratio on cellular structure formation," *PRL*, vol. 95, p. 068102, 2005.

[432] A. Zemel, I. Bischofs, and S. Safran, "Active elasticity of gels with contractile cells," *PRL*, vol. 97, p. 128103, 2006.

[433] A. Zemel and S. Safran, "Active self-polarization of contractile cells in asymmetrically shaped domains," *PRE*, vol. 76, p. 021905, 2007.

[434] F. Shaikh, A. Callanan, E. Kavanagh, P. Burke, P. Grace, and T. McGloughlin, "Fibrin: a natural biodegradable scaffold in vascular tissue engineering," *Cells Tissues Organs*, vol. 188, pp. 333–346, 2008.

[435] W. Kamphuis, C. Mamber, M. Moeton, L. Kooijman, J. Sluijs, A. Jansen, M. Verveer, L. deGroot, V. Smith, S. Rangarajan, J. Rodríguez, M. Orre, and E. Hol, "GFAP isoforms in adult mouse brain with a focus on neurogenic astrocytes and reactive astrogliosis in mouse models of alzheimer disease," *PLoS ONE*, vol. 7, p. e42823, 2012.

[436] F. Dijk, E. Kraal-Muller, and W. Kamphuis, "Ischemia-induced changes of AMPA-type glutamate receptor subunit expression pattern in the rat retina: a real-time quantitative PCR study," *Invest. Ophtalmol. Vis. Sci.*, vol. 45, pp. 330–341, 2004.

[437] J. Ye, G. Coulouris, I. Zaretskaya, I. Cutcutache, S. Rozen, and T. Madden, "Primer-BLAST: a tool to design target-specific primers for polymerase chain reaction," *BMC Bioinformatics*, vol. 13, p. 134, 2012.

[438] J. Noguera, A. Lecuona, and P. Rodríguez, "Limits on the resolution of correlation PIV iterative methods," *Experiments in Fluids*, vol. 39, pp. 305–313, 2005.

[439] R. Rezakhaniha, A. Agianniotis, J. Schrauwen, A. Griffa, D. Sage, C. Bouten, F. van de Vosse, M. Unser, and N. Stergiopulos, "Experimental investigation of collagen waviness and orientation in the arterial adventitia using confocal laser scanning microscopy," *Biomech. Model. Mechanobiol.*, vol. 11, pp. 461–473, 2012.

[440] S. Hess and W. Köhler, *Formeln zur Tensor-Rechnung*. Palm & Enke, 1980.

[441] L. Medved and J. Weisel, "Recommendations for nomenclature on fibrinogen and fibrin," *J. Thromb. Haemost.*, vol. 7, no. 2, pp. 355–359, 2009.

[442] Z. Yang, I. Mochalkin, L. Veerapandian, M. Riley, and R. F. Doolittle, "Crystal structure of native chicken fibrinogen at 5.5-Å resolution," *PNAS*, vol. 97, no. 8, pp. 3907–3912, 2000.

[443] W. Fowler, R. Hantgan, J. Hermans, and H. Erickson, "Structure of the fibrin protofibril," *PNAS*, vol. 78, no. 8, pp. 4872–4876, 1981.

[444] R. I. Litvinov, S. Yakovlev, G. Tsurupa, O. V. Gorkun, L. Medved, and J. W. Weisel, "Direct evidence for specific interactions of the fibrinogen αC-domains with the central E region and with each other," *Biochemistry*, vol. 46, no. 31, pp. 9133–9142, 2007.

[445] R. I. Litvinov, O. V. Gorkun, D. K. Galanakis, S. Yakovlev, L. Medved, H. Shuman, and J. W. Weisel, "Polymerization of fibrin: direct observation and quantification of individual B:b knob-hole interactions," *Blood*, vol. 109, no. 1, pp. 130–138, 2007.

[446] L. Lorand, "Factor XIII: Structure, activation, and interactions with fibrinogen and fibrin," *Annals New York Academy of Sciences*, vol. 936, no. 1, pp. 291–311, 2006.

[447] S. Acharya and D. Dimichele, "Rare inherited disorders of fibrinogen," *Haemophilia*, vol. 14, pp. 1151–1158, 2008.

[448] R. Tran, D. R. Myers, J. Ciciliano, E. L. T. Hardy, Y. Sakurai, B. Ahn, Y. Qiu, R. G. Mannino, M. E. Fay, and W. A. Lam, "Biomechanics of haemostasis and thrombosis in health and disease: from the macro- to molecular scale," *J. Cell. Mol. Med.*, vol. 17, no. 5, pp. 579–596, 2013.

[449] K. Gersh, K. Edmondson, and J. Weisel, "Flow rate and fibrin fiber alignment," *J. Thromb. Haemost.*, vol. 8, no. 12, pp. 2826–2828, 2010.

[450] R. A. Campbell, M. M. Aleman, L. D. Gray, M. R. Falvo, and A. S. Wolberg, "Flow profoundly influences fibrin network structure: Implications for fibrin formation and clot stability in haemostasis," *J. Thromb. Haemost.*, vol. 104, no. 6, pp. 1281–1284, 2010.

[451] S. S. Henriques, R. Sandmann, A. Strate, and S. Köster, "Force field evolution during human blood platelet activation," *Journal of Cell Science*, vol. 125, pp. 3914–3920, 2012.

[452] Z. Qin, L. Kreplak, and M. J. Buehler, "Nanomechanical properties of vimentin intermediate filament dimers," *Nanotechnology*, vol. 20, p. 425101, 2009.

[453] I. Schwaiger, C. Sattler, D. R. Hostetter, and M. Rief, "The myosin coiled-coil is a truly elastic protein structure," *Nature Materials*, vol. 1, pp. 232–235, 2002.

[454] H. Kang, Q. Wen, P. A. Janmey, J. X. Tang, E. Conti, and F. C. MacKintosh, "Nonlinear elasticity of stiff filament networks: strain stiffening, negative normal stress, and filament alignment in fibrin gels," *J. Phys. Chem. B*, vol. 113, pp. 3799–3805, 2009.

[455] F. J. Roska and J. D. Ferry, "Studies of fibrin film.II. small-angle x-ray scattering," *Biopolymers*, vol. 21, pp. 1833–1845, 1982.

[456] M. F. Müller and J. D. Ferry, "Small-angle x-ray scattering studies of fibrin film: Comparisons of fine and coarse films prepared with thrombin and ancrod," *Biopolymers*, vol. 28, pp. 1011–1018, 1989.

[457] D. K. Putnam, E. W. L. Jr., and J. Meiler, "Reconstruction of SAXS profiles from protein structures," *Computational and Structural Biotechnology Journal*, vol. 8, no. 11, p. e201308006, 2013.

[458] K. M. Meek and A. J. Quantock, "The use of X-ray scattering techniques to determine corneal ultrastructure," *Progress in Retinal and Eye Research*, vol. 20, no. 1, pp. 95–137, 2001.

[459] A. Martel, M. Burghammer, R. J. Davies, E. D. Cola, C. Vendrely, and C. Riekel, "Silk fiber assembly studied by synchrotron radiation SAXS/WAXS and Ramon spectroscopy," *JACS*, vol. 130, pp. 17070–17074, 2008.

[460] L. Stryer, C. Cohen, and R. Langridge, "Axial period of fibrinogen and fibrin," *Nature*, vol. 197, pp. 793–194, 1963.

[461] C. Longstaff, I. Varjú, P. Sótonyi, L. Szabó, M. Krumrey, A. Hoell, A. Bóta, Z. Varga, E. Komorowicz, and K. Kolev, "Mechanical stability and fibrinolytic resistance of clots containing fibrin, DNA, and histones," *The Journal of Biological Chemistry*, vol. 288, pp. 6946–6956, 2013.

[462] W. A. Voter, C. Cucaveche, A. E. Blaurock, and H. P. Erickson, "Lateral packing of protofibrils in fibrin fibers and fibrinogen polymers," *Biopolymers*, vol. 25, pp. 2359–2373, 1986.

[463] G. Caracciolo, M. D. Spirito, A. C. Castellano, D. Pozzi, G. Amiconi, A. D. Pascalis, R. Caminiti, and G. Arcovito, "Protofibrils within fibrin fibres are packed together in a regular array," *Thromb. Haemost.*, vol. 89, pp. 632–636, 2003.

[464] M. Missori, M. Papi, G. Maulucci, G. Arcovito, G. Boumis, A. Bellelli, G. Amiconi, and M. D. Spirito, "Cl^- and F^- anions regulate the architecture of protofibrils in fibrin gel," *Eur. Biophys. J.*, vol. 39, no. 6, pp. 1001–1006, 2010.

[465] I. Bucay, E. T. O. III, S. D. Wulfe, R. Superfine, A. S. Wolberg, M. R. Falvo, and N. E. Hudson, "Physical determinants of fibrinolysis in single fibrin fibers," *PLoS ONE*, vol. 10, no. 2, p. e0116350, 2015.

[466] A. S. Adhikari, A. H. Mekhdjian, and A. R. Dunn, "Strain tunes proteolytic degradation and diffusive transport in fibrin networks," *Biomacromolecules*, vol. 13, no. 2, pp. 499–506, 2012.

[467] I. Varjú, P. Sótonyi, R. Machovich, L. Szabó, K. Tenekedjiev, M. Silva, C. Longstaff, and K. Kolev, "Hindered dissolution of fibrin formed under mechanical stress," *J. Thromb. Haemost.*, vol. 9, pp. 979–986, 2011.

[468] W. Bras, I. P. Dolbnya, D. Detollenaere, R. van Tol, M. Malfois, G. N. Greaves, A. J. Ryan, and E. Heeley, "Recent experiments on a combined small-angle/wide-angle X-ray scattering beam line at the ESRF," *Journal of Applied Crystallography*, vol. 36, pp. 791–794, 2003.

[469] K. Jansen, A. Zhmurov, G. Portale, D. Merino, R. Litvinov, B. Vos, V. Tutwiler, N. Kurniawan, W. Bras, J. Weisel, V. Barsegov, and G. Koenderink, "Unfolding of fibrin gels under strain," manucript in preparation.

[470] W. Humphrey, A. Dalke, and K. Schulten, "VMD:Visual Molecular Dynamics," *J. Molec. Graphics*, vol. 14, pp. 33–38, 1995.

[471] Z. Yang, L. Pandi, and R. F. Doolittle, "The crystal structure of fragment double-D from cross-linked lamprey fibrin reveals isopeptide linkages across an unexpected D-D interface," *Biochemistry*, vol. 41, pp. 15610–15617, 2002.

[472] S. J. Everse, G. Spraggon, L. Veerapandian, and R. F. Doolittle, "Conformational changes in fragments D and double-D from human fibrin(ogen) upon binding the peptide ligand gly-his-arg-pro-amide," *Biochemistry*, vol. 38, pp. 2941–2946, 1999.

[473] W. Kabsch, "A solution for the best rotation to relate two sets of vectors," *Acta Cryst.*, vol. 32, pp. 922–923, 1976.

[474] P. Ferrara, J. Apostolakis, and A. Caflisch, "Evaluation of a fast implicit solvent model for molecular dynamics simulations," *Proteins*, vol. 46, pp. 24–33, 2002.

[475] P. Debye, "Zerstreuung von röntgenstrahlen," *Annalen der Physik*, vol. 351, pp. 809–823, 1915.

[476] O. Glatter and O. Kratky, eds., *Small Angle X-ray Scattering*. Academic Press, 1982.

[477] P. W. Stephens, J. A. Kaduk, T. N. Blanton, D. R. Whitcomb, S. T. Misture, and M. Rajeswaran, "Structure determination of the silver caboxylate dimer [Ag(O2C20H39)]2, silver arachidate, using powder X-ray diffraction methods," *International Centre for Diffraction Data*, 2012. ISSN 1097–0002.

[478] F. Ferri and M. Greco, "Growth kinetics and structure of fibrin gels," *PRE*, vol. 63, p. 031401, 2001.

[479] F. Ferri, M. Greco, G. Arcóvito, M. D. Spirito, and M. Rocco, "Structure of fibrin gels studied by elastic light scattering techniques: Dependence of fractal dimension, gel crossover length, fiber density on monomer concentration," *PRE*, vol. 66, p. 011913, 2002.

[480] K. M. Weigandt, D. C. Pozzo, and L. Porcar, "Structure of high density fibrin networks probed with neutron scattering and rheology," *Soft Matter*, vol. 5, pp. 4321–4330, 2009.

[481] A. E. González and G. Ramírez-Santiago, "Spatial ordering and structure factor scaling in the simulations of colloid aggregation," *PRL*, vol. 74, no. 7, pp. 1238–1241, 1995.

[482] M. D. Spirito, G. Arcovito, F. A. Bassi, F. Ferri, and M. Rocco, "Internal dynamics of semiflexibles fibrin networks," *AIP Conference Proceedings*, vol. 469, no. 1, pp. 627–632, 1999.

[483] A. Takahashi, R. Kita, T. Shinozaki, K. Kubota, and M. Kaibara, "Real space observation of three-dimensional network structure of hydrated fibrin gel," *Coilloid Polym. Sci.*, vol. 281, pp. 832–838, 2003.

[484] M. Papi, G. Arcovito, M. D. Spirito, G. Amiconi, A. Bellelli, and G. Boumis, "Simultaneous static and dynamic light scattering approach to the characterization of the different fibrin gel structures occuring by changing chloride concentration," *Applied Physics Letters*, vol. 86, p. 183901, 2005.

[485] R. Bateman, H. Leong, T. Podor, K. Hodgson, T. Kareco, and K. Walley, "The effect of thrombin concentration on fibrin clot structure imaged by multiphoton microscopy and quantified by fractal analysis," *Microsc. Microanal.*, vol. 11(Suppl 2), pp. 1018–1019, 2005.

[486] P. A. Evans, K. Hawkins, R. H. Morris, N. Thirumalai, R. Munro, L. Wakeman, M. J. Lawrence, and P. R. Williams, "Gel point and fractal microstructure of incipient blood clots are significant new markers of hemostasis for healthy and anticoagulated blood," *Thrombosis and Hemostasis*, vol. 116, no. 17, pp. 3341–3346, 2010.

[487] D. J. Curtis, P. R. Williams, N. Badiei, A. I. Campbell, K. Hawkins, P. A. Evans, and M. R. Brown, "A study of microstructural templating in fibrin-thrombin gel networks by spectral and viscoelastic analysis," *Soft Matter*, vol. 9, p. 4883, 2013.

[488] J.-M. Freyssinet, J. Torbet, G. Hudry-Clergeon, and G. Maret, "Fibrinogen and fibrin structure and fibrin formation measured by using magnetic orientation," *PNAS*, vol. 80, pp. 1616–1620, 1983.

[489] J. Teixeira, "Small-angle scattering by fractal systems," *J. Appl. Cryst.*, vol. 21, pp. 781–785, 1988.

[490] C. Yeromonahos, *Nanostructure des fibres de fibrine*. PhD thesis, Université de Grenoble, 2011.

[491] J. W. Weisel, G. N. Phillips, and C. Cohen, "The structure of fibrinogen and fibrin: II. architecture of the fibrin clot," *NYAS*, vol. 408, pp. 367–379, 1983.

[492] R. F. Doolittle and J. M. Kollman, "Natively unfolded regions of the vertebrate fibrinogen molecule," *PROTEINS: Structure, Function, and Bioinformatics*, vol. 63, pp. 391–397, 2006.

[493] L. E. Alexander, ed., *X-Ray diffraction methods in polymer science*. New York, Wiley-Interscience, 1969.

[494] S. Förster, A. Timmann, C. Schellback, A. Frömsdorf, A. Kornowski, H. Weller, S. V. Roth, and P. Lindner, "Order causes secondary Bragg peaks in soft materials," *Nature Materials*, vol. 6, pp. 888–893, 2007.

[495] T. Xu, D. Vavylonis, F.-C. Tsai, G. Koenderink, W. Nie, E. Yusul, I.-J. Lee, J.-Q. Wu, and X. Huang, "SOAX: A software for quantification of 3D biopolymer networks," *Scientific Reports*, vol. 5, p. 9081, 2015.

[496] G. Portale, "personal communication,"

[497] B. Li, C. Moshfegh, Z. Lin, J. Albuschies, and V. Vogel, "Mesenchymal stem cells exploit extracellular matrix as mechanotransducer," *Scientific Reports*, vol. 3, p. 2425, 2013.

[498] O. Peleg, T. Savin, G. V. Kolmakov, I. G. Salib, A. C. Balazs, M. Kröger, and V. Vogel, "Fibers with integrated mechanochemical switches : Minimalistic design principles derived from fibronectin," *Biophys. J.*, vol. 103, pp. 1909–1918, 2012.

[499] C. T. Mierke, "The fundamental role of mechanical properties in the progression of cancer disease and inflammation," *Reports on Progress in Physics*, vol. 77, no. 7, p. 076602, 2014.

[500] H. Mohammadi and C. A. McCulloch, "Impact of elastic and inelastic substrate behavior on mechanosensation," *Soft Matter*, vol. 10, pp. 408–420, 2014.

[501] A. Lesman, J. Notbohm, D. A. Tirrell, and G. Ravichandran, "Contractile forces regulate cell division in three-dimensional environments," *J.Cell Biol.*, vol. 205, no. 2, pp. 155–162, 2014.

[502] J. Starke, K. Maaser, B. Wehrle-Haller, and P. Friedl, "Mechanotransduction of mesenchymal melanoma cell invasion into 3D collagen lattices: Filopod-mediated extension-relaxation cycles and force anisotropy," *Experimental Cell Research*, vol. 319, pp. 2424–2433, 2013.

[503] J. Notbohm, A. Lesman, D. A. Tirrell, and G. Ravichandran, "Quantifying cell-induced matrix deformation in three dimensions based on imaging matrix fibers," *Integr. Biol.*, vol. 7, pp. 1186–1195, 2015.

[504] J. H.-C. Wang and J.-S. Lin, "Cell traction force and measurement methods," *Biomechan. Model Mechanobiol.*, vol. 6, pp. 361–371, 2007.

[505] U. Schwarz and J. Soiné, "Traction force microscopy on soft elastic substrates: A guide to recent computational advances," *Biochim. Biophys. Acta*, vol. 1853, pp. 3095–3104, 2015.

[506] C. T. Mierke, D. Rösel, B. Fabry, and J. Brábek, "Contractile forces in tumor cell migration," *Eur. J. Cell Biol.*, vol. 87, pp. 669–676, 2008.

[507] M. Bonilla, J. Stokes, M. Gidley, and G. Yakubov, "Interpreting atomic force microscopy nanoindentation of hierarchical biological materials using multi-regime analysis," *Soft Matter*, vol. 11, pp. 1281–1292, 2015.

[508] L. Selvaggi, M. Salemme, C. Vaccaro, G. P. andGiulia Rusciano, A. Sasso, C. Campanella, and R. Carotenuto, "Multiple-particle-tracking to investigate viscoelastic properties in living cells," *Methods*, vol. 51, pp. 20–26, 2009.

[509] I. Hasnain and A. Donald, "Microrheological characterization of anisotropic materials," *PRE*, vol. 73, p. 031901, 2006.

[510] Y. Tseng, T. P. Kole, and D. Wirtz, "Micromechanical mapping of live cells by multiple particle tracking microrheology," *Biophys. J.*, vol. 83, pp. 3162–3167, 2002.

[511] D. Wirtz, "Particle-tracking microrheology of living cells: principles and applications," *Annu. Rev. Biophys.*, vol. 38, pp. 301–326, 2009.

[512] S. Yamada, D. Wirtz, and S. C. Kuo, "Mechanics of living cells measured by laser tracking microrheology," *Biophys. J.*, vol. 78, pp. 1736–1747, 2000.

[513] M. Puig-De-Morales, M. Grabulosa, J. Alcaraz, J. Mollol, G. N. Maksym, J. J. Fredberg, and D. Navajas, "Measurement of cell microrheology by magnetic twisting cytometry with frequency domain demodulation," *J. Appl. Physiol*, vol. 91, pp. 1152–1159, 2001.

[514] D. Weihs, T. G. Mason, and M. A. Teitell, "Bio-microrheology: A frontier in microrheology," *Biophys. J.*, vol. 91, pp. 4296–4305, 2006.

[515] W. W. Admed, É. Fodor, and T. Betz, "Active cell mechanics: Measurements and theory," *BBA*, vol. 1853, pp. 3083–3094, 2015.

[516] M. Gardel, M. Valentine, J. Crocker, A. Bausch, and D. Weitz, "Microrheology of entangled F-actin solutions," *PRL*, vol. 91, no. 15, p. 158302, 2003.

[517] J. Liu, M. Gardel, K. Kroy, E. Frey, B. Hoffman, J. Crocker, A. Bausch, and D. Weitz, "Microrheology probes length scale dependent rheology," *PRL*, vol. 96, p. 118104, 2006.

[518] J. L. McGrath, J. H. Hartwig, and S. C. Kuo, "The mechanics of F-actin microenvironments depend on the chemistry of probing surfaces," *Biophys. J.*, vol. 79, pp. 3258–3266, 2000.

[519] F. G. Schmidt, B. Hinner, and E. Sackmann, "Microrheometry underestimates the values of the viscoelastic moduli in measurements on F-actin solutions compared to macrorheometry," *PRE*, vol. 61, no. 5, pp. 5646–5653, 2000.

[520] I. Wong, M. Gardel, D. Reichman, E. R. Weeks, M. Valentine, A. Bausch, and D. Weitz, "Anomalous diffusion probes microstructure dynamics of entangled F-actin networks," *PRL*, vol. 92, no. 17, p. 178101, 2004.

[521] B. S. Chae and E. M. Furst, "Probe surface chemistry dependence and local polymer network structure in F-actin microrheology," *Langmuir*, vol. 21, pp. 3084–3089, 2005.

[522] J. He and J. X. Tang, "Surface adsorption and hopping cause probe-size-dependent microrheology of actin networks," *PRE*, vol. 83, p. 041902, 2011.

[523] M. Kotlarchyk, E. Botvinick, and A. Putnam, "Characterization of hydrogel microstructure using laser tweezers particle tracking and confocal reflection imaging," *J. Phys. Condens. Matter*, vol. 22, no. 19, p. 194121, 2010.

[524] M. A. Kotlarchyk, S. G. Shreim, M. B. Alvarez-Elizondo, L. C. Estrada, R. Singh, L. Valdevit, E. Kniazeva, E. Gratton, A. J. Putnam, and E. L. Botvinick, "Concentration independent modulation of local micromechanics in a fibrin gel," *PLoS ONE*, vol. 6, no. 5, p. e20201, 2011.

[525] E. Kniazeva, J. W. Weidling, R. Singh, E. L. Botvinick, M. A. Digman, E. Gratton, and A. J. Putnam, "Quantification of local matrix deformations and mechanical properties during capillary morphogenesis in 3D," *Integr. Biol. (Camb).*, vol. 4, no. 4, pp. 431–439, 2012.

[526] M. Shayegan and N. R. Forde, "Microrheological characterization of collagen systems: From molecular solutions to fibrillar gels," *PLoS ONE*, vol. 8, no. 8, p. e70590, 2013.

[527] D. Velegol and F. Lanni, "Cell traction forces on soft biomaterials. I. microrheology of type I collagen gels," *Biophys. J.*, vol. 81, pp. 1786–1792, 2001.

[528] A. Parekh and D. Velegol, "Collagen gel anisotropy measured by 2-D laser trap microrheometry," *Annals of Biomedical Engineering*, vol. 35, no. 7, pp. 1231–1246, 2007.

[529] R. H. Abou-Saleh, S. D. Connell, R. Harrand, R. A. Ajjan, M. W. Mosesson, D. A. M. Smith, P. J. Grant, and R. A. Ariëns, "Nanoscale probing reveals that reduced stiffness of clots from fibrinogen lacking 42 N-terminal Bβ-chain residues is due to the formation of abnormal oligomers," *Biophys. J.*, vol. 96, pp. 2415–2427, 2009.

[530] J. Konings, J. W. Govers-Riemslag, H. Philippou, N. J. Mutch, J. I. Borissoff, P. Allan, S. Mohan, G. Tans, H. ten Cate, and R. A. Ariëns, "Factor XIIa regulates the structure of the fibrin clot independently of thrombin generation through direct interaction with fibrin," *Blood*, vol. 118, no. 14, pp. 3942–3951, 2011.

[531] P. Allan, S. U. D. Willige, R. Abou-Saleh, S. Connell, and R. Ariëns, "Evidence that fibrinogen γ' directly interferes with protofibril growth: implications for fibrin structure and clot stiffness," *Journal of Thrombosis and Haemostasis*, vol. 10, pp. 1072–1080, 2012.

[532] P. Allan, *Microrheology of Fibrin Clots*. PhD thesis, The University of Leeds, 2012.

[533] M. Jahnel, T. A. Waigh, and J. R. Lu, "Thermal fluctuations of fibrin fibres at short time scales," *Soft Matter*, vol. 4, pp. 1438–1442, 2008.

[534] D. Mizuno, D. Head, F. MacKintosh, and C. Schmidt, "Active and passive microrheology in equilibrium and nonequilibrium systems," *Macromolecules*, vol. 41, pp. 7194–7202, 2008.

[535] P. Pawelzyk, N. Mücke, H. Herrmann, and N. Willenbacher, "Attractive interactions among intermediate filaments determine network mechanics in vitro," *PLoS ONE*, vol. 9, no. 4, p. e93194, 2014.

[536] M. Buchanan, M. Atakhorrami, J. Palierne, F. MacKintosh, and C. Schmidth, "High-frequency microrheology of wormlike micelles," *PRE*, vol. 72, p. 011504, 2005.

[537] M. Valentine, Z. Perlman, M. Gardel, J. Shin, P. Matsudaira, T. Mitchison, and D. Weitz, "Colloid surface chemistry critically affects multiple particle tracking measurements of biomaterials," *Biophys. J.*, vol. 86, pp. 4004–4014, 2004.

[538] L. H. Wong, N. A. Kurniawan, H.-P. Too, and R. Rajagopalan, "Spatially resolved microrheology of heterogeneneous biopolymer hydrogels using covalently bound microspheres," *Biomech. Model Mechanobiol.*, vol. 13, pp. 839–849, 2014.

[539] M. Mak, R. D. Kamm, and M. H. Zaman, "Impact of dimensionality and network disruption on microrheology of cancer cells in 3D environments," *PLoS ONE*, vol. 10, no. 11, p. e1003959, 2014.

[540] L. Campo-Deaño, R. P. Dullens, D. G. Aarts, F. T. Pinho, and M. S. Oliveira, "Viscoelasticity of blood and viscoelastic blood analogues for use in polydymethylsiloxane in vitro models of the circulatory system," *Biomicrofluidics*, vol. 7, p. 034102, 2013.

[541] W. Stöber, A. Fink, and E. Bohn, "Controlled growth of monodisperse silica spheres in the micron size range," *Journal of Colloid and Interface Science*, vol. 26, pp. 62–69, 1968.

[542] J. Zhang, P. Zhan, Z. Wang, W. Zhang, and N. Ming, "Preparation of monodisperse silica particles with controllable size and shape," *J. Mater. Res.*, vol. 18, no. 3, pp. 649–653, 2003.

[543] A. J. Kim, V. N. Manoharan, and J. C. Crocker, "Swelling-based method for preparing stable, functionalized polymer colloids," *JACS*, vol. 127, pp. 1592–1593, 2005.

[544] A. Pralle, M. Prummer, E.-L. Florin, E. Stelzer, and J. Hörber, "Three-dimensional high-resolution particle tracking for optical tweezers by forward scattered light," *Microscopy Research and Technique*, vol. 44, pp. 378–386, 1999.

[545] K. Berg-Sørensen and H. Flyvbjerg, "Power spectrum analysis for optical tweezers," *Review of Scientific Instruments*, vol. 75, no. 3, pp. 594–612, 2004.

[546] A. J. Levine and T. Lubensky, "Two-point microrheology and the electrostatic analogy," *PRE*, vol. 65, p. 011501, 2001.

[547] M. Atakhorrami, J. Sulkowska, K. Addas, G. Koenderink, J. Tang, A. Levine, F. MacKintosh, and C. Schmidt, "Correlated fluctuations of microparticles in viscoelastic solutions: Quantitative measurement of material properties by microrheology in the presence of optical traps," *PRE*, vol. 73, p. 061501, 2006.

[548] B. Schnurr, F. Gittes, F. MacKintosh, and C. Schmidt, "Determining microscopic viscoelasticity in flexible and semiflexible polymer networks from thermal fluctuations," *Macromolecules*, vol. 30, pp. 7781–7792, 1997.

[549] T. G. Mason, "Estimating the viscoelastic moduli of complex fluids using the generalized Stokes-Einstein equation," *Rheol. Acta*, vol. 39, pp. 371–378, 2000.

[550] K. C. Neuman and S. M. Block, "Optical trapping," *Review of Scientific Instruments*, vol. 75, no. 9, pp. 2787–2809, 2004.

[551] M. C. Wang and G. Uhlenbeck, "On the theory of the Brownian motion II," *Review of Modern Physics*, vol. 17, pp. 323–342, 1945.

[552] M. Capitanio, G. Romano, R. Ballerini, and M. Giuntini, "Calibration of optical tweezers with differential interference contrast signals," *Review of Scientific Instruments*, vol. 73, no. 4, pp. 1687–1696, 2002.

[553] E. Fällman and O. Axner, "Influence of a glass-water interface on the on-axis trapping of micrometer-sized spherical objects by optical tweezers," *Applied Optics*, vol. 42, no. 19, pp. 3915–3926, 2003.

[554] K. C. Vermeulen, G. J. Wuite, G. J. Stienen, and C. F. Schmidt, "Optical trap stiffness in the presence and absence of spherical aberrations," *Applied Optics*, vol. 45, no. 8, pp. 1812–1819, 2006.

[555] K. M. Addas, C. F. Schmidt, and J. X. Tang, "Microrheology of solutions of semiflexible biopolymer filaments using laser tweezers interferometry," *PRE*, vol. 70, p. 021503, 2004.

[556] E. Schäffer, S. F. Nørrelykke, and J. Howard, "Surface forces and drag coefficients of microspheres near a plane surface measured with optical tweezers," *Langmuir*, vol. 23, pp. 3654–3665, 2007.

[557] P. P. Lele, J. W. Swan, J. F. Brady, N. J. Wagner, and E. M. Furst, "Colloidal diffusion and hydrodynamic screening near boundaries," *Soft Matter*, vol. 7, pp. 6844–6852, 2011.

[558] M. L. Sheely, "Glycerol viscosity tables," *Industrial and Engineering Chemistry*, vol. 24, no. 9, pp. 1060–1064, 1932.

[559] J. Segur and H. E. Oberstar, "Viscosity of glycerol and its aqueous solutions," *Industrial and Engineering Chemistry*, vol. 43, no. 9, pp. 2117–2120, 1951.

[560] C. Wu, M. A. Quesada, D. K. Schneider, R. Farinato, F. W. Studier, and B. Chu, "Polyacrylamide solutions for DNA sequencing by capillary electrophoresis: Mesh sizes, separation and dispersion," *Electrophoresis*, vol. 17, pp. 1103–1109, 1996.

[561] N. C. Stellwagen, "Apparent pore size of polyacrylamide gels: Comparison of gels cast and run in Tris-acetate-EDTA and Tris-borate-EDTA buffers," *Electrophoresis*, vol. 19, pp. 1542–1547, 1998.

[562] P. E. Rouse, "A theory of the linear viscoelastic properties of dilute solutions of coiling polymers," *The Journal of Chemical Physics*, vol. 21, no. 7, pp. 1272–1280, 1953.

[563] M. Rubinstein and R. H. Colby, eds., *Polymer Physics*. Oxford University Press, 2003.

[564] L.-J. Palade, V. Verney, and P. Attané, "A modified fractional model to describe the entire viscoelastic behavior of polybutadienes from flow to glassy regime," *Rheol. Acta*, vol. 35, pp. 265–273, 1996.

[565] Y. Abidine, V. M. Laurent, R. Michel, A. Duperray, L. I. Palade, and C. Verdier, "Physical properties of polyacrylamide gels probed by AFM and rheology," *EPL*, vol. accepted, 2015.

[566] P. D. Gennes, "Dynamics of entangled polymer solutions. I. The Rouse model," *Macromolecules*, vol. 9, no. 4, pp. 587–593, 1976.

[567] D. Chen, E. Weeks, J. Crocker, M. Islam, R. Verma, J. Gruber, A. Levine, T. Lubensky, and A. Yodh, "Rheological microscopy: Local mechanical properties from microrheology," *PRL*, vol. 90, no. 10, p. 108301, 2003.

[568] J. Y. Huh and E. M. Furst, "Coilloid dynamics in semiflexible polymer solutions," *PRE*, vol. 74, p. 031802, 2006.

[569] C. I. Fisher and S. C. Kuo, "Filament rigidity causes F-actin depletion from nonbinding surfaces," *PNAS*, vol. 106, pp. 133–138, 2009.

[570] R. Verma, J. Crocker, T. Lubensky, and A. Yodh, "Attraction between hard colloidal spheres in semiflexible polymer solutions," *Macromolecules*, vol. 33, pp. 177–186, 2000.

[571] S. Brinkers, H. R. Dietrich, F. H. de Groote, I. T. Young, and B. Rieger, "The persistence length of double stranded DNA determined using dark field tethered particle motion," *The Journal of Chemical Physics*, vol. 130, p. 215105, 2009.

[572] K. M. V. Citters, B. D. Hoffman, G. Massiera, and J. C. Crocker, "The role of F-actin and myosin in epithelial cell rheology," *Biophys. J.*, vol. 91, pp. 3946–3956, 2006.

[573] F. Amblard, A. Maggs, B. Yurke, A. Pargellis, and S. Leibler, "Subdiffusion and anomalous local viscoelasticity in actin networks," *PRL*, vol. 77, no. 21, pp. 4470–4473, 1996.

[574] D. C. Morse, "Viscoelasticity of tightly entangled solutions of semiflexible polymers," *PRE*, vol. 58, no. 2, pp. R1237–R1240, 1998.

[575] D. C. Morse, "Viscoelasticity of concentrated isotropic solutions of semifelxible polymers. 2. linear response," *Macromolecules*, vol. 31, pp. 7044–7067, 1998.

[576] A. Caspi, M. Elbaum, R. Granek, A. Lachish, and D. Zbaida, "Semiflexible polymer network: A view from inside," *PRL*, vol. 80, no. 5, pp. 1106–1109, 1998.

[577] C. A. R. Jones, L. Liang, D. Lin, Y. Jiao, and B. Sun, "The spatial-temporal characteristics of type I collagen-based extracellular matrix," *Soft Matter*, vol. 10, pp. 8855–8863, 2014.

[578] F. Gittes and F. MacKintosh, "Dynamic shear modulus of a semiflexible polymer network," *PRE*, vol. 58, no. 2, pp. R1241–R1244, 1998.

[579] M. Atakhorrami, G. Koenderink, J. F. Palierne, F. MacKintosh, and C. Schmidt, "Scale-dependent nonaffine elasticity of semiflexible polymer networks," *PRL*, vol. 112, p. 088101, 2014.

[580] D. A. Parry, "The molecular and fibrillar structure of collagen and its relationship to the mechanical properties of connective tissue," *Biophysical Chemistry*, vol. 29, pp. 195–209, 1988.

[581] S. V. Sandhu, S. Gupta, H. Bansal, and K. Singla, "Collagen in health and disease," *Journal of Orofacial Research*, vol. 2, no. 3, pp. 153–159, 2012.

[582] M. van der Rest and R. Garbone, "Collagen family of proteins," *The FASEB Journal*, vol. 5, pp. 2814–2823, 1991.

[583] S. Ricard-Blum, "The collagen family," *Cold Psring Harb Perspect Biol*, vol. 3, pp. 1–19, 2011.

[584] J.-Y. Exposito, U. Valcourt, C. Cluzel, and C. Lethias, "The fibrillar collagen family," *Int. J. Mol. Sci.*, vol. 11, pp. 407–426, 2010.

[585] G. W. Dombi, R. C. Haut, and W. G. Sullivan, "Correlation of high-speed tensile strength with collagen content in control and lathyritic rat skin," *Journal of Surgical Research*, vol. 54, pp. 21–28, 1993.

[586] A. J. Bailey, "Molecular mechanisms of ageing in connective tissues," *Mechanisms of Ageing and Development*, vol. 122, pp. 735–755, 2001.

[587] J. G. Snedeker and A. Gautieri, "The role of collagen crosslinks in ageing and diabeter - the good, the bad, and the ugly," *Muscles, Ligaments and Tendons Journal*, vol. 4, no. 3, pp. 303–308, 2014.

[588] A. Gautieri, S. Uzel, S. Vesentini, A. Redaelli, and M. J. Buehler, "Molecular and mesoscale mechanisms of osteogenesis imperfecta disease in collagen fibrils," *Biophys. J.*, vol. 97, pp. 857–865, 2009.

[589] E. Strauss, *Studien über die Albuminoide mit besonderer Berücksichtigung des Spongin und der Keratine*. Karl Winter's Universitätsbuchhandlung, 1904.

[590] Y. Fung, "Structure and stress-strain relationship of soft tissues," *Amer. Zool.*, vol. 24, pp. 13–22, 1984.

[591] S. L. Voytik, B. A. Rouder, J. E. Sturgis, K. Kokini, and J. P. Robinson, "Simultaneous mechanical loading and confocal reflection microscopy for three-dimensional microbiomechanical analysis of biomaterials and tissue constructs," *Microscopy and Microanalysis*, vol. 9, pp. 74–85, 2003.

[592] H. Screen, D. Bader, D. Lee, and J. Shelton, "Local strain measurement within tendon," *Strain*, vol. 40, pp. 157–163, 2004.

[593] R. E. Shadwick, "Elastic energy storage in tendons: mechanical differences related to function and age," *Journal of Applied Physiology*, vol. 68, pp. 1033–1040, 1990.

[594] R. E. Shadwick, "Mechanical design in arteries," *The Journal of Experimental Biology*, vol. 202, pp. 3305–3313, 1999.

[595] A. Gautieri, S. Vesentini, F. M. Montevecchi, and A. Redaelli, "Mechanical properties of physiological and pathological models of collagen peptides investigated via steered molecular dynamics simulations," *Journal of Biomechanics*, vol. 41, pp. 3073–3077, 2008.

[596] A. Gautieri, M. I. Pate, S. Vesentini, A. Redaelli, and M. J. Buehler, "Hydration and distance dependence of intermolecular shearing between collagen molecules in a model microfibril," *Journal of Biomechanics*, vol. 45, pp. 2079–2083, 2012.

[597] S. M. Pradhan, K. S. Katti, and D. R. Katti, "Structural hierarchy controls deformation behavior of collagen," *Biomacromolecules*, vol. 13, pp. 2562–2569, 2012.

[598] Y. Tang, R. Ballarini, M. J. Buehler, and S. J. Eppell, "Deformation micromechanisms of collagen fibrils under uniaxial tension," *J. R. Soc. Interface*, vol. 7, pp. 839–850, 2010.

[599] C. Koh and M. Oyen, "Branching toughens fibrous networks," *Journal of the Mechanical Behavior of Biomedical Materials*, vol. 12, pp. 74–82, 2012.

[600] T. C. Baradet, J. C. Haselgrove, and J. W. Weisel, "Three-dimensional reconstructuion of fibrin clot networks from stereoscopic intermediate voltage electron microscope images and analysis of branching," *Biophys. J.*, vol. 68, pp. 1551–1560, 1995.

[601] J. Maxwell, "On the calculation of the equilibrium and stiffness of frames," *Philosophical Magazine*, vol. 27, no. 1, pp. 294–299, 1864.

[602] Y. li Yang, L. M. Leone, and L. J. Kaufman, "Elastic moduli of collagen gels can be predicted from two-dimensional confocal microscopy," *Biophys. J.*, vol. 97, pp. 2051–2060, 2009.

[603] S. Kreger, B. Bell, J. Bailey, E. Stites, J. Kuske, B. Waisner, and S. Voytik-Harbin, "Polymerization and matrix physical properties as important design considerations for soluble collagen formulations," *Biopolymers*, vol. 93, no. 8, pp. 690–707, 2010.

[604] A. Licup, A. Sharma, and F. MacKintosh, "Elastic regimes of subisostatic athermal fiber networks," *ArXiv*, p. 1509.09212v2, 2015.

[605] A. Sharma, A. Licup, K. Jansen, R. Rens, M. Sheinman, G. Koenderink, and F. MacKintosh, "Strain-controlled criticality governs the nonlinear mechanics of fibre networks," *ArXiv*, p. 1506.07792, 2015.

[606] A. Guzman, M. J. Ziperstein, and L. J. Kaufman, "The effect of fibrillar matrix architecture on tumor cell invasion of physically challenging environments," *Biomaterials*, vol. 35, no. 25, pp. 6954–63, 2014.

[607] S. Newman, M. C. C. Allain, G. Forgacs, and D. Beysens, "Viscosity and elasticity during collagen assembly in vitro: Relevance to matrix-driven translocation," *Biopolymers*, vol. 41, pp. 337–347, 1997.

[608] J. Zhu and L. J. Kaufman, "Collagen I self-assembly: Revealing the developing structures that generate turbidity," *Biophys. J.*, vol. 106, pp. 1822–1831, 2014.

[609] J. Brokaw, C. Doillon, R. Hahn, D. Birk, R. Berg, and F. Silver, "Turbidimetry and morphological studies of type I collagen fiber assembly in vitro and the influence of fibronectin," *Int. J. Biol. Macromol.*, vol. 7, pp. 135–140, 1985.

[610] T. Wess, "Collagen fibril form and function," *Adv. Protein Chem.*, pp. 341–374, 2005.

[611] E. E. Antoine, P. P. Vlachos, and M. N. Rylander, "Tunable collagen I hydrogels for engineered physiological tissue micro-environments," *PLoS ONE*, vol. 10, no. 3, p. e0122500, 2015.

[612] K. C. Gersh, C. Nagaswami, and J. W. Weisel, "Fibrin network structure and clot mechanical properties are altered by incorporation of erythrocytes," *Thromb. Haemost.*, vol. 102, no. 6, pp. 1169–1175, 2009.

[613] D. Head, A. Levine, and F. MacKintosh, "Distinct regimes of elastic response and deformation modes of cross-linked cytoskeletal and semiflexible polymer networks," *PRL*, vol. 68, p. 061907, 2003.

[614] J. Wilhelm and E. Frey, "Elasticity of stiff polymer networks," *PRL*, vol. 91, no. 10, p. 108103, 2003.

[615] S. Alexander, "Amorphous solids: their structure, lattice dynamics and elasticity," *Physics Reports*, vol. 296, pp. 65–236, 1998.

[616] L. Landau and E. Lifshiftz, eds., *Theory of elasticity.* Pergamon Press, Oxford, 2nd ed., 1970.

[617] M. Archilli and D. Mantovani, "Tailoring mechanical properties of collagen-based scaffolds for vascular tissue engineering: The effects of pH, temperature and ionic strength on gelation," *Polymers*, vol. 2, pp. 664–680, 2010.

[618] Y. li Yang and L. J. Kaufman, "Rheology and confocal reflectance microscopy as probes of mechanical properties and structure during collagen and collagen/hyaluronan self-assembly," *Biophys. J.*, vol. 96, pp. 1566–1585, 2009.

[619] T. J. Wess and J. P. Orger, "Changes in collagen structure: drying, dehydrothermal treatment and relation to long term deterioration," *Thermochimica acta*, vol. 365, pp. 119–128, 2000.

[620] G. Forgacs, S. A. Newman, B. Hinner, C. W. Maier, and E. Sachmann, "Assembly of collagen matrices as a phase transition revealed by structural and rheologic studies," *Biophys. J.*, vol. 84, pp. 1272–1280, 2003.

[621] L. M. Jawerth, S. Münster, D. A. Vader, B. Fabry, and D. A. Weitz, "A blind spot in confocal reflection microscopy: The dependence of fiber brightness on fiber orientation in imaging biopolymer networks," *Biophys. J.*, vol. 98, no. 3, pp. L01–L03, 2009.

[622] A. Arrott and J. E. Noakes, "Approximate equation of state for nickel near its critical temperature," *PRL*, vol. 19, no. 14, pp. 786–789, 1967.

[623] F. MacKintosh and A. Licup, "personal communication,"

[624] F. MacKintosh, "personal communication,"

[625] R. B. Svensson, T. Hassenkam, C. A. Grant, and S. P. Magnusson, "Tensile properties of human collagen fibrils and fascicles are insensitive to environmental salts," *Biophys. J.*, vol. 99, pp. 4020–4027, 2010.

[626] P. A. Janmey, M. E. McCormick, S. Rammensee, J. L. Leight, P. C. Georges, and F. C. MacKintosh, "Negative normal stress in semiflexible biopolymer gels," *Nature Materials*, vol. 6, pp. 48–51, 2006.

[627] D. Karamichos, R. Brown, and V. Mudera, "Collagen stiffness regulates cellular contraction and matrix remodeling gene expression," *Journal of Biomedical Materials Research Part A*, vol. 83, no. 3, pp. 887–894, 2007.

[628] A. D. Doyle, R. J. Petrie, M. L. Kutys, and K. M. Yamada, "Dimensions in cell migration," *Current Opinion in Cell Biology*, vol. 25, pp. 642–649, 2013.

[629] M. J. Buehler, "Nature designs tough collagen: Explaining the nanostructure of collagen fibrils," *PNAS*, vol. 103, no. 33, pp. 12285–12290, 2006.

[630] D. Hulmes, A. Miller, D. Parry, K. Piez, and J. Woodhead-Galloway, "Analysis of the primary structure of collagen for the origins of molecular packing," *J. Mol. Biol.*, vol. 79, pp. 137–148, 1973.

[631] W. Traub, "Molecular assembly in collagen," *FEBS Letters*, vol. 92, no. 1, pp. 114–120, 1978.

[632] F. Grinnell, "Fibroblast mechanics in three-dimentional collagen matrices," *Journal of Bodywork and Movement Therapies*, vol. 12, pp. 191–193, 2008.

[633] E. Bell, H. Ehrlich, D. Buttle, and T. Nakatsuji, "Living tissue formed invitro and accepted as skin-euivalent tissue of full thickness," *Science*, vol. 211, no. 4486, pp. 1052–1054, 1981.

[634] M. A. Carlson and M. T. Longaker, "The fibroblast-populated collagen matrix as a model of wound healing: areview of the evidence," *Wound Repair and Regeneration*, vol. 12, pp. 134–147, 2004.

[635] V. Moulin, G. Castilloux, A. Jean, D. Garrel, F. Auger, and L. Germain, "In vitro models to study wound healing fibroblasts," *Burns*, vol. 22, no. 5, pp. 359–362, 1996.

[636] R. M. Ilagan, K. I. Guthrie, S. F. Quinlan, and H. S. Rapoport, "Linear mesurement of cell contraction in a capillary collagen gel system," *Biotechniques*, vol. 48, no. 2, pp. 153–155, 2009.

[637] M. A. Wozniak, R. Desai, P. A. Solski, C. J. Der, and P. J. Keely, "Rock-generated contractility regulates breast epithelial cell differentiation in response to the physical properties of a three-dimensional collagen matrix," *Journal of Cell Biology*, vol. 163, no. 3, pp. 583–595, 2003.

[638] F. Grinnel and W. M. Petroll, "Cell motility and mechanics in three-dimensional collagen matrices," *Annual Review of Cell and Developmental Biology*, vol. 26, pp. 335–361, 2010.

[639] D. G. Wallace and J. Rosenblatt, "Collagen gel systems for sustained delivery and tissue engineering," *Advanced Drug Delivery Reviews*, vol. 55, pp. 1631–1649, 2003.

[640] T. Wakatsuki and E. L. Elson, "Reciprocal interactions between cells and extracellular matrix during remodeling of tissue constructs," *Biophysical Chemistry*, vol. 100, pp. 593–605, 2003.

[641] M. Bitar, R. A. Brown, V. Salih, A. G. Kidane, J. C. Knowles, and S. N. Nazhat, "Effect of cell density on osteoblastic differentiation and matrix degradation of biomimetic dense collagen scaffolds," *Biomacromolecules*, vol. 9, pp. 129–135, 2008.

[642] M.-Y. Chen, L. Jeng, Y.-L. Sun, C.-F. Zhao, M. Zobitz, S. Moran, P. Amadio, and K.-N. An, "Contraction of collagen gels seeded with tendon cells," *Biorheology*, vol. 43, pp. 337–345, 2006.

[643] I. Harada, S.-G. Kim, C. S. Cho, H. Kurosawa, and T. Akaike, "A simple combined floating and anchored collagen gel for enhancing mechanical strength of culture system," *Journal of Biomedical Materials Research Part A*, vol. 80A, no. 1, pp. 123–130, 2006.

[644] M. Ahearne, S. L. Wilson, K.-K. Liu, S. Rauz, A. J. E. Haj, and Y. Yang, "Influence of cell and collagen concentration on the cell-matrix mechanical relationship in a corneal stroma wound healing model," *Experimental Eye Research*, vol. 91, pp. 584–591, 2010.

[645] M. Ahearne, Y. Yang, A. J. E. Haj, K. Y. Then, and K.-K. Liu, "Characterization of the viscoelastic properties of thin hydrogel-based constracts for tissue engineering applications," *J. R. Soc. Interface*, vol. 2, pp. 455–463, 2005.

[646] R. Brown, R. Prajapati, D. McGrouther, I. Yannas, and M. Eastwood, "Tensional homeostasis in dermal fibroblasts: Mechanical responses to mechanical loading in three-dimensional substrates," *Journal of Cellular Physiology*, vol. 175, pp. 323–332, 1998.

[647] D. Karamichos, R. Brown, and V. Mudera, "Complex dependence of substrate stiffness and serum concentration on cell-force generation," *Journal of Biomedical Materials Research Part A*, vol. 78, no. 2, pp. 407–415, 2006.

[648] J. P. Marquez, G. M. Genin, K. M. Pryse, and E. L. Elson, "Cellular and matrix contributions to tissue construct stiffness increase with cellular concentration," *Annals of Biomedical Engineering*, vol. 34, no. 9, pp. 1475–1482, 2006.

[649] G. Jenkins, K. L. Redwood, L. Meadows, and M. R. Green, "Effect of gel re-organization and tensional forces on $\alpha 2\beta 1$ integrin levels in dermal fibroblasts," *Eur. J. Biochem.*, vol. 263, pp. 93–103, 1999.

[650] E. Paluch, M. Piel, J. Prost, M. Bornens, and C. Sykes, "Cortical actomyosin breakage triggers shape oscillations in cells and cell fragments," *Biophys. J.*, vol. 89, pp. 724–733, 2005.

[651] A. Pizzo, K. Kokini, L. Vaughn, B. Waisner, and S. Voytik-Harbin, "Extracellular matrix (ECM) microstructural composition regulates local cell-ECM biomechanics and fundamental fibroblast behavior: a multidimensional perspective," *Journal of Applied Physiology*, vol. 98, pp. 1909–1921, 2005.

[652] J. J. Tomasek, C. J. Haaksma, R. J. Eddy, and M. B. Vaughan, "Fibroblast contraction occurs on release of tension in attached collagen lattices: Dependency on an organized actin cytoskeleton and serum," *The Anatomical Records*, vol. 232, pp. 359–368, 1992.

[653] T. A. Ulrich, T. G. Lee, H. K. Shon, D. W. Moon, and S. Kumar, "Microscale mechanisms of agarose-induced disruption of collagen remodeling," *Biomaterials*, vol. 32, pp. 5633–5642, 2011.

[654] S. I. Fraley, P.-H. Wu, L. He, Y. Feng, R. Krisnamurthy, G. D. Longmore, and D. Wirtz, "Three-dimensional matrix fiber alignment modulates cell migration and MT1-MMP utility by spatially and temporally directing protrusions," *Scientific Reports*, vol. 5, p. 14580, 2015.

[655] H. P. Ehrlich, D. J. Buttle, and D. H. Bernanke, "Physiological variables affecting collagen lattice contraction by human dermal fibroblasts," *Experimental and Molecular Pathology*, vol. 50, pp. 220–229, 1989.

[656] P. Delvoye, P. Wiliquet, J.-L. LevÃłque, B. V. Nusgens, and C. M. Lapiére, "Measurement of mechanical forces generated by skin fibroblasts embedded in a three-dimensional collagen gel," *The journal of investigative dermatology*, vol. 97, no. 5, pp. 898–902, 1991.

[657] K. Sato, S. Hattori, S. Irie, and S. Kawashima, "Spike formation by fibroblasts adhering to fibrillar collagen I gel," *Cell Structure and Function*, vol. 28, pp. 229–241, 2003.

[658] E. Hadjipanayi, V. Mudera, and R. A. Brown, "Guiding cell migration in 3D: A collagen matrix with graded directional stiffness," *Cell Motility and the Cytoskeleton*, vol. 66, pp. 121–128, 2009.

[659] J. Fringer and F. Grinnel, "Fibrobalst quiescence in floating or released collagen matrices," *Journal of Biological Chemistry*, vol. 276, no. 33, pp. 31047–31052, 2001.

[660] H. Mohammadi, P. A. Janmey, and C. A. McCulloch, "Lateral boundary mechanosensing by adherent cells in a collagen gel system," *Biomaterials*, vol. 35, pp. 1138–1149, 2014.

[661] D. J. White, S. Puranen, M. S. Johnson, and J. Heino, "The collagen receptor subfamily of the integrins," *The International Journal of Biochemistry & Cell Biology*, vol. 36, pp. 1405–1410, 2004.

[662] J. Jokinen, E. Dadu, P. Nykvist, J. Käpylä, D. J. White, J. Ivaska, P. Vehviläinen, H. Reunanen, H. Larjava, L. Häkkinen, , and J. Heino, "Integrin-mediated cell adhesion to type I collagen fibrils," *The Journal of Biological Chemistry*, vol. 30, pp. 31956–31963, 2004.

[663] D. Gullberg, K. R. Gehisen, D. C. Turner, K. Ahlen, L. S. Zijenah, M. J. Barnes, and K. Rubin, "Analysis of $\alpha 1\beta 1$, $\alpha 2\beta 1$ and $\alpha 3\beta 1$ integrins in cell-collagen interactions: identification of conformation dependent $\alpha 1\beta 1$ binding sites in collagen type I," *The EMBO Journal*, vol. 11, no. 11, pp. 3865–3873, 1992.

[664] J. Heino, "The collagen receptor integrins have distinct ligand recognition and signaling functions," *Matrix Biology*, vol. 19, pp. 319–323, 2000.

[665] V. Reyhani, P. Seddigh, B. Guss, R. Gustafsson, L. Rask, and K. Rubin, "Fibrin binds to collagen and provides a bridge for $\alpha V\beta 3$ integrin-dependent contraction of collagen gels," *Biochemical Journal*, vol. 462, no. 1, pp. 113–123, 2014.

[666] M. E. Cooke, T. Sakai, and D. F. Mosher, "Contraction of collagen matrices mediated by $\alpha 2\beta 1$A and $\alpha v\beta 3$ integrins," *Journal of Cell Science*, vol. 113, pp. 2375–2383, 2000.

[667] S. Popova, E. Lundgren-Åkerlund, H. Wiig, and D. Gullberg, "Physiology and pathology of collagen receptors," *Acta Physiol.*, vol. 190, pp. 179–187, 2007.

[668] L. Camper, K. Holmvall, C. Wängnerud, A. Aszódi, and E. Lundgren-Åkerlund, "Distribution of the collagen-binding integrin $\alpha 10\beta 1$ during mouse development," *Cell Tissue Res.*, vol. 306, pp. 107–116, 2001.

[669] S. Liu, X. Shi-wen, K. Blumbach, M. Eastwood, C. P. Denton, B. Eckes, T. Krieg, D. J. Abraham, and A. Leask, "Expression of integrin $\beta 1$ by fibroblasts is required for tissue repair in vivo," *Journal of Cell Science*, vol. 123, pp. 3674–3682, 2010.

[670] Y. Garcia, R. Collighan, M. Griffin, and A. Pandit, "Assessment of cell viability in a three-dimensional enzymatically cross-linked collagen scaffold," *Journal Mater Sci: Mater Med*, vol. 18, pp. 1991–2001, 2007.

[671] C.-L. Chiu, M. A. Digman, and E. Gratton, "Cell matrix remodeling ability shown by image spatial correlation," *Journal of Biophysics*, vol. 2013, p. 532030(8), 2013.

[672] B. M. Steinberg, K. Smith, M. Colozzo, and R. Pollack, "Establishment and transformation diminish the ability of fibroblasts to contract a native collagen gel," *The Journal of Cell Biology*, vol. 87, pp. 304–308, 1980.

[673] A. H. Dahlmann-Noor, B. Martin-Martin, M. Eastwood, P. T. Khaw, and M. Bailly, "Dynamic protrusive cell behaviour generates force and drives early matrix contraction by fibroblasts," *Experimental Cell Research*, vol. 313, pp. 4158–4169, 2007.

[674] B. Hinz, "Formation and function of the myofibroblast during tissue repair," *Journal of Investigative Dermatology*, vol. 127, pp. 526–537, 2007.

[675] M. Tulla, O. T. Pentikäinen, T. Viitasalo, J. Käpylä, U. Impola, P. Nykvist, L. Nissinen, M. S. Johnson, and J. Heino, "Selective binding of collagen subtypes by integrin $\alpha 1$I, $\alpha 2$I, and $\alpha 10$I domains," *Journal of Biological Chemistry*, vol. 276, no. 51, pp. 48206–48212, 2001.

[676] P. Nykvist, H. Tu, J. Ivaska, J. Käpylä, T. Pihlajaniemi, and J. Heino, "Distinct recognition of collagen subtypes by $\alpha 1\beta 1$ and $\alpha 2\beta 1$ integrins," *The Journal of Biological Chemistry*, vol. 275, pp. 8255–8261, 2000.

[677] C.-F. Tiger, F. Fougerousse, G. Grundström, T. Velling, and D. Gullberg, "$\alpha 11\beta 1$ integrin is a receptor for interstitial collagens involved in cell migration and collagen reorganization on mesenchymal nonmuscle cells," *Developmental Biology*, vol. 237, pp. 116–129, 2001.